



**Pilkington Library**

Author/Filing Title ..... *LEPPER* .....

Vol. No. .... Class Mark ..... *T* .....

**Please note that fines are charged on ALL  
overdue items.**

<i>LOAN COPY</i>	
------------------	--

0402219880



BADMINTON PRESS  
UNIT 1 BROOK ST  
SYSTON  
LEICESTER, LE7 1GD  
ENGLAND  
TEL: 0116 260 2917



**THE DEVELOPMENT AND TESTING OF A PARAMETRIC  
SONAR SYSTEM FOR USE IN SEDIMENT CLASSIFICATION  
AND THE DETECTION OF BURIED OBJECTS**

by


**Paul Andrew Lepper, BSc**

*Submitted in partial fulfilment of the requirements for the award of  
Doctor of Philosophy of Loughborough University*

October 1999

Supervisor: Professor Bryan Woodward, PhD, DIC, CEng, FIEE, FIOA, FRGS  
The Underwater Acoustics Research Group  
Department of Electronic and Electrical Engineering

© by Paul Lepper, 1999

 Loughborough University PLD Library
Date <u>May 00</u>
Class
Acc No. <u>040221988</u>

M000/658LB

## ABSTRACT

### **THE DEVELOPMENT AND TESTING OF A PARAMETRIC SONAR SYSTEM FOR USE IN SEDIMENT CLASSIFICATION AND THE DETECTION OF BURIED OBJECTS**

This thesis describes the work carried out in the development and testing of parametric sonar systems for application in the fields of seabed sediment characterisation and classification, and the detection of seabed embedded objects.

Parametric sonar systems offer a number of advantages over conventional sonar systems. This is especially true of the conflicting requirements of both seabed delineation and penetration required for a practical sub-seabed profiling system. Echoes from sub-bottom layers vary in strength dependant on both the boundary acoustic reflectivity and the absorption characteristics of the layer above. Absorption effects are usually frequency dependent, allowing better penetration to lower frequency signals. In both conventional and parametric sonar systems the degree of seabed delineation is related to the signal beam-width. A high directivity system provides a higher degree of seabed delineation and therefore smaller search area and reduced signal clutter. A parametric sonar offers advantages over a conventional sonar of the same physical size with a combination of a lower frequency and a narrow beam-width.

The programme of study described outlines the principles of non-linear signal generation using parametric sonar and the development and calibration of a 75 kHz parametric sonar and subsequent utilisation of the system in sediment classification experiments. Work involved in the development and testing of an alternate 40 kHz system is also described.

An investigation of the use of a parametric sonar for the detection of buried objects has also been carried out. This includes a description of the results from a study programme investigating scattering from cylindrical targets in the free field and partially embedded in the seabed.

The utilisation of a parametric sonar in a practical environment has also led to an investigation of the improvement of systems deployment. The correction of alignment errors due to ship motion has been investigated using electronic steering and discontinuous transmission techniques. Methods of assessment of alignment errors due to ship motion and seabed slope have also been studied. These include signal propagation modelling in both the water column and the sediment layers and bottom slope measurement using an acoustic signal.

## ACKNOWLEDGMENTS

I would like to express my especial thanks to my supervisor Professor Bryan Woodward for his encouragement, guidance and persistence. Similarly I would also like to thank Dave Goodson, Paul Connelly, Darryl Newborough and Chris Richards for their help, without which much of this work would not have been possible. I would also like to express my gratitude to Professor Jim Cook for his encouragement and assistance in the execution of this work.

I am grateful to the European Commission for the funding of various research projects that have allowed this work to take place and specifically all the partners on the REBECCA, ACUSTICA, DEO and SIGMA projects. In particular I would like to thank colleagues at the Indian Institute of Technology (Delhi) and the Foundation for Research and Technology - Hellas (Crete) for their help and hospitality during the periods that I was with them.

Thanks also to Eric Armstrong, Phil Copland and John Simmonds (Marine Laboratory, Fisheries Research Services, The Scottish Office) for their assistance in experiments conducted on Loch Duich trial site. Professor Tom Curtis and Andy Webb (Defence Evaluation and Research Agency, Winfrith Technology Centre) for their help in the development of hardware and software used in these projects. Thanks to Mike Somers OBE and associates from the Institute of Oceanographic Sciences Deacon Laboratory for their help with the transducer array. Thanks also to the crews of the IFREMER oceanographic research vessels *Thalia* and *Le Noroit* and the Belgian Navy research vessel *Belgica*.

I would also like to thank the technician staff in the Department of Electronic Electrical Engineering for their help in the construction of equipment and support during trials.

Finally thanks to my Mum and Dad and especially Lisa for everything.

## TABLE OF CONTENTS

<b>ABSTRACT</b>	<b>i</b>
<b>ACKNOWLEDGEMENTS</b>	<b>ii</b>
<b>TABLE OF CONTENTS</b>	<b>iv</b>
<b>CHAPTER 1</b>	
<b>INTRODUCTION</b>	<b>1</b>
1.1 General	1
1.2 Objectives and organisation of Thesis	3
<b>CHAPTER 2</b>	
<b>NON-LINEAR ACOUSTICS</b>	<b>5</b>
2.1 Non-linear effects in acoustics	5
2.2 Parametric wave equation	8
2.3 Non-linear sonar development	17
2.3.1 The parametric source	17
2.3.2 Non-linear receiver arrays	21
2.4 Conclusion	22
References	24
<b>CHAPTER 3</b>	
<b>PARAMETRIC SONAR DEVELOPMENTS</b>	<b>28</b>
3.1 Parametric sonar design constraints	28
3.2 LU / IOS parametric sonar system	33
3.2.1 Transducer array	33
3.2.2 Power output predictions	35
3.2.3 Impedance characteristics	36
3.3 Conclusion	42
References	43



## **CHAPTER FOUR**

<b>SYSTEM COMMISSIONING AND CALIBRATION</b>	<b>45</b>
4.1 Loch Duich field site	45
4.2 Experimental procedure	46
4.3 Test signals	48
4.4 Initial system tests	49
4.5 Primary frequency beam-patterns	50
4.6 'Dynamic' beam-pattern measurements	52
4.7 Primary frequency source level	56
4.8 Secondary frequency generation	61
4.9 Secondary frequency beam patterns	66
4.10 Secondary frequency source level	68
4.11 Conclusion	71
References	73

## **CHAPTER FIVE**

<b>SIGNAL SYNTHESIS / DATA CAPTURE SYSTEMS</b>	<b>74</b>
5.1 Introduction	74
5.2 Signal synthesis system hardware	74
5.2.1 Data loading phase	76
5.2.2 Transmit phase	77
5.2.3 Extended memory mapping	78
5.2.4 Additional control lines	79
5.3 Data capture system	80
5.3.1 Data capture hardware / software	80
5.3.2 Pre-conditioning filters	83
5.3.3 Auto-logging systems	85
5.4 Software signal generation	86
5.4.1 Non-linear signal synthesis	86
5.4.2 Linear Frequency Modulated (LFM) CHIRP signals	91
5.4.3 Beam steering	95
5.4.4 Sector scanning	99
5.5 Conclusion	102
References	103

---

## CHAPTER SIX

### USE OF A PARAMETRIC ARRAY IN THE CHARACTERISATION OF MARINE SEDIMENTS

	104	
6.1	Introduction	104
6.2	REBECCA project	106
6.2.1	Introduction	106
6.2.2	Project aims	106
6.2.3	Sea Trials	109
6.2.3.1	Loch Duich, Scotland	109
6.2.3.2	Rade de Brest ( <i>Thalia</i> )	109
6.2.3.3	Rade de Brest ( <i>Le Noroit</i> )	112
6.2.4	Sea trial results	114
6.2.5	Conclusion	118
6.3	SIGMA project	119
6.3.1	Introduction	119
6.3.2	Hardware and software developments	120
6.3.3	Sea Trials	123
6.3.3.1	Introduction	123
6.3.3.2	System deployment	124
6.3.3.3	Results	126
6.3.4	Conclusions	128
6.4	ACUSTICA project	130
6.4.1	Introduction	130
6.4.2	IIT parametric sonar system	131
6.4.2.1	Sonar system	131
6.4.2.2	Lake Edukki open water trial	132
6.4.2.3	Results	133
6.4.2.4	Conclusion (IIT parametric system)	136
6.4.3	Acoustic propagation modelling	136
6.4.4	Real time assessment of multi-path signal arrivals	141
6.5	Conclusions	142
	References	144

## **CHAPTER SEVEN**

### **FREE-FIELD EXPERIMENT WITH A CYLINDRICAL TARGET 149**

7.1	Introduction	149
7.2	Free-field measurement	150
7.3	Experimental deployment	153
7.4	Free field measurement equipment	155
7.4.1	Parametric source	155
7.4.2	Receiver systems	156
7.4.3	Target control system	157
7.4.4	System integration	160
7.5	Experimental procedure (free-field measurements)	162
7.5.1	Equipment deployment / system testing	162
7.5.2	Target measurements	163
7.5.3	Bottom scattering measurements	163
7.6	Results (free-field measurements)	165
7.6.1	Introduction	165
7.6.2	Ricker signal analysis	166
7.6.3	Free-field target echo analysis	172
7.7	Free-field measurement conclusion	182
	References	184

## **CHAPTER EIGHT**

### **DETECTION OF EMBEDDED OBJECTS 187**

8.1	Introduction	187
8.2	Seabed topography survey	187
8.3	Equipment deployment	189
8.4	Embedded target measurement equipment	193
8.4.1	Parametric source	193
8.4.2	Receiver systems (Embedded object)	194
8.4.3	System integration (Embedded object)	195
8.5	Experimental procedure (target embedded measurements)	197
8.5.1	Equipment deployment / system testing	197
8.5.2	Target aspect angle measurement	197
8.5.3	Acoustic measurement	201

8.5.4	Additional measurements	202
8.6	Results (seabed embedded object measurements)	203
8.6.1	Introduction	203
8.6.2	Acoustic data analysis	203
8.6.3	Non-acoustic measurements	216
8.7	Conclusions	219

## **CHAPTER NINE**

	<b>REAL-TIME CORRECTION OF TRANSMISSION PLATFORM IN INSTABILITIES USING A PARAMETRIC ARRAY</b>	<b>221</b>
9.1	Introduction	221
9.2	Tow-fish and streamer deployment	222
9.3	Ship and tow-fish motion	224
9.4	Dynamic stabilisation	226
9.4.1	Introduction	226
9.4.2	Error prediction	228
9.4.2.1	Introduction	228
9.4.2.2	Software models	228
9.4.2.3	Assumptions	230
9.4.3	Error measurement	232
9.4.4	Dynamic stabilisation using electronic beam-steering	233
9.4.4.1	Methodology	233
9.4.4.2	Results	236
9.4.5	Discontinuous transmissions	238
9.5	Seabed inclination	238
9.5.1	Seabed profile using back-scatter	238
9.5.2	Seabed slope through depth sounding	239
9.6	Conclusions	241
	References	243

**CHAPTER TEN**

<b>CONCLUSIONS</b>	<b>244</b>
10.1 System operation	244
10.2 Use of a parametric array for sediment classification	245
10.3 Detection of embedded objects	246
10.4 Summary	247
10.5 Future work	247

## CHAPTER ONE

# INTRODUCTION

### 1.1 General

A great deal of work has been done on the use of parametric, or non-linear, sonar systems since the 1950's. Much of this work stems from Westervelt's original papers [ref. Chapter 2 2.7, 2.8] in 1957 and 1963, in which he outlined a generalised form of a non-linear wave equation for sound propagation in a fluid. He pointed out that the generation of secondary frequency components is possible under certain conditions due to the non-linear propagation of a sound wave in water. The source of these signals act as if generated by an end-fire array of virtual sources existing within the water column.

Westervelt's model allowed prediction of the interaction effects of two acoustic waves of differing frequencies ( $f_1, f_2$ ) travelling in the same direction. Under certain conditions *secondary* frequency signals equivalent to the sum ( $f_1 + f_2$ ) and difference ( $f_1 - f_2$ ) of the two *primary* signals can be generated due to the non-linearity of the acoustic wave propagation. Both the sum and difference frequency signals possess a number of interesting characteristics when compared with conventional sound generation signals. The sum signal is however often quickly attenuated, being of a higher frequency than the primaries. The difference secondary signal ( $f_1 - f_2$ ) is therefore of primary interest in this study. Historical developments, both theoretical and experimental (outlined in more detail in Chapter 2) of Westervelt's original model, have led to a series of models encompassing a range of limiting factors for a practical non-linear sonar system.

These systems exhibit a much higher directivity than that seen with a conventional sonar of the same frequency and size. This low frequency, high directivity source is potentially useful in fulfilling the conflicting requirements of both resolution and penetration for a practical sub-seabed sonar system. Echo levels from sub-

bottom layers or objects are dependent on the boundary acoustic reflectivity and the absorption properties of the layer above. Absorption is usually seen to be frequency dependant, i.e. absorption increases with frequency. A lower frequency system would therefore provide better seabed penetration.

Depth resolution within sediments is dependent on the pulse width for a conventional sonar, or bandwidth in the case of pulse-compression systems. In both cases the resolution is also dependent on the beam-width of the system. The smaller the beam-width the better the resolution. The delayed arrival of back-scattered energy from the edges of the beam compared with the normal incidence resulting in an elongation in the pulse length. The broader beam would therefore exhibit a lower range resolution.

A linear system operating at the same frequency as the difference frequency of a non-linear system would have to be considerably larger to achieve the same beam-widths and therefore range resolution. Parametric systems also show reduced side-lobe radiation (outside the central main lobe), thus improving signal-to-noise due to reduced reverberation energy at the lower frequencies. These advantages are however balanced against the relatively poor efficiency of the secondary frequency generation, as only a relatively small proportion of the total applied power leads to generation of the non-linear signal.

Regardless of these limits the development of practical parametric sonar systems has received considerable attention in recent years. Applications including marine-sediment classification, buried-object detection and through-water communications have looked towards the possible use of non-linear systems in an underwater environment. This movement towards practical systems has also led to advances in the development of electronically steerable transducer arrays, allowing development of sector-scan non-linear sonar systems. The use of these systems at sea has led to the possibility of the real-time correction of transmission platform instabilities using dynamic phase-steering of a non-linear source.

## 1.2 Objectives and organisation of thesis

This study aims to outline various aspects of the development of a practical non-linear system. Despite the depth and extent of material based on the use of parametric sonars, a great deal of interest is still being shown in further developments in this field. This is especially true of improvements made in sub-bottom detection techniques. This is borne out by the involvement of Loughborough University in a number of projects looking at the use of parametric sonars for sediment classification and buried object detection. These have included the REBECCA (Reflection from Bottom, Echo Classification and Characterisation of Acoustical propagation), ACUSTICA (Acoustic Characterisation of Undersea Sediments To Initiate Commercial Applications) and the SIGMA (Sediment Identification for Geotechnics by Marine Acoustics) projects and buried object detection during the DEO (Detection of Embedded Objects) project.

This thesis discusses the development of a sonar system using well-established techniques. This is taken from initial development and testing to the practical application in a variety of environments and uses. This work is then extended to include the development of techniques to overcome problems experienced in the use of such a system in the *real world*.

- Chapter 1 Introduction.
- Chapter 2 Review of the basic principles relating to a non-linear sound source.
- Chapter 3 Design considerations and development of a new 75 kHz primary frequency phase steerable non-linear sonar system.
- Chapter 4 Results of the initial testing and calibration of the 75 kHz parametric sonar system, including trials conducted on the test range on Loch Duich on the West Coast of Scotland.



- Chapter 5 Discussion of the transmitter and receiver hardware and software developments, implicit in the signal synthesis and data capture requirements of a new sonar system.
- Chapter 6 The practical deployment of the 75 kHz parametric sonar for use in sediment classification measurements. Results from several ocean-going trials are presented. This chapter also discusses the development of a new non-linear sonar by the Indian Institute of Technology (IIT) and subsequent sea trials.
- Chapter 7 Description of the measurement of the free-field scattering properties of a thin-walled cylindrical target using a parametric array. Acoustic trials were carried out on Loch Duich in 1997. This involved the measurement of the back-scattered properties of various targets at a range of aspect angles whilst being insonified by a parametric array.
- Chapter 8 Description of the second phase experiment involving the measurement of back-scattered energy from a seabed-embedded target at a range of aspect and seabed incidence angles. Trials were again conducted on the acoustic test range on Loch Duich in 1998.
- Chapter 9 A discussion of the further developments in stabilisation of a practical sonar system at sea. The use of dynamic beam steering in at least one axis is considered for the real-time correction of transmission platform instabilities. Results of the implementation of such a system are presented.
- Chapter 10 Conclusions and further work.

## CHAPTER TWO

# NON-LINEAR ACOUSTICS

### 2.1 Non-linear effects in acoustics

The relationship between density changes and pressure variations due to the presence of the acoustic wave in water is non-linear. This relationship can be seen physically in certain conditions in the form of a progressive deformation of an acoustic waveform. Equation (2.1) shows the ratio of pressure and density of the propagation medium can be related to the speed of sound  $c$ , using the expression;

$$c = \sqrt{\left(\frac{\partial P}{\partial \rho}\right)}. \quad (2.1)$$

In the case of an isothermal gas, pressure  $P$  and density  $\rho$  have a linear relationship (a uniform change in pressure is accompanied by a linear change in density), giving rise to a constant speed of sound. In water however a non-linearity relationship exists between them, giving rise to variations in  $c$  with changes in pressure. This variation in sound speed at different parts of a periodic pressure waveform results in a deformation in the original waveform and the generation of new frequency components. In the case of a simple wave in a lossless gas this non-linearity may be traced to both kinematic and thermodynamic effects <sup>[2.1]</sup>. Kinetically, particles are in motion with a velocity  $u'$  regardless of the presence of an acoustic source. When observed from a stationary point, the fluid particles have a net speed of  $u' + c$ , where  $c$  is the speed of the acoustic wave. Velocity  $u'$  will act in a range of directions in line with and away from the direction of the wave propagation, leading to variations in the wave speed.

Thermodynamically, pressure variations due to the presence of an acoustic wave can lead to effective changes in the medium temperature. This alters the effective wave velocity at any point. With a positive acoustic pressure, a density increase is

seen and so the medium becomes "warmer". This in turn allows for an increase in the wave speed  $c$ . Inversely negative pressures result in a "cooling", thus reducing  $c$ . This is shown in equation (2.2) for an out-going signal, where  $\beta' = (\gamma + 1)/2$ , and  $\gamma = (C_p/C_v)$  is the ratio of the principal heat capacities at constant pressure and constant volume respectively. It can be shown <sup>[2.1]</sup>, as a result that

$$c = \left( \frac{dx}{dt} \right)_{u = \text{constant}} = \beta' u + c_0. \quad (2.2)$$

The variations in density and pressure will relate directly to variations in  $\gamma$ , which from equation (2.2) will be seen as variations in the wave speed along the line of propagation of the wave.

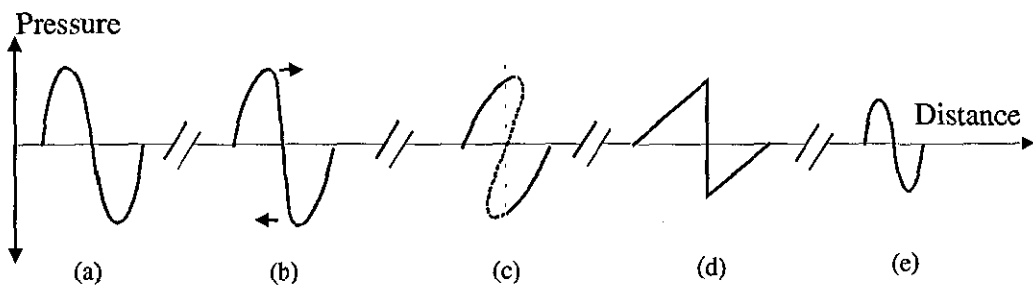


FIGURE 2.1 PROGRESSIVE NON-LINEAR DISTORTION OF A SINUSOIDAL WAVE

The variation with sound velocity with changes in pressure can be seen when considering a sinusoidal waveform as shown in Figure 2.1 (a). Variation of the pressure wave velocity with pressure cause the *peaks* of a sinusoidal waveform travel faster than the *troughs*, as shown in Figure 2.1 (b). If the deformation continues a theoretical condition shown in Figure 2.1 (c) would occur. This leads to a multi-valued waveform, clearly not possible in nature. In reality the sinusoidal signal forms *saw-tooth* like waveform, as seen in Figure 2.1 (d). Inherent in the generation of this is the production of harmonics of the primary acoustic wave <sup>[2.2]</sup>. This shock wave formation <sup>[2.3]</sup> results in a deterioration of the signal waveform and a reduction in amplitude. The higher frequency harmonic signals are however more highly attenuated than the primary. This allows the waveform eventually to

return to a sinusoid, as shown in Figure 2.1 (e). Due to the amplitude limitations imposed on acoustic waves due to this effect the associated waveforms are often termed *finite amplitude waves*.

Similarly in a loss-less fluid wave propagation is characterised by the relationship between particle velocity and the local thermodynamic state. This state is expressed for a simple wave travelling into a medium at rest by the relationship  $\lambda = \pm u$  where  $u$  is the particle velocity and the sign relates to the direction of propagation of either a incoming or outgoing wave. For a isentropic flow (the entropy of every particle is the same and remains so) the equation of state can then be expressed as  $P = P(\rho)$  with the pressure as a function of density. The thermodynamic property  $\lambda$  relating to the particle velocity  $u$  is given by the expression <sup>[2.1]</sup>

$$\lambda = \int_{\rho_0}^{\rho} \frac{c}{\rho} d\rho' .$$

An expression similar to equation (2.2) for a gas can then be derived illustrating the propagation speed of a given point on the waveform

$$\left( \frac{dx}{dt} \right)_{u=\text{constant}} = u \pm c .$$

The relationship between  $u$  and the density  $\rho$  leading to local variations in sound wave velocity due to the presence of an acoustic wave. The propagation of a sound wave in a fluid of sufficient amplitude will undergo similar distortions to those seen in Figure 2.1.

The generation of sub-harmonics (below the fundamental or primary frequency) is also possible due to the interaction of an acoustic wave with impurities in the water in the form of gas bubbles <sup>[2.4]</sup>. These gas bubbles have their own relative motion, which, when acted on by an acoustic wave propagating in the fluid, causes a transfer of energy from the wave to the bubbles. This has the effect of trying to drive the gas bubble at its own resonant frequency. The bubble's motion

is, however, non-linear with the effect that it can generate sub-harmonics of the acoustic driving frequency. These bubbles have been observed as a result of marine micro-organisms and in the wake of ships. The existence of micro-bubbles due to small solid particles in the water has also been considered as a source of this non-linear interaction.

One effect of the non-linear propagation of sound in water is seen in the interaction of two tones of frequency  $f_1$  and  $f_2$ , leading to the production of secondary frequency signals at the sum ( $f_1 + f_2$ ) and difference ( $f_1 - f_2$ ) frequencies. The exploitation of both sum and difference frequency signals in water, due to the non-linearity of the acoustic wave propagation in water, has received considerable interest in terms of experimental measurement and mathematical formation since the 1950's by numerous authors [2.5, 2.6]. Of primary interest in the current study is the use of the difference frequency generated signals, the subscript  $s$  will therefore be used to describe the secondary-frequency difference signal.

## 2.2 Parametric wave equation

Westervelt first carried out the development of a mathematical solution for the interactions of two acoustic sources in a fluid, in the formation of his theory of 'Scattering of sound by sound' [2.7, 2.8]. This included the development of an inhomogeneous wave equation for the pressure amplitude ( $P_s$ ) of the difference frequency wave and the theoretical prediction of directivity patterns and beam widths for non-linear systems.

Initial investigations included studies of the interaction effects due to the non-linearity of sound propagation in water between two plane waves travelling in the same direction. The original works utilised methods that have become known as quasi-linear or *source density* theory. The sources for Westervelt's wave equation can be found in the development of an exact equation for waves in fluids, by Lighthill [2.9, 2.10]. Lighthill's equation is

$$\frac{\partial^2 \rho}{\partial t^2} - c_0^2 \nabla^2 \rho = -c_0^2 \square^2 \rho = \frac{\partial^2 T_{ij}}{(\partial x_i \partial x_j)} \quad (2.3)$$

where  $T_{ij}$  is the difference in effective stresses in real flow and the stresses in a uniform acoustic medium at rest. This can be described as

$$T_{ij} = (\rho u_i u_j + P_{ij}) - (c_0^2 \rho \partial_{ij}) + D_{ij} \quad (2.4)$$

where  $\rho u_i u_j$  is often called the instantaneous Reynold's stress tensor or momentum flux tensor and is described as the rate at which momentum in the  $x_i$  direction crosses unit surface area in the  $x_j$  direction. Compressive stress  $P_{ij}$  is simply the hydrostatic pressure in the absence of sound. The stress of a uniform acoustic medium at rest is given by  $(c_0^2 \rho \partial_{ij})$ . In the case of a perfect fluid the effect of viscous stress  $D_{ij}$  is considered negligible.

$\square^2$  is the d'Alembertian operator,  $\left[ \nabla^2 - \frac{1}{c_0^2} \frac{\partial^2}{\partial t^2} \right]$

and  $\nabla^2$  is the Laplacian operator  $\left[ \frac{\partial^2}{\partial x^2} + \frac{\partial^2}{\partial y^2} + \frac{\partial^2}{\partial z^2} \right]$ .

Westervelt's original model assumed two collimated plane waves, of differing frequencies, travelling in the same direction with amplitudes below the onset of saturation (the point at which non-linear generation from a single frequency signal can occur, Section 2.1). This assumes an interaction region within the near-field (Fresnel region) of the primary waveforms. A number of basic assumptions were made in this model:

- i) The interaction between the primary waves is so small that no appreciable error is detected if one is mathematically treated as if the other were not present.
- ii) The 2nd order interaction products in each element of volume are

treated as if they were due to sources within that volume, i.e. each acts as a virtual source.

- iii) The resulting field is calculated, treating the virtual sources stated above, as if they were real.
- iv) The wavelets emerging from these virtual sources have no further non-linear interaction with themselves or the primary waves.

These conditions may only be assumed when the wave amplitude is below the point at which the onset of cavitation is seen. Similarly the distance from the acoustic source (i.e. the distance over which the combined interaction of the wave is calculated) must not approach the *discontinuity distance* (i.e. the distance beyond which the non-linear deformation of the primary signal becomes significant). Velocity is defined in terms of the *Eulerian* co-ordinate system, in which an object is considered stationary with respect to an undisturbed fluid in the absence of an acoustic wave.

The equations of motion and continuity for acoustic waves in a non-viscous fluid are given in (2.5), (2.6)<sup>[2,33]</sup>. Equation (2.5) shows the relationship between the pressure gradient and the product of mass of fluid per unit volume, multiplied by the vector acceleration of the particle, where  $u$  is the vector particle velocity. Equation (2.6) is known as the continuity equation and relates the divergence of the vector rate of mass flow (net rate of mass flow out of a fixed unit volume) to the rate of change of density in that volume. The equation of state (2.7) is given in the form of a power series and defines the differential or excess pressure in a volume element, defined as  $P$  and used from now on, to changes in density, from an initial value of density  $\rho_0$  without an acoustic field present.

$$\nabla P = \rho \frac{d}{dt} u \tag{2.5}$$

$$\nabla \cdot (u\rho) = -\frac{\delta\rho}{\delta t} \quad (2.6)$$

From equation (2.4) the excess pressure  $P$  is only a function of excess density  $\rho$ , giving the power series of the form

$$P = \sum_{n=1}^{\infty} \frac{1}{n!} \left( \frac{d^n P}{d\rho^n} \right)_{\rho=\rho_0} \rho^n \quad (2.7)$$

Through expansion we find:

$$P = c_0 \rho + \sum_{n=2}^{\infty} \frac{1}{n!} \left( \frac{d^n P}{d\rho^n} \right)_{\rho=\rho_0} \rho^n. \quad (2.8)$$

Expansion of the first two terms of the power series in equation (2.7) gives

$$P = A \left( \frac{\rho - \rho_0}{\rho_0} \right) + \frac{B}{2} \left( \frac{\rho - \rho_0}{\rho_0} \right)^2 \quad (2.9)$$

where the coefficients A and B are given by

$$A = \rho_0 \left( \frac{\partial P}{\partial \rho} \right)_0 = \rho_0 c_0^2 \quad (2.10)$$

and

$$B = \rho_0 \left( \frac{\partial^2 P}{\partial \rho^2} \right)_0 \approx \rho_0^2 \left( \frac{\partial^2 P}{\partial \rho^2} \right)_0.$$

Using the assumption outlined earlier by Westervelt the primary waves are considered to interact within a given volume. The calculation of the scattered or secondary frequency signal pressure field due to the non-linearities within a small portion of the total volume was then possible. This effect was described as due to



the uniform distribution of virtual sources of volume density  $q$  created by the non-linear action of the primary waves. The dimension of these virtual volume elements is assumed to be infinitesimally small.

From the earlier assumptions the secondary signals produced by the interaction of two waves travelling in the same direction are treated as having linear propagation properties and that no further interaction takes place between either of the two primary or the secondary signals. Similarly the fact that each of the sources is then treated as if propagating in a linear fashion has led to the use of the terms 'quasi-linear' or 'source-density' for the approach.

This method gives  $qdv$  as the source strength associated with elemental volume  $dv$ . The source density  $q$  is then a function of the position of the particular volume element within the interaction volume <sup>[2.11]</sup>.

Westervelt obtained the expression for source-density as

$$q = \frac{1}{\rho_0^2 c_0^4} \frac{\partial}{\partial t} (P_i)^2 \left[ 1 + \frac{\rho_0}{2c_0^2} \left( \frac{d^2 P_i}{d\rho^2} \right)_{\rho=\rho_0} \right] \quad (2.11)$$

where  $q$  is the simple source strength density resulting from the primary waves of pressure  $P_i$ .

From Lighthill's equation for arbitrary fluid motion (2.3) Westervelt obtained the expression,

$$\square^2 P_s = -\rho_0 \left( \frac{\partial q}{\partial t} \right) \quad (2.12)$$

where  $P_s$  is pressure of the secondary frequency signal and  $q$  is from (2.11).

Rearranging gives the inhomogeneous wave equation for the secondary frequency pressure amplitude

$$\nabla^2 P_s - \frac{1}{c_0^2} \frac{\partial^2 P_s}{\partial t^2} = -\rho_0 \frac{\partial q}{\partial t}. \quad (2.13)$$

The pressure  $P_i$  of the two primary waves may be expressed in the form

$$P_i = P_0 \exp(-\alpha x [\cos(\omega_1 t - k_1 x) + (\omega_2 t - k_2 x)]) \quad (2.14)$$

Assuming  $|\omega_1 - \omega_2| \ll \omega_1$  and  $\omega_1, \omega_2$  are similar frequencies, the wave numbers are  $k_1 = \omega_1 / c_0$  and  $k_2 = \omega_2 / c_0$ . The attenuation coefficient  $\alpha$  is assumed constant for each of the primary waves. Inserting equation (2.14) into the expression for source density (2.11) gives the complex form of the difference frequency component of source strength density  $q$ , where  $|\omega_1 - \omega_2| = \omega_s$  and  $k_s = \omega_s / c_0$ . The source density is assumed to be distributed evenly along the  $x$ -axis and is given by

$$q = \frac{1}{\rho_0 c_0^4} \left[ 1 + \frac{1}{2} \frac{\rho_0}{c_0^2} \left( \frac{d^2 P}{d\rho^2} \right)_{\rho=\rho_0} \right] P_0 (-i\omega_s) \exp(-i\omega_s t + i(k\omega_s + 2i\alpha)x) \quad (2.15)$$

where  $i$  is the root of  $-1$  and  $P_0$  is the undisturbed pressure.

The difference frequency pressure  $P_s$  from equation (2.12) can then be expressed in the vector form  $P_s(\mathbf{r}, \theta)$  as

$$P_s(\mathbf{r}) = -\frac{i\omega_s \rho_0}{4\pi} \int \frac{q e^{i k_s |\mathbf{r} - \mathbf{r}'|}}{|\mathbf{r} - \mathbf{r}'|} dV \quad (2.16)$$

$\mathbf{r}$  and  $\mathbf{r}'$  are the position vectors of the observer and the elemental volume relative to the origin and  $\theta$  is the angle from the  $x$ -axis (the transmission axis) of the projector to the vector  $\mathbf{r}$  using the geometry outlined in <sup>[2.8]</sup>. Equation (2.16) can then be further simplified to

$$P_s = -\frac{i\omega_s \rho_0 S_0}{4\pi} \int_0^l \frac{q e^{i k_s r}}{r} dx \quad (2.17)$$

where  $S_0 dx$  is the elementary volume per unit source distance. Distance  $l$  is the distance before  $q$  is attenuated to a negligible value. If  $R > \omega_s / (\alpha_s c_0)$  and the integration is carried out over a distance  $l$  where  $l \gg \alpha^{-1}$  then the integral is expressed as

$$P_s = \frac{(\omega_s^2 \rho_0 A') \exp(i(k_s R_0 - \omega_s t))}{(8\pi R_0)(i\alpha + k_s \sin^2(\theta/2))} \quad (2.18)$$

$$\text{where } A' = -i\omega_s \frac{1}{\rho_0^2 c_0^4} \left[ 1 + \frac{\rho_0}{2c_0^2} \left( \frac{d^2 P}{d\rho^2} \right)_{\rho=\rho_0} \right] P_0^2.$$

The original work involved the use of a circular array where the distance  $R_0$  is the Rayleigh distance for a circular array which defines the boundary region between Fresnel and Fraunhofer diffraction.

$$R_0 = \frac{\pi \alpha^2}{\lambda_0} \quad (2.19)$$

The coefficients  $A$  and  $B$  from the power series stated in equation (2.8) are often combined in the form

$$\beta = 1 + \frac{B}{2A}. \quad (2.20)$$

Expansion gives

$$\beta \approx \left[ 1 + \frac{\rho_0}{2c_0^2} \left( \frac{d^2 P_i}{d\rho^2} \right)_{\rho=\rho_0} \right] \quad (2.21)$$

$B/A$  is described as the non-linearity ratio and  $\beta$  is termed the parameter of non-linearity for a fluid, taken as 3.5 for water.

The expression for  $q$  in equation (2.11) can then be rewritten as

$$q = \frac{\beta}{\rho_0^2 c_0^4} \frac{\partial (P_i)^2}{\partial t}.$$

Berktaf and Leahy <sup>[2,12]</sup> extended the generalised form of the difference frequency pressure at a point  $P_s(r, \theta)$  from Westervelt's model to include effects introduced by the finite size of the transducer aperture to give

$$P_s(r, \theta) = \frac{\omega_s^2 P_1 P_2 S \beta}{4\pi \rho_0 c_0^4 r} \cdot \frac{\exp[-(\alpha_s + ik_s)r]}{[\alpha_T + ik_s(1 - \cos\theta)]} \quad (2.22)$$

where  $P_1$  and  $P_2$  are the amplitudes of the primary pressure wave and  $S$  is the cross-sectional area of the collimated beam. The attenuation coefficient  $\alpha_T$  is taken as

$$\alpha_T = \alpha_1 + \alpha_2 - \alpha_s. \quad (2.23)$$

Equation (2.22) can then be rewritten in terms of the acoustic powers  $W_{1,2}$  transmitted at each of the primary frequencies where

$$W_{1,2} = \frac{SP_{1,2}^2}{2\rho_0 c_0}. \quad (2.24)$$

Giving an expression for secondary sound pressure level in terms of primary power

$$P_s(r, \theta) = \frac{\omega_s^2 (W_1 W_2)^{1/2} \beta}{2\pi c_0^3 r \alpha_T} \cdot \exp[-(\alpha_s + ik_s)r] D_r(\theta) \quad (2.25)$$

where

$$D_r(\theta) = \frac{1}{[1 + i \left( \frac{2k_s}{\alpha_T} \right) \sin^2 \left( \frac{\theta}{2} \right)]}. \quad (2.26)$$

A simplified form shows that the amplitude of  $P_s$  is related the square of the

difference frequency ( $f_s$ ) and the square of the product of the primary pressure levels, making the above assumptions

$$P_s = \text{const.}(f_s)^2 P_i^2 \quad (2.27)$$

with  $f_s = f_1 - f_2$ . Equation (2.27) shows that the secondary frequency pressure amplitude is dependent on both the amplitude and the difference frequency generated by the two primary waves. The fundamental frequency  $f_0$  is defined as the midpoint of the two primaries  $\frac{f_1 + f_2}{2}$ .

The difference frequency pressure amplitude is considered as radiating from a series of virtual sources uniformly distributed throughout the interaction region of the primary frequency signals. The interaction region based on Westervelt's original assumptions is the area of the collimated beams of the primaries by the distance extended along the transmission axis defined by the absorption ( $\alpha_{1,2}$ ) of the primary signals. The effective source distribution is equivalent to that seen with an *end fire array* (a linear array where a time delay is applied to each element in turn, to allow beam forming along the axis of the array). Source strengths at both the sum and difference frequencies fall with distance at a rate equal to the function  $e^{-(\alpha_1 + \alpha_2)}$ . This has led to the likening of the 'virtual array' to an end-fire array with exponential 'taper'.

The original model assumes that the primaries interact in the form of a collimated beam of diameter  $b$ . Taking the directivity pattern for an ideal end-fire array and multiplying by the diffraction pattern for a finite aperture of width  $b$ , gives a total directional function with a half amplitude beam width of <sup>[2.7]</sup>

$$\theta_{\frac{1}{2}} \approx 4 \sqrt{\frac{\alpha}{k_s}}. \quad (2.24)$$

The directivity pattern in this case is found to form a beam of the same order of

size as the primary beam-pattern and a considerably narrower than that achievable using a conventional transducer of a similar size.

## 2.3 Non-linear sonar development

### 2.3.1 The parametric source

With an interaction region in the near-field of the primary waves, small signal absorption forms the major limiting effect in Westervelt's original model. This solution is only valid for observation a long way from the interaction region. These effects were later seen experimentally by Bellin and Beyer <sup>[2.13]</sup>. Beam formations described by this model are usually derived from low power, high primary frequency sources. In the case of the Bellin and Beyer experiments, primaries of 13 and 14 MHz were used with power around 40 W per frequency. The effects of the finite size of the projector if the interaction region is well within the near-field was discussed by Naze and Tjotta <sup>[2.14]</sup> (considering two beams at right angles) and Berktaay <sup>[2.11]</sup>. Extensions to Westervelt's original model were developed by Berktaay <sup>[2.12]</sup> when he considered near-field projector aperture effects. These were later verified experimentally by Hobaek <sup>[2.15]</sup> and by Muir and Blue <sup>[2.16]</sup>. Arrays where the primaries are sufficiently absorbed within the near-field are often described as *absorption limited*.

Lowering of the primary frequencies has led to a reduction in the small signal absorption, therefore allowing generation of virtual arrays in the far-field of the primaries. Early investigations into scattering within the far-field were carried out by Lauvstad and Tjotta <sup>[2.17]</sup>, Berktaay and Leahy <sup>[2.12]</sup>, Muir and Willette <sup>[2.18]</sup> and Rolleigh <sup>[2.19]</sup>, who have developed models based on the spherical spreading diffraction patterns of the far-field. Later a weak interaction model for both the near and far-field was developed by Fenlon <sup>[2.20]</sup>. Experimental investigation carried out by Konrad, Mellen and Nelson <sup>[2.21]</sup> and Hamilton, Mello and Moffett <sup>[2.22]</sup> show examples of low-amplitude, far-field interactions. These arrays are often referred to as *spreading loss* or *diffraction limited*, but small signal absorption is still the prominent device limiting the generation of the difference frequency signal.

An increase in input power eventually leads to a virtual array length limited by non-linear absorption in the near-field. This case is often termed *saturation limited* due to the degradation of the virtual array due to saturation of the primary signals. In approaching saturation, deformation of the waveform (generation of harmonics and eventually shock wave formation) due to non-linear effects becomes dominant in limiting the virtual array length. Models for this case have been developed by Bartrum <sup>[2.23]</sup> and Merklinger <sup>[2.24]</sup> amongst others.

A fourth case is also possible, utilising saturation limitation in the far-field. This system is often difficult to use because non-linear attenuation (saturation) in the far-field occurs relatively slowly and small signal absorption often becomes more prominent. Models encompassing beam formations in all of these cases have since been developed. Moffett and Mellen <sup>[2.25]</sup> developed theoretical models encompassing both near and far-field effects where the array limiting mechanism either small signal absorption or saturation.

The use of amplitude modulation schemes for improved efficiency was pointed out by Merklinger <sup>[2.26]</sup>. Using a single carrier simply switched at the secondary frequency, improvements of between 2 and 6 dB are theoretically possible. Experimental proof of improvements in the order of 2.5 dB were demonstrated by Eller <sup>[2.27]</sup> and Bjorno, Christoffersen and Schreiber <sup>[2.28]</sup>. Investigation of *self-demodulation* was also carried out theoretically and experimentally more recently by Averkiou, Lee and Hamilton <sup>[2.29]</sup>.

Moffett and Mellen's model <sup>[2.25]</sup> defined the complex parametric gain ( $g$ ) of a system as the ratio of the on-axis far-field secondary pressure amplitude to that of one of the primary components. Similarly the parameter  $\chi$  is given as a measure of whether shock wave formation occurs within the near or far-field and the phase angle  $\gamma$  of the complex parametric gain indicates in which zone most of the generation takes place. If  $\gamma$  is close to zero the source generation takes place mostly within the near-field whereas  $\gamma$  close to  $-90^\circ$  relates to far-field generation. The parameter  $\chi$  is given by

$$\chi = \frac{2\pi\beta P_0 R_0 f_0}{\rho_0 c_0^3}. \quad (2.25)$$

Formulas for the four cases introduced earlier can then be produced as follows:

- 1) In the case the array is small-signal absorption limited within the near-field so that

$$\chi \ll 1 \quad \text{and} \quad \frac{2\alpha R_0 f_0}{f_s} \gg 1$$

where  $\alpha$  is the primary frequency absorption coefficient equal to  $\alpha_1$  and  $\alpha_2$ , and  $\alpha_1$  and  $\alpha_2$  are assumed to be equal.

The parametric gain is then given as

$$|g| \rightarrow \frac{\chi}{4\alpha R_0} \left( \frac{f_s}{f_0} \right)^2 \quad (2.26)$$

and the directivity function  $|D(\theta)|$  is given by

$$|D(\theta)|^2 \rightarrow \frac{|D_{ap}(\theta)|^2}{\left[ 1 + \left( \frac{2\pi}{\alpha\lambda_s} \right)^2 \sin^4 \left( \frac{\theta}{2} \right) \right]} \quad (2.27)$$

where  $|D_{ap}(\theta)|$  is an source aperture correction factor.

- 2) Small-signal absorption limited in the far-field so that

$$\chi \ll 1 \quad \text{and} \quad \frac{2\alpha R_0 f_0}{f_s} \ll 1$$

In this case

$$|g| \rightarrow \frac{\chi}{2} \frac{f_s}{f_0} E_1 \left( \frac{2\alpha R_0 f_0}{f_s} \right) \quad (2.28)$$

where  $E_1$  is an exponential integral function.



The directivity pattern is given by

$$|D(\theta)|^2 \rightarrow |D_0(\theta)|^4 \quad (2.29)$$

Near-axis transmission and

$$|D(\theta)|^2 \rightarrow |D_{ap}(\theta)|^2 \left( d_0 E_1 \left( \frac{2\alpha R_0 f_0}{f} \right) \sin^2 \left( \frac{\theta}{2} \right) \right)^{-2} + |D_0(\theta)|^4$$

For points far off axis,  $d_0$  is defined as a primary beam directivity factor.

$|D_0(\theta)|$  is the primary pressure directivity pattern.

- 3) Saturation limited within the near-field so that

$\chi \gg 1$  and  $\chi \gg 2\alpha R_0$ . In this case

$$|g| \rightarrow \frac{2\pi}{3\sqrt{6}} \left( \frac{f_s}{f_0} \right)^2 \quad (2.30)$$

and

$$|D(\theta)|^2 \rightarrow |D_{ap}(\theta)|^2 \left[ 1 + \left( \frac{16\pi^2 R_0}{3\sqrt{6}\chi\lambda_s} \right)^2 \sin^4 \left( \frac{\theta}{2} \right) \right]^{-1} \quad (2.31)$$

- 4) Saturation limited with the far-field

$\chi \ln \left( \frac{f_0}{f_s} \right) \ll 1$  and  $\ln(2\alpha R_0 \frac{f_0}{f_s}) \ll 0$

$$|g| \rightarrow \frac{2\pi}{3\sqrt{6}} \left( \frac{f_s}{f_0} \right) \quad (2.32)$$

and

$$|D(\theta)|^2 \rightarrow |D_0(\theta)|^4 \quad (2.33)$$

near-axis transmission and

$$|D(\theta)|^2 \rightarrow |D_{ap}(\theta)|^2 \left( \left( \frac{4\pi d_0}{\chi 3\sqrt{6}} \right) \sin^2 \left( \frac{\theta}{2} \right) \right)^{-2} + |D_0(\theta)|^4$$

far off the axis

where  $\frac{f_o}{f_s}$  is often referred to as the step-down ratio.

A fifth case has also been investigated, it involves the saturation of the secondary components compared to the saturation limiting of the primaries seen in cases 3 and 4 above.

Equations (2.26-2.33) demonstrate the high directivity achievable with a low frequency source for a relatively small transducer compared with a conventional sonar system. This is however balanced by the relative inefficiency seen in the non-linear conversion process. Moffet and Mellen <sup>[2,25]</sup> show experimental and theoretical evidence of parametric gains for a variety of sources ranging from -25 dB to -75 dB.

Further developments in the practical application of parametric or non-linear sonar systems have been made to date, some aspects of which are the subject of this thesis. The development of more refined modelling of the non-linear effects in fluids has also continued to the point where accurate representation of the non-linear interaction is possible for most circumstances.

### 2.3.2 Non-linear receiver arrays

Westervelt also put forward the idea of a parametric receiver array. A low frequency plane wave signal is allowed to interact with a locally generated higher frequency signal (often termed a *pump*). The sum or difference frequency signals resulting from the non-linear interaction is received on another transducer. The low frequency signal is then extracted. The net result is a gain in this signal due to the non-linear interaction, as described by Berktaay <sup>[2,30]</sup>. Arrays of this type

generally fall into two types, low and high amplitude. Investigation of the 'low amplitude' pump array ignoring the finite amplitude effects was carried out by Barnard, Willette, Trunchard and Shooter <sup>[2.31]</sup>, amongst others. Experiments were also conducted to investigate acoustic saturation within a parametric receiver by Berktaf and Al Temini <sup>[2.32]</sup>.

Various models have been developed to describe this process by the above and other authors and some agreement with experimental data has been obtained. In general the development of a parametric receiver array still has some serious problems to overcome, although initial investigation reveals the possibility of the eventual practical implementation of such a system.

## 2.4 Conclusion

The non-linearity of a sound wave in water has been studied in some detail by various authors. The formation of various models in particular in the last 40 years has led to a good understanding of the fundamental effects involved. More recent years have seen the development of practical non-linear sonar systems.

Secondary frequency signal amplitude has been shown to be dependant on the primary frequency pressure amplitude and inversely proportional square of the step-down-ratio for near-field limited cases and just the step-down-ratio in the far-field. Hence for the near-field limited cases

$$P_s \propto P_1 P_2 \left( \frac{f_s}{f_0} \right)^2 \quad (2.34)$$

and for far field cases

$$P_s \propto P_1 P_2 \left( \frac{f_s}{f_0} \right) \quad (2.35)$$

These approximations are however complicated by the exact determination of the interaction region and the various limiting mechanisms involved.

Both experimental measurement and mathematical derivation have illustrated the combined characteristics of high directivity, low frequency and the relatively small transducer size associated non-linear sources when compared with conventional sonar systems. Recent years have seen increasing interest in the use of non-linear acoustics for a number of applications included seabed and sub-seabed sediment characterisation, buried object detection and communications.

## REFERENCES: Chapter 2

---

- 2.1 Blackstock D.T.  
Non-linear acoustics (theoretical)  
*American Institute of Physics Handbook*, 3<sup>rd</sup> Edition, McGraw-Hill Book Company Inc, New York, 3n., pp. 3.183 – 3.204,
- 2.2 McDaniel O.H.  
Harmonic distortion of spherical sound waves in water  
*J.Acoust.Soc.Am.*, Vol. 38, pp. 644-647, 1975.
- 2.3 Blackstock D.T.  
Propagation of plane sound waves of finite amplitude in non-dispersive fluids  
*J.Acoust.Soc.Am.*, Vol. 34, pp. 9-30, 1962.
- 2.4 Urick R.J.  
Principles of Underwater Sound  
*McGraw-Hill Book Company*, 2<sup>nd</sup> edition, ISBN 0-07-066086-7, pp. 76, 1975.
- 2.5 Beyer R.T.  
Non-linear Acoustics  
*Written for the Naval Ship Systems Command*, Department of the Navy, 1974.
- 2.6 Bjorno L.  
Parametric acoustic arrays  
*Aspects of signal processing*, Part 1, D. Reidel Publishing company, Dordrecht-Holland, pp. 33-59, 1977.
- 2.7 Westervelt P.J.  
Scattering of sound by sound  
*J.Acoust.Soc.Am.*, Vol. 29, No. 2, pp. 199-203, 1956.
- 2.8 Westervelt P.J.  
Parametric acoustic array  
*J.Acoust.Soc.Am.*, Vol. 35, No. 4, pp. 535-537, 1963.
- 2.9 Lighthill M.J.  
On sound generated aerodynamically: I. General Theory  
*Proceedings of the Royal Society (London)*, Vol. 211A, pp. 564-587, 1952.
- 2.10 Lighthill M.J.  
On sound generated aerodynamically: I. General Theory  
*Proceedings of the Royal Society (London)*, Vol. 222A, pp. 1-32, 1954.

- 
- 2.11 Berktaý H.O.  
Possible exploitation of non-linear acoustics in underwater transmitting applications  
*J.Sound.Vib.*, Vol. 2, No. 4, pp. 435-461, 1965.
- 2.12 Berktaý H.O., Leahy D.J.  
Far-field performance of parametric transmitters  
*J.Acoust.Soc.Am.*, Vol. 55, No. 3, pp. 539-546, 1974.
- 2.13 Bellin J.L.S. and Bayer R.T.  
Experimental investigation of an end-fire array  
*J.Acoust.Soc.Am.*, Vol. 34, No. 8, pp. 1051-1054, 1962.
- 2.14 Naze J. and S. Tjøtta S.  
Non-linear interaction of two sound beams  
*J.Acoust.Soc.Am.*, Vol. 37, No. 4, pp. 174-175, 1965.
- 2.15 Hobaek H.  
Experimental investigation of an acoustical end-fire array  
*J.Sound.Vib.*, Vol. 6, No. 3, pp. 460-463, 1967.
- 2.16 Muir T.G. and Blue J.E.  
Experiments on the acoustic modulation of large amplitude waves  
*J.Acoust.Soc.Am.*, Vol. 46, No. 1, pp. 227-232, 1969.
- 2.17 Lauvstad V. and Naze J.  
Problems of scattering sound by sound  
*J.Acoust.Soc.Am.*, Vol. 34, No. 8, pp. 1045-150, 1962.
- 2.18 Muir T.G. and Willette J.G.  
Parametric acoustic transmitting array  
*J.Acoust.Soc.Am.*, Vol. 52, No. 5, pp. 1481-1486, 1972.
- 2.19 Rolleigh R.L.  
Difference frequency pressure within the interaction region of a parametric array  
*J.Acoust.Soc.Am.*, Vol. 58, No. 5, pp. 964-971, 1975.
- 2.20 Fenlon F.H.  
A weak interaction model for the axial difference frequency field of symmetric and asymmetric parametric acoustic transmitting arrays  
*J.Sound and Vib.*, Vol. 64, No. 1, pp. 17-30, 1979.
- 2.21 Konrad W.L., Mellen R.H. and Nelson J.L.,  
Far-field interactions in the parametric radiator  
*J.Acoust.Soc.Am.*, Vol. 52, pp. 122-123A, 1972.

- 
- 2.22 Hamilton R., Mello P. and Moffett M.B.  
Parametric acoustic waveform generation from spherical primary fields.  
*J.Acoust.Soc.Am.*, Vol. 54, pp. 343(A), 1973.
- 2.23 Bartram J.F.  
A useful analytical model for the parametric acoustic array  
*J.Acoust.Soc.Am.*, Vol. 52, No. 3(2), pp. 1042-1044, 1972.
- 2.24 Merklinger H.M.  
High intensity effects in the parametric transmitting array  
*J.Acoust.Soc.Am.*, Vol. 52, pp. 122(A), 1972.
- 2.25 Moffett M.B. and Mellen R.H.  
Model for parametric acoustic sources  
*J.Acoust.Soc.Am.*, Vol. 61, No. 2, pp. 325-337, 1977.
- 2.26 Merklinger H.M.  
Improved efficiency in the parametric transmitting array  
*J.Acoust.Soc.Am.*, Vol. 558, No. 4, pp. 784-787, 1975.
- 2.27 Eller A.I.  
Application of the USDR type E8 transducer as an acoustic parametric source  
*J.Acoust.Soc.Am.*, Vol. 56, No. 6, pp. 1735-1739, 1974.
- 2.28 Bjorno L., Christoffersen B. and Schreiber M.P.  
Some experimental investigation of the parametric acoustic array  
*Acustica*, Vol. 35, pp. 99-106, 1976.
- 2.29 Averkiou A. Lee Y. and Hamilton M.F.  
Self-demodulation of amplitude and frequency modulated pulses in a thermoviscous fluid.  
*J.Acoust.Soc.Am.*, Vol. 94, No. 5, pp. 2876-2883, 1993.
- 2.30 Berktaý H.O.  
Parametric amplification by use of acoustic non-linearities and some possible applications  
*J.Sound.Vib.*, Vol. 2, No. 4, pp. 462-470, 1965.
- 2.31 Barnard G.R., Willette J.G., Truchard J.J. and Shooter  
Parametric acoustic receiving array  
*J.Acoust.Soc.Am.*, Vol. 52, pp. 1437-1441, 1972.

- 
- 2.32 Berklay H.O. and Al Temini C.A.  
Virtual arrays for underwater reception  
*J.Sound.Vib.*, Vol. 9, No. 2, pp. 295-307, 1969.
- 2.33 Welsby V.G.  
The non-linear interaction of acoustic waves  
*Underwater Acoustics*, Edited by Stephens R.W.B., Wiley-Interscience  
pp. 199-216, 1970.



## CHAPTER THREE

# PARAMETRIC SONAR DEVELOPMENTS

### 3.1 Parametric sonar design constraints

Previous studies carried out at Loughborough University involved the investigation of parametric sources with primary frequencies centred on 20 kHz and 40 kHz [3.1, 3.2, 3.3, 3.4]. Both systems were piston-element rectangular-arrays with element spacings of  $1 \lambda$  (where  $\lambda$  is the primary frequency wavelength). These were configured as a rectangular matrix arranged with 16 x 16 elements in the case of the 40 kHz and 8 x 8 elements for the 20 kHz. With  $\lambda = 3.75$  cm and  $\lambda = 7.5$  cm for 40 kHz and 20 kHz respectively, both arrays were of a similar size with an area of approximately 3600 cm<sup>2</sup>.

The length of the virtual array for secondary frequency signal generation for both these sources can be approximated by the term:

$$\text{Virtual array length (m)} \approx (2\alpha)^{-1} \quad (3.1)$$

where  $\alpha$  is the small signal absorption in (*nepers.m<sup>-1</sup>*) at the fundamental frequency  $f_0$ . The conversion factor for (*dBm<sup>-1</sup>*) to (*nepers.m<sup>-1</sup>*) is given by:

$$\alpha(\text{nepers.m}^{-1}) = \frac{\alpha(\text{dBm}^{-1})}{20 \log_{10}(e)} \quad (3.2)$$

$$\alpha(\text{nepers.m}^{-1}) = \frac{\alpha(\text{dBm}^{-1})}{8.6859}$$

The effective virtual array length can vary in the range of  $10(2\alpha)^{-1}$  to  $\alpha^{-1}$  depending on whether a majority of the secondary frequency generation takes place in the near or the far-field of the array [3.5]. The approximation of  $(2\alpha)^{-1}$  is, however, felt to be valid here due to the attenuation of the source density resulting

in secondary frequency generation being related to an exponential decay of the form  $e^{-2\alpha r}$  where  $r$  is the distance from the source [3.6]. The treatment of the parametric virtual array as an end-fire array with an exponential taper is seen from the literature [see Chapter 2]. This taper is often expressed as an exponential decaying function  $T'$  where

$$T' \propto e^{-(\alpha_1 + \alpha_2 r)}$$

where  $\alpha_1$  and  $\alpha_2$  are the attenuation coefficients of the two primary signals present. The absorption coefficient  $\alpha$  associated with fundamental frequency is taken as being close to the mean value of  $\alpha_1$  and  $\alpha_2$  when the two primary frequencies  $f_1, f_2$  are evenly spaced around the fundamental  $f_0$ . The interaction length of the two primaries is therefore inversely proportional to  $2\alpha$ .

In the case of 20 kHz and 40 kHz systems the virtual array length in salt water were estimated as 1500 m and 400 m respectively.

Requirements such as operational water depth and the degree of seabed penetration needed for the REBECCA project suggested the use of a higher primary frequency than previously investigated. At 80 kHz the virtual array length is approximately 100 m in salt water, which is much closer to the desired operational water depths of 50-100 m envisaged for the REBECCA experiments. The existing systems at 40 kHz and 20 kHz would both experience truncation of the virtual array at these ranges and corresponding loss in secondary frequency signal level and beam-broadening. The possibility of secondary frequency regeneration [3.7] from primary frequency signals reflected from the seabed was also considered. Difficulties could be experienced in the discrimination of reflected secondary frequency signal and secondary frequency signals regenerated from reflected primary frequency signals returning on the same path.

Higher primary frequencies also provided theoretically narrower primary and secondary beam-patterns than those for a transducer array of comparable size at

the lower frequencies <sup>[3.8]</sup>. In the case of 40 kHz and 20 kHz beam-pattern widths of  $2.75^0$  and  $5.4^0$  were measured respectively for rectangular transducer arrays of  $3600 \text{ cm}^2$ . Both arrays were physically large and heavy making them difficult to use in the proposed REBECCA deployment (see Chapter 6). The use of a higher frequency array would potentially allow similar directivity characteristics to those seen in the earlier system but with a smaller physical size.

It was seen as advantageous to providing a finer degree of seabed discrimination than that experienced by a broader beam-pattern and a shorter virtual array length, better matched to the proposed operation. These advantages were balanced against the effects of increased losses due to small signal absorption at higher primary frequencies. This resulting in reduced primary and therefore secondary frequency source level and ultimately limiting the system's overall operational performance. Similarly, the increased step-down-ratio (*SDR*) resulting from using the same secondary frequency range (1 kHz – 15 kHz) for higher primary frequency results in a reduction in the theoretical parametric gain of the system <sup>[3.5]</sup>. In the case of a majority of secondary frequency generation taking place in the far-field, secondary source level ( $SL_D$ ) at the difference frequency ( $f_s$ ) is inversely proportional to  $(SDR)^2$  and for near-field generation  $(SDR)^4$ . Optimum system performance is therefore a compromise between the need for a short virtual array, whilst allowing far-field operation, and a low step-down-ratio.

Another consideration in overall system performance is the effects of cavitation. Losses in sonar performance can be seen due to the generation of a bubble cloud in front the array, caused by a 'rupturing' of the water during the negative pressure cycle <sup>[3.9]</sup>. This can lead to a reduction of acoustic power and beam broadening due to absorption and scattering. Cavitation effects can also include a deterioration of the array face and a reduction in the array's acoustic impedance. The threshold point for the onset of cavitation are often expressed in terms of watts per square centimetre ( $\text{W} / \text{cm}^2$ ) in terms of the effective area of the array face. This can be used to calculate the maximum working pressure at the array face. The effects of cavitation can be reduced by operation at greater depths and therefore increased ambient pressure or the lowering of acoustic power at the array face.

These effects worsen at lower frequencies. For the 20 kHz array a limit of 6 W / cm<sup>2</sup> at 30 m reduces to 1 W / cm<sup>2</sup> when the array is brought to the surface. This compares with 9 W / cm<sup>2</sup> at 30 m and 2 W / cm<sup>2</sup> at the surface for the 40 kHz array. For an array effective surface area 3600 cm<sup>2</sup> the total acoustic power limit 32.4 kW at 30 m and 7.2 kW at the surface for the 40 kHz system. These limits are however reduced to 21.6 kW and 3.6 kW respectively for the 20 kHz system. In the later case, power levels greater than 3.6 kW and shallow water operation could be severely limited by the onset of cavitation.

Operation avoiding cavitation losses also has to be balanced against the effects of saturation and *shock wave formation*. As the intensity of the waveform increases a distortion of the wave-front can take place, resulting in signal attenuation and the generation of distortion signal frequency components. For a saturated parametric array in seawater the shock wave front distance  $l$  equals the Rayleigh distance  $R_0$  from the transducer array. The Rayleigh distance is given by:

$$R_0 = \frac{A}{\lambda} \quad (3.6)$$

where  $A$  is the transducer surface area.

Estimation of the approach of shock wave formation can be made using a quantity known as the *scaled-up source level* ( $SL^*$ ) given by:

$$SL^* = SL_0 + 20\log(f_0) \quad (3.7)$$

where  $SL_0$  is the fundamental primary frequency source level in dB re 1  $\mu$ Pa at 1 m (rms) and  $f_0$  is the frequency in kHz respectively. For salt water, shock front formation has been shown to occur at  $SL^*$  values of equal to or greater than 280.5 dB re 1  $\mu$ Pa at 1 m. For the 20 kHz and 40 kHz systems, primary frequency source levels ( $SL_0$ ) of 236 dB and 256 dB give scaled up source levels of 262 dB and 278 dB respectively. The later case is extremely close to the 280.5 dB limit for shock wave formation. Work has been conducted suggesting that the usable source level to avoid saturation effects is somewhat lower than the shock wave front formation

limit<sup>[3.10]</sup>. This was seen during tests carried out with the 40 kHz system, when the observed source level was 3 dB down on the predicted level based on uniform increases of input power from a low power level<sup>[3.5]</sup>.

The advantages of higher frequency systems for shorter array lengths, higher directivity and higher cavitation limits should be balanced against increased losses in signal level due to small signal absorption and saturation. The 60 - 80 kHz region also approaches a trough in the ambient deep-sea noise spectrum, as shown in Figure 3.1<sup>[3.11]</sup>. The reduced noise level provides a better platform for the sonar design considerations and a potentially improved signal-to-noise performance ratio. Primary frequencies in this range were therefore considered as a reasonable compromise at the water depths and desired secondary frequencies of interest for a new system.

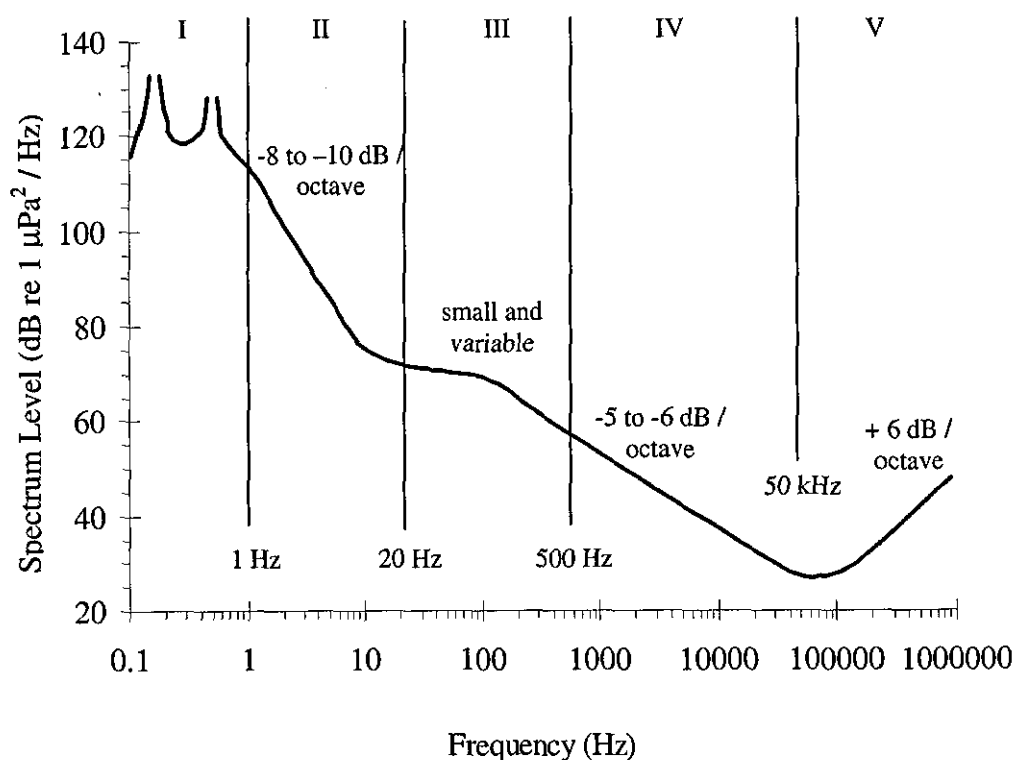


FIGURE 3.1 SPECTRUM OF DEEP-SEA NOISE (from Urick 1983)

## 3.2 LU / IOS parametric sonar system

### 3.2.1 Transducer array

A 75 kHz transducer array for use as a practical parametric source was leased from IOS (The Institute of Oceanographic Sciences Deacon Laboratory). The array itself consists of 729 elements arranged in a 27 x 27 element matrix with a front face machined from a single piece of titanium with a total area of 42 x 58 cm. With an effective piston head diameter of 12 mm for each element the total active area for all the elements is approximately 825 cm<sup>2</sup>. Elements were evenly spaced with a 16 mm pitch (0.8 $\lambda$  at 75 kHz), giving an effective square array aperture of 1850 cm<sup>2</sup>. Each element is formed using a stack of lead zirconate titanate (PZT) ceramic discs, pre-tensioned to piston heads that form part of the titanium front face, shown in Figure 3.2.

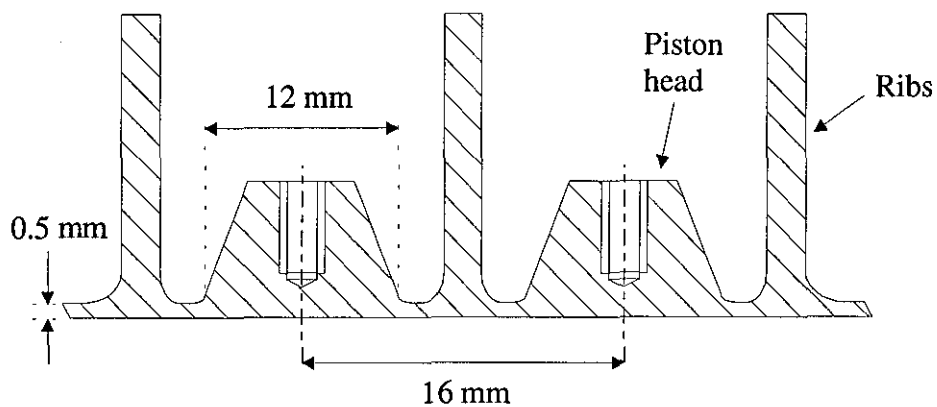


FIGURE 3.2 TITANIUM FRONT FACE CONSTRUCTION FOR ADJACENT ELEMENTS

All elements were originally wired in parallel with a total array impedance in water of approximately 5.3 $\Omega$  and capacitance, including 200 m of cable, of 163 nF at 75 kHz. The array was then reconfigured into 13 staves of 54 elements as shown in Figure 3.3. The remaining 27 elements were wired as a single staff for use as a receiver array. Reconfiguration allowed the use of electronic steering techniques by application of a phase difference to each staff [see chapter 5].

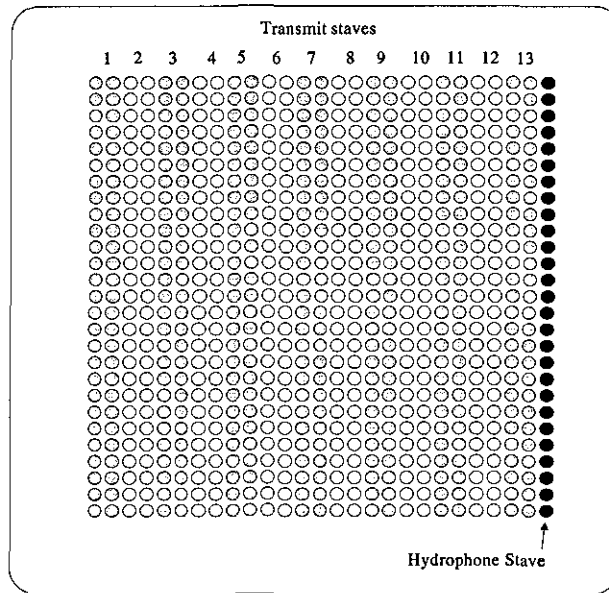


FIGURE 3.3 RE-CONFIGURED STAVES OF 75 kHz TRANSDUCER ARRAY

Ignoring the receiver stave and considering each element head diameter as 12 mm gives a total projection area  $A$  ( $13 \times 54 = 702$  transmit elements) of  $794 \text{ cm}^2$ . This corresponds to a theoretical primary frequency Directivity Index  $DI_P$  of 34 dB, given by:

$$\text{Directivity Index } (DI_P) = 10 \log \left[ \frac{4\pi A}{\lambda^2} \right] \quad (3.8)$$

where  $A$  ( $\text{m}^2$ ) is the active projection area and  $\lambda$  (m) is the wavelength at 75 kHz, for a rectangular array, taking the piston area alone. The total area occupied by all active transmit elements, including the spaces between them is approximately  $1760 \text{ cm}^2$ , giving an equivalent  $DI_P$  of 37 dB. A  $DI_P$  of 35 dB is assumed in subsequent calculations as a reasonable approximation of the directivity index based on both the total element area and the total aperture area. The array active area  $1760 \text{ cm}^2$  corresponds to approximately  $20\lambda \times 20\lambda$  at 75 kHz, giving a theoretical beam width of  $3^\circ$  in both planes.

External connections were made using a 60-metre 14 core cable from PDM NEPTEC Ltd. This allowed a safe working voltage of  $250 \text{ V}_{\text{rms}}$ . Each core is

individually screened, allowing the use a single umbilical cable with little cross-talk interference between adjacent signal cores. Electrical connection to the array itself was made through two front face mounted connectors, as shown in Figure 3.4. These were connected to a rear-mounted interface module with a single waterproof connector. Connection to the receiver array was also made using the umbilical cable terminating in a co-axial connector at the dry end. This arrangement was used to replace the original single channel, 200-metre cable used when all the elements were connected in parallel.



FIGURE 3.4 75 kHz TRANSMIT TRANSDUCER ARRAY

### 3.2.2 Power output predictions

A safe working limit of  $600 V_{pp}$  was set for the maximum drive voltage across each element. The array had in its original configuration a resistive load (in water) at resonance of  $5.3 \Omega$  (729 elements) and  $5.5 \Omega$  for all transmit staves in its new configuration (702 elements). Maximum *rms* power across the array is therefore 8.18 kW. The transducer elements were assumed to be approximately 80% electro-acoustic efficient, giving a theoretical maximum acoustic power  $P_A$  output



of 6.54 kW. Assuming a primary frequency directivity index  $DI_P$  of 35 dB (section 3.2.1), the source level can be estimated using <sup>[3.12]</sup>:

$$SL = 171 + DI_P + 10\log(P_A) \text{ dB re } 1 \mu\text{Pa at } 1\text{m} \quad (3.9)$$

Giving a maximum primary frequency source level SL of 244.2 dB re 1  $\mu\text{Pa}$  at 1m. Saturation effects have been ignored here, but by calculating the scaled-up source level  $SL^*$  from (3.7) for 75 kHz tone,  $SL^*$  is estimated as 281.7 dB re 1  $\mu\text{Pa}$  at 1m kHz. This is in excess of the 280.5 dB re 1  $\mu\text{Pa}$  at 1m threshold source level needed for shock wave formation <sup>[2.25]</sup>. The theoretical source level of 244 dB re 1  $\mu\text{Pa}$  at 1m would therefore be attenuated due to the effects of saturation at the onset of shock wave formation. Saturation effects therefore limit maximum power output of this array when operated close to voltage limit of 600  $V_{pp}$  across the transducer elements. The effects of cavitation could, however, be limited provided that the transducer array is operated in sufficient water depth.

### 3.2.3 Impedance characteristics

Data from the impedance characteristics of the transducer array in its original configuration was used to predict the re-configured response. The near-resonance admittance plot for the array in water in its the original array configuration on a 200 m cable is shown in Figure 3.5. Modelling of the array is possible using a series-tuned LCR circuit as shown in Figure 3.6. The input admittance of the array  $Y_I$ , when considered in terms of an acoustic projector, can be represented in terms of two admittance components representing both the electrical and mechanical properties of the transducer array <sup>[3.13]</sup>

$$Y_I = \frac{I}{V} = Y_e + Y_m \quad (3.10)$$

where  $Y_e$  and  $Y_m$  represent equivalent input admittance for the electrical and mechanical characteristics of the transducer array. The electrical component or *clamped admittance* ( $Y_e$ ) is the effective admittance of the ceramic material whilst

'clamped', i.e. eliminating any physical movement. This is modelled using *leakage resistance* ( $R_l$ ) in parallel with the clamped or static capacitance ( $C_0$ ), as shown in Figure. 3.6. The clamped admittance is given by:

$$Y_e = \frac{1}{R_l} + j\omega C_0. \quad (3.11)$$

Mechanical or *motional* contributions to  $Y_m$  are modelled using a simple LCR series tuned circuit.  $L$  and  $C$  are known as the compliance of the transducer, where  $C$  is the effective *stiffness* of an oscillating material, and  $L$  is the effective mass of the material. The series resistor represents the *motional impedance* ( $Z_m$ ), which comprises of two series resistors, the *radiation impedance* ( $Z_R$ ) related to the medium the oscillator is in and the *loss resistance* ( $Z_M$ ) representing the mechanical behaviour of the oscillator itself. *Radiation impedance* and *loss impedance* are mostly resistive and are commonly represented as  $R_R$  and  $R_M$  respectively. The total admittance ( $Y$ ) of the equivalent circuit can then be given by:

$$Y = \frac{1}{R_l} + j\omega C_0 + \frac{1}{R_R + R_M + j\left[\omega L - \frac{1}{\omega C}\right]} \quad (3.12)$$

where  $C$  represents is the stiffness of the ceramic  $L$  the mass. At the resonance frequency ( $\omega_0$ ) contributions from  $L$  and  $C$  are equal and opposite and therefore eliminated. Similarly if  $R_l$  is sufficiently large it is often treated as open circuit. From the admittance diagram the static capacitance ( $C_0$ ) can be calculated from the susceptance ( $B_0$ ) of the transducer at resonance frequency, such that:

$$C_0 = \frac{B_0}{\omega_0}. \quad (3.13)$$

Similarly, the resistance ( $R$ ) of the array can be calculated from the diameter of the admittance circle  $D_w$  in water using:

$$\frac{1}{R} = \frac{1}{R_R + R_M} = D_w. \quad (3.14)$$

Comparison can be made with an in-air measurement. The acoustic radiation impedance in air is small in comparison with mechanical impedance. Radiation resistance is therefore eliminated from the expression and the total resistance is taken as:

$$\frac{1}{R} = \frac{1}{R_M} = D_A. \quad (3.15)$$

The diameter of the circle in water is typically smaller than that seen in air. The leakage resistance  $R_l$  in the equivalent circuit can also be calculated using:

$$R_l = \frac{1}{G_0} \quad (3.16)$$

where  $G_0$  is the leakage conductance shown in Figure 3.5, before and after the resonance circle effects.

Electroacoustic efficiency ( $\eta$ ) can then be calculated by comparison of the admittance plots for both in-water and in air using:

$$\eta = \frac{D_w(D_A - D_w)}{D_A(D_w + G_0)}. \quad (3.17)$$

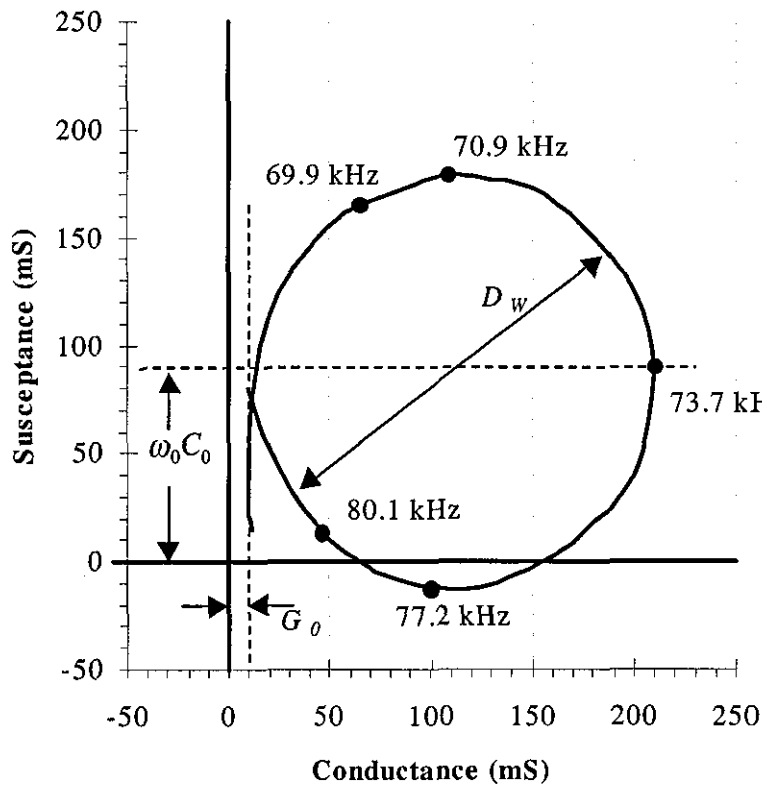


FIGURE 3.5. ADMITTANCE CIRCLE 75 kHz TRANSMIT ARRAY IN WATER IN ITS ORIGINAL CONFIGURATION WITH 200 m OF CABLE

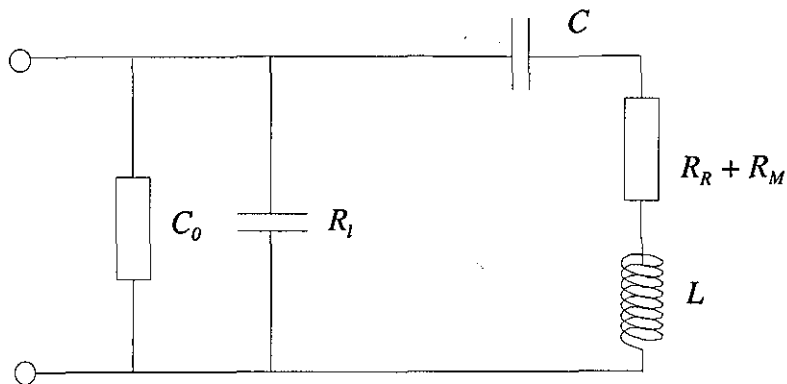


FIGURE 3.6. TRANSDUCER ARRAY EQUIVALENT CIRCUIT

From the in-water admittance circle shown in Figure 3.5 the array capacitance  $C_0$  was estimated to be 183 nF. This is the total capacitance of all transducer elements in parallel and the original (200 m) cable such that:

$$C_0 = C_{array} + C_{cable} \quad (3.18)$$

With a measured cable capacitance ( $C_{cable}$ ) of 20 nF the capacitance of the elements alone is then taken as 163 nF. For 729 elements in parallel, the capacitance of an individual element of 224 pF was calculated. This is then used to recalculate the re-configured stave capacitance  $C_{stave}$  of 54 elements. In addition the capacitance of a new 65-m cable was considered. This was higher than the previous cable, with a value equivalent to 199 pF m<sup>-1</sup>. The total stave capacitance was therefore estimated at 25 nF per stave including the cable. This figure was later modified to an average value of 31 nF per stave by subsequent direct measurement of the electrical characteristic of the array using a HP-4192A Hewlett Packard impedance analyser. These results are listed in Table 3.1. The measured value appears slightly higher than the calculated values; this was most likely due to neglecting the connector capacitance and inaccuracies in the original cable capacitance figures used in the original estimate.

A similar process was used to calculate the stave resistance ( $R_{stave}$ ) from the admittance circle in Figure 3.5. The initial array resistance of 5.1  $\Omega$  (729 elements) was estimated with a corresponding stave resistance of 68.9  $\Omega$  (54 elements). From Table 3.1 a reasonable agreement was seen with later measured values.

The measured values were then used to calculate the matching inductance needed to eliminate the capacitive loading effect of each stave on the power amplifier modules. The addition of a *choke* inductor across the capacitive load is sometimes used to reduce the capacitive loading effect. Alternately the inductance of the secondary of the power amplifier output transformer is matched to the capacitive load of the array and cable at the resonance frequency. Impedance matched transformers were then designed to provide a sufficient step-up ratio from the power amplifier modules to generate 600 V<sub>pp</sub> across the elements and a secondary winding inductance matched to eliminate the load capacitance. The GANALEX G9V cores that were selected provide a 1:5.7 turns ratio, achieving drive levels of 600 V<sub>pp</sub> at 75 kHz and a secondary winding inductance of 0.15 mH. Additional

care was taken to avoid the generation of signal harmonics other than those desired via the parametric effect in the water column. Generation of these unwanted frequency components is possible when operating the transformer core close to its magnetic flux density, saturation point. Consideration was therefore made in the design of the transformers of the peak flux density and permeability stability within the core at the predicted operational power levels and frequencies.

Stave	Resistance ( $\Omega$ )	Capacitance (nF)
1	70.25	30.30
2	67.26	31.70
3	67.26	31.65
4	69.91	30.45
5	69.21	30.74
6	70.10	30.36
7	67.61	31.49
8	67.68	31.46
9	61.05	34.93
10	63.59	33.51
11	64.28	33.15
12	66.80	31.89
13	64.53	33.03
<b>Mean</b>	<b>66.89</b>	<b>31.9</b>
Receiver	92.90	22.88

TABLE 3.1 TRANSDUCER ARRAY ELECTRICAL CHARACTERISTICS AT 75 kHz

Power amplification was achieved using thirteen 1 kW linear MOSFET power amplifiers. Using the designed transformers these impedance matched to the cable and transducer allowing 600 V<sub>pp</sub> signal generation at frequencies up to 85 kHz. Particular care was taken to ensure that no non-linearity existed in the amplifiers or the transformer stages.

### 3.3 Conclusion

The requirement of a small, high directivity, low frequency source in relatively shallow water depths (< 100 m) during the REBECCA project led to the consideration of a new parametric array. Previously developed parametric sources at 20 and 40 kHz were felt unsuitable due to long virtual array lengths and relatively large physical size. Theoretically a higher primary frequency provides a shorter array length and increased directivity for a similar size array. This is however balanced by the increased step-down-ratio for higher primaries and similar secondary frequencies, resulting in a reduction in secondary frequency source level. Primary frequency operation in the range 60-80 kHz was therefore considered better suited to the operational requirements.

A suitable array was found in the form of a 75 kHz source leased from Institute of Oceanographic Sciences. The array itself is formed using 729 elements in a 27 x 27 matrix, with a corresponding aperture area of around  $20 \lambda \times 20 \lambda$  giving a theoretical beam-width at the primary frequency of around  $3^\circ$ . The elements were arranged into 13 staves of 54-elements and a single 27-element staff allowing electronic beam-steering in one plane over a  $\pm 18^\circ$  sector. A theoretical maximum source level of 244 dB re 1  $\mu$ Pa at 1 m based on maximum input power was calculated. This suggested that the primary frequency source levels would be limited by saturation effects. The onset of cavitation could however be avoided by operation at sufficient depths. The expected array characteristics combined with its physical smaller size were felt to provide a reasonable compromise of the various design parameters under consideration.

## REFERENCES: Chapter 3

---

- 3.1 Goodson A.D., Griffiths J.W.R., Gida A.S. and Cook J.C.  
A high power flexible sonar transmitter  
*Proceedings IERE 5th Conference on Electronics for Ocean Technology*,  
Vol. 8, No. 3, pp. 101 - 112, 1987.
- 3.2 Cook J.C., Goodson A.D. and Griffiths J.W.R.  
Low frequency sector scanning using NLA  
*Proceedings of the NATO Underwater Acoustic Data Processing  
Conference*, Kingston, Ontario, Canada, pp. 5 - 9, 1988.
- 3.3 Cook J.C., Goodson A.D. and Griffiths J.W.R.  
A sector scanning sonar system using transmitter scanning  
*Proceedings of the UDT Conference, Undersea Defence Technology*,  
London, pp. 718 - 724, 1988.
- 3.4 Cook J.C., Goodson A.D. and Griffiths J.W.R.  
A parametric scanning sonar.  
*Proceedings of the UDT Conference, Undersea Defence Technology*,  
London, pp. 425 - 532, 1990.
- 3.5 Cook J.C., Goodson A.D. and Griffiths J.W.R.  
Experience with a versatile NLA sonar system.  
*Proceedings of the Institute of Acoustics*, Vol. 14, No. 3, pp. 27 - 52,  
1992.
- 3.6 Welsby V.G.  
The non-linear interaction of acoustic waves.  
*Underwater Acoustics*, Edited by Stephens R.W.B, Wiley-Interscience, pp.  
199-216, 1970.
- 3.7 Muir T.G., Mellenbrunch L.L. and Lockwood J.C.  
Reflection of finite-amplitude waves in a parametric array  
*J.Acoust.Soc.Am*, Vol. 62, No. 2, pp. 271-276, 1977.
- 3.8 Bjorno L.  
Parametric acoustic arrays  
*Aspects of Signal Processing*, Part I, D. Reidel Publishing Company,  
Dordrecht- Holland, pp. 33-59, 1977.
- 3.9 Urick R.J.  
Principles of Underwater Sound  
*McGraw- Hill Book Company*, Second Edition, pp. 70 -75, 1975.



- 
- 3.10 Berkta y H.O.  
Parametric sources – design considerations in the generation of low frequency signals.  
*Ocean Seismoacoustics*. Low frequency acoustics, Plenum Press NATO ASI series V, IV, pp. 16.
- 3.11 Richardson J.W., Greene C.R. Jr, Malme C.I. and Thomson D.H.  
Marine Mammals and noise  
*Academic press*, ISBN: 0-12-588441-9, pp. 95, 1995.
- 3.12 Waite A.D.  
Sonar: for practicing engineers  
Epic Printing Services, Dorchester, ISBN 0 9528033 1 3 Second edition, pp. 3, 1998.
- 3.13 Woodward B.  
A course on principles of transducers  
Short course 9.1 of a series on digital communications, signal processing and sonar, Dept. Electronic and Electrical Engineering, Loughborough University (UK), Unpublished.

## CHAPTER FOUR

# SYSTEM COMMISSIONING AND CALIBRATION

### 4.1 Loch Duich field site

Initial commissioning and calibration of the system took place at an acoustic trial site in a sea loch, Loch Duich, on the West Coast of Scotland, between the 12th and 17th June 1993. The trial site is operated by the Marine Laboratory, Fisheries Research Services (FRS), part of the Scottish Office. The site itself comprises a moored raft and an on-shore base station. Figure 4.1 shows the general layout of the trial site. The raft has a small equipment enclosure and hydraulic lifting system for equipment deployment.

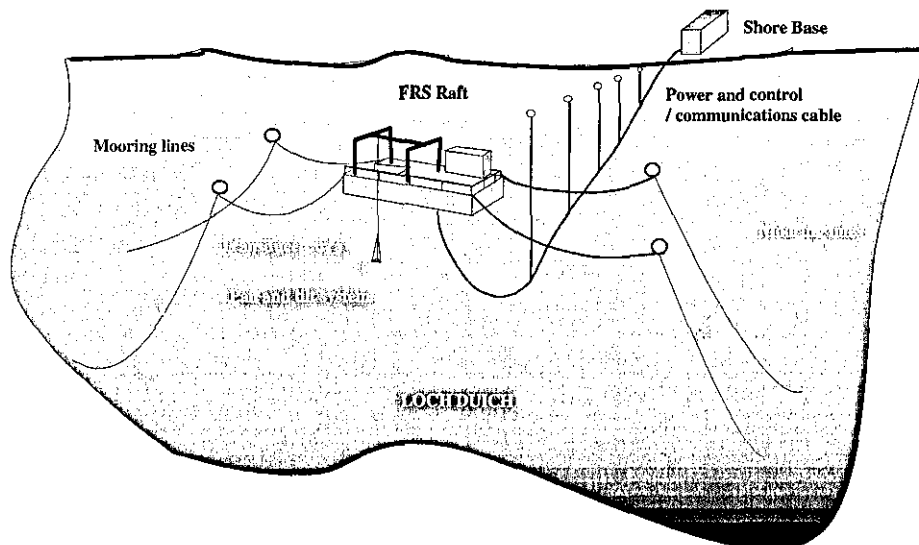


FIGURE 4.1 RAFT DEPLOYMENT LOCH DUICH FIELD SITE.

The results represented here were obtained during the first sea water trial of the modified I.O.S transducer array.

The raft has a 240V single-phase mains power supply feed laid across the seabed from the base station. The raft is 10 m x 5 m with a 3 m square moon pool. It is normally deployed approximately 500 m from shore in 90 m water depth (this

varied with tidal movement).

The transducer array was deployed in a suspended triangular frame containing a pan-and-tilt facility. The frame was suspended using three wire ropes from a single suspension point under the raft giving a greater degree of stability in the frame regardless of raft movement. Control of the array's orientation was possible using the pan-and-tilt over in two mutually perpendicular axes from either the raft or remotely from the shore base. The transducer array was deployed with the transmission axis vertical. Mechanical pan-and-tilt adjustment of the array of up to  $\pm 20^\circ$  from the vertical were then possible in either axis. The array was arranged such that one of the pan-and-tilt planes was parallel with the array's own *scanning* axis.

The control instrumentation (computers, transmit modules, data capture electronics and oscilloscope) and the power amplifiers were placed within an enclosure on the raft. This also housed the raft controls for the pan-and-tilt, hydraulic lifting system. All these were operated from on-board the raft. The on-shore facility acted as a base for operations not directly involved in the taking of measurements. Personnel and equipment was transported to and from the raft using a small outboard boat. The equipment was taken to the water's edge using a Land Rover.

#### 4.2 Experimental procedure

The transducer array was deployed with its transmission axis vertical at a depth of 12 m to minimise cavitation effects. Two single-element ball hydrophones (S/N 30235/01 and S/N 30235/02) from Sonar Products International were suspended directly below the transducer array within the main beam of the array in both axis. The first a HS-150 (13 mm diameter) at 16 m and a HS-70 (25 mm diameter) 64 m below the array face.

The array was initially *wetted* for approximately 24 hours before driving at full

power. This minimised the chances of damage to the array titanium face and signal degradation due to cavitation. The pan-and-tilt facility was then used to ensure that the array was facing directly towards the hydrophones, by observing the maximum signal whilst scanning the mechanically in either axis. This method was used for measuring source level at both the primary and secondary frequencies. Beam patterns were plotted in both axes by mechanical adjustment of the pan-and-tilt over a  $\pm 20^\circ$  sector and observing the changes in signal level on the two hydrophones. The axis parallel to the array's own *scanning axis* is referred to as the *scanned axis*, the other as *un-scanned*. Sector scanned signals were observed at various angles in the *scanned* plane, again using the pan-and-tilt to move in the *scanned* plane. Beam patterns in the hydrophone were observed at various angles by allowing the beam to scan across the hydrophone. The configurations for both methods of beam plotting are shown in Figure 4.2.

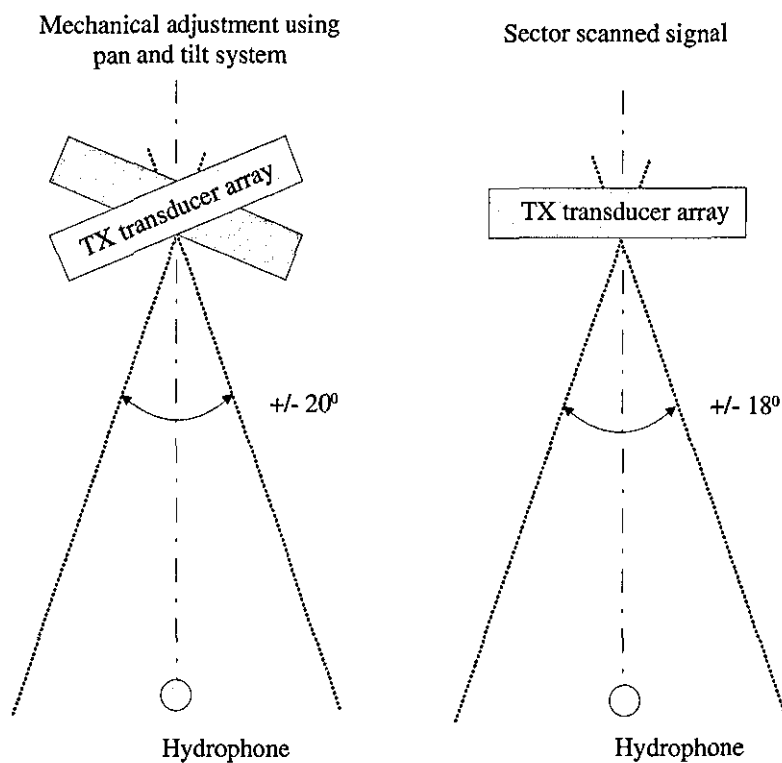


FIGURE 4.2 ARRAY CONFIGURATION USING THE PAN AND TILT FACILITY FOR MECHANICALLY ADJUSTED PRIMARY BEAM PLOTS AND SECTOR SCANNING BEAM PLOTS

### 4.3 Test signals

Three main test signals were used during the trial. All signals were generated mathematically and then written to memory housed in the transmit modules. A more detailed description of signal synthesis techniques and hardware generators is given in Chapter 5. The basic signals used in initial calibrations are summarised below.

- i) The initial installation, primary source level measurements and primary beam plots are made using a pulsed continuous wave (CW) signal of duration 4 ms. These were constant amplitude, constant frequency sinusoidal waveforms generated at frequencies ranging from 70 kHz to 80 kHz.
- ii) Secondary Pulsed CW difference frequency signals generated by driving the array with two primary frequencies  $f_1$  and  $f_2$  were utilised. The two primary signals are summed and the complex waveform transmitted. On summation of the resultant complex waveform is then halved to restore the maximum amplitude to that seen with a single primary. Both primaries are of constant amplitude and frequency with frequencies equally spaced around the resonance or fundamental frequency of 75 kHz. A 5 kHz non-linear generation signal is therefore generated by summing and halving the primary sinusoidal waveforms generated at 72.5 kHz and 77.5 kHz.
- iii) Sector scanning signals are generated at the primary frequencies (70 kHz to 80 kHz). Phase steering of the array is possible by the introduction of a phase difference in the primary waveforms applied to each stave of the transducer array. If the phase relationship between staves can be made to vary during the waveform's progression, the beam can perform an within-pulse sweep across a sector.
- iv) Secondary frequency sector scanned in the range 1-13 kHz. Appropriate

scanning of two primaries allows generation of an in-pulse secondary frequency sector scan.

#### 4.4 Initial system tests

Initially the amplifiers were tested in the laboratory against a dummy load, simulating the resistive and reactive loading effects seen by the amplifiers when connected to the transducer array. This defined the maximum output drive voltage of  $600 V_{pp}$ . The array itself was then tested to determine optimum stave responses. This was done by transmitting a series of single frequency pulses at full power but delayed for each stave. Figure 4.3 shows a series of 13 pulses (one for each stave) transmitted using a 75 kHz sinusoid at full power.

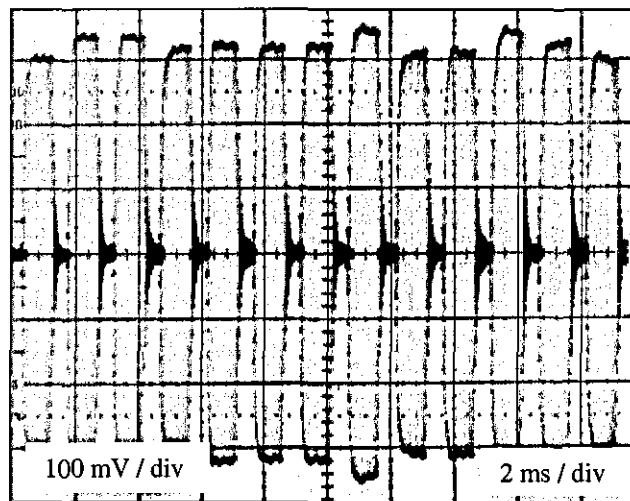


FIGURE 4.3 75 kHz TRANSMISSION ON STAVES 1-13

Each of the pulses represents the response of an individual stave. Figures 4.4 and 4.5 show similar traces for signals transmitted at 72.5 kHz and 77.5 kHz respectively. Figure 4.4 shows a reduction in the response of the first 7 staves; in Figure 4.5 it is evident that a similar relative power reduction is seen by staves 9 to 13. This suggests a frequency selective variation in the elements across the transducer array face. The outputs could then be equalised by adjusting the amplifier gains. This was decided against as the effect of the frequency selective

nature of the array elements could worsen as signals were transmitted at frequencies away from the resonance frequency. The effects of the staves seen at 72.5 kHz and 77.5 kHz appear balanced about the 75 kHz response and was seen as a reasonable compromise.

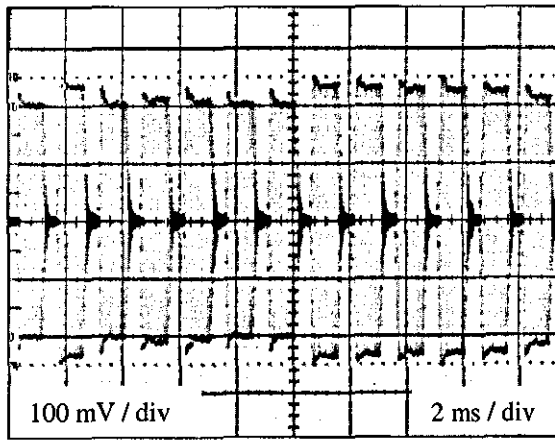


FIGURE 4.4 72.5 kHz RESPONSE

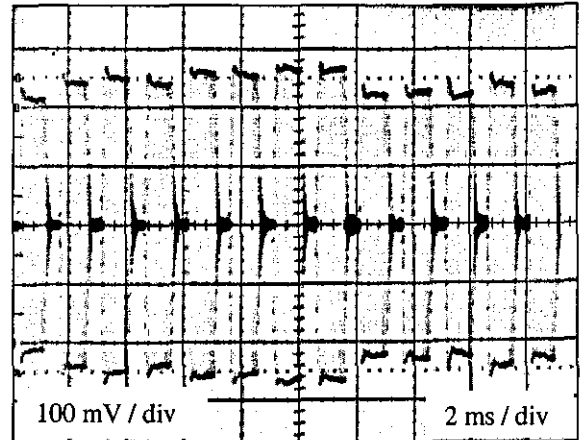


FIGURE 4.5 77.5 kHz RESPONSE

#### 4.5 Primary frequency beam-patterns

Primary beam patterns were measured in both scanned and un-scanned axes at a range of different frequencies. Single frequency pulses 1 ms long were transmitted at 1/4 full power for each of the frequencies of interest. The signal level was monitored on the near hydrophone S/N 30235/01 using an oscilloscope. Figure 4.6 shows the normalised response of the transmitter at 75, 72.5 and 77.5 kHz.

Figure 4.6 illustrates a degree of asymmetry around the main beam (centre lobe). This is most likely due to slight variations in the optimum frequencies for individual elements across the face of the array. With the grading of the elements during manufacture to allow minimum variation in frequency response between adjacent elements, an overall frequency variation across the transducer array's face is therefore possible. This effect is also seen in Figures 4.3 to 4.5. where changes in the frequency response across the face of the array, previously discussed in section 4.4, are evident.

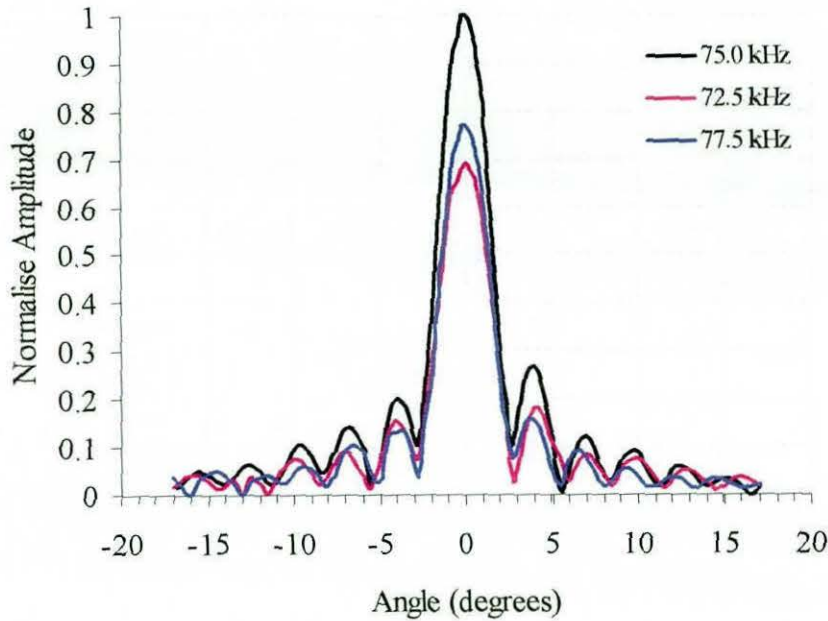


FIGURE 4.6 NORMALISED PRIMARY FREQUENCY BEAM-PATTERN SCANNED AXIS

The beam-patterns show a beam-width of  $2.5^\circ$  at the  $-3$  dB points. This is a little lower than the initial estimate of a  $3^\circ$  beam expected with a  $20\lambda$  array. These estimates are, however, based on a  $\lambda$  pitched array. The current configuration means with the elements at  $0.8\lambda$  pitch, may account for the discrepancy. A closer correlation was found using the expression for a rectangular array <sup>[4.1]</sup>:

$$\Phi_{-3dB} = 2 \sin^{-1} \left[ \frac{2.78}{kb} \right] \quad (4.1)$$

where  $k$  is the wave-number of the frequency of interest and  $b$  is the array width in that axis. Considering an equivalent rectangular array with  $b = 0.428$  m and  $k = 314$  at 75 kHz in water, a theoretical  $-3$ dB beam-width of  $2.4^\circ$  is calculated.

The beam-width appears relatively constant for a range of different drive frequencies. Each of the beam patterns show several sidelobes, the first of which is approximately 12 dB down and the second 14 dB down on the centre lobe level, giving an average reduction in the first side-lobes of 13 dB, again well within expected levels for primary frequency side lobes. No significant differences were



observed for the beam patterns in the un-scanned axis for the same frequencies although the un-scanned axis has a slightly larger array aperture (27 elements wide compared with 26 for the scanned axis). The beam width is again approximately  $2.5^\circ$  at the -3 dB points, with a similar degree of stability for different in primary frequencies.

#### 4.6 'Dynamic' beam-pattern measurements

A sector-scanning signal was used to obtain dynamically a beam-pattern with a fixed hydrophone. The hydrophone was placed at the  $0^\circ$  position and a sector was scanned over  $\pm 18^\circ$ . As seen in Figure 4.7 below, the beam sweeping across a sector has the effect of generating a beam-pattern as it passes the hydrophone. The known sector of sweep and the pulse duration give a sweep rate that allows an estimation of the beam-width from the time axis observed on the oscilloscope output. Figure 4.7 compares well with the original beam plots observed in Figure 4.6. This plot has a similar degree of asymmetry in the side-lobes that observed in the original beam plots. The asymmetry appears reversed due to the direction of the scan.

The pan-and-tilt assembly was then used to orient the array through a range of angles, so observing the swept beam at various points along its path. Figures 4.8 – 4.11 show the scanning nature of the beam pattern along a 10 ms pulse.

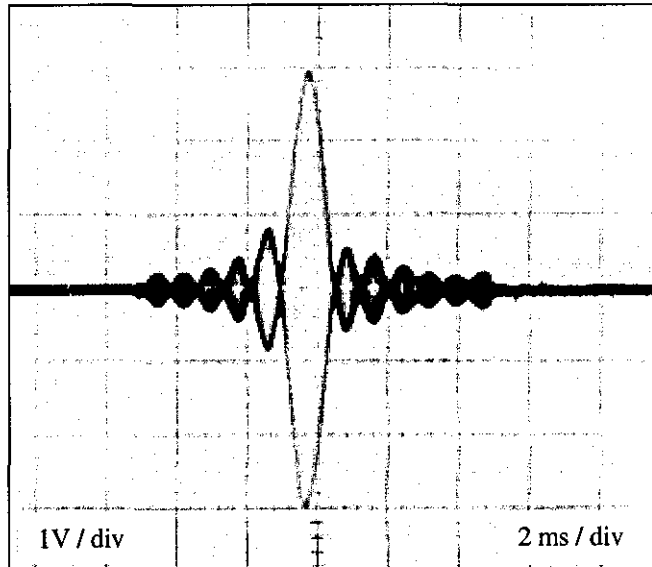


FIGURE 4.7 SCANNING SIGNAL 75 kHz, 10 MS PULSE, SWEEP FREQUENCY 100 Hz,  
ARRAY ORIENTATION 0°.

Figure 4.11 demonstrates the full sweep capability of the transmitter system. With the array orientated at approximately either  $\pm 18^\circ$  the signal is seen to wrap around (re-forming of the beam-pattern at the opposite extreme of the phase steered range) due to the  $2\pi$  ambiguity introduced in the inter-stave phase relationship. A maximum inter-stave phase difference effectively limits steer angle to a  $36^\circ$  sector.

(The limit imposed in phase steering discussed further in section 5.4.3.)

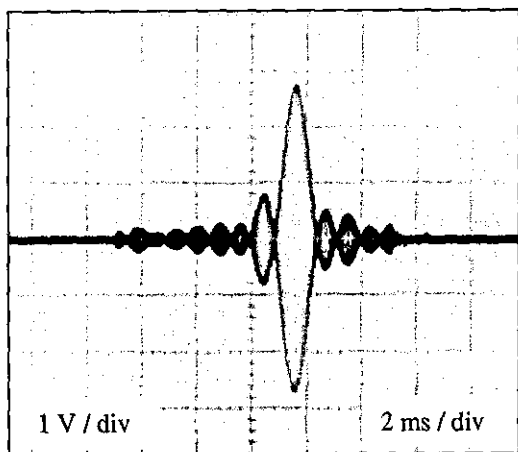


FIGURE 4.8 SCANNING SIGNAL 75 kHz,  
100 Hz SWEEP ARRAY ORIENTED  $+5^\circ$

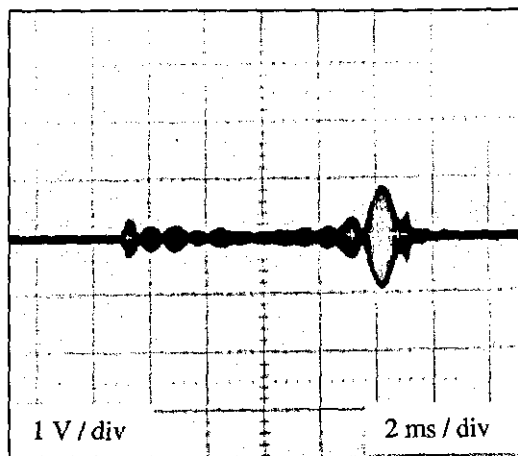


FIGURE 4.9 SCANNING SIGNAL 75 kHz,  
100 Hz SWEEP ARRAY ORIENTED  $+15^\circ$

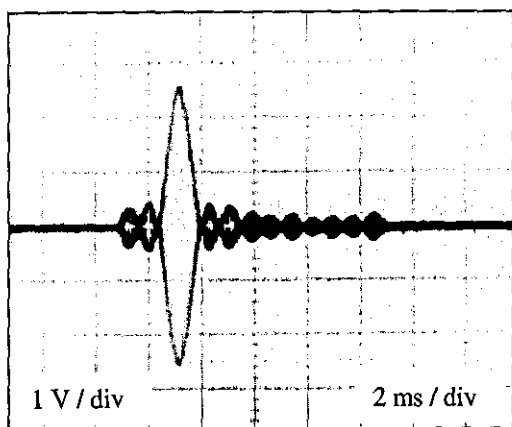


FIGURE 4.10 SCANNING SIGNAL 75 kHz,  
100 Hz SWEEP ARRAY ORIENTED  $-10^\circ$

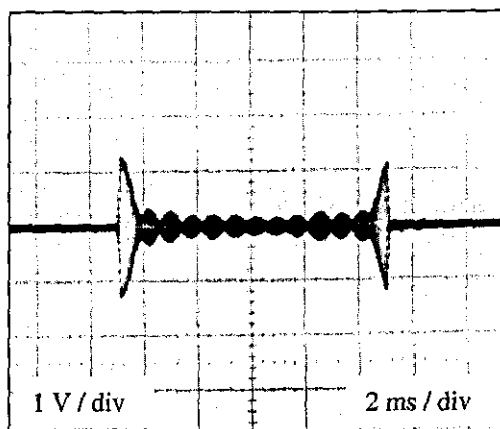


FIGURE 4.11 SCANNING SIGNAL 75 kHz,  
100 Hz SWEEP ARRAY ORIENTED  $+18^\circ$

Increased / decreased sweep frequencies would allow for multiple / partial sector swept signals during a single transmission pulse. Similar control could be achieved through variations in the pulse length, although this latter method is limited to a maximum pulse length of 32 ms with the present hardware configuration. Variations made in the start phase of each individual stage's signal should allow control of the scan phase, i.e. starting angle. Figures 4.7 to 4.11 demonstrate a scan from left to right as observed on an oscilloscope. Similar signals may be developed to allow scanning from the centre outwards or even a continuous sweep forwards and backwards across the sector during the

transmission pulse. These signals also demonstrate the *phase steering* capabilities of the transducer array.

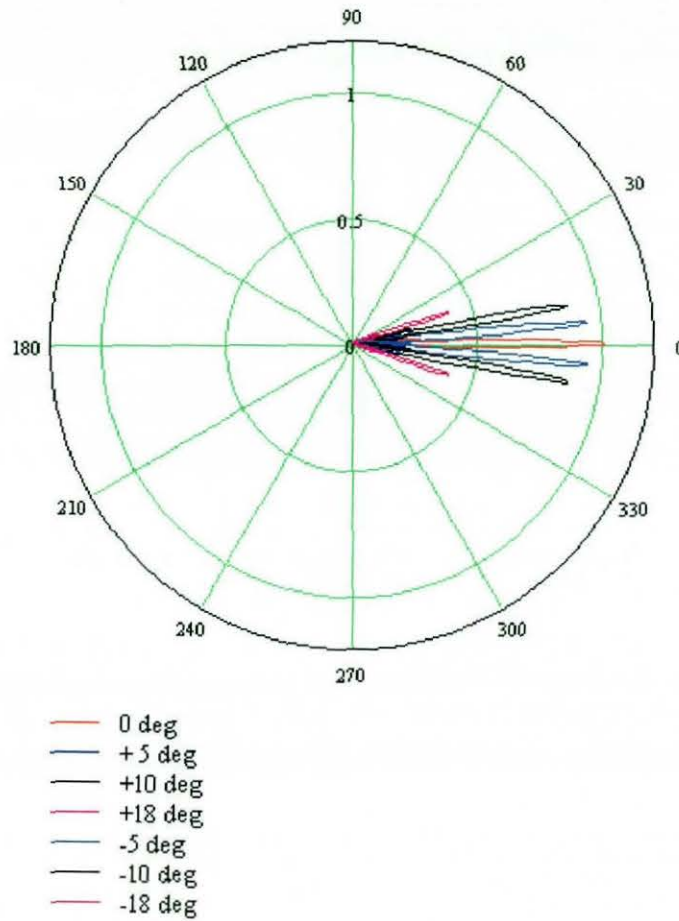


FIGURE 4.12 POLAR BEAM PLOTS SECTOR SCANNED 75 kHz PRIMARY FREQUENCY SIGNAL

The normalised polar response for a 75 kHz primary frequency signal whilst being swept is shown in Figure 4.12. This illustrates high directivity of the primary frequency beam and the sector-scanning angle of  $36^\circ$  for the hydrophone placed at a range of discrete angles across the scanning axis. A reduction in signal level is seen as the sweep signal moves away from the array's normal transmission axis ( $0^\circ$  position). A rapid deterioration to about  $-8$  dB of the full-scale level is observed in signals for greater than  $\pm 15^\circ$  as the sweep approaches the  $2\pi$  ambiguity point at  $\pm 18^\circ$ . The reduction in level can be described mathematically due to the directional pattern being described as the product of the pattern for a

linear array of staves and that of a single staff. The reduction in signal level observed in the extremes of the steer limit follows the broader beam-pattern observed from a single staff alone. This pattern is further superimposed on that for a single element <sup>[4.2]</sup>.

#### **4.7 Primary frequency source level**

Initial measurements of source level were made at primary frequencies of 72, 73, 74, 75, 76, 77 and 78 kHz. Drive limitations of the transducer staves gave a maximum voltage of 600 V<sub>pp</sub> per staff. Full drive voltage signals of 1 ms duration were transmitted at each of the frequencies of interest. These signals were monitored as they intercepted the near hydrophone (S/N 30235/01) placed 18 metres below the surface of the transducer. Figure 4.13 shows a series of pulses ranging in frequency from 72 kHz to 78 kHz from left to right. With equal power applied to each staff this clearly demonstrates the bandwidth characteristics of the array about its resonance frequency.

Source level measurements were made at range of 65 m with the hydrophone (1" ball 30235/01) placed in the centre of the beam vertically below the transducer array, which was itself deployed at 15 m water depth. Observations were made at frequencies from 67 kHz to 83 kHz. Measurements were carried out at full drive power and at 1/4 power. Due to instabilities in the raft movement, peak level observations of the pulse were made over several minutes.

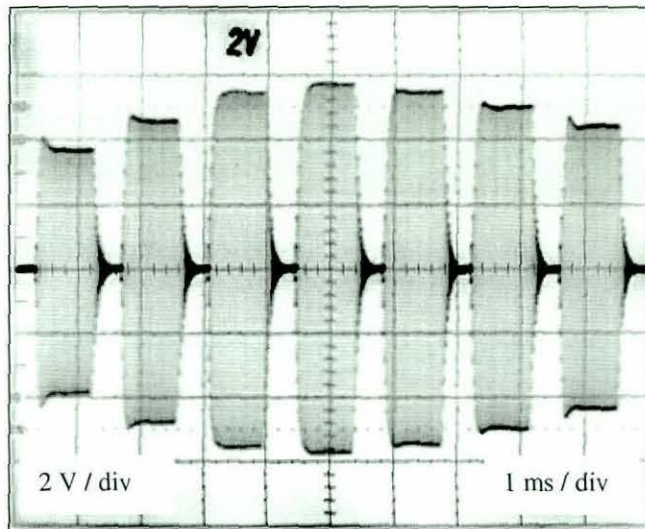


FIGURE 4.13 TRANSDUCER FREQUENCY RESPONSE, WITH PRIMARY FREQUENCY SIGNALS 72, 73, 74, 75, 76, 77 AND 78 kHz SHOWN LEFT TO RIGHT RESPECTIVELY

Source level was given by:

$$\text{Source Level (dB)} = 20 \log (V_{\text{rms}}) + 20 \log (r) + \alpha r - M_{\text{H}} \text{ (dB)} \quad (4.2)$$

where: SL is in dB re 1  $\mu\text{Pa}$  at 1m

$M_{\text{H}}$  = Hydrophone Sensitivity (dB) / -202 dB re 1 V/ $\mu\text{Pa}$

$r$  = Transmission path range (m) / 65 m

$\alpha$  = Absorption coefficient at 75 kHz / 0.029 dB/m

Figure 4.14 shows the apparent and estimated source level based on the measurements at full, 1/4 and 1/25 power levels. Based on measurements at full power, an apparent source level of 240 dB re 1  $\mu\text{Pa}$  at 1m was measured at 75 kHz. The input drive power was then reduced by a factor of four and measurements repeated. Measurements based on 1/4 power were then scaled by a factor of four to a theoretical source level. In the case of a 75 kHz signal a source level of 243 dB re 1 $\mu\text{Pa}$  at 1m was achieved. The difference due to the onset of saturation limiting effects at the point of shock wave formation at a particular frequency is approached. The effective reduction in input power, minimising the

effect of saturation, and the subsequent scaling back up provides a source level figure closer to that theoretically predicted based on array properties and input power but ignoring saturation. A single source level at 75 kHz at 1/25 power was also calculated. This was then used to interpolate maximum source level based on the effects of saturation from the two previous curves. A maximum source level of just below 245 dB re 1  $\mu$ Pa at 1m at 75 kHz, showed a close correlation with the theoretically predicted level of 244.2 dB re 1  $\mu$ Pa at 1m predicted in section 3.2.2.

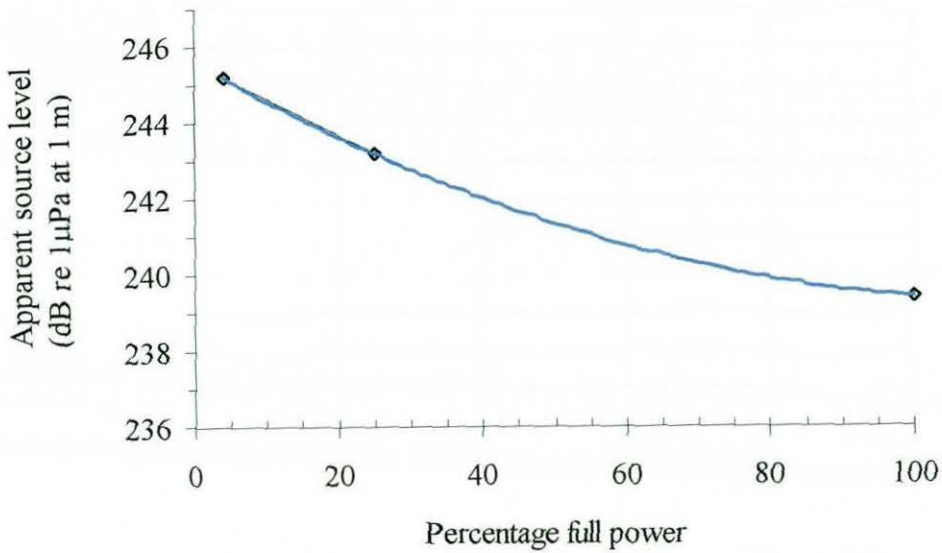


FIGURE 4.14 APPARENT SOURCE LEVEL CALCULATED AT DIFFERENT INPUT DRIVE VOLTAGE

This curve in Figure 4.14 shows the apparent source level estimates based on reading taken at full, 1/4 and 1/25 full power for a 75 kHz, 4 ms long continuous wave signal. The effects of saturation are also illustrated in Figure 4.15. The array itself is clearly working well within the onset of the effects of saturation at most primary frequencies of interest. Below 70 kHz saturation effects become less noticeable due to the reduced this is most likely due to the reduced level of the shock wave formation limit seen at the higher frequencies.

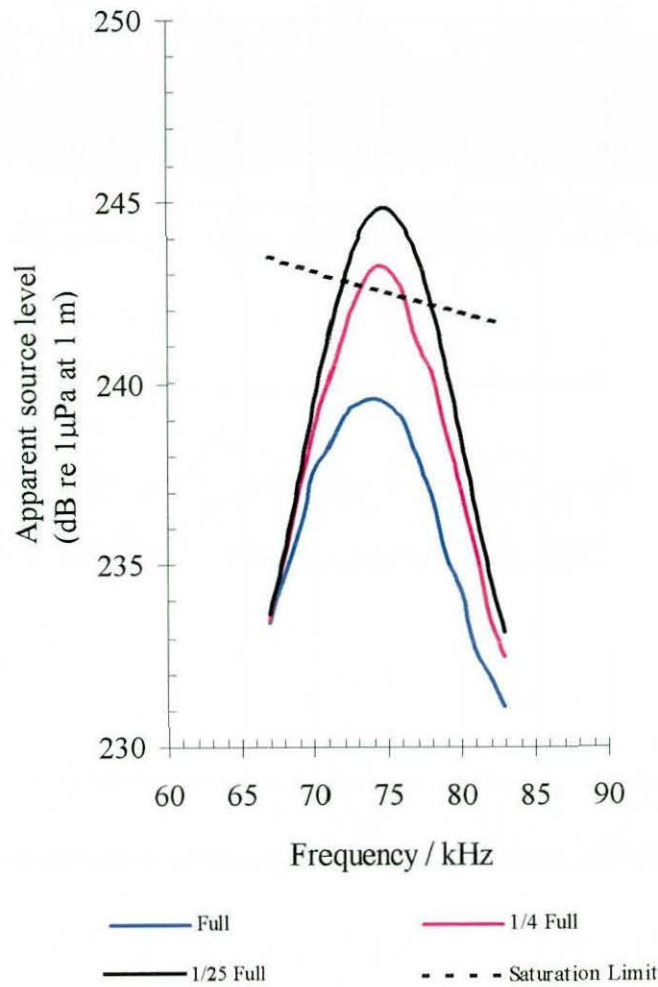


FIGURE 4.15 APPARENT AND ESTIMATED PRIMARY FREQUENCY SOURCE LEVEL

In the 75 kHz case calculating the scaled-up source level ( $SL^*$ ) using equation (3.7) gives  $SL^{*(75 \text{ FULL})}$  is within 4 dB of shock wave formation limit for  $SL^*$  of 280.5 dB re 1  $\mu\text{Pa}$  at 1m kHz. The scaled up source level ( $SL^{*(75 \text{ 1/25})}$ ) based on readings at 1/25<sup>th</sup> full power is 2 dB above where shock wave formation would take place at 75 kHz. Previous observations [3.10] have shown the effective available signal may be well below the shock wave formation limit. This effect can be seen at the lower frequencies in Figure 4.15. The lower frequency signals have higher effective shock formation limits and a reduced source level due to the band-width limitations of the transducer and higher headroom in the frequency factor shown in equation (4.2). The difference between the full power and scaled-up measurement is negligible, These curves gradually part as the resonance



frequency is approached and source level and frequency increase. This is compared with the equivalent frequency above 75 kHz where the effects of saturation are still evident due to the lower effective shock wave formation level even though the point of shock wave formation has not actually been reached. The apparent source level based on scaled-up readings at 1/25<sup>th</sup> full power are therefore considered the maximum achievable source level at the primary frequencies.

Figure 4.15 shows the primary resonance between 74 kHz and 75 kHz with a bandwidth at the -3 dB points of approximately 6.5 kHz. This corresponds to a Q of 11.5 at a resonant frequency of 75 kHz. These values are close to those of the initial measurements made using a HP 4192A LF impedance analyser. In this case the average bandwidth is approximately 6.3 kHz and the Q is 11.9 but the measured transducer resonance point was slightly lower at 73.7 kHz. Figures 4.16-4.18 show single frequency sinusoidal pulses of constant amplitude for 75.0 kHz, 72.5 kHz and 77.5 kHz respectively. Transducer ringing effects can also be seen at various frequencies. Figure 4.16 shows the full power in water response of the transducer array for a 4 ms long pulse at 75 kHz.

Comparison can be made with the 72.5 kHz and 77.5 kHz responses. The 75 kHz response shows a degree of symmetry in the ringing up and ringing down response times. The response is also characteristic in both cases to that seen in a critically damped system. The 72.5 and 77.5 kHz response is similar to each other but lack the symmetry seen at 75 kHz and show a slight over shoot in the rise up effect. The effect on pulse envelope shape for a different primary frequency is also shown in Figure 4.13. These effects later proved significant in the generation of Ricker pulse signals.

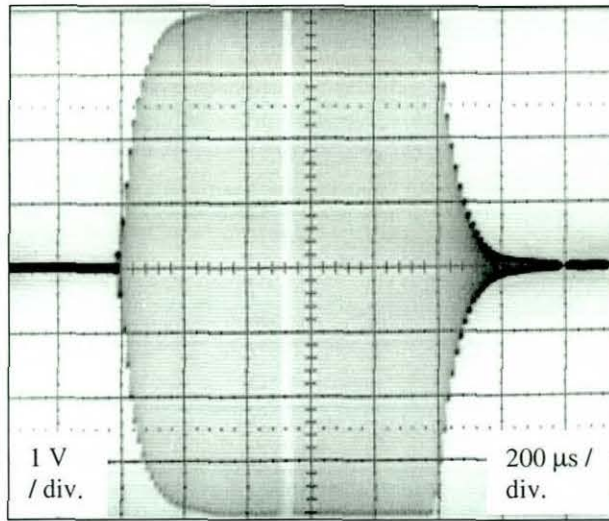


FIGURE 4.16 75 kHz RESPONSE FULL POWER

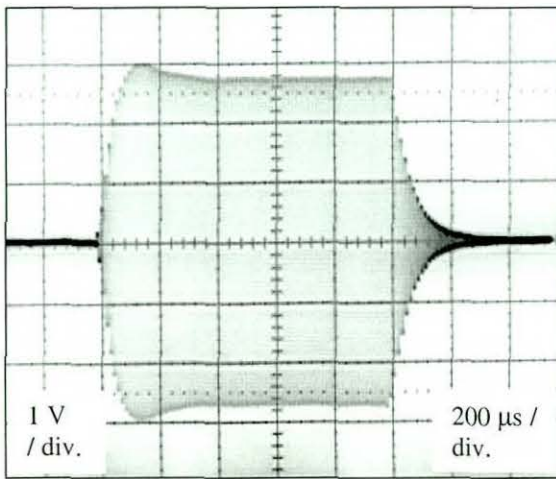


FIGURE 4.17 72.5 kHz RESPONSE FULL POWER

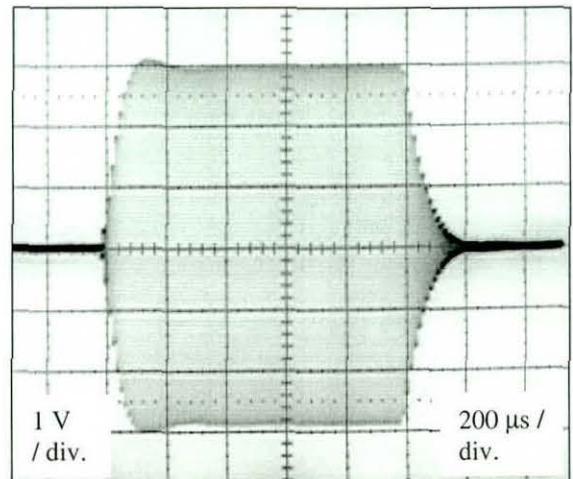


FIGURE 4.18 77.5 kHz RESPONSE FULL POWER

#### 4.8 Secondary frequency generation

Secondary frequency generation was tested using a primary frequency signal formed from the sum of two sinusoidal signals of frequency equally spaced about the resonance frequency. In the case of a 5 kHz secondary frequency, primary frequencies of 77.5 and 77.5 kHz were summed and the complex resultant signal transmitted.

Signals were monitored using the 25 mm ball hydrophone (S/N 30235/1). This

was placed in the main beam 65 m from the face of the array. The array was deployed vertically looking down towards the seabed. Figure 4.19 shows the time axis response recorded using the LU data capture system. Data is archived directly to disk on a multi-channel recorder. The system has a sample frequency of 250 kHz. Various preconditioning filters and pre-amplifiers were used. The response shown in figure 4.19 includes the direct signal and a bottom-reflected signal recorded with a 100 kHz bandwidth. Spectral analysis and time domain signals shown here were carried out using MATLAB software.

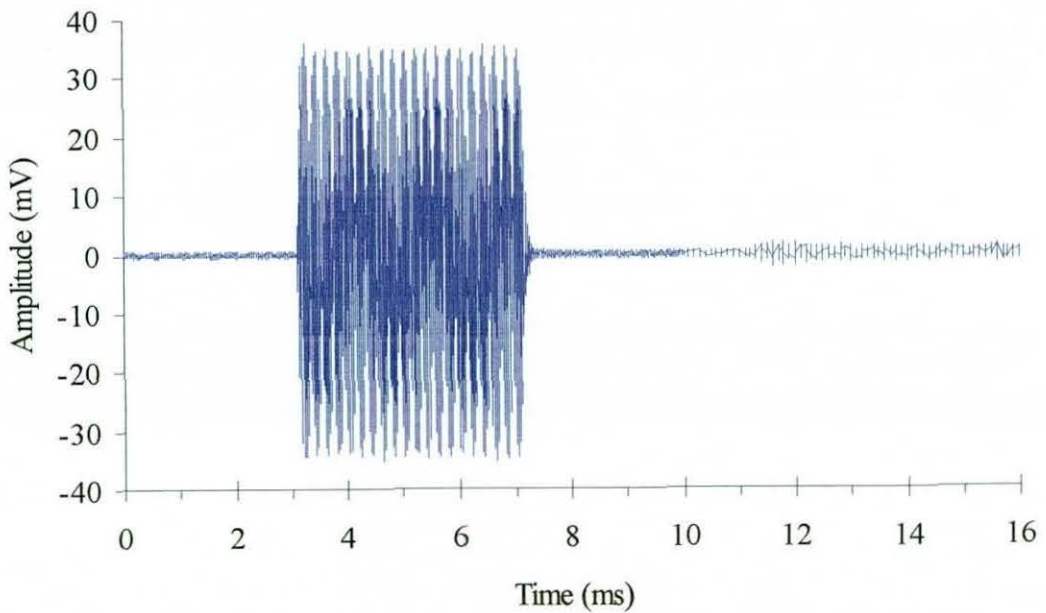


FIGURE 4.19 DIRECT AND BOTTOM-SCATTERED ECHO,  
5 kHz NON-LINEAR GENERATION SIGNAL

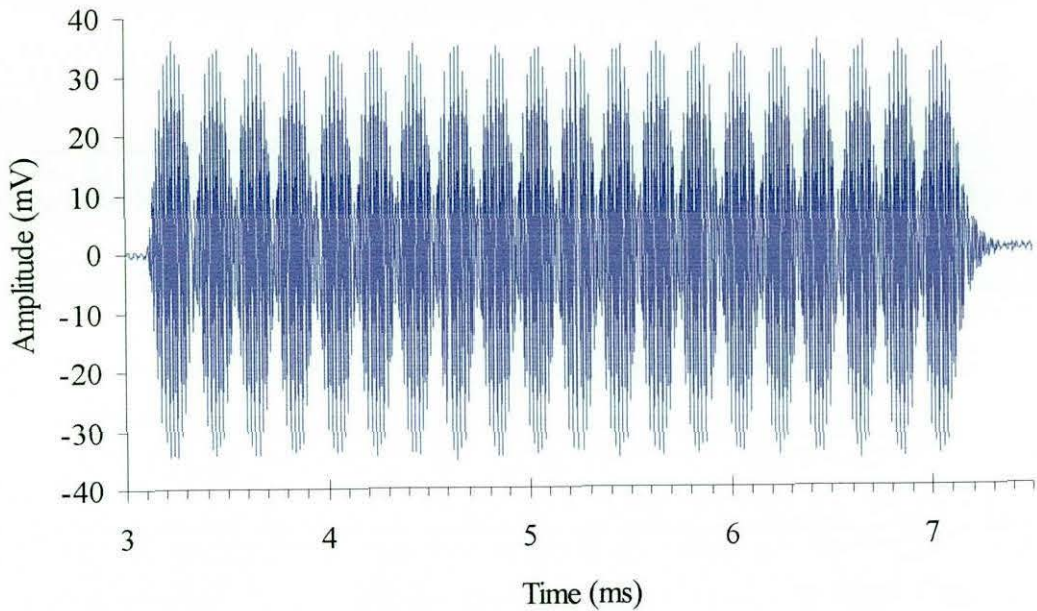


FIGURE 4.20 DIRECT NON-LINEAR GENERATION SIGNAL,  
5 kHz DIFFERENCE FREQUENCY

Figure 4.20 shows an expanded view of the direct signal. The amplitude modulation effects on the pulse envelope for the combined two carrier frequencies can be seen. Transducer ringing effects are visible in the beginning and end of the pulse, similar to the response of the individual sinusoidal signals at the same frequencies observed in Figures 4.17 and 4.18 at the primary frequencies. The low pass filtered response of the 5 kHz generation signal recorded on a separate channel shown in Figure 4.21. A 20 kHz cut-off low pass filter was used, effectively removing the combined primary frequency components of 72.5 and 77.5 kHz seen in Figures 4.19 – 4.20. The remaining signal is due to non-linear generation effects within the water column. Some distortion is seen in the waveform, most likely to the onset of saturation effects in the primary frequencies used in the secondary frequency generation.

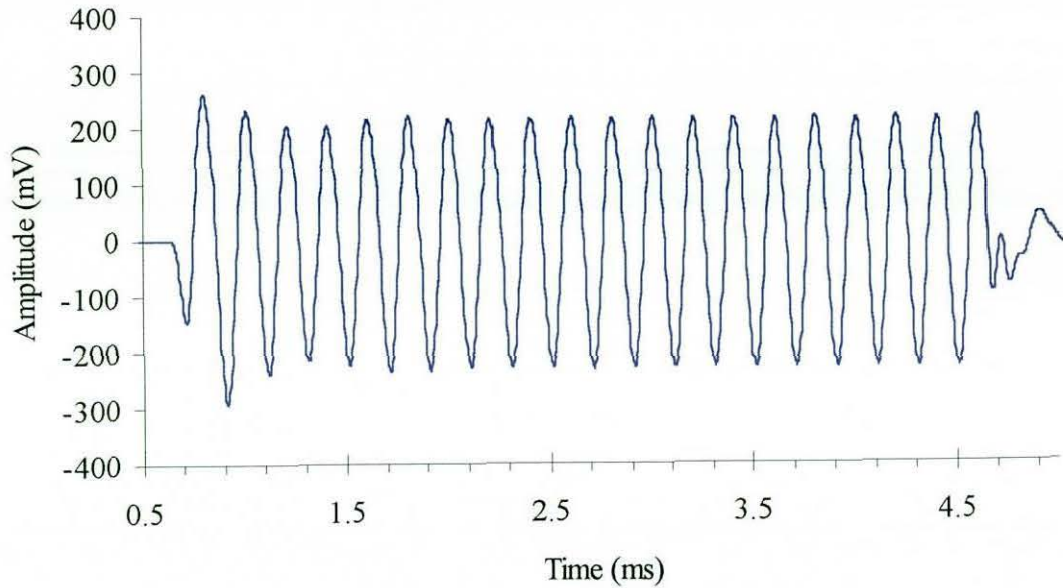


FIGURE 4.21 5 kHz SECONDARY FREQUENCY SIGNAL

The amplitude difference between plots in Figures 4.19 – 4.20 and 4.21 are due to increased gain introduced by the low band-pass filters used to separate the non linear signal component. Transducer ringing effects are also visible in the secondary frequency signal due to the distortion of the pulse envelope at the primary frequencies as the transmit array rings up and then down again.

Figure 4.22 shows the full power, spectral density of the pulse shown in Figure 4.19. Its principle features are the two primary frequencies at 72.5 and 77.5 kHz and a strong secondary frequency at 5 kHz, equivalent to the difference between the two primary frequencies. Harmonics of the primary frequencies are also evident above and below them. Inter-modulation effects between these, resulting in secondary frequency generation of signal level at 10 and 15 kHz. A strong interference signal was also observed at 32 kHz due to electrical interference within the recording system.

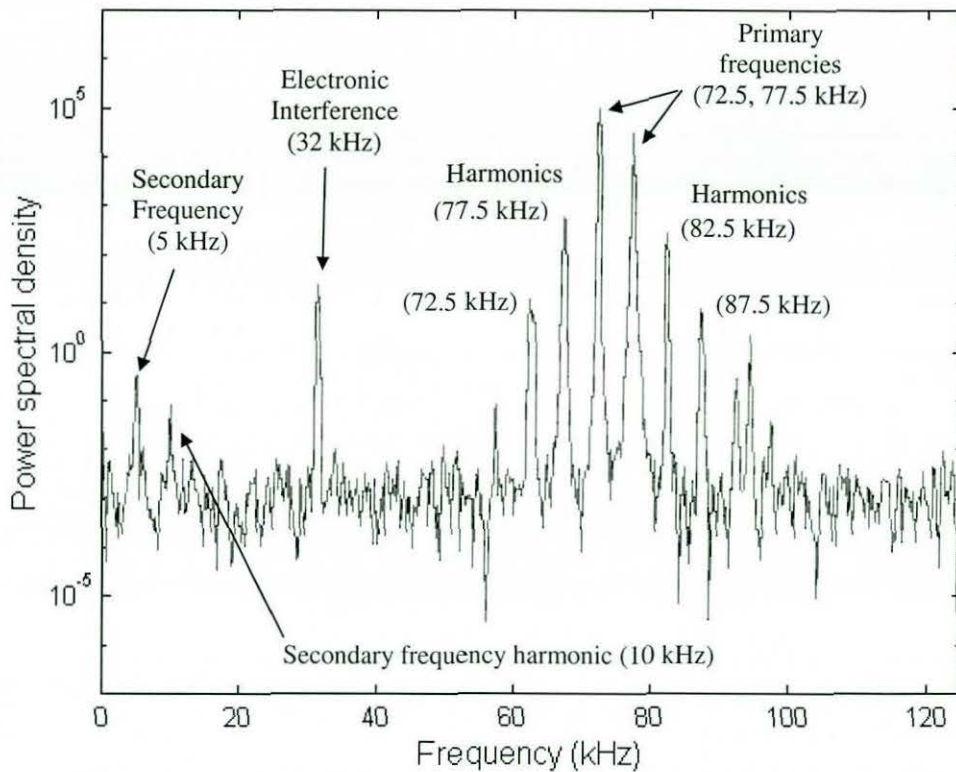


FIGURE 4.22 POWER SPECTRAL DENSITY OF A TRANSMITTED PULSE

Similar analysis of the filtered response shown in Figure 4.23 illustrates the strong secondary frequency generation. Both the difference frequency signal (5 kHz) and harmonics are more evident due to the relative reduction in primary frequency components following filtering and increased gain at lower frequencies.

Spectral analysis was carried out using a 1024 point FFT at a 250 kHz sample rate corresponding to an approximate 4 ms window. Signals were also bandwidth limited by the recording system to 1 – 100 kHz in the wide band case and 1-20 kHz in the low-pass filtered.

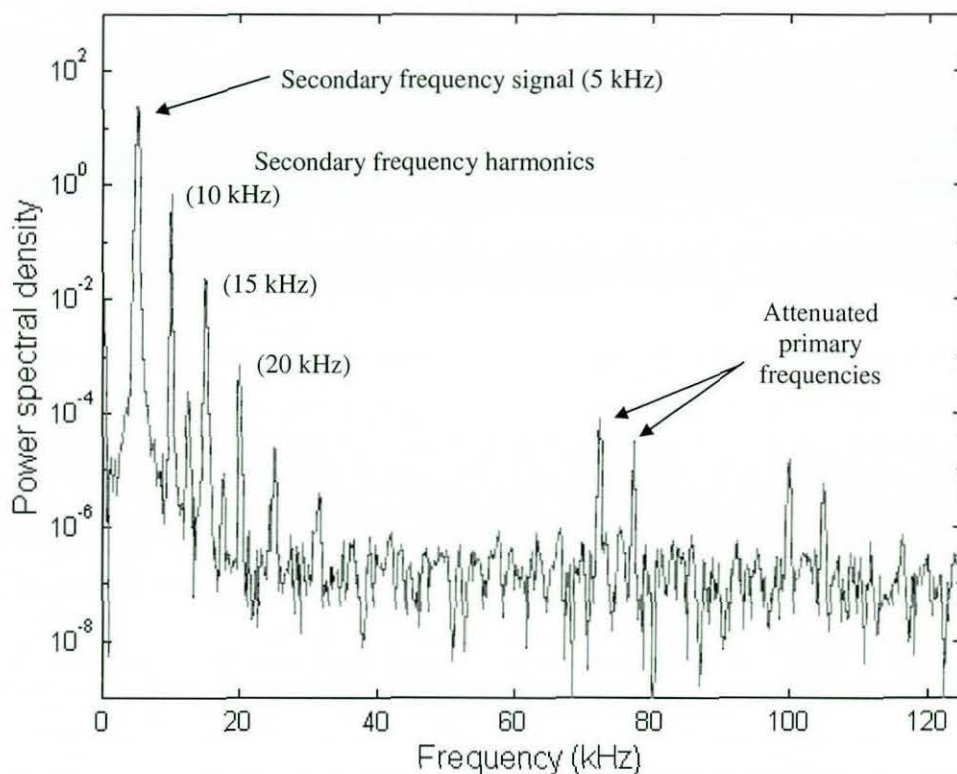


FIGURE 4.23 SPECTRAL ANALYSIS FILTERED RESPONSE 5 kHz SECONDARY FREQUENCY GENERATION SIGNAL AND HARMONICS.

#### 4.9 Secondary frequency beam patterns

Secondary frequency beam-patterns were measured at a range of frequencies by monitoring the low-pass filtered response with a single ball hydrophone (S/N 302525/02) placed 65 m below the array face. The array was then mechanically moved in both the scanned and un-scanned axis while monitoring the hydrophone signal on an oscilloscope. Narrow-band passive filters were used at each of the frequencies of interest. Figure 4.24 shows the normalised beam-plots for a 5 kHz CW non-linear generation signal.

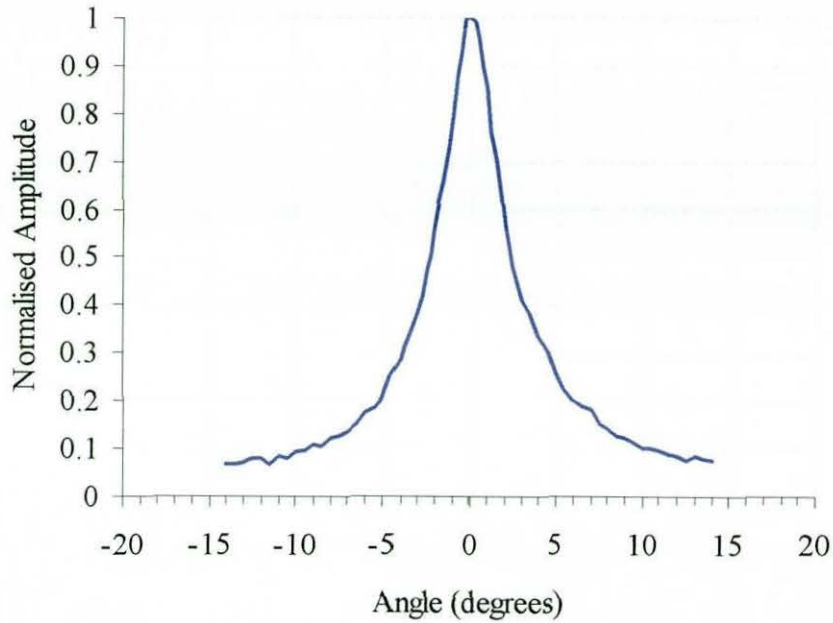


FIGURE 4.24 5 kHz SECONDARY FREQUENCY BEAMPATTERNS, SCANNED AXIS

Figure 4.24 demonstrates the lack of side-lobes over an angular range of  $\pm 15^\circ$ , which is comparable with that for primary frequencies shown in Figure 4.6. The pattern itself shows that some energy is still contained in the *skirts* of the main lobe although no obvious side lobes are present. The beam-width for the 5 kHz signal at the -3 dB points of around  $3^\circ$  which corresponds closely to the theoretically predicted value  $2.89^\circ$ , given by equation (4.3), based on Westervelt's [2.71] original parametric model.

$$\theta_{-3dB} = 4 \left[ \frac{\alpha}{k_s} \right]^{\frac{1}{2}} \text{ radians} \quad (4.3)$$

where  $\alpha$  is the absorption coefficient for the fundamental primary frequency  $f_0$  taken as  $0.00334 \text{ n.m}^{-1}$  and  $k_s$  is the difference frequency wave number. This shows the highly directive nature of the secondary frequency component compared with that available for conventional sonar of similar frequency and array size. A 5 kHz conventional sonar of the same size as the current parametric system would have a beam-width of approximately  $36^\circ$ .

The sector-scanning technique was also used to monitor signals in the range 1–13



kHz; the 3 and 11 kHz responses are shown in Figure 4.25. At the lower frequencies a beam broadening is observed up to  $5^\circ - 6^\circ$  at the  $-3$  dB points. Above 5 kHz little variation in the beam widths of the range  $2.5^\circ - 3^\circ$  was observed. Similar beam patterns and beam-widths were observed in the un-scanned axis.

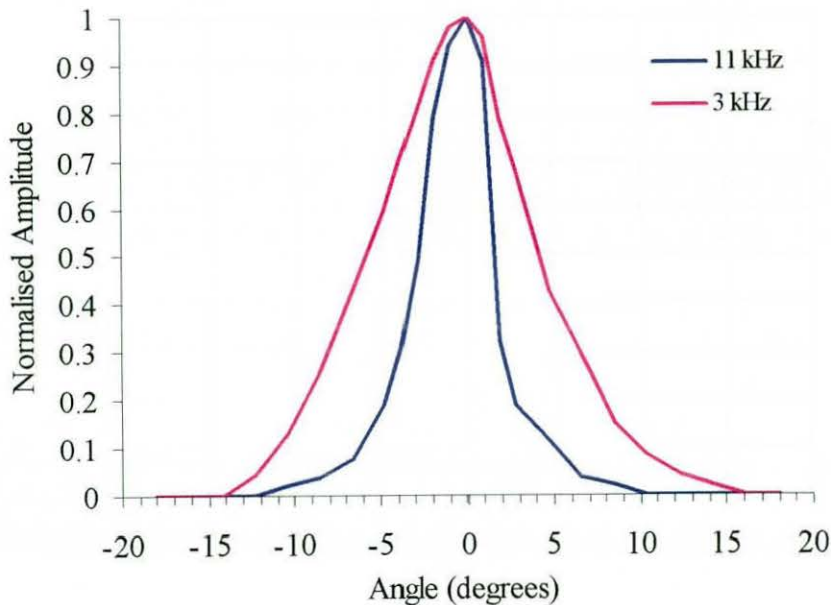


FIGURE 4.25 3 kHz AND 11 kHz SECONDARY FREQUENCY BEAM PATTERNS, SCANNED AXIS

#### 4.10 Secondary frequency source level

Measurements of difference frequency source levels were made using ball hydrophone (S/N 30235/01) at a range of 65 m below the transducer face. With a virtual array length of approximately 100 m, ranges of this order were required for optimum non-linear generation. However due to depth limitations, only ranges of around 65 m were used. At 65 m a predicted loss of less than 1 dB in the difference frequency source level was considered acceptable.

A series of test signals was applied with full power to the transducer array. These were generated at various difference frequencies, ranging from 1 kHz to 13 kHz.

As with the primary frequency source level calculation the equation (4.2) was used and the following parameters applied

$M_H$	=	Hydrophone Sensitivity (dB) / -205 dB re 1 V/ $\mu$ Pa
$r$	=	Transmission path range (m) / 65 m
$\alpha$	<	0.001 dB/m absorption coefficient 1-13 kHz range

In this case attenuation  $\alpha$  was considered negligible at these frequencies and ranges, typically less than 0.001 dBm<sup>-1</sup>. Secondary source levels are shown graphically in Figure 4.26. The error bars are based on error estimates on the hydrophone calibration at these lower frequencies.

Figure 4.26 shows an increase in secondary source level with frequency consistent with theoretical models due to the decreased step down ratio at higher frequencies. However above 5 kHz there is a levelling out of the source level and above 7 kHz less than 1 dB variation. The reduction in achieved source level is due to the bandwidth limitation of the carrier frequencies used for the secondary frequency generation. The effective parametric gain increase due to the reduced step down ratio is balanced by the loss of primary frequency source level at the higher frequencies. Figure 4.15 shows the effective loss in primary source level as the carriers move away from the resonance frequency. A peak secondary source level was observed of 196 dB re 1  $\mu$ Pa at 1m, with less than on 2 dB variation in the range 7 – 13 kHz.

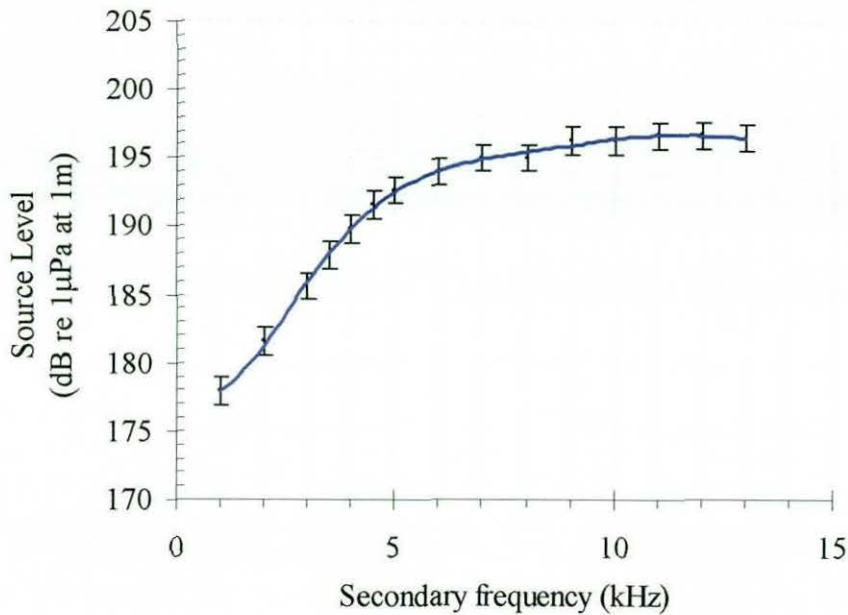


FIGURE 4.26 SECONDARY FREQUENCY SOURCE LEVEL

Comparison of the 5 kHz signal can be made with the primary frequencies of interest. Figure 4.15 shows that the peak source level at 72.5 and 77.5 kHz for a pure tone. Division of the available power between the two gives a combined source level of around 243 dB re 1 μPa at 1m. This is approximately 50 dB above the measured secondary source level for 5 kHz of 192.6 dB re μPa at 1m. Comparison with the full power curve Figure 4.15 gives an average primary source level for the combined signal of approximately 238 dB re μPa at 1m. This is within 5 dB of the theoretically expected primary to secondary source level ratio of 40 dB. Comparison again at 10 kHz, however, gives a primary-to-secondary source level ratio much closer to 40 dB. A general increase in the primary-to-secondary frequency source level ratio was seen at the lower frequencies. Measured levels were, however, much closer to theoretically expected levels at the upper end of the frequencies observed. Some disparity between measured and theoretical levels may be due to the slight truncation of the virtual array in the measurement area.

It is also possible to calculate the sonar's effectiveness through use of the sonar equations. The Figure Of Merit gives a measure of the sonar's efficiency. This

figure can then be used to estimate expected echo levels with various applications of the parametric sonar system.

The Figure of Merit (FOM) is given as <sup>[3,12]</sup>

$$\text{FOM} = \text{SL}_D - \text{NL} + \text{DI}_R - \text{DT} \quad (4.4)$$

where:

$\text{SL}_D$  = (Maximum secondary frequency Source Level) = 196 dB re 1 $\mu$ Pa at 1m.

$\text{DI}_R$  = Receiver Directivity Index assumed to be (dB) = 0 dB.

NL = Total Noise Level (dB) = 84.5 dB re 1 $\mu$ PaHz<sup>-1/2</sup>.

DT = Detection Threshold (dB) = 6 dB.

Sea noise spectrum level is taken as 45 dB re 1 $\mu$ PaHz<sup>-1/2</sup> at 1m at 9 kHz <sup>[4,3]</sup> and  $\text{BW}_R$ , the receiver bandwidth is taken as 20 kHz. Total noise is then given as: Sea Noise Level + 10log( $\text{BW}_R$ ) = 45 + 43 = 88 dB re 1 $\mu$ Pa. Receiver directivity is taken as 0 dB due to the use of a omni-directional hydrophone and the Detection Threshold is set at 6 dB.

The Figure of Merit for non-linear operation of the parametric system at 9 kHz is therefore given by:

$$\text{FOM} = 196 - 88 + 0 - 6 = 102 \text{ dB rat } 9 \text{ kHz}$$

The Figure of Merit can then be used to determining echo excess of the sonar used in a active mode if a target strength and target range is known.

#### 4.11 Conclusion

Initial tests showed the operation of the array was well within expected parameters. A peak primary frequency source level of 245 dB re 1 $\mu$ Pa at 1m was measured for a single tone at the resonance frequency of 75 kHz. Secondary frequency signals were measured at a range of 65 m for frequencies between 1-13

kHz with a relatively uniform with a peak source level of 196 dB re 1 $\mu$ Pa at 1m for frequencies above 7 kHz. The array, however, has a primary frequency bandwidth of 6.5 kHz. This limits the potentially higher gains expected from higher secondary frequencies due to the reduced primary frequency energy available.

Both primary and secondary beam-patterns were measured over a  $\pm 20^\circ$  sector. Primary half power beam-widths of  $2.5^\circ$  were observed at 75 kHz in two axes. Secondary frequency beam-widths in the range  $2.5^\circ - 6^\circ$  were seen for the frequencies ranging 3 – 11 kHz. These patterns also exhibited little or no side-lobe energy typical of non-linear generation. The measurement of both primary and secondary beam-patterns was within expected theoretical values.

Electronic beam-steering was demonstrated in one axis for both primary and secondary frequencies over a  $\pm 18^\circ$  sector.

#### REFERENCES: Chapter 4

---

- 4.1 Woodward B., Hole S.K. and Forsythe W.  
Transducer design for a correlation log  
*Ultrasonics*, Vol. 31, No. 1, pp. 21–33, 1993.
- 4.2 Tucker D.G.  
Applied Underwater Acoustics.  
pp. 164-181.
- 4.3 Etter P.C.  
*Underwater acoustic modelling, principles, techniques and applications*  
Elsevier Science Publishers Ltd, pp. 159 - 162, 1991.

## CHAPTER FIVE

# SIGNAL SYNTHESIS / DATA CAPTURE SYSTEMS

### 5.1 Introduction

Modern sonar systems often require complex signal synthesis techniques. This is particularly true of a parametric sonar system, which requires the computation of a range of complex signals that are then amplified and applied to a transducer array. Signal generation is further complicated by the use of phase steering techniques, where by, an inter-stave phase variation is calculated and applied to the parametric signal.

Many simple sonar systems that require only a limited range of output signal types generate these signals with electronic hardware. More complex systems adopt computer-based signal synthesis, which allows a much higher degree of signal complexity and versatility. Due to the signal complexity of a phase-steered parametric sonar system and the wide variety of signal types used in its application, a variety of signal synthesis techniques were employed in this work in conjunction with interfacing and signal hardware systems.

### 5.2 Signal synthesis system hardware

A personal computer (PC) based signal synthesis system was developed in conjunction with the Defence and Evaluation Research Agency (DERA), Winfrith (UK). The use of personal computers allowed the development of complex signal synthesis as a relatively small but versatile low cost package. With the increase in the availability of powerful and compact computers, the signal synthesis system can be made to be easily portable and simple to deploy in a wide range of working environments. Initial work was done before the developments described here on a simple 4-bit resolution system linked to a Z80 processor <sup>[5.1]</sup>. This was later

replaced by a *transputer* based system using a IBM PC as a control interface [5.2, 5.3]. With the advent of the 75 kHz IOS/LU transducer array, a new 16-bit resolution, PC based system was developed. The system itself has up to 16 parallel channels allowing the simultaneous generation of 16 different signals up to 32 ms long. Thirteen channels are required for signal generation across each of the staves of the IOS/LU array (Chapter 3). The additional spare channels are used for trigger and synchronisation signal generation.

Hardware interfacing is done via the computer ISA (Industrial Standard Architecture) bus to external memory and Digital-to-Analogue (D-to-A) circuitry. An IBM compatible 486 DX2 desktop computer was initially used and control software was developed using a DOS-based Borland PASCAL v7.0. Figure 5.1 shows the system diagram for a 16-channel transmitter system.

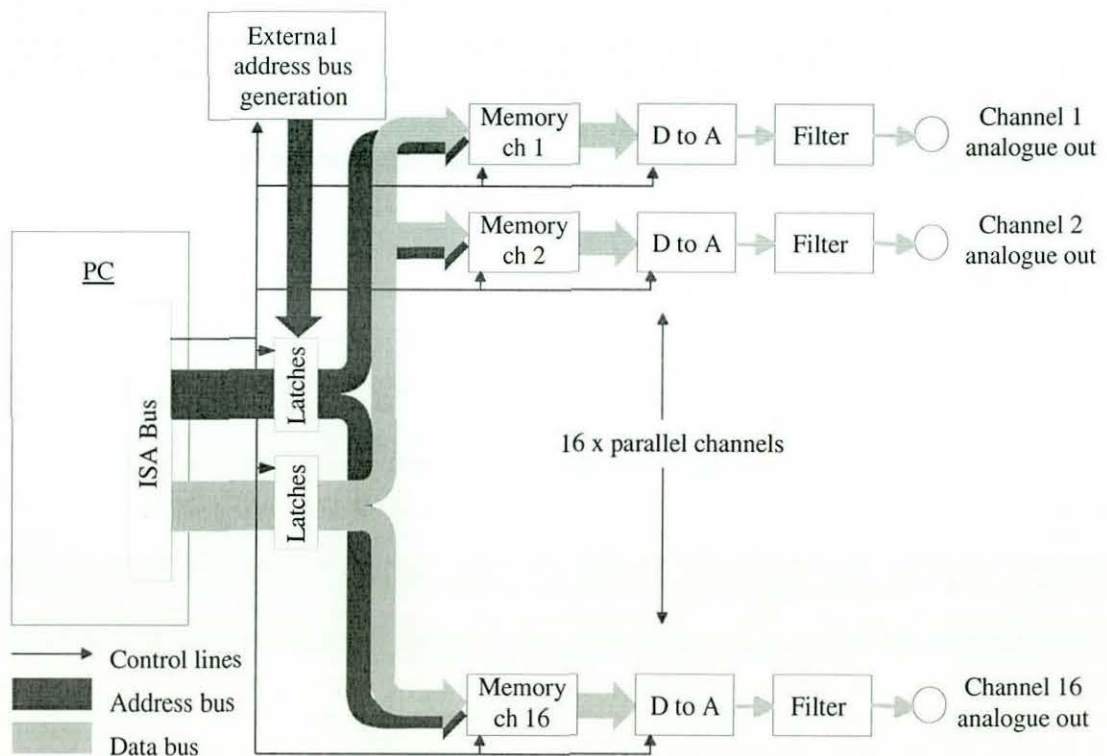


FIGURE 5.1 SYSTEM DIAGRAM PC BASED TRANSMITTER SYSTEM

Various control interfacing is also done across the same ISA slot, with 8-bit data lines in PC memory area \$300 (in hexadecimal). Software codes in these memory



addresses are decoded by external firmware logic using ASICS integrated circuits. These control lines are used to establish read / write conditions for the external memory and the D-to-A output enable lines.

System operation is in two modes. The required waveforms are first loaded into each of the external memory blocks. Then, on transmission, data is simultaneously clocked out of all memory to provide signal generation on 16 parallel channels.

### **5.2.1 Data loading phase**

Control lines are used to select a channel in turn. Firmware logic is used to decode control signals that enabled / disabled address and data bus latches across the ISA bus. The appropriate memory block is made 'read enabled' and direct mapping of data across the ISA address bus is then possible. Mapping across the data bus is done to a 16-bit resolution. The external memory for each channel is achieved using four 64 k x 4 bit static RAM memory integrated circuits (CY7C192 from Cypress). This allows development of the 16-bit data bus split into 4 x 4 bit *nibbles*, one per memory module. Sixteen-bit data is written directly across the bus in every other memory location in the PC memory from location \$A000:0000 to \$A000:FFFF, corresponding to 64 k words. The mapping technique used in hardware is limited to 8 bit bytes. Both the even and odd memory locations in PC memory were therefore needed for a 16-bit word development across the ISA bus. This 16 bit data was then translated into the external memory directed by the even part of the ISA bus address, with the odd numbered addresses in the external memory left unused. Total usable memory allocation per channel is therefore 32 k words (16-bits) spread over a 64 k word memory area.

The waveforms are generated mathematically in software and written directly into the PC memory and therefore the external memory block for that channel. Firmware logic is also used to automatically disable the D-to-A output during the memory write phase to avoid the generation of random analogue signals on the data bus whilst writing to memory and possibly damaging the power amplifiers or array.

### 5.2.2 Transmit phase

Due to the use of static RAM, the loaded waveform data is retained unless overwritten or the system was powered down, freeing the computer processor for other functions. A *begin to transmit* signal is received through the ISA bus, using memory area \$300. This is decoded using firmware logic and the counters / dividers are reset. Firmware logic is then used to switch the address bus using tri-state octal buffer / drivers (74ACT541 Phillips) to the external address bus generation. A 16 MHz quartz crystal output is divided down to a 4 MHz clock signal, which is then used to generate a 16-bit address bus at a 1 MHz sample rate, as shown in Figure 5.2.

The Least Significant Bit (LSB) of the address bus output Q0 is tied to 0V, equivalent to logic 0. This ensures then only even address locations i.e. \$0000, \$0002, \$0004 etc. are accessed.

The data bus is then applied to a 16-bit monolithic D-to-A converter (PCM55, from Burr Brown), which provides 16-bit resolution. The theoretical dynamic range for 16-bits of 96 dB is, however, limited to a practical value of around 90 dB due to noise and linearity limits. Full voltage range operation is  $\pm 3V_p$  although typical operation is over a  $\pm 2.5V_p$  voltage swing. With a 1 MHz sample rate and a 32 k word memory area, a maximum signal generation period of 32.768 ms is possible.

The quantization of the generated signal was *smoothed* using a low-pass filter at 100 kHz. Operation of the parametric system rarely requires signal generation of greater than 85 kHz, which is well within the filter bandwidth. Typical operation of a 75 kHz sinusoidal signal with a 1 MHz sample rate gives over 13 samples per period, providing considerable over-sampling in the signal production with correspondingly good signal reproduction at the frequencies of interest. The smoothed analogue signal is then applied directly to the power amplifiers for transmission.

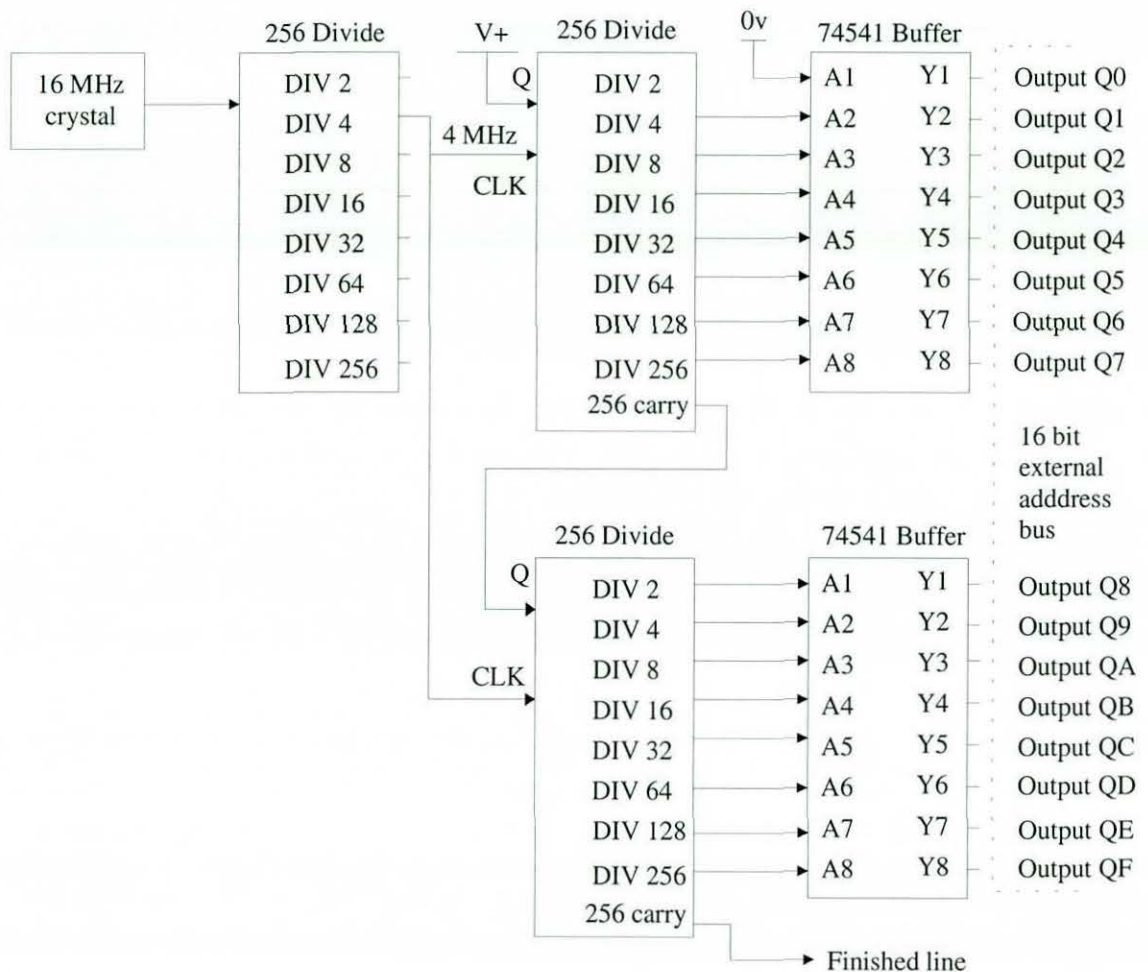


FIGURE 5.2 TRANSMIT PHASE ADDRESS BUS GENERATION

### 5.2.3 Extended memory mapping

On reception of the *begin to transmit signal* the external address bus is generated over the range 0 – 64 k words. When complete the system is reset and waits until reception of the *next begin to transmit signal*. Due to the generation of the entire 64 k memory block, care must be taken with signal pulse lengths of less than 32 k words (32.768 ms). The unused memory must be set to a mid-rail value corresponding to the 0V position of the bi-polar D-to-A. Similarly, to change the signal type on any channel requires that the new waveform is computed and loaded over the top of the existing memory data. System requirements of rapid signal type change led to the reconfiguring the 32 k-word memory into 8 x 4 k-word blocks, or *pages*, each corresponding to 4.096 ms, as shown in Figure 5.3.

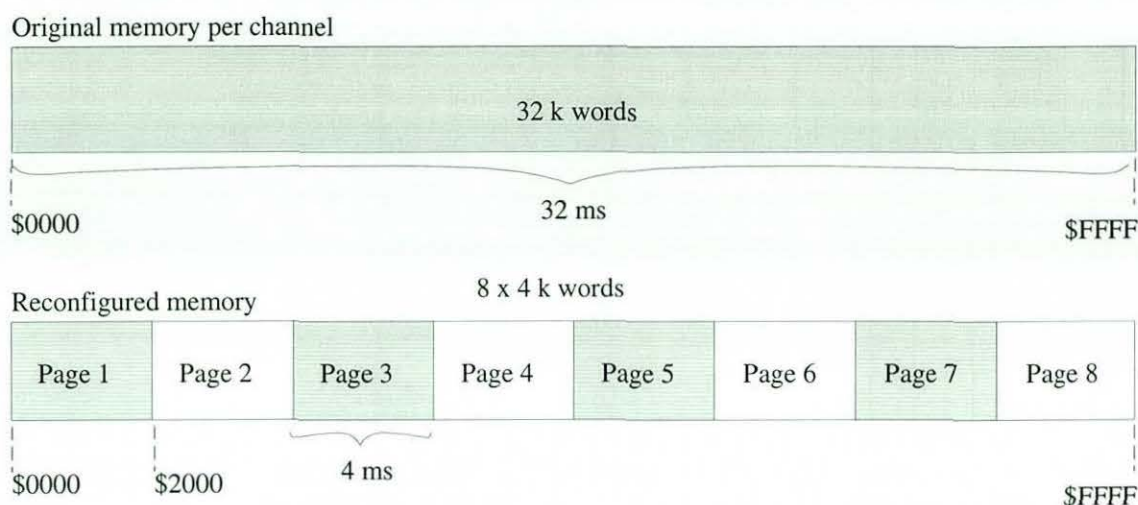


FIGURE 5.3 RECONFIGURED MEMORY ALLOWING PAGE ACCESS

Control of the three highest bits from the address bus QD, QE and QF, shown in Figure 5.2, are handled by firmware logic mapped to PC memory area \$302. Software control of the start address is then possible, allowing pre-loading and transmission of any one of eight 4 ms signals. Each signal type can be loaded into any of the eight memory areas separated by a \$2000 word memory block. The appropriate memory area can then be selected and the *begin to transmit* signal then unloads data from the corresponding memory block. This allows near-instantaneous access under software control to any one of eight pre-loaded signals.

#### 5.2.4 Additional control lines

Various control lines have also been made available. Bits 0 and 1, the LSB and LSB + 1 of channel 16, can be programmed using masks, which allows normal signal generation using the upper 14 bits, with extra signals encoded into the lower 2 bits. Logic levels from these bits are then be used for LED indication during the transmit pulse and TTL trigger synchronous with the start of the transmit pulse. These lines have also been used to control relays disabling the receiver circuits during the transmit phase to protect them from high voltage levels. The logic levels are then reversed at the end of the transmit pulse, thereby re-enabling the receiver system for the reception of echo data.

### 5.3 Data capture system

A multi-channel data capture system was developed in parallel with the transmitter system, which included prototype circuit boards developed in conjunction with DERA Winfrith. Software was also developed, providing real-time displays in both the time and frequency domain. Data from the capture system could be written to a computer hard disk, providing an efficient storage medium.

#### 5.3.1 Data capture hardware / software

The hardware is again based on an ISA bus interface in a PC, as shown Figure 5.4. Data is stored on up to sixteen parallel channels to 16-bit resolution. The receiver system operates in a similar way to the transmitter system by operating in two modes, one for data capture and the other for data read operation. Firmware logic under software control is used to switch between modes and allows a high degree of versatility in system operation.

*In the data capture phase, software controls via the ISA bus are decoded using firmware logic contained on the PC interface board. Up to 16 high-speed monolithic balanced input sample-and-hold amplifiers (SHC5320, Burr-Brown) are then enabled. These devices have a fast acquisition time of no greater than 1.5  $\mu$ s and a holding mode settling time 350 ns, easily allowing operation at sample frequencies of around 500 kHz. The outputs are then fed to 16 parallel 16-bit analogue-to-digital converters (PCM78P, Burr-Brown). These are low noise devices with a fast conversion time, and 16-bit resolution at the sample rates of interest and a 5.5 V<sub>pp</sub> dynamic range.*

Once the conversion is made the 16-bit digital data is transferred from each channel in turn to a single memory block on the PC interface card. The memory is arranged in two 8-bit x 512 k medium speed static RAM blocks (8512, Hitachi). These devices allow a maximum conversion and store rate of 250 kHz. External

logic is used to generate the address bus to provide the memory addressing and the A-to-D converter clock signals. Once the clock is started, data conversion continues until the memory bus is full, providing a *time-windowed* capture system. At 250 kHz sampling for 16 channels a data capture window of 16 ms is possible.

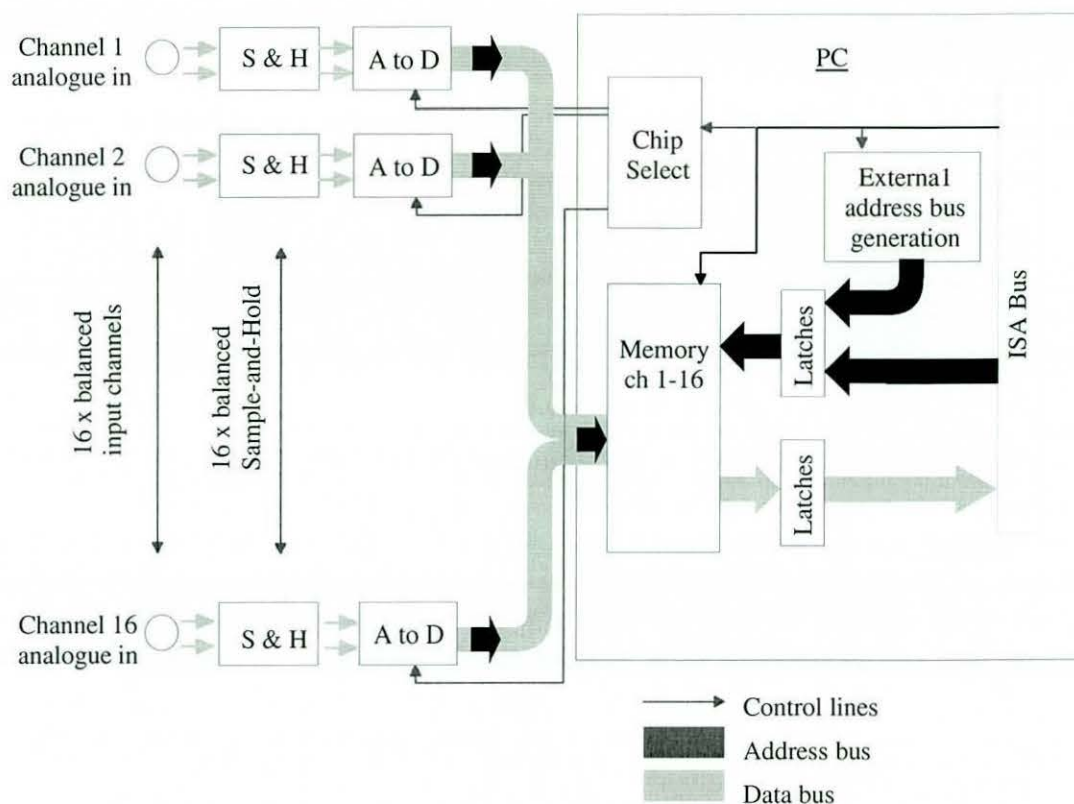


FIGURE 5.4 MULTI-CHANNEL DATA CAPTURE SYSTEM

The 250 kHz clock provides a 125 kHz Nyquist sampling limit. This is further limited to a 100 kHz bandwidth by preconditioning filters just before the sample-and-hold inputs. Various other pre-amplifiers are used before the main capture board depending on application.

A later modification allows more control of the upper four bits of the memory address from software links. This allows for software reconfiguring of the memory allowing fewer channels to be used, thereby providing longer capture windows. Table 5-1 shows the channel-window selection options with the reconfigured system. Actual selection of the number of channels is given using

logic linked to software address lines. Once the number of channels is selected a *start-to-capture* signal is then used. The external memory address bus is then started and the sample and holds and the A-to-D's are enabled.

Number of channels	Capture window
16	16 (ms)
8	32 (ms)
4	64 (ms)
2	128 (ms)
1	256 (ms)

TABLE 5-1 CHANNEL-WINDOW DISTRIBUTION OPTIONS FOR RECEIVER SYSTEM

Once the capture is complete data can then be read from the memory into the computer across the ISA bus. This is organised sequentially, i.e. first byte of channel 1, first byte of channel 2, etc., until the end of the memory block is reached. Static RAM is used in the memory block to allow the data to remain there until the computer is free to unload it. On reading, individual channels are separated and time scans of multiple channels are displayed in *real-time* on the screen. A Fast Fourier Transform (FFT) is also generated to provide *real-time* spectral analysis of a selected channel. A 1024 point FFT with a rectangular window is obtained, corresponding to approximately 4 ms of a specific channel. The 1024 points provides a FFT bandwidth of 125 kHz at 250 kHz sampling, providing a good match to the bandwidth limitations of the pre-conditioning filters and the A-to-D converters. On-screen controls allow channel selection of displayed channels and the FFT window position.

Software developments in both DOS and Windows95 operating systems have allowed control of both the transmitter and receiver systems with a single computer. Data capture software is used to provide the transmitter 'go' signals then to wait for a given transmission path delay corresponding to the signal propagation distance. Signals are then captured on multiple channels for a given

time window size. On completion of the capture window period, data can then be read in and displayed as time-scans and FFT's on the screen. Data from all channels can also be written directly to computer hard-disk, providing an efficient multi-channel storage system.

Software was also developed to allow the reading back of stored data. Each channel for each capture window is viewable in the internal format, which provides a higher data density and therefore requires less disk space, making the data storage for multiple channels more efficient. This, however, makes the extraction of a single data channel more complicated. The development of view-and-convert software allows quick and efficient surveying of the data in the internal format for all channels and then conversion of selected channels to a more generic data format. Typical used formats include ASCII TEXT either 'TAB' or 'comma' delimited. These formats are widely accepted by signal analysis software packages including MATLAB, MATHCAD and the spreadsheet EXCEL.

### **5.3.2 Pre-conditioning filters**

Typical operation of the data capture system uses 1-4 channels, allowing a window period of 64 ms, in comparison with a 16 ms window when data is recorded on 16 channels. Various pre-conditioning filters were used with the first four channels. These are split into higher bandwidth channels in the range 1.6 – 100 kHz for recording primary and secondary frequency components and narrower-band systems of various gains for secondary frequencies only, as shown in Figure 5.5.

The amplifiers are balanced input-output devices, allowing direct connection to the balanced input of the data capture system. An AD743 low-noise amplifier front end is used. The low noise differential input combined with a high-pass filter defining the lower limit of the total band-pass. The –3 dB break point is set to 1.6 kHz to reduce lower frequency shipping noise whilst still allowing capture of the lower secondary frequencies of interest. Then a gain stage and a 5th order elliptical low-pass filter define the upper limit of the band-pass. The output is then



fed to a balanced output amplifier stage. The AD743 provides good input loading characteristics when driven by a capacitive transducer typical of hydrophones and ceramic transducers, making it ideal as a low-noise initial buffer amplifier. Over-voltage diode protection is also included at the first stage to eliminate the risk of damage to the internal circuit due to large voltages on the input.

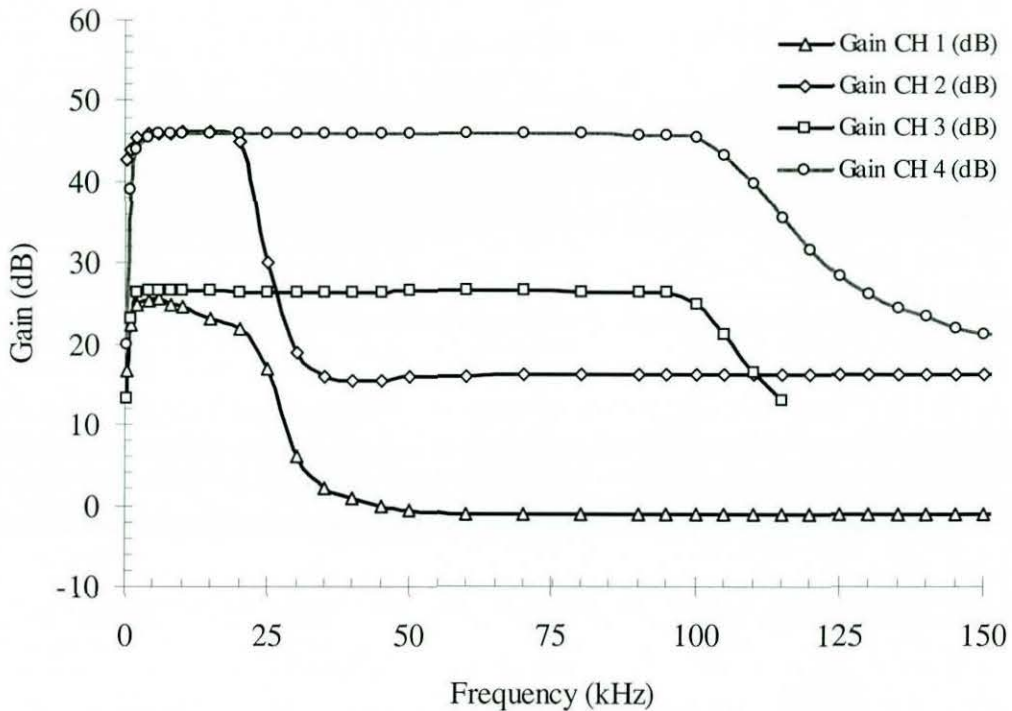


FIGURE 5.5 GAIN-BANDWIDTH CHARACTERISTICS OF PRE-CONDITIONING FILTERS

Figure 5.5 shows the gain-bandwidth configuration for the four channels. Channels 3 and 4 are left broadband to allow data capture of primary and secondary frequency signals. Channels 1 and 2 are bandwidth limited to an upper limit of around 20 kHz, covering the secondary frequency range of interest. For each pass-band the gains were defined between 26 and 46 dB, providing reasonable signal levels for most applications. The amplifier inputs are usually driven unbalanced to provide an extra +6 dB of gain from the designed 20 and 40 dB for balanced input operation. A number of different transducers are typically used with the system, including single element spherical ball hydrophones, ring

hydrophones and the receiver array on the parametric sonar transducer array.

### 5.3.3 Auto-logging systems

Auto-logging systems are included in all software where possible. Typical operation of the system involves selection of the transmitter pulse type and properties. The waveforms are then calculated and loaded into the transmitter. Computer control is then used to transmit the signal and capture the returned data, either in terms of reflected echoes or the direct signal recorded on a hydrophone some distance down range. All system parameters for each transmission and capture are logged automatically allowing improved logging for later data analysis. Data is again stored in an ASCII TEXT format in files that are easily read during an analysis phase.

System software is also linked with a GARMIN 12 GPS system, which provides a serial data burst of GPS data every second. This signal is decoded and the GPS real time clock is used to update the computer system time, which is then used as the clock master for all logging files. The use of GPS allows an extremely accurate time synchronisation of events over large distances. The use of dedicated GPS cards within the PC can make the accuracy internationally to within nanoseconds, although accuracy from a small hand held unit in the order of milliseconds is sufficient for most operational use. The use of *threading* in the Windows95 operating system allows this operation to take place in parallel with the main transmitter-receiver functions of the software, i.e. the transmitter-receiver functions are not interrupted when GPS data is made available, allowing the two systems to work unsynchronised.

Interfacing with other systems also allows additional data to be included in the logs. This includes ship position from the GPS, external sensors like pitch and roll, and target position. This and transmitter-receiver parameter data are then stored automatically, minimising the risk of lost data. All logging systems are linked to acoustic data retrieval software, allowing efficient analysis of acoustic data with data parameters displayed at the same time.

## 5.4 Software signal generation

Initial software developments took place using a DOS-based development language Borland Pascal. This provided relative ease of system control across the ISA bus with the development of a relatively user-friendly front-end programme. Later code developments utilised firstly the Windows 3.11 Pascal language and later Windows 95 operating system. Development in the Windows-based operating systems was carried out using the DELPHI development packages. The Windows format provides considerable improvement in the user interface but was more problematic on hardware control. The development of commercial Windows components, allowing direct memory mapping across the ISA bus, allowed the re-development of the existing code into the newer operating systems. The introduction of the Windows 95 operating system also offered the possibility of 32-bit processing applications previously unavailable under the DOS operating system. This has allowed development of *threaded* systems with more than one application running in parallel from a single processor. This was utilised to integrate a number of systems (discussed further in Chapters 6 and 7) into a single software package and the development of *real-time* applications (Chapter 9).

### 5.4.1 Non-linear signal synthesis

Signal synthesis of the generation of parametric signals is carried out in software and the developed waveforms are loaded into the external hardware modules ready for transmission. Two types of non-linear signal generation are used, summed-sinusoidal and Amplitude Modulation (AM).

Summed-sinusoidal waveforms are generated from the addition of two primary frequency sinusoidal waveform functions. Described by the functions  $F_1(t)$  and  $F_2(t)$  at frequencies  $(f_1, f_2)$ . The two are summed mathematically, the resulting waveform then has an envelope modulation effect similar to that seen in Figure 5.6 (a). This shows the beginning of the combined sinusoidal waveform for generation of a difference frequency signal ( $f_D = f_1 - f_2$ ) at 5 kHz, where  $f_1$  and  $f_2$  are equally spaced about the transducer resonance frequency ( $f_0$ ). The combined

waveform  $F_{summed}(t)$  can then be expressed in terms of equation (5.1).

$$F_{summed}(t) = Amplitude * \left[ \frac{F_1(t) + F_2(t)}{2} \right] \quad (5.1)$$

with :

$$F_1(t) = \sin(2\pi.f_1.t + \phi_1) \quad (5.2)$$

and

$$F_2(t) = \sin(2\pi.f_2.t + \phi_2) \quad (5.3)$$

where:

$$f_1 = f_0 - \frac{f_D}{2} \quad (5.4)$$

$$f_2 = f_0 + \frac{f_D}{2} \quad (5.5)$$

so that

$$f_D = f_2 - f_1 \quad (5.6)$$

If the start phases  $\phi_1$  and  $\phi_2$  of the two primary frequency wave functions  $F_1(t)$  and  $F_2(t)$  are the same the combined waveform function  $F_{summed}(t)$  begins with constructive summing of the waveforms in terms of the secondary frequency modulation. This can result in a sharp edge at the beginning of the signal depending on the start phase, in the pulse envelope, as shown in Figure 5.6(a). A *soft start* option can be achieved by the introduction of an  $180^\circ$  phase shift in one of the primary frequency waveforms. Such that:

$$F_1(t) = \sin(2\pi.f_1.t + \phi_1 + \pi) \quad (5.7)$$

The waveforms are then summed in the normal way, forming a smoother start in the modulation effect seen in the waveform envelope, as shown in Figure 5.6 (b).

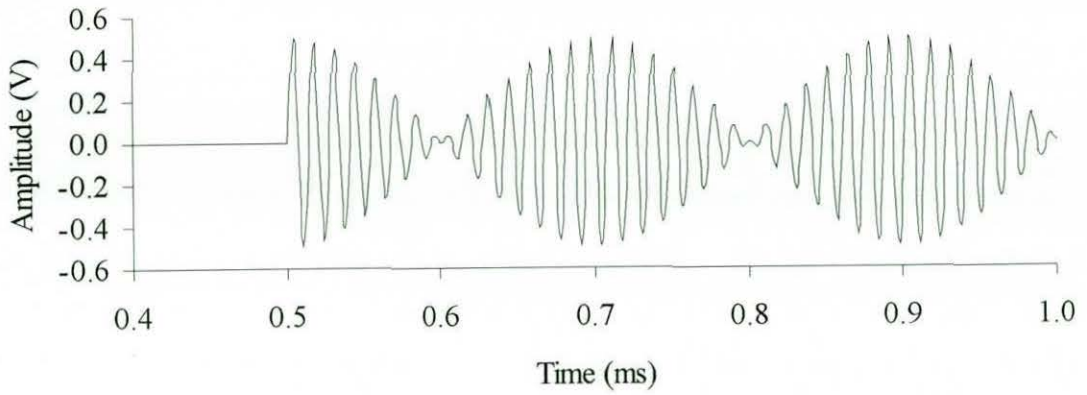


FIGURE 5.6 (a) SUMMED SINUSOIDAL AMPLITUDE MODULATION, 5 kHz

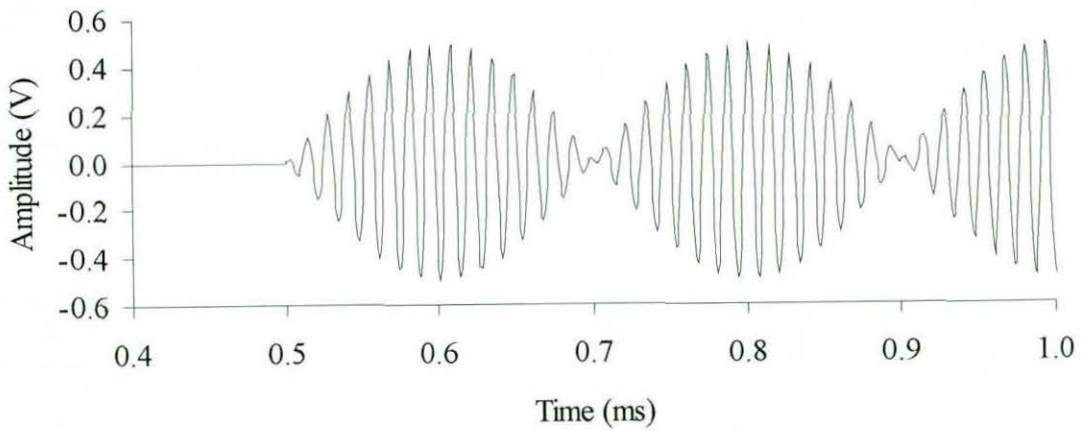


FIGURE 5.6 (b) *SOFT START* SUMMED SINUSOIDAL AMPLITUDE MODULATION

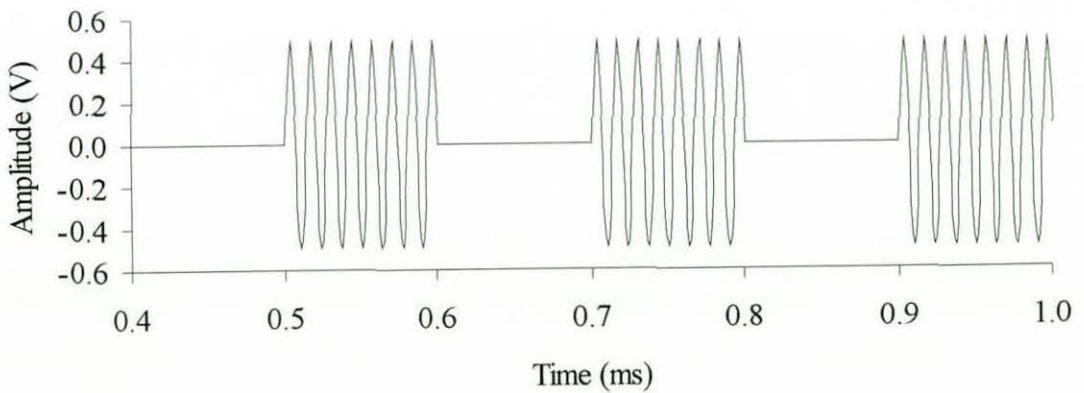


FIGURE 5.6 (c) AMPLITUDE MODULATION (AM) 5 kHz SECONDARY FREQUENCY GENERATION

On application to the water, secondary frequency component generation can take place at the sum frequency ( $f_1 + f_2$ ) and difference frequency ( $f_2 - f_1$ ). The period

of the envelope of the waveform in Figure 5.6 (a) and 5.6 (b) shows the difference frequency  $f_D$ . The higher sum signal ( $f_1 + f_2$ ) is more highly attenuated so is not considered in the subsequent use of the parametric system.

Figure 5.7 shows a typical frequency response of a summed sinusoidal waveform recorded within the water column. Recordings were made at a range of 65 m from the array face, allowing time for secondary frequency generation at the difference frequency of 5 kHz. This is achieved using a transmitted pulse similar to that seen in Figure 5.6 (b). The spectral analysis of the signal illustrates the two primary frequency components at 72.5 and 77.5 kHz and a strong secondary frequency component at 5 kHz. Harmonics of the primary frequencies are also evident above and below the resonance frequency. Inter-modulation effects between these result in secondary frequency generation of components at 10 and 15 kHz <sup>[5.4]</sup>. A strong interference signal may also be observed at 32 kHz and 94 kHz due to electrical interference in the recording system. The primary frequency carrier signals and harmonics show a typical response to that seen in Double Side Band Suppressed Carrier (DSBSC) modulation schemes.

Comparison can be made with an Amplitude Modulation (AM) technique, as shown in Figure 5.6(c). A single carrier signal is simply switched on and off at the required modulation frequency. Figure 5.8 shows the in-water frequency response of a 5 kHz signal generated using the AM technique. Instead of two carrier frequencies, a single carrier at the resonance frequency (75 kHz) is seen, with harmonics 5 kHz above and below the main carrier. The first two harmonics either side of the centre frequency are therefore separated by 10 kHz in comparison with the 5 kHz separation of the two primaries of the summed sinusoidal scheme. Due to the harmonic separation of the amplitude modulation scheme twice the array bandwidth is required for similar signal generation in comparison with summed-sinusoidal method. Amplitude modulation can offer some increased parametric efficiency <sup>[5.5]</sup>, this is, however, balanced by the requirement of double the transducer bandwidth. Due to the limited bandwidth of the array of 6.5 kHz the summed-modulation scheme was used extensively during the systems operation.

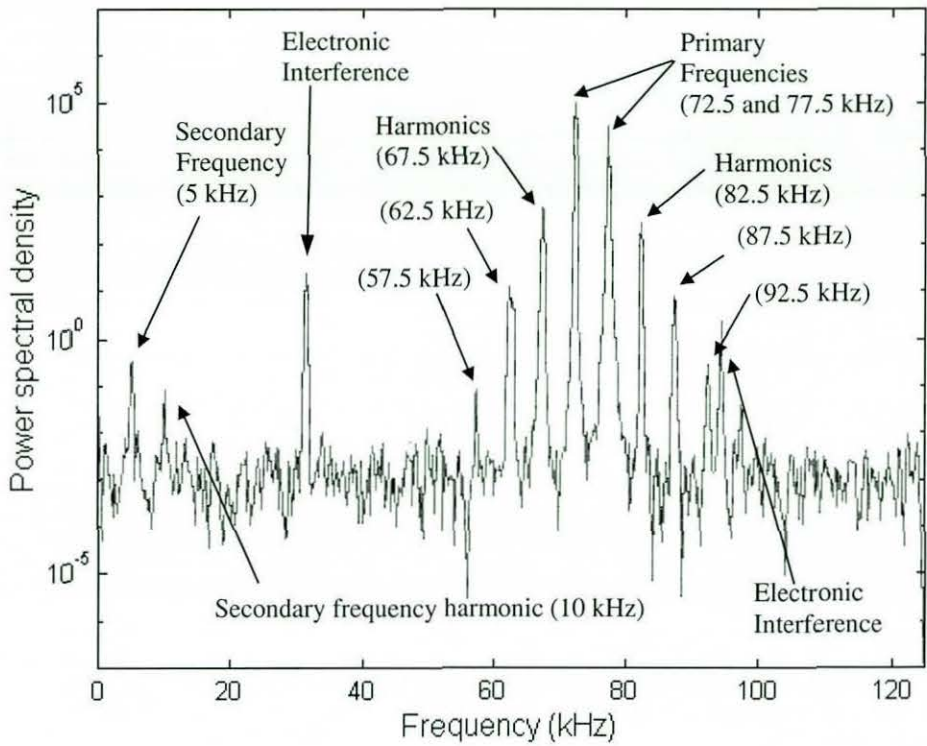


FIGURE 5.7 POWER SPECTRAL DENSITY SUMMED-SINUSOIDAL MODULATION

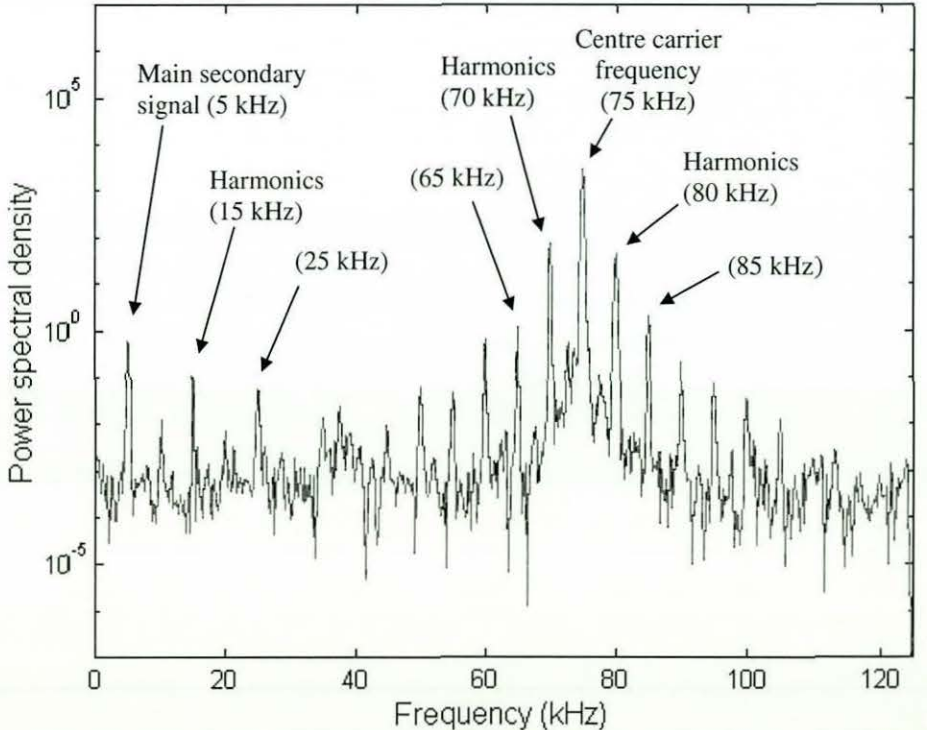


FIGURE 5.8 POWER SPECTRAL DENSITY AMPLITUDE MODULATED SCHEME

Figure 5.8 also shows secondary frequency generation at 5 kHz. Secondary frequency harmonics are also present at twice the separation from the main secondary frequency signal due to the larger separation of the primary frequency harmonics in the AM case. In this case, secondary frequency harmonics are visible at 15 and 25 kHz compared with the 5 kHz separation seen in Figure 5.7. Figure 5.8 shows a slightly lower peak spectral density compared with Figure 5.7 due to a difference in range to the hydrophone from the transmit array for the two recordings.

Spectral analysis is carried out using a 1024-point FFT at a 250 kHz sample rate, corresponding to an approximate 4 ms window. Signals are also bandwidth-limited by the recording system from 1 – 100 kHz.

#### **5.4.2 Linear Frequency Modulated (LFM) CHIRP signals**

Another commonly used pulse type is the Linear Frequency Modulation (LFM) or *chirp* signal. A linear variation in the generated frequency takes place during the length of the pulse between two defined frequencies. Figure 5.9 shows an example of the linear change in frequency between  $f_{c1}$  and  $f_{c2}$  during the course of the transmit pulse ( $t_2-t_1$ ) for a down sweep LFM pulse. Linear chirps at parametric secondary frequencies are achieved by the linear variation of two primaries such that the difference between them is equal to the required secondary frequency variation at any point during the pulse.



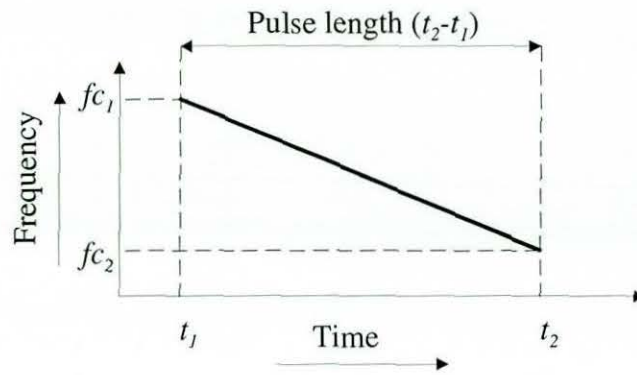


FIGURE 5.9 FREQUENCY DISTRIBUTION DURING TRANSMIT PULSE FOR A LINEAR FREQUENCY MODULATED (LFM) *DOWN SWEEP* SIGNAL

The waveform is expressed in a similar form to the summed continuous wave sinusoidal signal shown in equations (5.1)-(5.3). An addition term is added, allowing the difference frequency ( $f_D$ ) to vary as a function of time so that equations (5.4) and (5.5) are rewritten as

$$f_1 = f_0 - \frac{f_D(t)}{2} \quad (5.8)$$

$$f_2 = f_0 + \frac{f_D(t)}{2} \quad (5.9)$$

The function of difference frequency  $f_D(t)$  for a linear variation can then be expressed as:

$$f_D(t) = fc_1 + \Delta f_D \cdot \frac{t}{\Delta T} \quad (5.10)$$

where

$$\Delta T = \text{sample period} = (\text{sample rate})^{-1} \quad (5.11)$$

and

$t$  varies between  $t_1$  and  $t_2$

and  $\Delta f_D$ , the step change in difference frequency is given by:

$$\Delta f_D = \frac{(fc_2 - fc_1)}{n} \quad (5.12)$$

where

$$n = \text{No. of sample points in the signal} = \text{pulse length} \times \text{sample rate} \quad (5.13)$$

The relative magnitudes of the start and stop frequencies,  $fc_1$  and  $fc_2$  respectively, define the direction of the variation. From equation (5.12)  $\Delta f_D$  is negative if  $fc_1 > fc_2$ , defining the sweep as downwards as shown in the example in Figure 5.9. Figure 5.10 (a) shows the generation pulse for a secondary 4ms long waveform for 6 – 12 kHz *up-sweep* using summed sinusoidal modulation. Comparison can be made with Figure 5.10 (b), showing the transmitted signal recorded within the water column some distance away from the transducer array. The amplitude variation along the pulse is due to the moving of the two primary frequencies away from the centre frequency and the bandwidth of the array limiting the primary frequency signal level. Figure 5.10 (c) shows the low-pass filtered response of the wide-band signal from Figure 5.10 (b), illustrating the secondary frequency component only. In contrast, an increase in amplitude is seen with increased frequency due to the balancing of increased parametric gain at higher difference frequencies, as shown in Figure 4.26. Figure 5.10 (b-c) also illustrate a degree of pulse elongation in the *real* signal from the generation signal, Figure 5.10 (a), due to ringing effects in the transducer array. This is particularly evident in the filtered response, Figure 5.10 (c), where a short duration amplitude increase is evident at the beginning of the pulse.

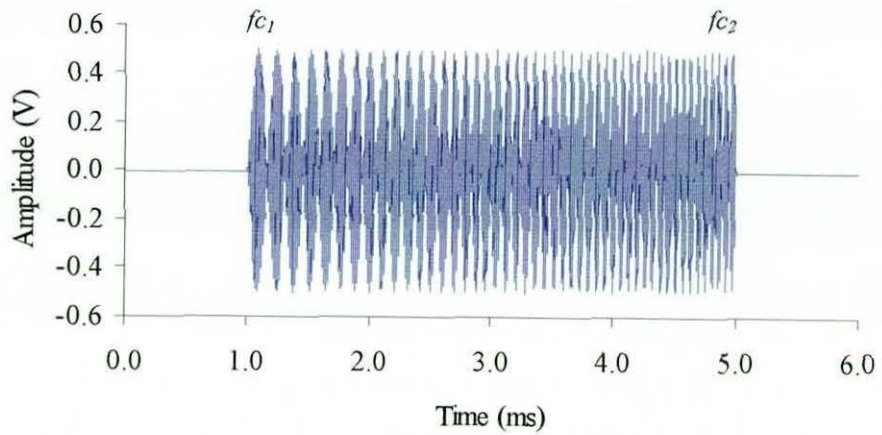


FIGURE 5.10 (a) LFM 6-12 kHz PARAMETRIC GENERATION SIGNAL

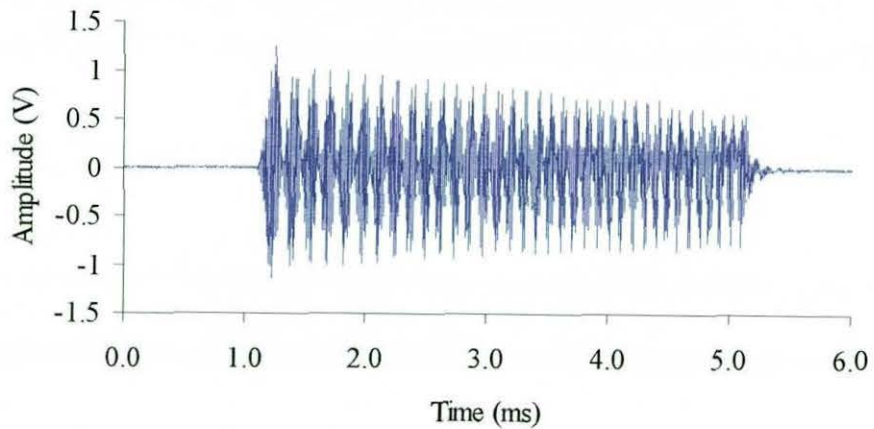


FIGURE 5.10 (b) WIDE-BAND RESPONSE 6-12 kHz LFM CHIRP IN WATER

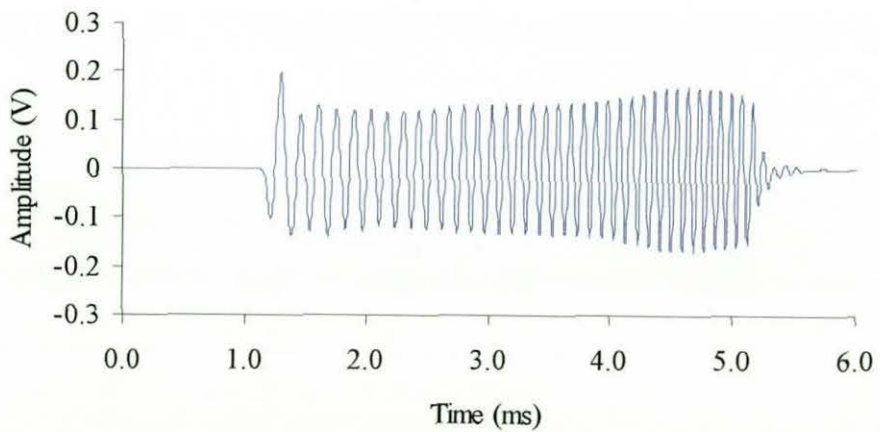


FIGURE 5.10 (c) NARROW-BAND RESPONSE 6-12 kHz LFM CHIRP IN WATER

### 5.4.3 Beam steering

Beam forming in one plane is possible due to the arrangement of the transducer array into 13 staves. The addition of a fixed time lag or phase difference between the signals applied to adjacent staves results in the formation of the main lobe of the transmitter away from the normal transmission axis, as shown in Figure 5.11.

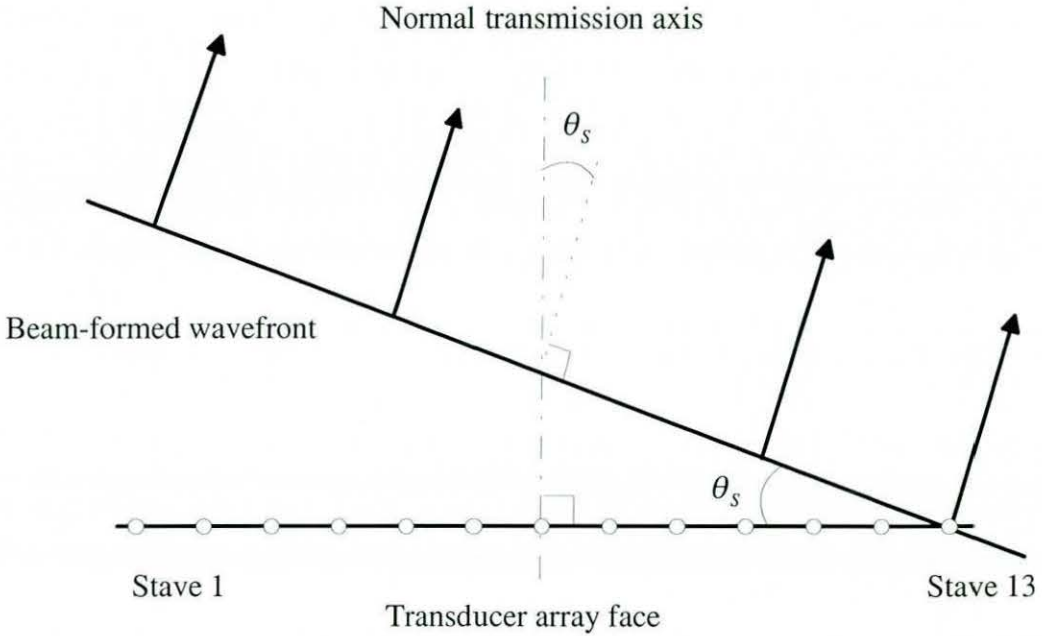


FIGURE 5.11 BEAM-FORMING THE TRANSDUCER ARRAY

The steered angle ( $\theta_s$  radians) is given by:

$$\theta_s = \sin^{-1} \left[ \frac{\theta_l \lambda}{2\pi \cdot S} \right] \quad (5.14)$$

where  $\theta_l$  is the phase lag or difference between adjacent staves in radians,  $\lambda$  is the signal wavelength and  $S$  is the element spacing across the face of the array. Each staff is made up of 54 elements arranged in two parallel lines of 27. The element pitch is 16 mm the inter-staff pitch is therefore 32 mm. Equation (5.14) also illustrates the beam steering and sector scanning limitations discussed in Chapter 4.

The theoretical scan sector limit of one radians phase difference exists between staves. For values  $\theta_i$  values greater than  $\pm\pi$  are equivalent in magnitude to  $\theta_i - 2\pi$ , which in practice will reform the beam at the opposite end of the sector-scan, as seen in Figure 4.11. For a 32 mm staff spacing at 75 kHz with  $\theta_i = \pi$  the maximum steered angle ( $\theta_s$ ) from equation (5.14) equals  $18.2^\circ$ . This closely matches the  $\pm 18^\circ$  scanning sector observed in Section 4.6.

Figure 5.12 shows the generated waveforms for a 75 kHz CW signal beam-formed at  $+1^\circ$  for each of the 13 staves. The inter-stave phase relationship is calculated using equation (5.14). Comparison can be made for the same signal type beam-formed at the equivalent of  $-2^\circ$  shown in Figure 5.13. Both sets of waveforms are arranged so that the inter-stave spread is symmetrical about the centre staff (staff 7) with a zero phase start value. The direction of the phase relationship and the magnitude of the difference between two adjacent staves define the direction and the degree of steering in the beam-formed signal. A positive phase lead for the first staff, as in Figure 5.11, is arbitrarily defined as a positive steer direction.

A similar effect can be achieved by the introduction of a time lag at the start of each staff signal. Figure 5.14 shows a uniform time difference between the first three staves. All signal types are identical with a zero crossing start phase value. In this case the inter-stave time lag ( $t_l$ ) can be expressed in terms of ( $\theta_i$ ) from equation 5.14 and the frequency of the generated waveform ( $f_0$ ) as

$$t_l = \frac{\theta_i}{2\pi \cdot f_0} \quad (5.15)$$

By this method angular resolution is limited by the sample rate of the generating signal. In the case of a 1 MHz sample rate for generation of a 75 kHz signal a minimum inter-stave time lag of 1  $\mu$ s is possible corresponding to a minimum steering step of  $2.68^\circ$ . Comparison can be made with the waveform phase technique for a 16-bit amplitude resolution, which results in a the minimum inter-

stave phase difference of  $5.47 \times 10^{-3}$  degrees allowing a steering resolution of  $0.03^\circ$ . Time lag steering does however offer the advantage that each waveform applied to the transducer array has a zero crossing start phase, allowing a smoother start-up to the pulse and avoiding the rapidly changing start edges inherent with the phase steering method.

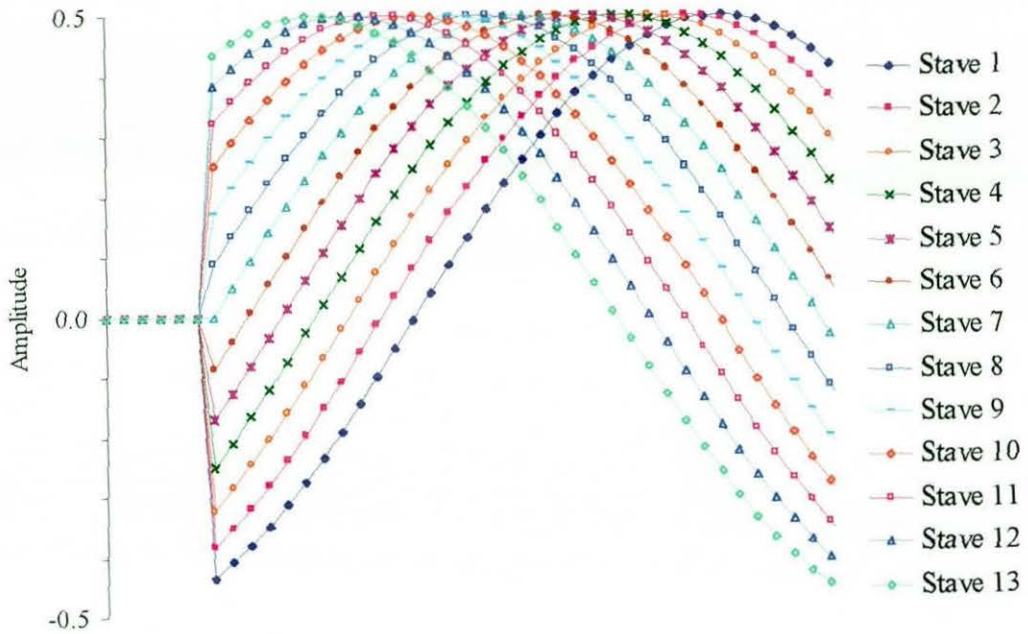


FIGURE 5.12 TRANSMIT BEAM-STEERING  $+1^\circ$  USING PHASE SHIFTING

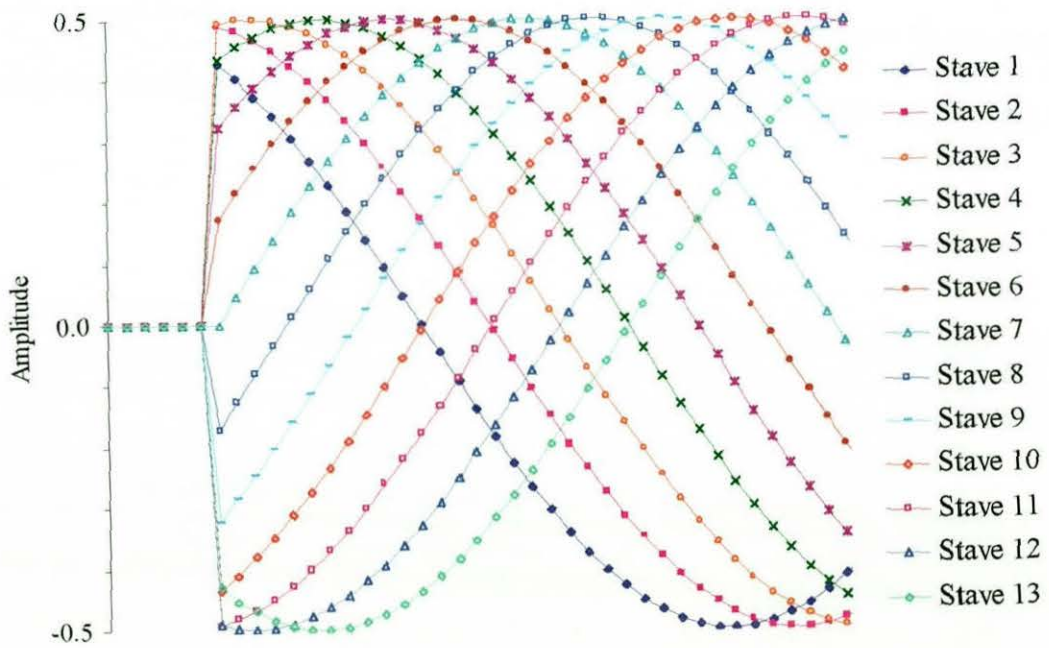


FIGURE 5.13 TRANSMITTER BEAM-STEERING  $-2^\circ$  USING PHASE SHIFTING

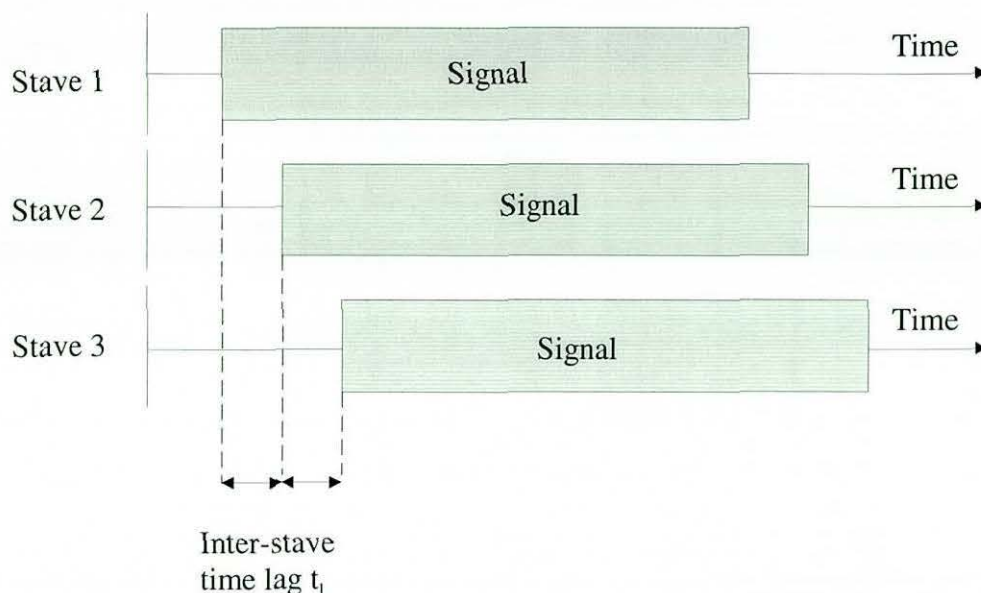


FIGURE 5.14 BEAM-FORMING USING INTER-STAVE TIME LAG

#### 5.4.4 Sector scanning

Figures (4.7 – 4.11) show examples of sector-scanned waveforms allowing generation of the beam-patterns in a hydrophone. Introduction of varying inter-stave phase differences during the pulse allows a corresponding variation in the steering direction. This is implemented by applying a frequency shift in the signals across the face of the array. Signals are generated with a constant frequency difference ( $\Delta f$ ) arranged around the required centre frequency  $f_{sweep}$ . Table 5-2 shows the frequency distribution for a CW pulse centred on frequency  $f_{sweep}$  across the staves of the array.

The speed of the sector scan is controlled by the frequency difference ( $\Delta f$ ) such that a full scan corresponding to the full steering sector ( $\pm 18^\circ$ ) can be achieved within a pulse length of period  $T$  with.

$$\Delta f = \frac{1}{T} \quad (5.16)$$



Stave 1	$f_{sweep} - 6\Delta f$	73.50	kHz
:	:	:	
Stave 5	$f_{sweep} - 2\Delta f$	74.50	kHz
Stave 6	$f_{sweep} - \Delta f$	74.75	kHz
Stave 7	$f_{sweep}$	75.00	kHz
Stave 8	$f_{sweep} + \Delta f$	75.25	kHz
Stave 9	$f_{sweep} + 2\Delta f$	75.50	kHz
:	:	:	
Stave 13	$f_{sweep} + 6\Delta f$	76.50	kHz

TABLE 5-2 STAVE-FREQUENCY DISTRIBUTION FOR A 4 ms SECTOR SCANNING PULSE

A full sector scan ( $\pm 18^\circ$ ) is achieved in a 4 ms signal using a difference frequency of 250 Hz.

The direction and speed of the scan can be controlled by the frequency difference distribution across the array face. A double scan can be achieved within a single 4 ms pulse by using a 500 Hz frequency difference. The signal in this case will scan across the entire sector in 2 ms and then reform at the beginning of the sector to restart the scan for the second pass. The introduction of inter-stave start phases also allows selection of the start position of a scan corresponding with phase steering techniques described previously.

Table 5-2 shows the frequency distributions for a single sector scan within a 4 ms pulse with frequencies distributed about 75 kHz. The generated waveform is therefore made up of components from 73.5 – 76.5 kHz with a wider frequency distribution of the non-scanned 75 kHz signal. The spectral differences of the transmitted signal are shown in Figure 5.15. The scanned signal for a 4 ms pulse shows a wider energy distribution with lower peak energy compared with the pure 75 kHz signal used in the non-scanned case.

Development of sector-scanning secondary frequency generation signals was also implemented. An inter-stave frequency difference is applied to two carriers with a constant carrier difference for any given stave. Similarly, scanned secondary frequency LFM or chirp signals were developed. These have been used in sector scanning displays, allowing frequency coding of the transmit bearing. A linear sweep in frequency with a linear sector scan allows translation of a target-reflected signal back to its original transmit bearing regardless of its arrival time and therefore range to target.

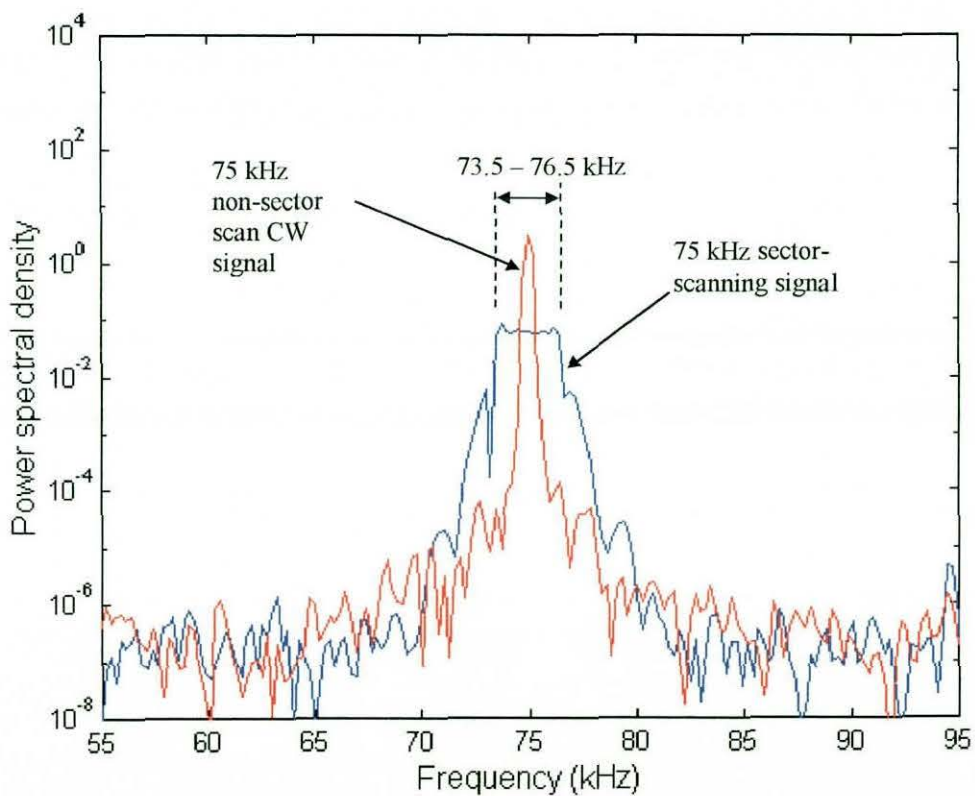


FIGURE 5.15 FREQUENCY DISTRIBUTION 75 kHz 4 ms CW PULSE  
SCANNING AND NON-SCANNING

## 5.5 Conclusion

Developments in both hardware and software have provided considerable versatility in terms of complex signal generation and data capture systems. The use of software based signal synthesis allows generation of a variety of signals for use with the parametric sonar, including continuous wave, chirp and sector scanning waveforms. Application of phase difference between staves has also allowed beam-steering in one axis over a  $\pm 18^\circ$  sector.

Under software control multiple waveforms are computed and then loaded into external memory where they are then available for transmission. Data capture is available on up to 16 parallel channels to a 100 kHz bandwidth. Data is then stored directly to hard disk. The integration of signal synthesis, data capture and other systems has allowed operation from a single piece of software and therefore a single computer considerably enhancing the practicality of the system.

## REFERENCES: Chapter 5

---

- 5.1 Goodson A.D.  
A multi-mode sonar transmitter  
*MPhil thesis*, Loughborough University, 1989.
- 5.2 Griffiths J.W.R., Payne D.B., Rafik T.A., Wood W.J. and Zhang J.  
A versatile sonar transmitter signal generator  
Conference Proceedings, *Applications of transputers*,  
Edited by Pritchard and Scott, pp. 381-385, 1990.
- 5.3 Griffiths J.W.R. and Rafik T.  
A multichannel versatile sonar source  
*High time bandwidth product waveforms in radar and sonar*, IEE  
Colloquium, 1991.
- 5.4 McDaniel O.H.  
Harmonic distortion of spherical sound waves in water  
*J. Acoust. Soc. Am.*, Vol. 38, pp. 644 – 647, 1965.
- 5.5 Merklinger H.M.  
Improved efficiency in a parametric transmitting array  
*J. Acoust. Soc. Am.*, Vol. 58, No. 4, pp. 784 – 787, 1975.

## CHAPTER SIX

# USE OF A PARAMETRIC ARRAY IN THE CHARACTERISATION OF MARINE SEDIMENTS

### 6.1 Introduction

Investigation of the relationship between the propagation of sound in both the water column and within the seabed sediments has opened the possibility of the development of new systems and methodologies for remote sensing of sediment properties <sup>[6.1-6.2]</sup>. The investigation of sound propagation in undersea sediments has received considerable interest from numerous research groups. This work was primarily to establish a correlation between the acoustical properties of the sediments and their geotechnical properties (density, reflection factor, sound velocity, attenuation, dispersion etc.). Classification of sediments by remote means falls into the range of interest of numerous industries, including geology, off-shore engineering, sound propagation modelling, pipe lines and cables route mapping and dredging applications.

The use of parametric sources has received considerable interest in recent years in the field of sediment classification from a number of researchers <sup>[6.3-6.6]</sup>. Higher frequencies are more highly attenuated in sediments than in the water column <sup>[6.7]</sup> leading to poor seabed penetration. This has led to a system requirement of a low frequency source with a high directivity <sup>[6.8]</sup>. A more directional source provides a higher precision of seabed delineation and reduced reverberation noise, due to the reduction in unwanted signals from areas not directly under investigation. A parametric source provides a highly directional low frequency source of relatively small size, compared with a conventional sonar <sup>[6.9]</sup>, offering some advantages for use as a practical sub-seabed profiling system.

Work with the current parametric system described in Chapters 3, 4 and 5 commenced with the European Commission funded MAST II REBECCA<sup>\*1</sup> project, starting in summer 1992. Work undertaken in this project primarily involved the development of the sonar system, including system commissioning and calibration trials held at the Loch Duich trial site in Scotland and full system sea trials held off the French coast, in July and November 1994.

This work was later extended with the MAST III SIGMA<sup>\*2</sup> project, starting in 1997. This project involved several sea-going trials using the existing Loughborough parametric sonar system. The project also saw the development of stabilisation techniques, for use in a sea-going environment, with the parametric sonar and several refinements to the existing system, based on lessons learnt during the REBECCA project.

Work in the development of a new parametric sonar system for sediment classification also took place at the Indian Institute of Technology, in conjunction with the Loughborough University research group, under the ACUSTICA<sup>\*3</sup> project. This was funded as part of the European Commission's International Scientific Co-operation Programme. This project involving the development of a new parametric sonar system, culminating in an open water trial held on Lake Edukki, in Southern India in February 1994 and the development and refinement of direct and inverse techniques, for the extraction of sediment parameters from bottom-scattered acoustic signals.

---

\*1 REBECCA (Reflection from Bottom, Echo Classification and Characterization of Acoustical Propagation).

\*2 SIGMA (Sediment Identification for Geotechnics by Marine Acoustics).

\*3 ACUSTICA (Acoustic Characterisation of Undersea Sediments to Initiate Commercial Applications).

## 6.2 REBECCA project

### 6.2.1 Introduction

The REBECCA (Reflection from Bottom, Echo Classification and Characterization of Acoustical Propagation) project led to the development and initial testing of the parametric sonar system, described in Chapters 3 and 4. The use of a parametric source by the Underwater Acoustics Research Group at Loughborough University, for sub-sea sediment classification <sup>[6.11-6.12]</sup> was first investigated under this joint research project, carried out as part of the European Commissions MAST II programme by a consortium of research groups from France, Denmark, Greece and the UK. The size and frequency range of existing parametric sonar systems developed by the Loughborough research group <sup>[6.10]</sup> was considered unsuitable for the deployment of an oblique incidence parametric sonar.

The following sections are a brief description of the overall project, followed by details of the development and use of the LU-parametric sonar system for sediment classification.

### 6.2.2 Project aims

The main aim of the REBECCA project was a multidisciplinary approach to undersea sediment classification using acoustics. Geotechnical and geophysical measurements were conducted as 'ground truthing' for development of remote acoustic testing techniques. Similarly real acoustic data and scaled tank tests were used to validate developments in the direct and inverse algorithms.

The main aspects of the project were:

- 1) Geotechnical (post analysis of sediment cores GEODIA, France or *in-situ* measurements, using a geotechnical module, operated by IFREMER, France).
- 2) Geophysical (measurement using refracted and reflected seismic survey techniques, carried out by GEODIA, France).

- 3) Remote acoustic sensing (use of two different parametric sonar systems, developed and operated by TUD, Denmark and Loughborough, UK).
- 4) Development of various algorithms for solving the inverse problem of sediment classification from received bottom scattered signals, carried out by FORTH, Crete.
- 5) Scaled tank experiments, including multi-layered and varying impedance systems, carried out by CPE, Lyon, France and LMA, Marseille, France.

The deep-sea geotechnical module, deployed by IFREMER, allowed *in-situ* measurement of a range of geo-physical sediment parameters, in sediment depths of up to 2 m <sup>[6.13]</sup>. This module was used in conjunction with a Kullenburg corer cable of core lengths up to 10 m. Actual penetration depths were dependant on the size of weights used and the sediment type. Post analysis of the cores was carried out by IFREMER.

A range of seismic surveying techniques <sup>[6.14]</sup> were carried out by GEODIA. These included the measurement of refracted pressure wave velocity and sediment layer thickness from 5 – 10 m, using a water gun fed with compressed air and a shear wave generation system capable of generating horizontal shock waves perpendicular to the array line. Both these seismic sources were deployed from a sledge, towed along the seabed behind a surface vessel. Data reception was via an array of 10-20, 3-dimensional gimbal mounted geophones, dragged across the seabed behind the sledge.

Finally two parametric sonar systems were deployed, a single-element transducer source used in a vertical 'echo sounder mode' operated by TUD <sup>[6.15]</sup> and a phase-steerable source developed by the LU. Both systems were deployed from a tow-fish, deployed behind a surface vessel, at a depth of approximately 10 m. Bottom-scattered signals from the TUD vertical system were captured using a single element hydrophone, mounted next to the transmitter. Investigation of oblique angle insonification was made using the phase-steerable LU parametric source. This was deployed looking backwards, away from the ship. Seabed forward-scattered signals were then received by a multiple-element streamer array towed



*behind the fish.*

Additional work by research groups at FORTH, LMA and CPE involved the development of direct and inverse techniques to extract sediment parameters from received acoustic data. Scaled tank experiments investigating acoustic propagation in sediment layers were used to validate theoretical derivatives and numerical models and to validate the inverse algorithms. Models included the refraction of parametric signals at the sediment–water interface and the propagation of parametric signals.

Experimental work culminated in an open water sea trial for commissioning the system held in July 1994 in the area of the Rade de Brest off the French coast, and an all-system trial held in August 1994 near the Isles de Glenan, south of Concarneau, Brest, France.

## 6.2.3 Sea-trials

### 6.2.3.1 Loch Duich, Scotland

Two commissioning trials were held at the acoustic test facility on Loch Duich Scotland, in June 1993 and May 1994. These trials primarily involved the testing and calibration of the LU 75 kHz parametric sonar system. The results of these trials have been reported in detail in Chapters 3 and 4.

### 6.2.3.2 Rade de Brest (*Thalia*)

The first deployment of the system took place in a system testing trial held off the French coast in the area of the Rade de Brest. Both parametric sonars were deployed inside a free flooding-fish, towed behind the IFREMER research vessel, *Thalia*, shown in Figure 6.1.

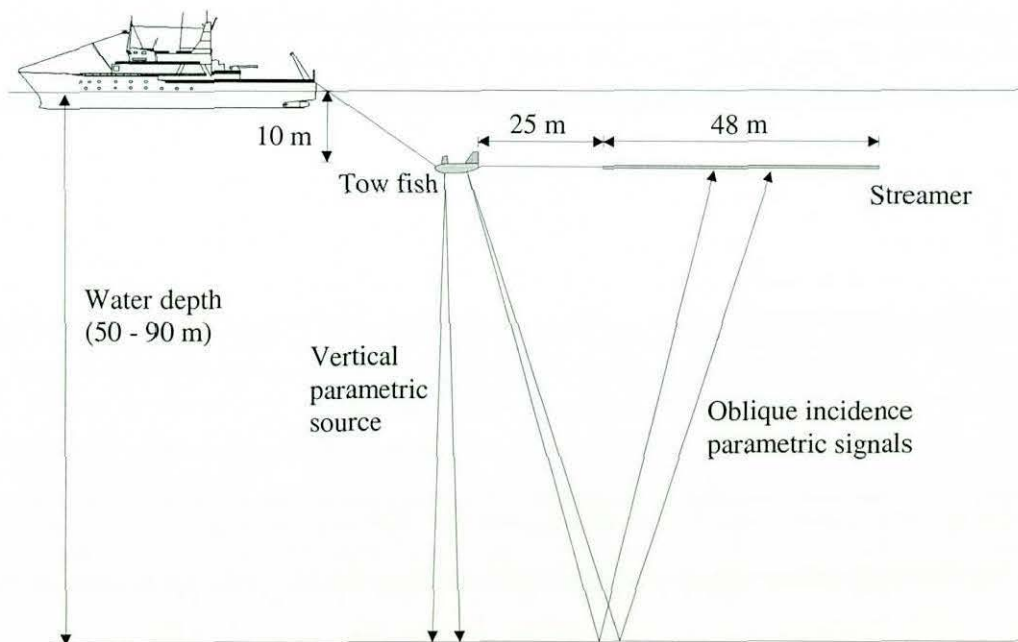


FIGURE 6.1 EXPERIMENTAL DEPLOYMENT, *THALIA* TRIAL 1994

The TUD transmitter-receiver system was deployed vertically. Adjustment of the mechanical deployment angle of the LU array was possible at  $10^\circ$ ,  $15^\circ$  and  $20^\circ$  from the horizontal. Electronic beam steering was then used to adjust the seabed

incidence angle over a  $\pm 18^\circ$  sector, in the fore-aft plane, to allow bottom-scattered signal reception at the streamer array.

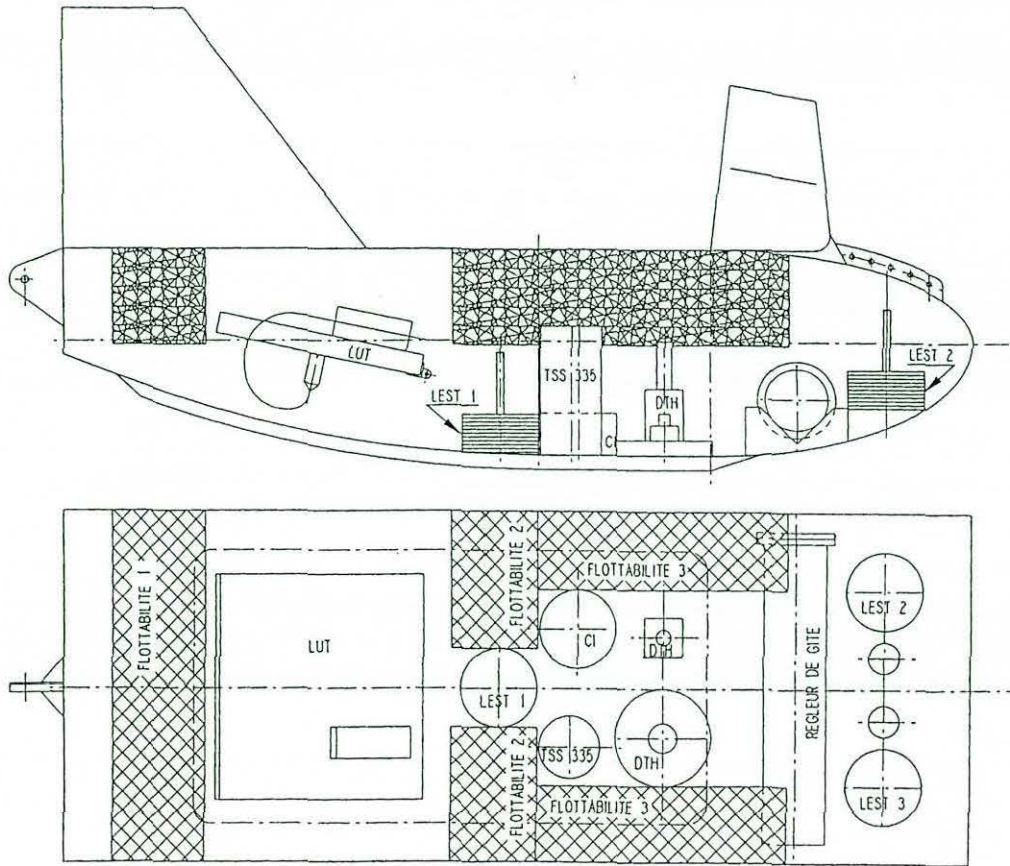


FIGURE 6.2 REBECCA PROJECT TOW-FISH CONSTRUCTION  
(diagram courtesy of IFREMER)

Figure 6.2 shows the tow-fish developed by IFREMER. The tow-fish itself was constructed from aluminium, making it relatively easy to handle. Transmission of the LU array took place from within the free-flooded body of the fish, through a 2 mm polycarbonate window on the underside. Figure 6.3 shows the LU array, visible through the window, with the TUD transmitter and receiver transducers, as the tow fish was being deployed from the back of *Thalia*. Tests carried out on the polycarbonate window showed transmission losses of around 0.6 dB at 75 kHz.



FIGURE 6.3 REBECCA PROJECT TOW-FISH UNDERSIDE VIEW

Additional sensors in the tow-fish were used to measure pitch, roll and depth. This data was then sent to the surface via the umbilical cable where it was displayed in real-time. Adjustment of the tow-fish trim in the roll axis was possible through computer-controlled positioning of weights within the tow-fish. Cabling for all sensors, the two transmission systems and the receiver array, were collected into a single umbilical bundle.

The receiver system used a 24-channel receiver array. Each channel was made up of three hydrophones, placed 0.3 m apart. The channels were then spaced at 2 m intervals providing a total acoustic aperture of 46 m. The tow-fish to streamer offset was set to 25 m, allowing seabed incidence angles in a 50 m water depth of between  $17.5^\circ$  and  $50.7^\circ$ , with the LU parametric source for signal reception at the front and back of the receiver array, respectively.

The TUD source was operated in a vertical 'echo sounder mode'. The source was a single, wide band element resonant at 12 kHz, shown in Figure 6.3. Seabed and sub-seabed echoes were monitored using a high sensitivity Reson hydrophone (type TC4004), placed next to the source. The system was operated independently

to the LU parametric system. Signal generation was carried out using a Gaussian envelope, pulse generator with a 40 kHz carrier frequency. Data output was recorded on a thermal graphic paper recorder, using Time Variable Gain (TVG) pre-amplification of receiver echoes synchronised with the transmission pulse.

The *Thalia* trial took place in July 1994, as an initial system commissioning and testing process. The two parametric systems, the receiver array recording system and tow-fish attitude and depth sensor systems, were tested for the first time together, whilst deployed from the back of a surface vessel, on two short cruises from the port of Brest. System integration tests were carried out between the LU parametric source and the IFREMER receiver array. The feasibility of the tow – fish - streamer deployment, from a surface vessel was assessed. Seabed reflected acoustic transmissions from both parametric systems were recorded, via the streamer array and the TUD receiver element, in water depths between 30-60 m, at tow speeds 2-4 knots.

### 6.2.3.3 Rade de Brest (*Le Noroit*)

Experimental work for REBECCA culminated in a full systems sea cruise, in August 1994, using the IFREMER vessel *Le Noroit*. The trial was divided into two parts. Geophysical and geo-technical measurements were scheduled in three sites of varying water depths, 40 m in the Rade de Brest, 90 m South of Quessant Island (48°12 N – 04°38 W) and 70 m out of the Rade de Brest (48°18 N – 04°38 W).

The geo-technical module operated by IFREMER, and the geophysical sledge operated by GEODIA, was deployed from an A-frame winch system, from the rear of the 50 m long research vessel, *Le Noroit*. Figure 6.4 shows the geo-technical module. This was lowered to the seabed, where *in-situ* measurements of geo-technical properties were carried out in the first 2 m of sediment.



FIGURE 6.4 GEO-TECHNICAL MODULE



FIGURE 6.5 ACOUSTIC TOW-FISH DEPLOYMENT AND SHRIMP SYSTEM

Figure 6.5 shows the deployment of the tow-fish from the A-frame at the stern of the vessel, from the second phase of the experiment. In the foreground the sledge system can be seen. Measurements using both the geo-technical module and the geophysical sledge were attempted as *ground truthing* for the remote acoustic systems later tested in the same area.

The acoustic systems trials were carried out during 23-25<sup>th</sup> August 1994. Both systems were operated in the three zones near the Isles de Glenan. The system was operated in each zone on approximately 1 km long tracks. Each zone was covered with multiple tracks, using different signal types and seabed incidence angles. Signal types from the steerable parametric source included 5 kHz CW, 8-4 and 4-8 kHz chirp signals, 4 kHz  $\pm$  18° sector scanned signal.

Acoustic recordings were made by both systems, including the hydrophone in the tow-fish for the vertical signals from the TUD parametric source and the receiver streamer array for the forward-scattered signals from the LU source. Additional data, from the tow-fish pitch-roll attitude and depth sensors, was also recorded. The LU system was operated continuously over a 30-hour period, at the three test sites.

#### **6.2.4 Sea-trial results**

Due to ship time constraints, there was only limited time available for testing all the systems during the main sea-trial held in August 1994. This, combined with bad weather (up to Sea State 7), made deployment of the geo-technical module and the geophysical system difficult and the results of geo-physical and geo-technical surveys were therefore limited.

Similar difficulties were experienced with acoustic trials. Analysis of pitch and roll instabilities in tow-fish attitude, shown in Figures 6.6 and 6.7, showed considerable potential for misalignment of the forward-scattered signal with the receiver array. Any error in tow-fish roll of greater than  $\pm$  1.5°, due to the 3°

beam-width, would result in a port or starboard displacement of the seabed forward-scattered signal missing the streamer. Similarly errors in the pitch axis of the tow-fish could result in fore-aft displacement of the bottom-scattered signal, potentially resulting in loss of signal on the streamer.

Figures 6.6 and 6.7 show that the instability worsened with increased ship based motion due to worsening weather conditions. Both graphs show roll movement errors in excess of  $\pm 1.5^\circ$ , most likely resulting in transmitter-receiver misalignment. These errors were seen to considerably worsen with increased sea-state activity. Later analysis of acoustic data on the streamer over the trial period showed poor data reception for a large number of transmissions, most likely due to the transmitter-receiver misalignment. Figure 6.7 does not include tow-fish depth data, due to a fault in the sensor.

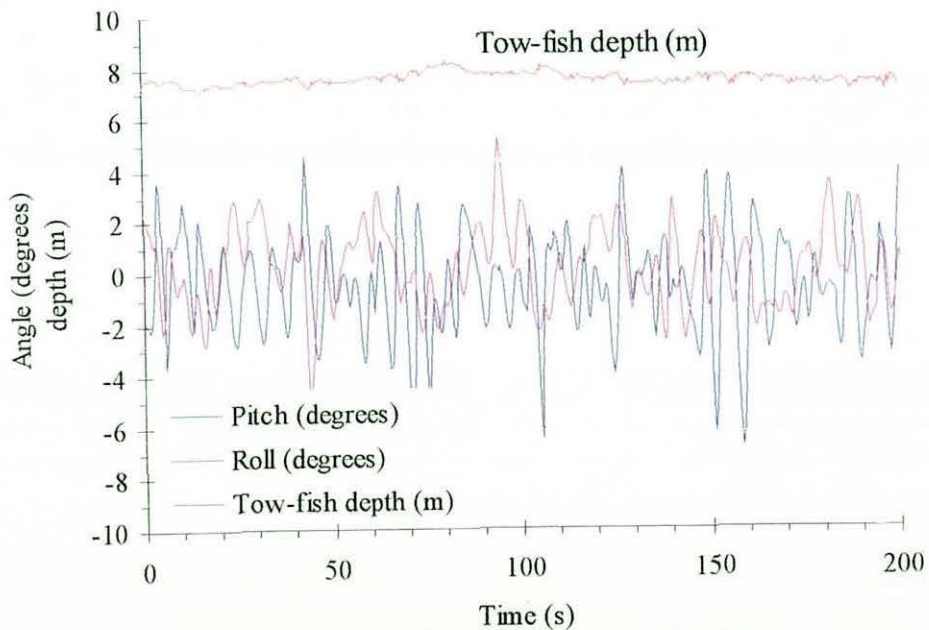


FIGURE 6.6 TOW-FISH PITCH AND ROLL ATTITUDE ERRORS AND DEPTH SEA-STATE 3



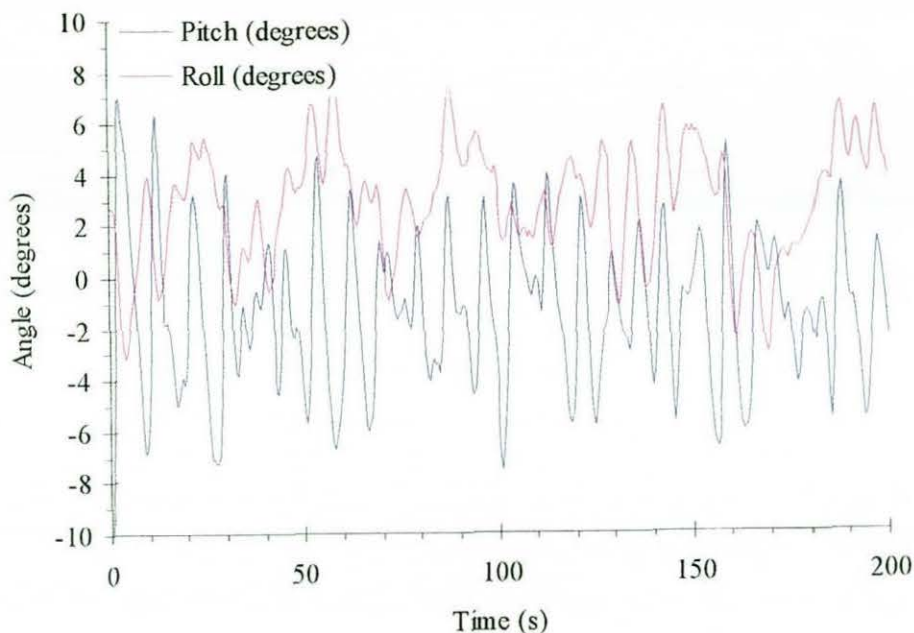


FIGURE 6.7 TOW-FISH PITCH AND ROLL ATTITUDE ERRORS AND DEPTH SEA-STATE 4-7

Due to poor data reception during the *Le Noroit* trials, no analysis of receiver data was possible. Data from the earlier trial held on *Thalia*, did show that the concept of non-normal insonification of the seabed, using a parametric source and forward-scattered data collection from a towed streamer was feasible in reasonable weather conditions. Figures 6.8 and 6.9 show forward-scattered data from the parametric source on 12 hydrophone channels for a 5 kHz CW signal and a 4 kHz Ricker signal (see section 7.6.2). Hydrophone 1 is the furthest from the source. Both these diagrams show a good signal-to-noise ratio, for the low frequency non-linear signals with the main signal arrival placed uniformly across the streamer array.

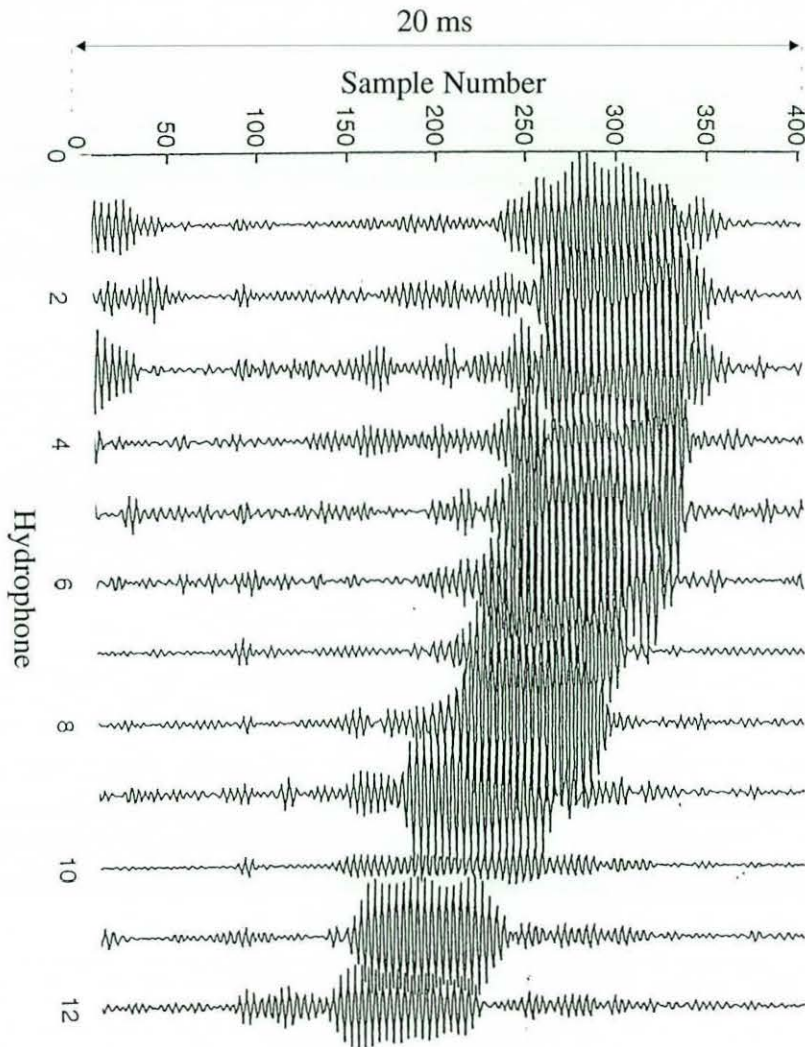


FIGURE 6.8 5 kHz CW SEABED SCATTERED SIGNAL

Recordings were made using the DELPH24 system, designed for seismic survey recordings. The system had 24 channels, digitised at 12 kHz to 16-bit resolution. This was reconfigured to allow a 20 kHz sampling rate, using 12 channels to a 10 kHz bandwidth. Preamplifiers within the streamer provided 72 dB of gain, before data acquisition at the depth system. Three additional channels within the DELPH were used to record the tow-fish and attitude and depth sensor data at a 6 kHz bandwidth. Serial data with each transmission was also recorded from the transmitter system, containing the transmit pulse parameters.

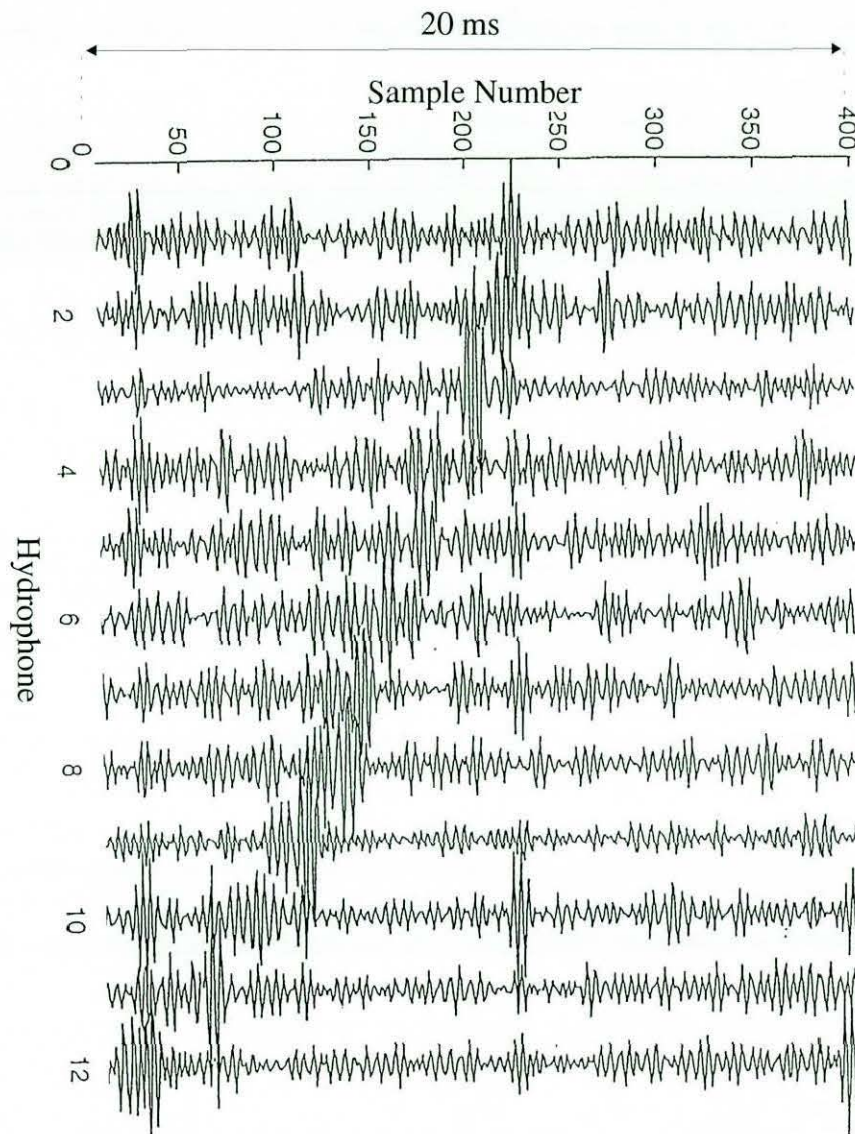


FIGURE 6.9 4 kHz RICKER SEABED-SCATTERED SIGNAL

### 6.2.5 Conclusion

The REBECCA project showed that the parametric source had potential as an acoustic-surveying tool due to its low frequency, highly directive nature <sup>[6.16]</sup>. The low frequencies (1-10 kHz) provided good seabed penetration and high directivity, giving the potential for reduced reverberation noise and better seabed delineation.

The first sea trial on *Thalia* showed that the transmission of oblique incidence angles and forward-scattered data reception was feasible. This would then hopefully provide, via inversion methods, information about the scattering

medium. The high directivity of the parametric sources, however, proved problematic in the later *Le Noroit* trial, due to instabilities in the transmission platform, experienced in worsening sea conditions. This motion combined with the narrow beam-width resulted in transmitter–receiver misalignment making reliable data collection difficult.

Future work was therefore planned to utilise dynamic stabilisation techniques [6.17-6.18], using phase steering of the parametric source to compensate in real-time for errors in transmission orientation. In addition, modelling of the transmission propagation path should provide a better idea of the likely errors in transmitter – receiver alignment, allowing real-time compensation. Research covering both these areas is discussed in the follow sections covering the SIGMA and ACUSTICA projects and in more detail in Chapter 9.

In parallel with the sea trials in the REBECCA and SIGMA projects, theoretical and scaled modelling experiments were carried out. These included both multi-layered systems and continuously varying impedance systems [6.19]. These were primarily used to validate theoretical solutions and numerical models for the propagation of sound within sediment and the water column. These models were also used in the validation of new inverse algorithms [6.20] for eventual use with acoustic data.

## **6.2 SIGMA project**

### **6.3.1 Introduction**

The SIGMA project (Sediment Identification for Geotechnics by Marine Acoustics) was a three-year project that started in 1997. Similar to the earlier REBECCA project, the aim of this project was a multidisciplinary approach to the investigation of the relationship between the acoustic parameters of marine sediments (reflection factor, sound velocity, attenuation, dispersion etc.) and their geophysical and geotechnical properties (sediment type, grain size distribution, cohesion, gas content etc.).

Many of the same partners from the REBECCA project were again involved with the SIGMA project, forming a natural continuation of the work. This project allowed the continued development of a remote acoustic sensing methodology and technology for non-intrusive measurement of marine sediments. A similar approach was adopted, including the use of a vertically-deployed parametric source operating in a mono-static mode and a steerable oblique incidence parametric source operating bi-statically with a towed hydrophone array. This had an identical configuration to that shown earlier in Figure 6.1. The multidisciplinary approach was formed in the further development of the parametric acoustic systems, for operation from a towed body and 'ground truthing', using bottom-operated seismic and geotechnical systems, coring and bottom sampling techniques. This was supplemented by scaled and numerical modelling of sound propagation in a variety of sediment layer systems <sup>[6.21-6.24]</sup> and the further development of robust inverse procedures <sup>[6.25]</sup> for application to 'real' acoustic data. These procedures were to be further developed to include 'noise' and transmitter – receiver characteristics.

From lessons learnt during the REBECCA project, the use of dynamic beam-steering was investigated to compensate in real time for errors in transmission platform attitude, due to ship movement. This involved the development of hardware and software for the detection and correction of errors, for a system operating in a realistic sea-going situation. Sea trials were conducted in November 1998 and June 1999 from the Belgian Navy research vessel, *Belgica*.

### **6.3.2 Hardware and software developments**

The correction of transmission platform instabilities was carried out, by firstly detecting errors in the platform attitude and then modelling of the likely propagation path of the acoustic signal to the receiver, via the seabed and sub-seabed layers based on the predicted error. This was then used to calculate a corrected steer angle to compensate for the error. Software then allowed selection and transmission of a pre-computed signal that was the closest match to the required steer angle in real-time. The number of pre-computed signals and pulse

lengths was limited by the signal synthesis memory allocation. In the previously described system real-time access was possible to eight pre-programmed signals. Each of these could be computed at different phase steering angles up to 4 ms long as shown in Figure 5.3.

With a  $\pm 10^\circ$  error, potential corrections to within  $\pm 1.4^\circ$  were possible, for the previously described geometries (water depth, tow-fish depth, streamer length, streamer offset, etc.). This could be further improved with a greater number of pre-programmed bearings, providing improved correction resolution. This combined with the requirement of long (up to 30 ms) frequency modulated chirp signals [6.26], for use with pulse compression techniques [6.27], meant a need for greater memory allocation and improved software control. Within this new project, improved signal synthesis hardware was used, initially developed by DERA (Winfrith, UK). This allowed a greater number of longer pre-programmed pulses compared with the earlier system. The improved system provided near instantaneous access to 16 pre-programmed signals on 32 channels, with up to 40 ms pulse lengths.

Improved software was developed to include the new signal synthesis and the integration of the multiple systems now needed for the real-time dynamic stabilisation. This included the redevelopment of the system software into a Windows 95 operating system.

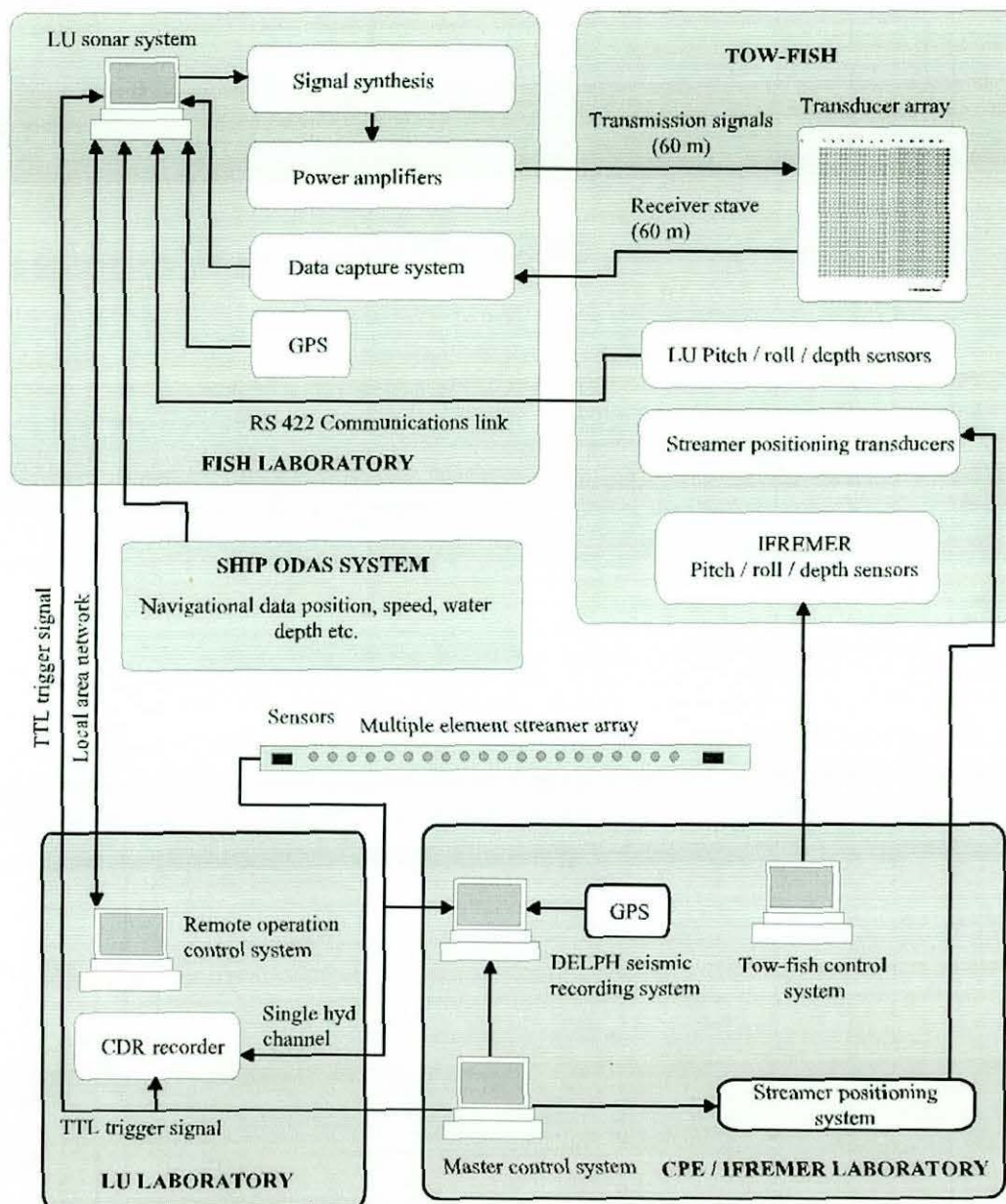


FIGURE 6.10 SIGMA TRIALS SYSTEM DIAGRAM

Figure 6.10 shows a system diagram for the SIGMA trials' acoustic systems. The operation of pitch / roll and depth sensor systems, in parallel with signal synthesis, data capture and the ship's ODAS data system (providing navigational data, etc.), was essential from a single piece of software, to achieve real time dynamic stabilisation and overall system control. Software was therefore developed in the Windows 95 operating system, utilising the multiple threading properties available

with 32 bit processing. Figure 6.11 shows an example of a real time multi-channel display, developed in conjunction with other software systems utilising the original 16 channel data capture system described in Chapter 5.

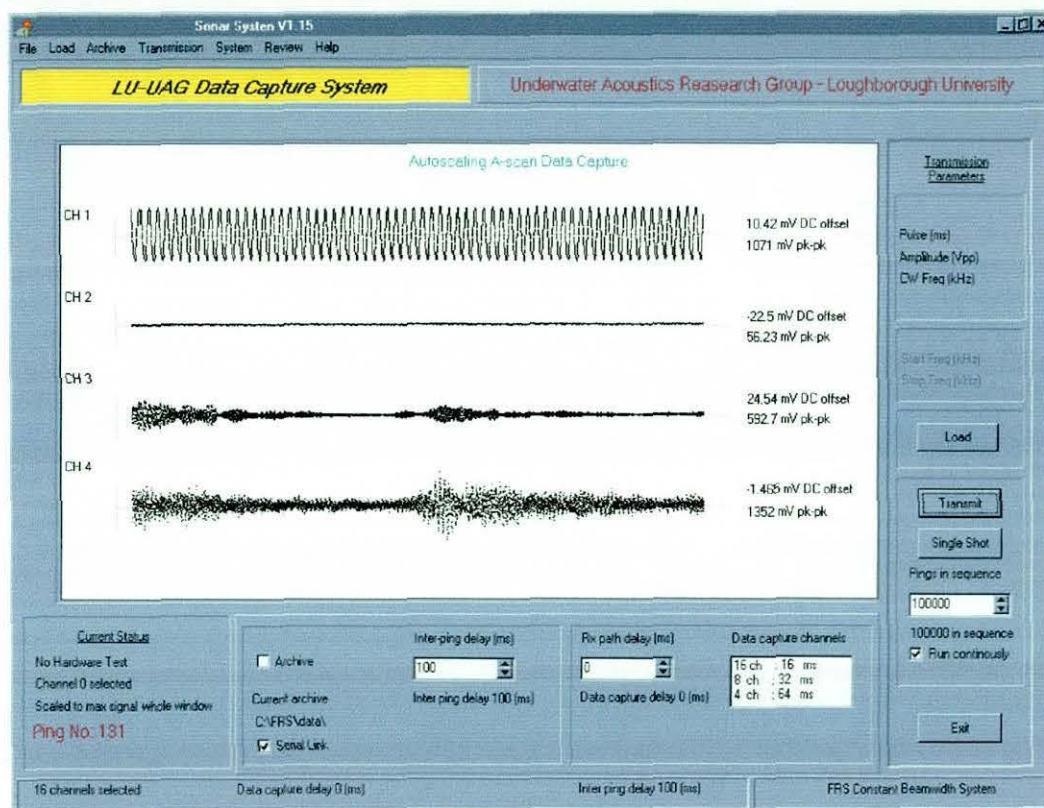


FIGURE 6.11 REAL TIME MULTI-CHANNEL DISPLAY SOFTWARE

The extended maximum pulse length of the improved signal synthesis system also allowed the investigation of pulse compression techniques to provide improved signal-to-noise for bottom and sub-bottom scattered echoes. This allowed the use of long LFM ‘chirp’ signals. These could then be processed using matched filters leading to enhanced echo levels for a similar range resolution <sup>[6.27]</sup> to that seen with a shorter unprocessed pulse.

### 6.3.3 Sea trials

#### 6.3.3.1 Introduction

Two sea trials were carried out, firstly in November 1998 and then in June 1999, using the Belgian Navy acoustic research vessel, Belgica. The 51 m-long vessel



had a rear mounted A-frame winching system similar to that employed in the previous REBECCA trials and was capable of running on either diesel or electric motors, making its self-noise extremely low. An internal data collection system (ODAS), allowed collection and redistribution of data from a wide variety of ship based sensors, including (D-GPS position, water depth, Speed Over Ground (SOG), Course Over Ground (COG), pitch, roll, heave, etc.) This data was made available to other systems via a serial data burst, once a second.

The first trial was a system commissioning trial and feasibility study, for the newly developed acoustic systems, in a practical ocean-going environment. The second trial involved intensive surveying of a well-known area of seabed, ranging in water depth from 45 to 90 m, using all available systems. These included remotely operated parametric systems, bottom operated geophysical measuring equipment using high-resolution seismic surveying techniques, physical coring (1-3 m penetration) and surface grabs to a sediment depth of 30 cm.

#### **6.3.3.2 System deployment**

The main parametric sonar system was placed in a fish laboratory close to the rear of the ship due to limited cable lengths. It was then remotely operated using Desklinc remote control software, via a Local Area Network (LAN), set up with another computer in the main laboratory area.

Data from the ships ODAS system and the LU pitch / roll / depth sensors in the tow-fish were taken in via serial data links. A master control system was used to provide synchronisation triggers for all transmitter / receiver systems. GPS systems were used on both the transmitter and receiver to provide accurate timing synchronisation for all transmitter / receiver data logs.

Bottom-scattered data from the oblique incidence parametric source were recorded during the first trial on the 48-element hydrophone array. The array itself was 48 m long, with hydrophone spacings of 0.5 m, in the centre 16 m section and 2 m in the front and end sections, as shown in Figure 6.12. Data was recorded using two

DELPH24 systems, with a 12 kHz sampling rate to a 16-bit accuracy.

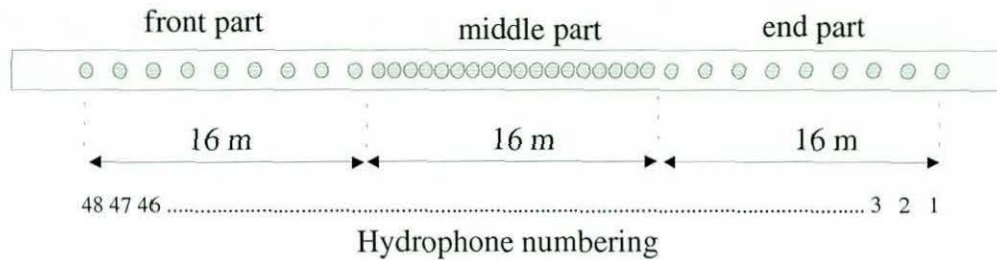


FIGURE 6.12 HYDROPHONE DISTRIBUTION WITHIN STREAMER ARRAY

This array was later replaced by a 12 m, 24-element, evenly-spaced array, due to the unavailability of equipment. In both cases a 35 m VIM was used between the tow-fish and the streamer array.

All transmitter systems were deployed in a similar way to that adopted for the previously described trials using the IFREMER tow-fish. Additional systems included a streamer-positioning array, using three spatially separated transmitters on the tow-fish. These transmitted three synchronous wide-band chirp signals. The direct path signal was then monitored on eight hydrophones in the streamer array. Using pulse compression techniques, accurate time of arrival comparisons were made and hence an estimation of hydrophone position relative to the tow-fish.

A redesigned vertical parametric system was also deployed. The lower frequency parametric component was to be used to determine sub-seabed bathymetry and the high frequency component to measure seabed roughness and topography. The high frequency back-scattered component from the oblique incidence array was also monitored using the receiver stave on the transmit array. Recordings of this and a single hydrophone channel from the streamer were made via the LU data capture system and directly to CD, using an analogue input CDR recorder. CTD profiles in the water column were also carried out periodically during the course of the experiments.

### 6.3.3.3 Results

The first sea trial took place in November 1998, in the SAMDI area off the French coast, in water depths 55-65 m. This trial was primarily to test the systems integration and the feasibility of both the deployment of two parametric sources and data reception of bottom echoes and sub-bottom reflected echoes from a towed body. This was done in conjunction with geophysical measurements, in the same area obtained for 'ground truthing'.

Due to extreme weather conditions, acoustic trials were limited to two days and geophysical measurements during one day out of eight. Eight profile runs were carried out using the acoustic systems on the 11<sup>th</sup> and 15<sup>th</sup> November, each covering water depths in the range 55-65 m. Noise measurements and geotechnical data were also obtained when the weather permitted.

All tested systems performed well, given the prevailing weather conditions. The concept of bi-static data collection from the oblique-incidence steerable system deployed from a tow-fish seemed feasible in good sea conditions with good signal-to-noise for a high percentage of bottom-reflected data.

The second trial took place between the 10<sup>th</sup> and the 15<sup>th</sup> June 1999. Intensive surveying was carried out along a varying depth (40 – 90 m) single profile track, between 47.41.40671 N, 4.18.591 W and 47.43.05911 N and 4.16.71918 W off the French coast near Concarneau. Multiple signal types were transmitted, including CW tone signals at 3, 5 and 7 kHz and both long (40 ms) and short duration (4 ms) chirp signals at 3-6 kHz. Additional measurements were made using the bottom-deployed SHRIMP system with P and S wave generators. Recordings were made using gimbal-mounted geophones towed along the seabed. Data reception in both cases was of good quality. Multiple cores were obtained at various points on the profile, providing some evidence of a thin sediment layer.

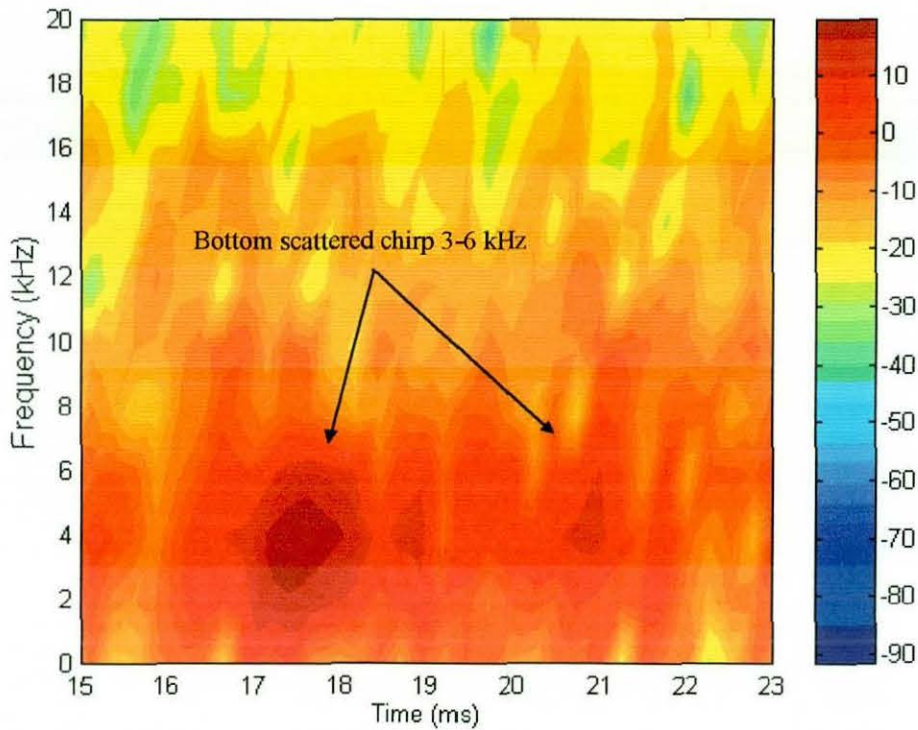


FIGURE 6.13 BOTTOM-SCATTERED 3-6 kHz CHIRP SIGNAL RECEIVED ON THE STREAMER ARRAY

Figure 6.13 shows an example of a spectrogram for seabed scattered data from a single hydrophone in the streamer array for a 3-6 kHz chirp. The colour scale represent the power spectral density in dB.

A dynamic stabilisation technique was also tested. This showed considerable improvement in data reception, not only in off-setting fore-aft pitch errors due to tow-fish motion, but also in the ability to maintain data reception on the relatively small streamer array, with a changing water depth (40-90 m). This was possible due to the acquisition of water depth data from the ship's echo sounder and real time modelling of the through-water propagation path. The stabilisation techniques used are discussed in more detail in Chapter 9.

Figure 6.14 shows acoustic data for a single track taken during the SIGMA trial. The vertical axis is time in 1000 of seconds. The total scale representing just over 25 minutes. The horizontal axis is the windowed data capture period in ms. Each

horizontal line represents a single transmission. The input data then represents the envelope detected signal on a single hydrophone.

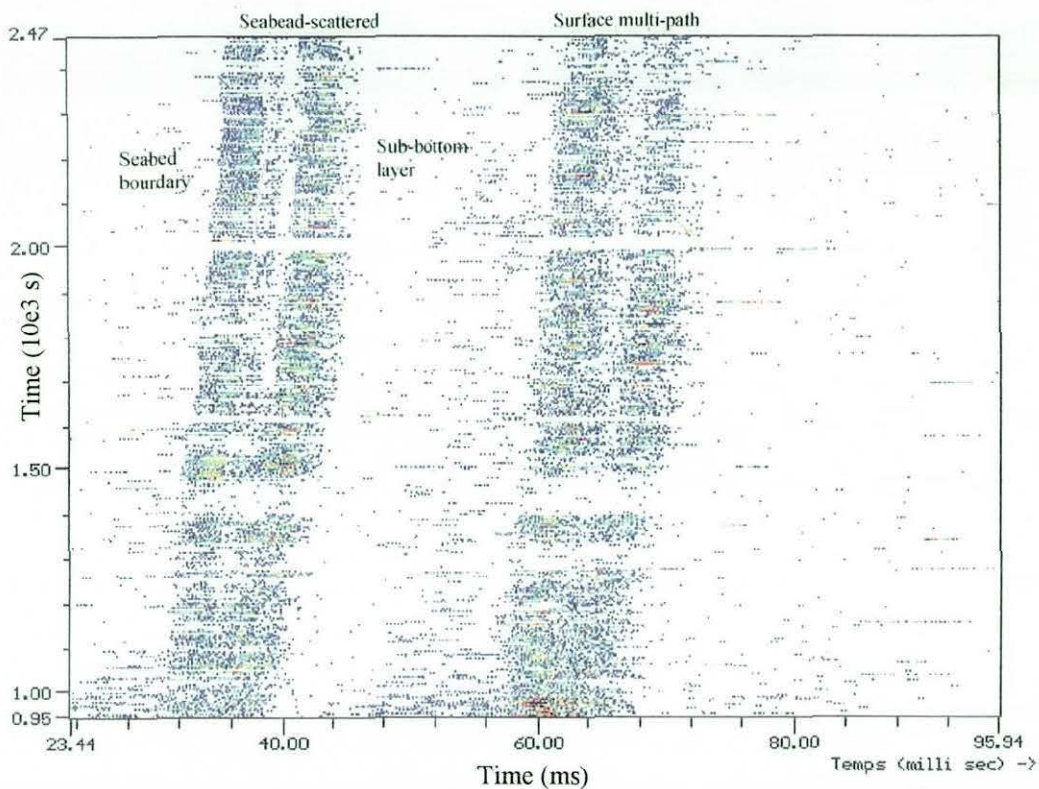


FIGURE 6.14 ENVELOPE DETECTED ACOUSTIC SIGNALS SIGMA TRIALS  
*Image courtesy of CPE, France.*

Evidence of both bottom and sub-bottom layer echoes are clearly visible for a majority of the profile. The signal is then repeated due to the arrival of a multi-path of the seabed-scattered signal arriving via the surface. The lower part of the chart shows a merging of the sediment layer into a single echo. This area was believed to be rock based with no soft sediment covering. As the profile extends into deeper water a second echo is formed from what is believed to be from a sediment rock boundary.

### 6.3.4 Conclusions

Both the REBECCA and SIGMA projects have demonstrated the potential for the use of parametric sonar systems in the remote acoustic sensing of marine sediment and the assessment of geophysical properties, via inverse procedures. The

development of dynamic stabilisation techniques used with a phase-steered parametric array and real-time through water and sediment propagation modelling, has considerably enhanced the potential of any system for operation in an ocean going environment. The tracking of a high directivity, low frequency acoustic source, operating in a bi-static mode, in variable water depths, and with compensation of transmission platform instabilities, was shown to be possible, allowing good data reception on a relatively small receiver array.

The improved quality and quantity of sediment-reflected acoustic data, combined with both scaled and mathematical models and the continuing development of inverse techniques, should lead to the development of a practical, remote, acoustic sensing system for marine sediment classification.

## **6.4 ACUSTICA project**

### **6.4.1 Introduction**

The ACUSTICA (Acoustic Characterisation of Undersea Sediments to Initiate Commercial Applications) project started in 1995 as part of the European Commission's International Scientific Co-operation Programme. The project involved partners from three institutes. The Indian Institute of Technology (Instrument Design and Development Centre) IIT.IDDC; the Foundation for Research and Technology – Hellas (Institute of Applied and Computational Mathematics) FORTH.IACM in Crete and the Underwater Acoustics Group, Loughborough University.

This project ran over a three-year duration, with the aim of taking a strong multidisciplinary approach to achieve improvements in sediment classification techniques using acoustic systems. The research topics within this project strongly overlapped with research conducted in the REBECCA and SIGMA projects. The project involved the use and development of two parametric sonar systems, the previously described LU 75 kHz system and a new 40 kHz parametric system developed by IIT in India in co-operation with the Loughborough research group. Open water trials, using each system, were conducted on Loch Duich in Scotland and Lake Edukki in Southern India. FORTH further developed inverse algorithms for application to data collected in sea trials. Work was also conducted in the development of interactive non-linear propagation models, to allow the estimation of seabed-incident signals for application to inverse techniques at various ranges from the source. Software models were developed to predict acoustic propagation within the water column and in sediment layers, to enhance data collection when operating in realistic ocean-going environments.

## 6.4.2 IIT parametric sonar system

### 6.4.2.1 Sonar system

A compact parametric sonar system was developed at IIT in Delhi, using a  $16\lambda \times 2\lambda$  array configuration, with a primary frequency resonance at 40 kHz. The array was configured into 16 staves of 2 elements, as shown in Figure 6.15, allowing scanning of a  $60^\circ$  sector with a  $3.6^\circ$  beam.

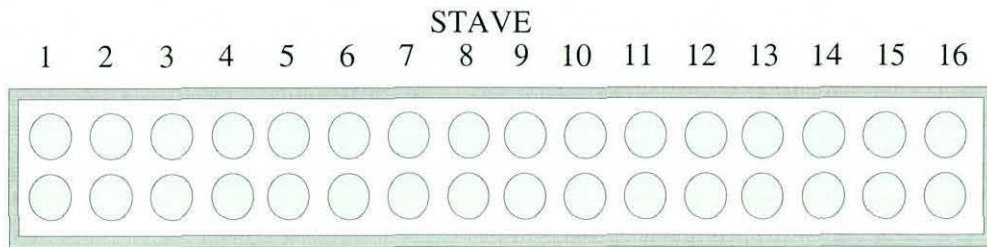


FIGURE 6.15 IIT 40 kHz PARAMETRIC TRANSMIT ARRAY CONFIGURATION

Compact linear power amplifiers were developed, rated at 200 W each, providing a maximum theoretical primary frequency source level of 229.3 dB re  $1 \mu\text{Pa}$  at 1m for a single tone <sup>[6.28]</sup>. The linear amplifiers were designed to provide a lightweight, high efficiency system for ease of use. Additional features included the ability to disconnect amplifier output and power supply systems under software control. This feature was included in the transmission and signal synthesis software to minimise noise from the amplifiers during a listen phase of the transmission cycle.

Signal synthesis was initially carried out using a transputer-based system, but this was then redesigned to use a PC-based multi-channel system. Computed waveforms were mapped to external memory across the ISA bus. These could then be clocked out of the memory on receipt of a PC-controlled logic level. A 16-channel, 8-bit resolution system was developed, mapping to sixteen 128 k x 8 bit memory modules. Additional encoding was built into the transmitter software to perform an amplifier enable/disable signal. The amplifier output stage and power supply were only connected via a software enable signal, just before the



transmission phase, then disconnected shortly afterwards to minimise noise during the listen phase. Control logic was also used to trigger a Time Variable Gain (TVG) pre-amplifier linked to the receiver system.

Data capture was achieved using a single element hydrophone. Signals were then conditioned and applied to a spectrum analyser, based on a TMS320C30 DSP system. A sector scanning receiver system was developed, based on the DPS system output <sup>[6.29]</sup>. Sectors scanning non-linear waveforms were encoded using a 2.4-4.8 kHz linear chirp signal. The frequency component was then decoded back into bearing information by the receiver system, allowing the development of a 60° sector scanned parametric sonar system.

#### **6.4.2.2 Lake Edduki open water trial**

Field trials of the parametric system were carried out at the Underwater Acoustics Research Facility, Edduki Lake near Cochin, Kerala State, Southern India in February 1996. Edduki reservoir is part of a fresh water hydroelectric system supplying power for a large proportion of the state of Kerala. The facility is run by the Naval Physical Oceanographic Laboratory (NPOL) under the control of the Indian Ministry of Defence. The test site consists of a floating raft, a landing craft and support vessels. The main platforms and landing craft were moored together, forming a single platform around 40 m long, in approximately 25 m water depth. Water depths were much lower than expected at that time of year (normally around 45 m) due to unusual weather during the second monsoon period, October to December, 1995.

The transmit array, deployed on the end of a 5 m long shaft, allowed horizontal transmission to a receiver hydrophone at a range of 37.8 m at the other end of the combined floating platform. Using this arrangement primary and secondary frequency source levels were measured. Mechanical adjustment of the array orientation allowed the measurement of primary and secondary frequency beam-patterns. The array was then reoriented downwards, to collect forward-scattered

data from the seabed. The receiver hydrophone was moved to different horizontal ranges from the transmitter, allowing data collection of bottom scattered data at three different incident angles 26.2°, 28.8° and 31.2°. Seabed incidence was estimated, taking into account bottom slope believed to be around 4.2°.

### 6.4.2.3 Results

The Edduki lake experiment was primarily designed for the evaluation and calibration of the newly developed IIT parametric sonar system. Due to operation in a 'fresh' water environment the system was tested well within the virtual array length. The majority of the system parameters were unaffected in the move from fresh water to salt water operation (directivity, transmitted power, efficiency, etc.). Of primary concern is a significant reduction in the attenuation coefficient ( $\alpha$ ) seen in fresh water at the frequencies of interest. The virtual array length of the parametric source is inversely proportional to the attenuation factor, measured for that medium. This is usually taken as  $(2\alpha)^{-1}$  but can be up to ten times larger depending on whether a majority of the secondary frequency generation takes place in the near-field or the far-field of the array. At higher frequencies, in excess of 1 MHz, little difference in the attenuation coefficient is seen between fresh and salt water. Below 100 kHz, however, significant variations between the two cases are seen. As an upper limit, comparison of salt water and distilled water attenuation coefficient can have a 30:1 ratio. In a more normal case, lakes and reservoirs usually exhibit some salinity, giving a still significant 10:1 reduction in attenuation in comparison with salt-water<sup>[6.30]</sup>. In practice the virtual array length a 40 kHz array, using the expression  $(2\alpha)^{-1}$  is around 617 m and 6172 m for salt and fresh water respectively, assuming an  $\alpha$  of  $0.81 \times 10^{-3}$  nepers.m<sup>-1</sup> and  $0.081 \times 10^{-3}$  nepers.m<sup>-1</sup>.

Although measurements were carried out well within the virtual array length, evidence of non-linear generation was seen and the measurements of primary and secondary frequency beam-patterns were made. Assessments of source levels were also made based on the available data. Figure 6.16 and 6.17 show primary

and secondary frequency source level estimates.

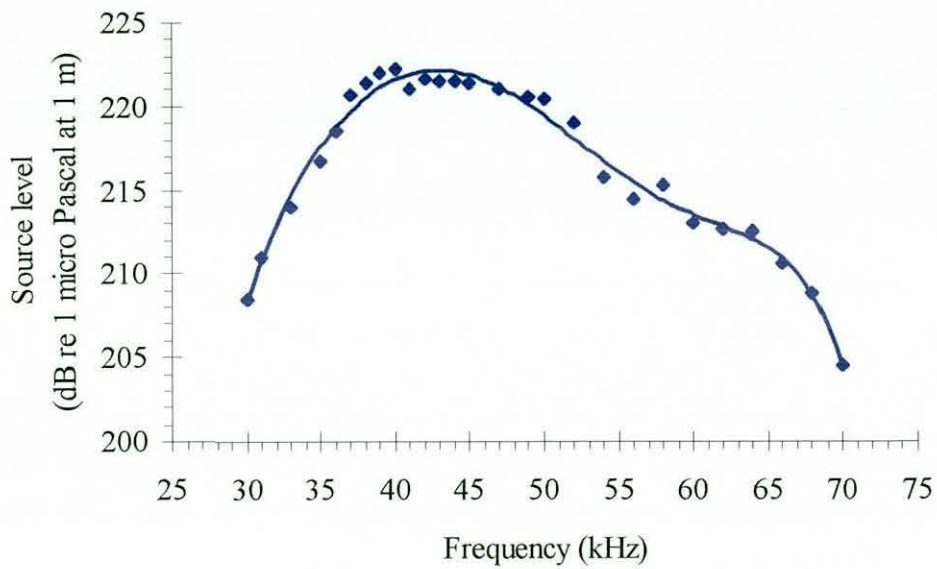


FIGURE 6.16 PRIMARY FREQUENCY SOURCE LEVEL

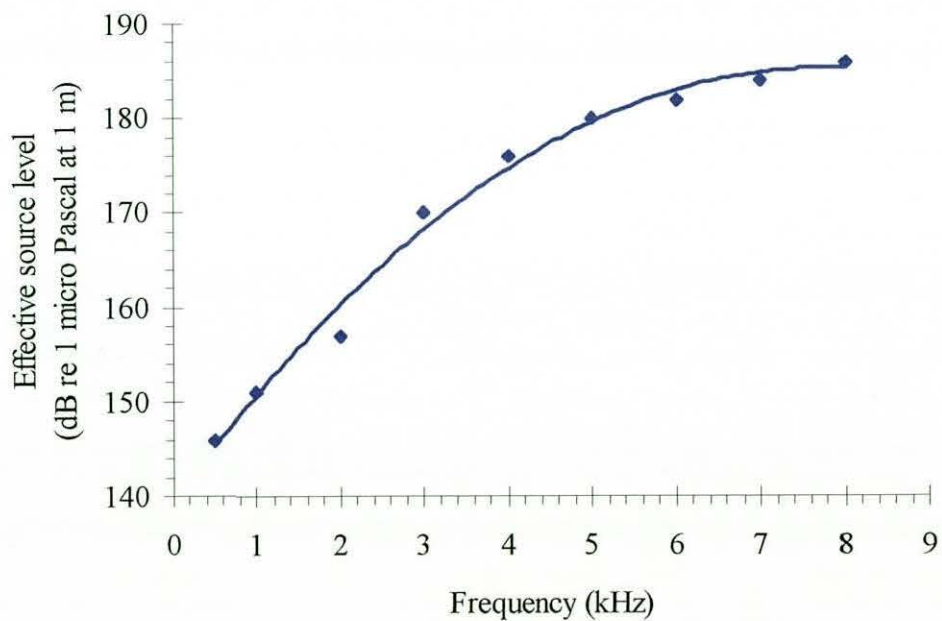


FIGURE 6.17 SECONDARY FRERQUENCY SOURCE LEVEL

Figure 6.16 shows the broad-band response of the 40 kHz elements used in the array, with a peak measured source level for 40 kHz at around 222 dB re  $1\mu\text{Pa}$  at 1 m and a bandwidth of around 14 kHz, compared with 6 kHz for the LU array. The

primary source level is lower than the theoretically predicted level due to reduced input power limits imposed by operation from a generator power supply. The effective source levels at the secondary frequencies, shown in Figure 6.17, however showed a good correlation with the theoretically predicted levels <sup>[6.31]</sup> based on the reduced primary frequency source levels.

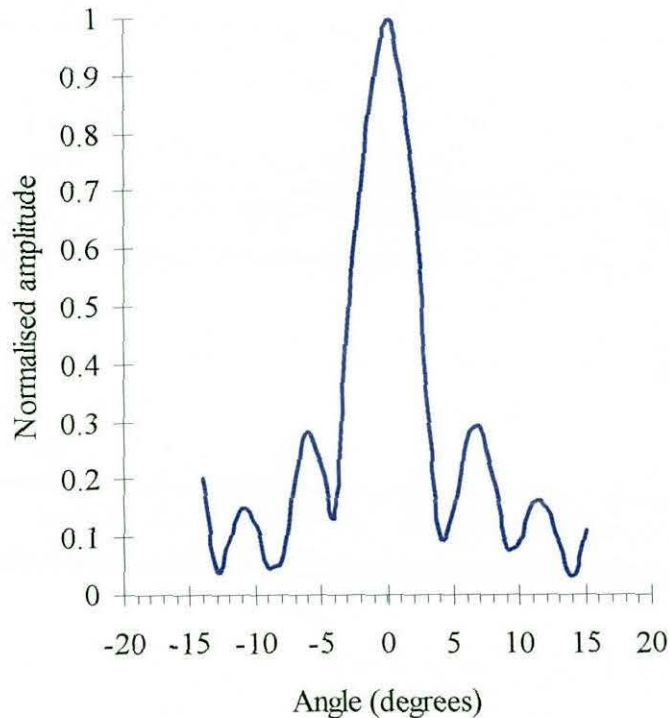


FIGURE 6.18 STEERABLE AXIS BEAM PATTERN AT 40 kHz

Figure 6.18 shows the primary frequency beam-pattern at 40 kHz in the phase steerable plane of the transducer array. The  $-3$  dB beam-width of  $4^\circ$  measured in the steerable axis compared well with theoretical predictions of around  $3.4^\circ$  from equation (4.1). Assessment of secondary frequency beam-widths in this axis also showed reasonable correlation with expected values, with measured figures varying from  $3.3^\circ$  at 1 kHz to  $2.6^\circ$  at 8 kHz.

The performance of a non-linear sector-scanning capability was tested by transmitting along the reservoir. Range and bearing information was obtained from observed echoes from a dam wall, at ranges above 600 m, demonstrating

good repeatability and a phase steering capability over a  $\pm 30^\circ$  sector.

#### **6.4.2.4 Conclusions (IIT parametric system)**

The IIT compact phase-steerable parametric sonar system was designed and later tested on a fresh water lake. The system performed well, within expected limits, demonstrating a good correlation between measured and theoretical estimated values. Peak primary frequency source levels of 222 dB re 1  $\mu$ Pa at 1 m were obtained and secondary frequency generation was achieved, from 0.5 to 8 kHz, with effective source levels ranging up to 187 dB re 1  $\mu$ Pa at 1 m. Primary and secondary frequency beam-patterns in the scanned direction showed a good correlation with theoretical estimates. Electronic beam forming and the use of a sector-scanned display were also proven. The system demonstrated considerable potential for application as a compact, easily handleable parametric sonar system for eventual use in acoustics for sediment classification.

#### **6.4.3 Acoustic propagation modelling**

One of the tasks undertaken during the ACUSTICA project was the development of ray path models for acoustic propagation through water and sediment layers. This allowed the prediction of acoustic propagation in realistic sea conditions, in both the water column and sediment layers in a range of geometries. Software models were primarily developed, to allow the real-time visualisation of acoustic propagation and the prediction in transmitter-receiver alignment errors, therefore providing the potential for real time correction and increasing the likelihood of good data reception. Models also gave considerable insight into echo identification, through timing predictions, including prediction of both seabed and surface-generated multi-path signals.

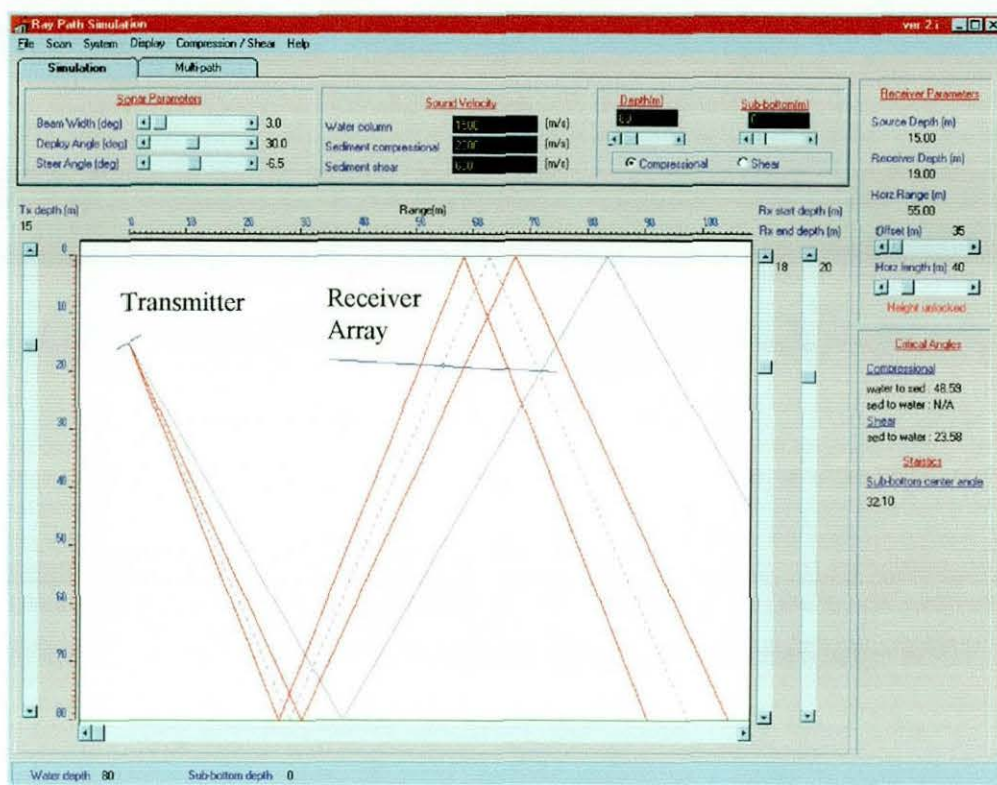


FIGURE 6.19 PARAMETRIC ARRAY THROUGH-WATER SIMULATION

Figure 6.19 shows a simulation of a  $3^\circ$  beam bottom-scattered signal for reception on a receiver array. The display shows the beam centre (dashed) and the  $-3$  dB limits of the acoustic signal. The above example illustrates that a  $-6.5^\circ$  steer angle is needed to align to the centre of the receiver array, for the above deployment geometry.

Reliable data collection for a sediment classification system required consideration of likely through-sediment propagation modes. Figure 6.20 shows a non-normal incidence signal arriving at the seabed and the resultant refracted and reflected signals at the water sediment interface. The pressure wave interaction at the water-sediment interface can also lead to shear wave excitation <sup>[6.32]</sup> as well as compressional refraction energy propagation within the sediment, at incidence angles  $\theta_i \neq 0$ .

The signal arrives at an angle of  $\theta_i$  and resultant forward-scattered signals are seen

at a similar angle  $\theta_{fs}$ . Application of the refraction law in terms of both the compressional and the shear wave velocities,  $c_{Csed}$ ,  $c_{Csub}$  (sediment, sub-bottom) and  $c_{Ssed}$ ,  $c_{Ssub}$  and the velocity in water,  $c_{wat}$  gives

$$\theta_C = \arcsin\left[\frac{c_{Csed}}{c_{wat}} \sin(\theta_i)\right] \text{ and } \theta_S = \arcsin\left[\frac{c_{Ssed}}{c_{wat}} \sin(\theta_i)\right]$$

Using the above expressions the compression and shear wave propagation angles  $\theta_C$  and  $\theta_S$  can be calculated.

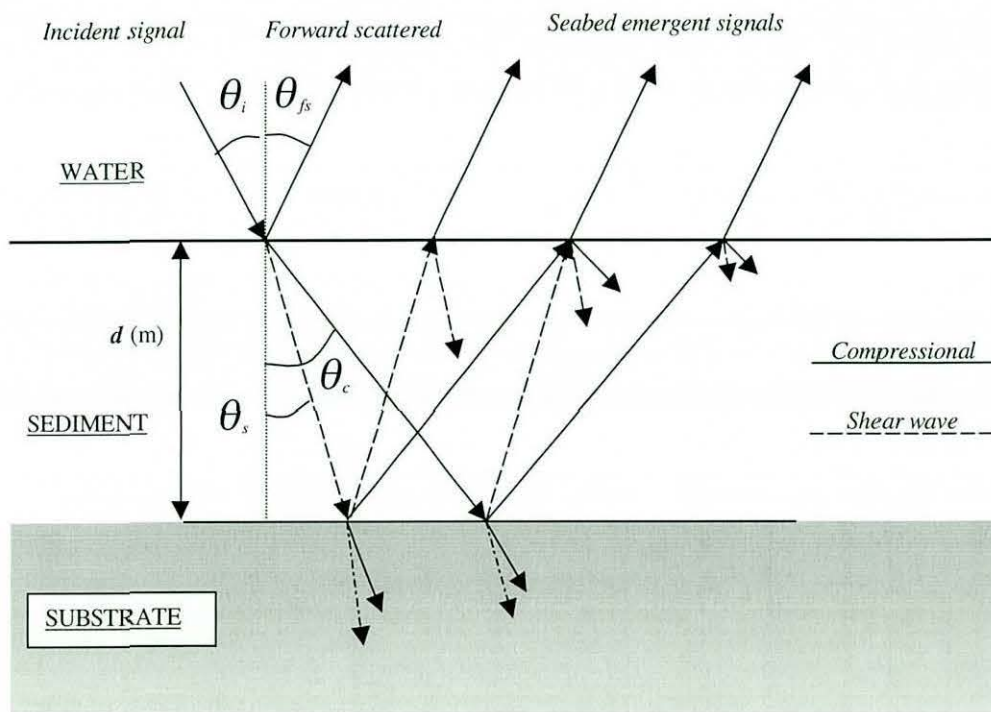


FIGURE 6.20 COMPRESSIONAL AND SHEAR WAVE PROPAGATION IN A FINITE SEDIMENT LAYER

The propagation of both compressional and shear waves were therefore considered. The regeneration of both wave types at each boundary interface is possible. The secondary layer is assumed to be semi-infinite and propagation into this layer is ignored, as the detection of energy at the receiver after penetrating this layer is unlikely. Regeneration of multiple, internally reflected signals at both the water-sediment and sediment-substrate layer was considered for both the shear and compressional case. Variation in shear wave velocities are seen from  $180 \text{ ms}^{-1}$

for silt, to  $450 \text{ ms}^{-1}$  for sand-clay and compressional wave velocities of  $1850 \text{ ms}^{-1}$  for coarse sand and  $1490 \text{ ms}^{-1}$  for silt [6,20]. The resultant signals can then generate both compressional and shear wave excitation signals, which can be reflected back towards the surface at the sediment-substrate interface. Acoustic energy is then either reflected back into the sediment at the sediment-water boundary interface or may emerge back into the water column.

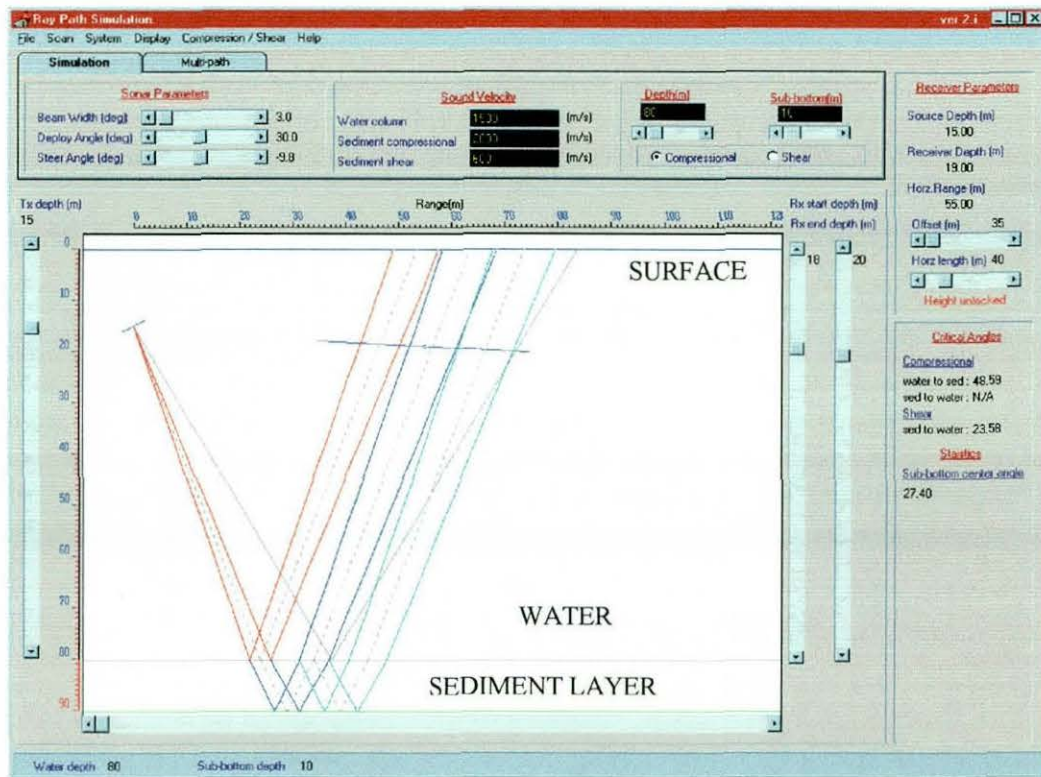


FIGURE 6.21 MULTIPLE SEABED EMERGENT SIGNAL MODELLING DUE TO COMPRESSIONAL WAVE PROPAGATION WITHIN A SEDIMENT LAYER

Figure 6.21 shows multiple reflected, compressional wave propagation for a 10-m thick sediment layer. The model shows distinct emergent signals arriving at the receiver, based on multiple internal reflections within the sediment layer.



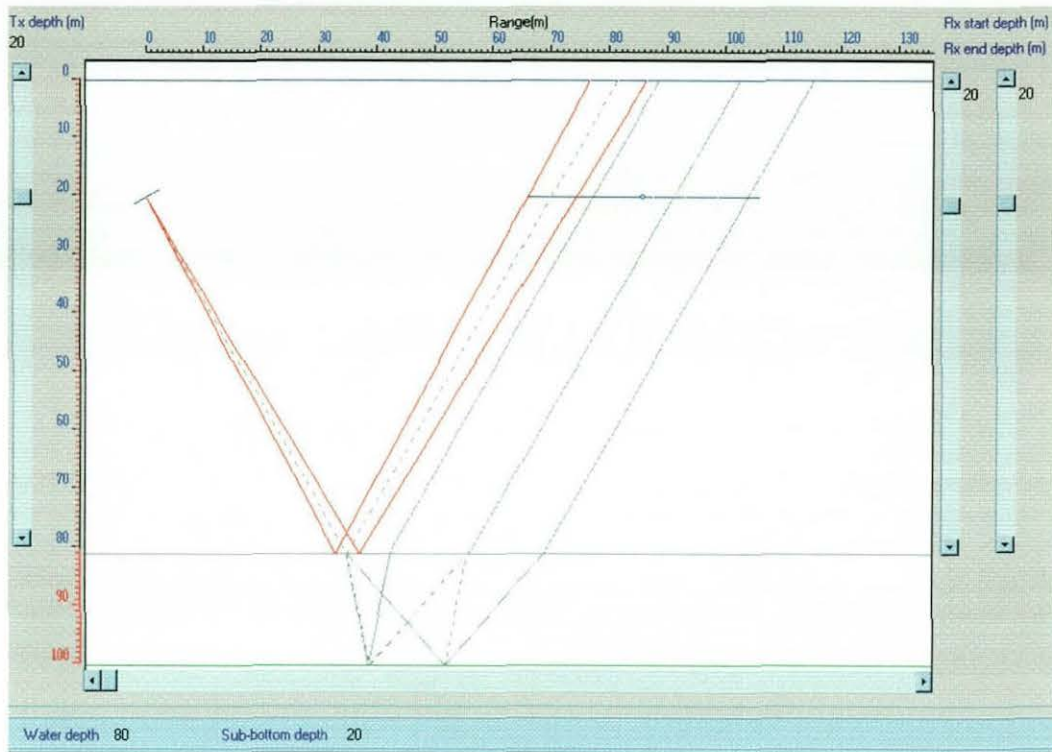


FIGURE 6.22 SHEAR WAVE PROPAGATION WITHIN A SINGLE SEDIMENT LAYER

The possibility of compressional-to-shear and shear-to-compressional excitations, even for a single layer, has led to the complex modelling of multiple emergent signals, as shown in Figure 6.22. This shows some of the possible complex compressional wave interactions and resultant emergent signals. Only the centre line of the symmetrical beam is shown for clarity. Modelling of all possible propagation modes illustrates the potentially highly complex nature of the received signal at the receiver array, even in terms of compressional and shear wave excitations for a relatively simple single-layered case.

Post analysis of possible sediment propagation paths can considerably enhance the analysis of received data at the hydrophone array. Comparisons of signals received from varying propagation modes allow inverse techniques to be used for the eventual classification of the sediment layer <sup>[6.33]</sup>. These tools were further developed during the SIGMA project, to provide real-time predictions of the propagation path for bottom and sub-bottom reflected signals, used in the real-time correction of transmitter receiver alignments.

#### 6.4.4 Real time assessment of multi-path signal arrivals

Models were also developed to allow the prediction of seabed and surface multi-paths, including both first and second seabed and surface multi-path signals. This again provided a powerful tool for the visualisation of complex signal arrivals at a receiver array. Prediction of the propagation times for both the surface and seabed multi-paths could be compared with real signals, allowing prediction of the source range and depth, by comparison of the arrival times with the direct signal [6.34]. Figure 6.23 shows both first and second multi-path model, for the geometries shown in Figures 6.21. The receiver is taken as the middle of streamer array.

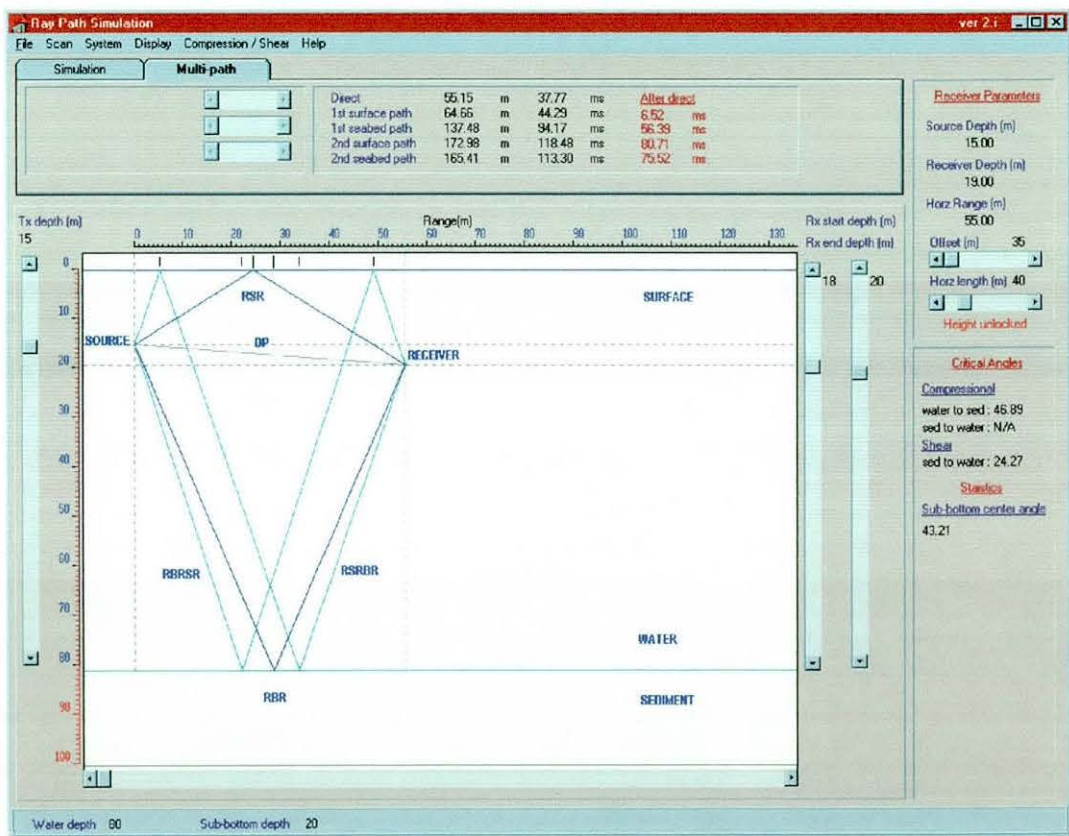


FIGURE 6.23 FIRST AND SECOND MULTI-PATH PREDICTION

The following labels are defined for the first and second surface and seabed paths [6.35]

DP	Direct path
RSR	Refracted-Surface-Reflected
RBR	Refracted-Bottom-Reflected
RSRBR	Refracted-Surface-Reflected-Bottom-Reflected
RBRSR	Refracted-Bottom-Reflected-Surface-Reflected

Algorithms were also developed to obtain the range and depth of an acoustic source, with no knowledge of the transmission time, by comparison of the arrival times of the multi-path signal with the direct signal. This passive tracking technique were first applied to anti-submarine warfare <sup>[6.35]</sup> and later adapted to the tracking of marine mammals <sup>[6.36-6.37]</sup>. The tools developed also provided valuable insight into the complex signal arrivals, seen on a receiver array in a range of geometries. They were also incorporated into the real-time, dynamic stabilisation system developed to enhance visualisation of signal reception in realistic sea conditions.

## 6.5 Conclusions

A range of software tools has been developed over all three projects, allowing the enhancement of the visualisation of sound propagation within the water column and sediment layers. These have been used for the real time prediction of signal reception whilst at sea and the post analysis of complex signal arrivals of real data on a receiver array. Modelling of both shear and compressional wave propagation was carried out in real-time for application to dynamic stabilisation techniques. Modelling of multi-path signals also provided valuable insight into the complex signal arrivals observed in data recorded in sea trials.

The development and testing of two parametric sonar systems was carried out as part of various multidisciplinary international projects. The LU system was developed and first tested on open water trials held on Loch Duich in Scotland. This was then deployed ocean-going experiments, designed to investigate the use of remote sensing of marine sediments using acoustics. Later developments included improved signal generation techniques and the investigation and

implementation in both hardware and software for the dynamic stabilisation of a parametric source. This was to achieve real time correction of transmitter-receiver alignment errors due to transmission platform instabilities. These systems were tested in open sea conditions and demonstrated the potential for the use of a parametric source in the investigation of marine sediment geo-physical properties.

An additional compact phase-steerable parametric sonar system was designed and tested in an open water trial in Lake Edduki in Southern India. System parameters were tested and the general performance was satisfactorily evaluated. This, in conjunction with the development of improved inversion techniques, should lead to a better understanding of the relationship between marine sediment geo-physical characteristics and through sediment acoustic propagation and the eventual development of techniques for the non-intrusive remote sensing of marine sediment using acoustics.

## REFERENCES: Chapter 6

- 6.1 Lambert D. N., Walter D. J., Young D. C., Griffin and Benjamin K.C.  
Developments in acoustic sediment classification,  
*Proc. IEEE Oceanic Engineering Society Oceans'98 Conference*,  
Nice, Vol. 1, pp.26-31, 1998.
- 6.2 Woolsey J. R. and McGee T. M.  
Monitoring of the water column and sub-bottom sediment using  
acoustic arrays in the Northern Gulf of Mexico,  
*Proc. IEEE Oceanic Engineering Society, Oceans'98 Conference*,  
Nice, Vol. 1, pp.442-443, 1998.
- 6.3 Moren P. and Pihl J.  
Sub-bottom characterisation using a parametric sonar,  
*Proc. IEEE Oceanic Engineering Society, Oceans'98 Conference*,  
Nice. Vol. 3, pp. 1828-1832, 1998.
- 6.4 Pettersen P., Hovem J. M., Lovik A. and Knudsen T.  
A new sub-bottom profiling sonar using a non-linear sound source,  
*The Radio and Electronic Engineer*,  
Vol. 47, No. 3, pp 105-111, 1997.
- 6.5 Caiti A. Zoppoli R.,  
Seafloor parameters identification from parametric sonar data,  
*Proc. 4<sup>th</sup> European Conference on Underwater Acoustics*,  
Rome, Italy, Vol. 1, pp 307-312, 1998.
- 6.6 Woodward B, Cook J C Goodson AD and Lepper P.  
A phase steered parametric array for sub-bottom profiling;  
*Proceedings of the 6<sup>th</sup> International Conference on Electronic  
Engineering in Oceanography, Cambridge, UK*,  
IEE Conference Publication No 394, 19-21 July 1994, pp 77-82, 1994.
- 6.7 Urlick R. J.,  
Principles of underwater sound,  
*McGraw-Hill Book Company*,  
2<sup>nd</sup> edition, ISBN 0-07-066086-7, pp. 103, 1975.
- 6.8 Muir T. G., Horton C.W. Sr and Thompson L.A.,  
The penetration of highly directional acoustic beams into sediment,  
*Journal of Sound and Vibration*,  
Vol. 64, No. 4, pp. 539-551, 1979.
- 6.9 Woodward B., Goodson A. D., Cook J. C. and Lepper P. A.  
Sea bed characteristics using non-linear acoustics;  
*Proc. 2<sup>nd</sup> European Conference on Underwater Acoustics*,  
Copenhagen, Denmark, 4-8 July 1994, Edited by Bjorno L, Elsevier

Science Publishers BV, ISBN 92-826-8000-2, ISSN 1018-5593, pp 875-880, 1994.

- 6.10 Cook J. C., Goodson A. D. and Griffiths J.W.R,  
Experience with a versatile NLA sonar system,  
*Proceedings of the Institute of Acoustics*,  
Vol.14, part 3, pp. 27-52, 1992.
- 6.11 Woodward B., Cook J. C., Goodson A. D. and Lepper P. A.  
The REBECCA project: Acoustical remote sensing with a parametric sonar,  
*Proc. of the 2<sup>nd</sup> MAST Days and EUROMAR Market*,  
7-10 November 1995, Sorrento, Italy, 1995.
- 6.12 Cook J. C., Goodson A. D., Lepper P. A. and Woodward B.  
The Loughborough University parametric sonar system'  
*Proceedings of the 1<sup>st</sup> European Workshop on Parametric Arrays*,  
April 1995, C.P.E Lyon, Lyon, France, pp. 35-38, 1995.
- 6.13 Richardson J.W., Greene C.R. Jr, Malme C.I. and Thomson D.H.  
Marine Mammals and noise  
*Academic Press*, ISBN: 0-12-588441-9, pp. 136-146, 1995.
- 6.14 Chotiros N. P.,  
Acoustic penetration of sandy shallow water sediment in the 500 to 1000 Hz band,  
*Proc. IEEE Oceanic Engineering Society, Oceans'98 Conference*,  
Nice, Vol. 1, pp. 22-25, 1998.
- 6.15 Engelbrecht S., A space-time approach for seabed characterisation,  
*Proc. 3<sup>rd</sup> European Conference on Underwater Acoustics*,  
Heraklion, Crete, Vol. 2, pp.632-636, 1996.
- 6.16 Cook J C, Goodson A D, Lepper P A and Woodward B  
The design and evaluation of a phase steered parametric sonar system intended for sediment characterisation,  
*Journal of the Society for Underwater Technology*,  
Vol. 22, No 2, , ISSN 0141 0814, pp 43-54, 1996.
- 6.17 Lepper P.A. and Woodward B.,  
Techniques for achieving dynamic stabilisation of a sonar array platform,  
*Journal of the Acoustical Society of India*,  
Vol. XXIII, No. 5, 1995.
- 6.18 Woodward B. and Lepper P. A.  
Real time dynamic beam steering with a parametric array,  
*Proceedings of the 1<sup>st</sup> European Workshop on Parametric Arrays*,  
April 1995, C.P.E Lyon, Lyon, France, pp 39-42, 1995.

- 6.19 Favretto-Anres N. and Sessarego J. P.,  
The Stonely-Scholt wave and love wave: combination of  
inhomogeneous plane waves. Application to acoustical  
characterisation of sediments,  
*Proc. 3<sup>rd</sup> European Conference on Underwater Acoustics, Heraklion,*  
Crete, Vol. 2, pp. 595-600, 1996.
- 6.20 Papadakis P. J. and Piperakis G. S.,  
An inverse procedure for the reconstruction of a sea bottom consisting  
of two elastic materials,  
*Proc. 3<sup>rd</sup> European Conference on Underwater Acoustics, Heraklion,*  
Crete, Vol. 2, pp 619-624, 1996.
- 6.21 Vandenplas S., Abdellatif B. T., Peirlinckx L. and Biesen L. V.,  
Experimental study of wave propagation models for sediments by  
calibrated transmission experiments on a laboratory scale,  
*Proc. IEEE Oceanic Engineering Society, Oceans'98 Conference,*  
Nice, Vol. 1, pp. 385-389, 1998.
- 6.22 Temsamani A. B., Peirlinckx L., Vandaplas S. and Biesen L. V.,  
Identification of parametric models for ultrasonic reflection  
experiments performed on sediments at oblique incidence, *Proc.*  
*IEEE Oceanic Engineering Society, Oceans'98 Conference,*  
Nice, Vol. 1, 513-517, 1998.
- 6.23 Cisneros Z., Peirlinckx L., Wartel S. and Biesen L. V.,  
Experimental modelling of wave propagation through marine  
sediments in controlled measurement conditions,  
*Proc. 3<sup>rd</sup> European Conference on Underwater Acoustics,*  
Heraklion, Crete, Vol. 2, pp. 589-594, 1996.
- 6.24 Taroudakis M. I., Papadakis P.J. and Sklavos S. G.,  
Bottom characterisation using parametric array data,  
*Proc. 3<sup>rd</sup> European Conference on Underwater Acoustics,*  
Heraklion, Crete, Vol. 2, pp. 625-630, 1996.
- 6.25 Peirlinckx L., Dunon Y. and Biesen L. V.,  
Application of system identification techniques to wave propagation  
modelling in a multi-layered systems: A mature solution to the inverse  
problems,  
*Proc. 3<sup>rd</sup> European Conference on Underwater Acoustics,*  
Heraklion, Crete, Vol. 1, pp 361-366, 1996.
- 6.26 LeBlanc L. R., Mayer L., Rufino M. Schock S. G. and King J.,  
Marine sediment classification using the chirp sonar,  
*J. Acoust. Soc. Am,*  
Vol. 91, No. 1, pp. 107-115, 1992.

- 6.27 Berfield M., Cook C. E., Paolillo J. and Palmieri C. A.,  
Matched filtering, pulse compression and waveform design. *The Microwave Journal*,  
Vol. 7, No. 10, pp 57-64, 1964.
- 6.28 Vyas A.L., Balji Raj V.S.,  
Design and testing of a compact parametric sonar,  
*Proceedings of the World Congress on Ultrasonics*,  
Yokohama, Japan, 24-27 August 1997.
- 6.29 Vyas A.L., Balji Raj V.S.,  
A TMS320c30 Based VGA display system for a parametric sonar receiver,  
*Journal of the Acoustical Society of India*,  
Vol. XXIII, No. 4, pp.175-179, 1995.
- 6.30 Etter P.C.,  
Underwater acoustic modelling (principles, techniques and applications),  
*Elsevier Science Publishers Ltd*,  
ISBN 1-85166-528-5, 1991.
- 6.31 Fenlon F.H.,  
A weak interaction model for the axial difference field of symmetric and asymmetric parametric acoustic transmitting arrays,  
*J. Acoust. Soc. Am.*, Vol. 61, pp. 325-337, 1997.
- 6.32 Vadmar P.J.,  
Ray path analysis of sediment shear wave effects on bottom reflection loss,  
*J. Acoust. Soc. Am.*, Vol. 68, No 2, pp. 639-648, 1980.
- 6.33 Tolstoy A. and Chapman N.R.,  
Benchmarking geoacoustic inversion in shallow water,  
*Proc. 4<sup>th</sup> European Conference on Underwater Acoustics*,  
Rome, Italy, Vol. 1, pp. 347-352, 1998.
- 6.34 Lepper P.A., Kaschner K, Connelly P.R and Goodson A.D.,  
Development of a simplified ray path model for estimating the range and depth of vocalising marine mammals,  
*Proc. Institute of Acoustics*,  
Vol. 19, Part 9, pp. 227-234, 1997.
- 6.35 Waite A.D.  
Sonar (for practising engineers),  
*Epic Printing Services, Dorchester*,  
ISBN 0 9528033 1 3, pp.114-118, 1998.



- 6.36 Kaschner K., Goodson A. D., Connelly P. R. and Lepper P. A.,  
Species characteristics features in communication signals of cetaceans:  
Source level estimates for some free ranging North Atlantic  
odontocetes,  
*Institute of Acoustics, Underwater Bio-Sonar and Bioacoustics*,  
ISSN: 309 8117, Vol. 19(9), pp. 217-226, 1997.
- 6.37 Kaschner K., Lepper P. A. and Goodson A. D.,  
Analysis of Cetacean sounds obtained from a hydrophone attached to  
a pelagic trawl,  
*11<sup>th</sup> Annual Conference of the European Cetacean Society, Stralsund,*  
*Germany, in European Research on Cetaceans – 11,*  
Edited by Evans P, Parson E and Clark S,  
published: Kiel University, pp. 26-29, 1997.
-

## CHAPTER SEVEN

# FREE-FIELD EXPERIMENT WITH A CYLINDRICAL TARGET

### 7.1 Introduction

The use of acoustic systems for the detection of sediment-embedded objects has received considerable interest <sup>[7.1, 7.2, 7.3]</sup> in recent years due to the use of acoustics as a viable means of underwater imaging. The acoustic location and monitoring of a range of objects is under consideration from cargoes such as shipping containers, oil drums, military ordnance, sub-seabed pipelines and cables, either deliberately placed or accidentally lost. Acoustic systems for use in the detection and classification of these objects, either fully or partially buried in underwater sediments, have applications in environmental monitoring, oil exploration, telecommunications, industry and the military.

The parametric sonar system offers a number of advantages over a conventional sonar system for the detection and classification of sediment embedded objects. Search-type sonar would require a narrow beam for good seabed delineation, i.e. relatively small seabed insonification area and a low frequency (1-10 kHz) operation, providing better seabed penetration. Lower directivity systems provide back-scattered information from the seabed over a larger area, making it difficult to detect the relatively small acoustic signature of the object being looked for. Similarly, as with the water column, lower frequency signal levels are less attenuated by sediment, allowing better penetration and higher target echo strengths and therefore deeper buried detection ranges within the sediment. This combined with the relatively small size of the transducer array has led to considerable interest in the use of parametric systems for buried object detection [6.4].

Results presented here cover the work carried out as part of the MAST III DEO (Detection of Embedded Objects) project. This involved two parallel sets of

experiments carried out with two parametric sonar systems, the 40 kHz TOPAS (TOpographic PARametric Sonar) system <sup>[7.4]</sup> and the 75 kHz LU parametric system. The primary target type of interest was a thin walled elastic cylindrical shell with flat end-caps. Experiments <sup>[7.5, 7.6]</sup> with the TOPAS system were conducted at La Spezia in Northern Italy by SACLANTCEN<sup>\*1</sup>. These included the free-field measurement of target scattered data for a cylindrical target at various aspect angles and a buried target at a range of seabed incidence and aspect angles. The Loughborough research group and TNO-FEL<sup>\*2</sup> of the Netherlands carried out similar set of experiments on Loch Duich, Scotland <sup>[7.7, 7.8]</sup>. Other activities undertaken as part of the DEO project were the modelling of back-scattering from cylindrical target <sup>[7.9]</sup> and the seabed <sup>[7.10]</sup> by Thomson Marconi Sonar (TMS)<sup>\*3</sup>, in France. This was complemented the development of detection and classification techniques <sup>[7.11, 7.12]</sup> by DIBE<sup>\*4</sup> at the University of Genova and Alenia Difesa<sup>\*5</sup> both in Italy.

The work covered in this thesis includes a description of the free-field DEO experiment carried out on Loch Duich in 1997 in this chapter and a description of seabed-embedded target trail held on Loch Duich in 1998 in Chapter 8. Both chapters include some provisional analysis of the received target scattered data.

## 7.2 Free-field measurement

The free-field measurements of a target was conducted both in Italy and Scotland as a prelude to determining the target 'resonance' characteristics as an eventual aid to target classification whilst embedded in sediment. The complex nature of an acoustic wave interaction with a target in the free-field can lead to the generation of a variety of back-scattered echoes from a number of excitation and propagation modes. The nature, size and position of these in time of arrival can then be related to the target geometry, orientation, construction material, interior material (hollow

---

\*1 SACLANTCEN (SACLANT Undersea Research Center)

\*2 TNO-FEL (TNO -Physics and Electronic Laboratory)

\*3 TMS (Thomson Marconi Sonar )

\*4 DIBE (Dept Biophysical and Electronic Engineering, University of Genova)

\*5 ALENIA (ALENIA DIFESA Divisione Sistemi Navali)

or solid targets), etc. The establishment of a free-field acoustic 'signature' for a particular target could then be used in target classification. This signature is often expressed as a 'form function' and is a representation of the target back-scattered pressure versus frequency for a particular target <sup>[7.13]</sup>. This is obtained by dividing the Fourier transform of the echo by the Fourier transform of the direct signal. The separation of the nulls in this function can then be related to the geometry of the body and the various modes of scattering wave families.

In the use of high frequency systems the predominate effect in the echo structure is the specular return from the outer shell of the target. Lower frequency (1-20 kHz) insonification has been considered to enhancement of elastic scattering and diffraction from geometrical discontinuities (such as the cylinder body to end-cap interface). 'Resonance' scattering includes a variety of differing periodical returns from a target. These effects can be divided into a various families of wave excitation or propagation including classes of surface borne waves and multiple-internal reflections <sup>[7.14]</sup>. Surface borne waves can then be sub-divided into shell borne, outer fluid borne and inner fluid borne depending on the target type and filling. An understanding of these and a variety of other multi-mode resonances <sup>[7.15]</sup> can give an estimate of the geometrical and geophysical target properties (i.e. shell thickness, material and inner fluid). There has been considerable historical interest both experimentally and theoretically in the understanding of back-scattered echo structure for a variety of target types. The acoustic scattering from solid and air-filled simple shapes has been studied by numerous authors <sup>[7.16, 7.17, 7.18, 7.19 7.20, 7.21]</sup>, to name a few. This work has been further extended in recent years to include fluid-filled cases borne out by the respective work of the DEO partners and other research groups and development of a better understanding of near-field and far-field scattering effects from an variety of target types <sup>[7.22, 7.23]</sup>.

The first experiment to be conducted under the DEO project using the LU parametric array took place on Loch Duich, Scotland in May 1997. Target echo data for a thin-walled elastic shell target, Figure 7.1, was measured at various aspect angles by rotating the target in the water column whilst being insonified. Target echo data was monitored using a streamer hydrophone array held statically

and also by a number of single element hydrophones. Target echoes were considered for various signal types, including continuous wave (CW) secondary frequency signals in the range 2-12 kHz, chirp (LFM) signals over the same range and Ricker pulses.

Similar target types were used in Scotland and Italy but of differing sizes. The SACLANTCEN target was a 2 m long by 0.5 m diameter cylindrical shell constructed from galvanised steel with welded flat end-caps, with a wall thickness of 6 mm. The second target used in Scotland was designed to be a half-scale model, measuring 1 m long by 0.25 m diameter to allow easier handling during the experiment. The wall thickness was however maintained at 6 mm. A scaled wall thickness was considered to have insufficient strength of material to allow the target to be deployed when air filled, as the water pressure could distort the cylinder shape at greater depths, thereby altering the acoustic characteristics. In both sets of experiments similar frequencies were used giving a  $ka$  range of 1.1-6.3 and 2.1-12.6 for the Scottish and Italian experiments respectively. The dimensionless quantity  $ka$  is given as the product of the target radius ( $a$ ) and the wave number ( $k$ ) of the isonification signal, where  $k$  is equal to  $2\pi/\lambda$ . Both targets air-filled and water-filled were insonified, at a range of aspect angles and signal types.

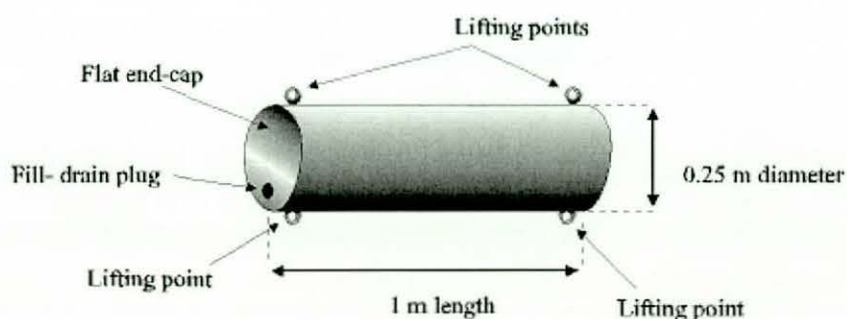


FIGURE 7.1 CYLINDRICAL TARGET LOCH DUICH EXPERIMENTS

### 7.3 Experimental deployment

The loch Duich trial site is a sea loch on the West Coast of Scotland that is operated by the Fisheries Research Services (FRS) Marine Laboratory, of the Scottish Office. The site includes a raft that is generally moored over water depths of between 40 and 100 m approximately 300 m to 1 km from shore and a shore-base providing power and fibre optical communication with the raft. A more detailed description of the trial site facilities is given in Chapter 4.

Figure 7.2 shows the trial site deployment. Two parallel *tramlines* were deployed from the FRS raft, extending 100 m with a 4 m spacing, using 8 mm steel wire. The *tramlines* were then used to moor a second *target raft* from which the target was suspended below a target control system. The transmitter was deployed from a triangular framed pan-and-tilt system lowered from the moon pool on the FRS raft. The parametric sonar system and target control computer were housed on a small enclosure this raft. The receiver hydrophone array was deployed vertically between the main raft and target, again using the *tramlines* as a guide. The streamer signals were taken back to the shore to the TNO-FEL shore base via a seabed cable. A fibre-optic link between the raft and shore provided a communication and transmitter-receiver synchronisation.

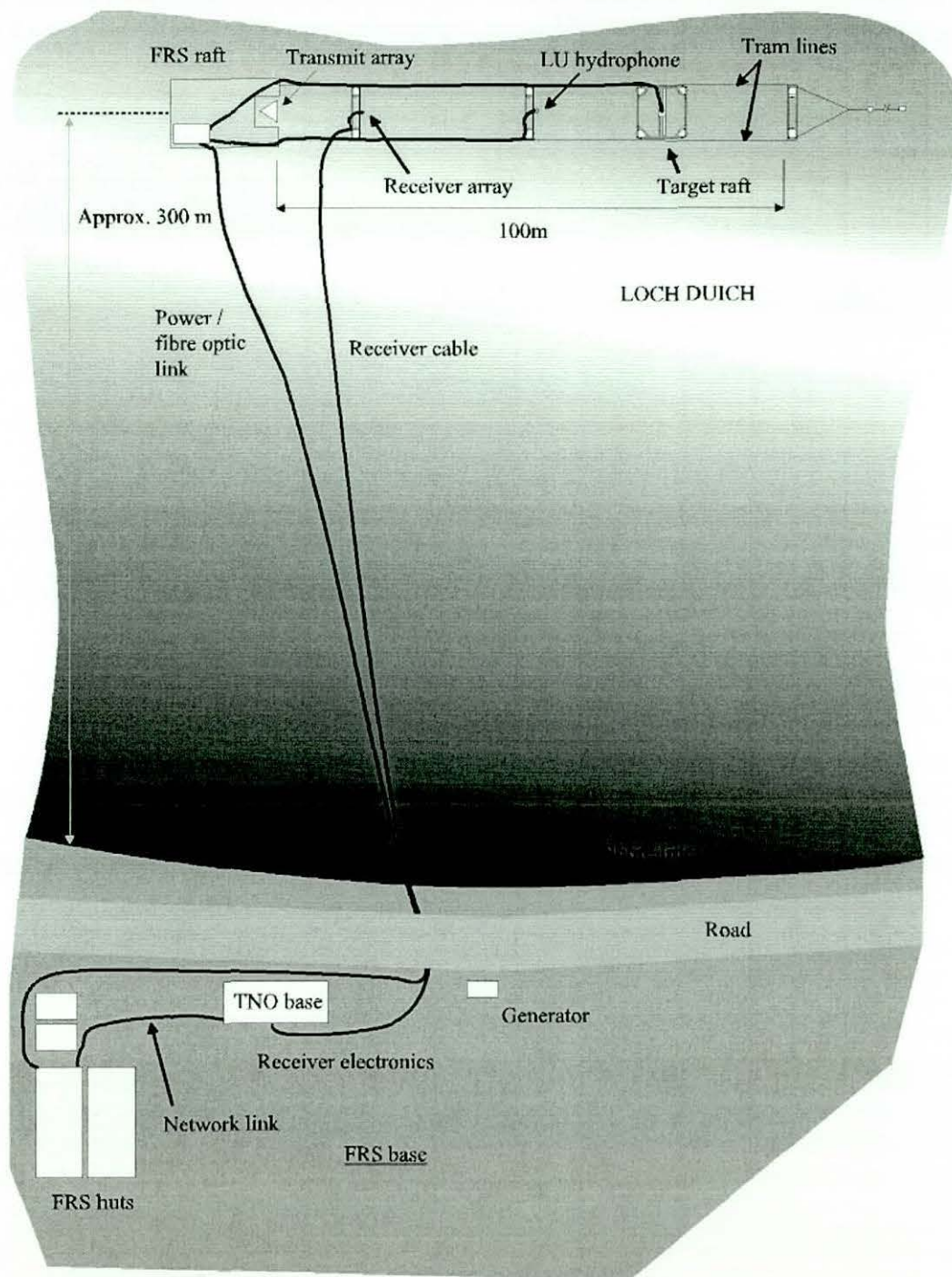


FIGURE 7.2 LOCH DUICH TRIAL SITE DEPLOYMENT, DEO EXPERIMENTS

Figure 7.3 shows the side view of the deployment. The transmitter and the target were all suspended from the surface at a depth of 16 m with the transmission axis deployed horizontally directed towards the target 66 m away. The receiver array and a ball hydrophone were placed between the transmit array and the target,

allowing the monitoring of both direct and target echo signals. The receiver array was deployed vertically with its acoustic centre at 16 m depth and approximately 15 m horizontally displaced from the centre of the target. The hydrophone was placed between the streamer and the target approximately 5.5 m from the target.

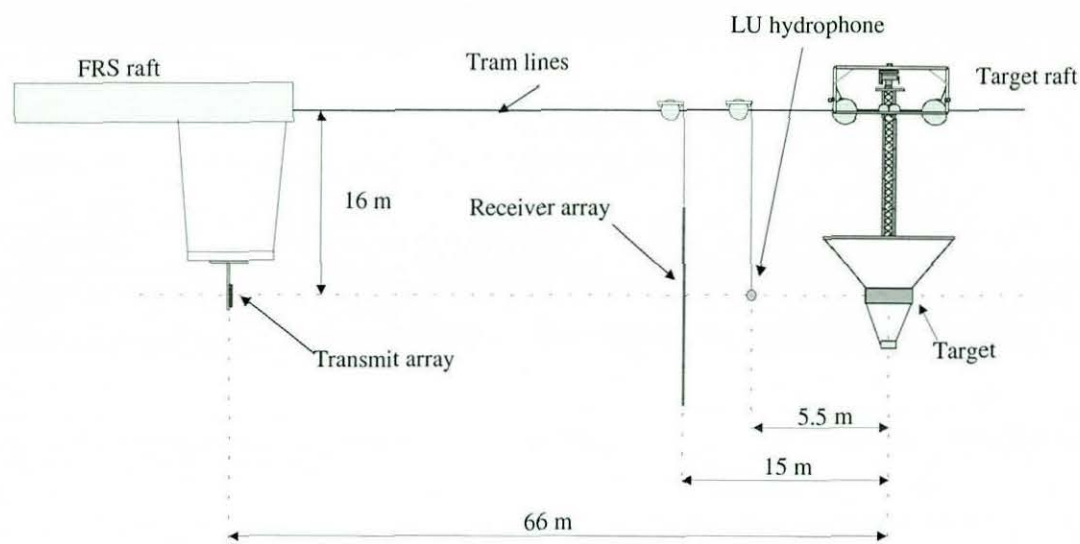


FIGURE 7.3 FREE-FIELD EXPERIMENT DEPLOYMENT

Control of the pan-and-tilt system is possible from a small enclosure on the FRS raft or remotely from the FRS shore base. The motor control computer controlling the target aspect angle relative to the transmit array was also housed in the enclosure on the main raft.

## 7.4 Free field measurement equipment

### 7.4.1 Parametric source

The LU parametric array, was deployed with its transmission axis parallel to the surface, at a depth of 16 m, to minimise the effects of cavitation when operating the transmitters at full power. The pan-and-tilt system was suspended from the using three wires, to prevent the transmitter rotating relative to the FRS raft. Some movement was however expected, resulting in transmitter–target misalignment due to surface and tidal conditions during the experiment. Alignment tests were



therefore made at the beginning of each test sequence to minimise the effects of these conditions. The transmitter was operated from a small enclosure on the FRS raft. At 66 m range a 3° beam will give an approximate footprint diameter of approximately 3.5 m in the region of the target.

#### **7.4.2 Receiver systems**

Two receivers were used, a multi-element streamer array operated by TNO-FEL and a single element hydrophone operated by LU. The LU hydrophone was placed close to the target and was used for alignment of the transmitter and the target. Both direct signal and target echoes were monitored. Adjustments were made in the beam alignment, in elevation using the pan-and-tilt mechanical adjustment and the transmit array phase-steered beam in azimuth. A HS150 12 mm ball hydrophone was chosen because of its good receiver sensitivity at the primary frequencies (-202 dB re 1V/ $\mu$ Pa). Signals were taken directly from the hydrophone, via a co-axial cable, back to the FRS raft. Primary frequencies were observed on an oscilloscope and sampled by the PC-based capture system at a 250 kHz sampling rate, bandwidth limited to 100 kHz. The secondary frequency components were also observed after filtering with various passive and active filters.

The TNO receiver array was a 20-element linear streamer with hydrophone spacings of 0.5 m giving an effective acoustic aperture of 9.5 m. The streamer was an oil-filled PVC hose, 15 m long, 60 mm diameter. Hydrophone elements were low-pass filter limited to 10 kHz via pre-amplifiers and anti-aliasing filters. Each hydrophone element was type Benthos AQ4 with a receiver sensitivity -172 dB re 1V/ $\mu$ Pa ( $\pm 1.5$  dB) before gain. A total cable length of around 500 m was used to bring the acoustic signal to the shore. Temperature and pressure sensors were also included towards the front of the streamer. An additional module, including a 2-pitch sensor and a compass (Fluxgate, KVH Industries) was also used. Data from the hydrophones and the pressure and temperature sensors were integrated into a single 41-core copper conductor cable. The cable has a PVC-coated stainless steel outer jacket, with a 6.3 mm diameter central stress member, making it suitable for

towing. Connection was then made to a 32-channel submersible data acquisition unit (POD) where signals are digitised before recording. The 20 hydrophone channels were simultaneously sampled at 50 kHz. The additional 12 channels used for the other sensors, sampled at 120 kHz. A 60 m fibre-optic cable was then used for the final connection to the shore-based interface. Copper conductor lines are also included for power for the POD module and the streamer sensors. The fibre-optic interface was then used to reconstruct the analogue waveforms before recording.

All data samples were then recorded simultaneously using a 32-channel AMPEX DCRSi digital recorder, with a maximum input data rate of 13.375 Mbytes/sec allowing 1 hours recording. Both acoustic channels (50 kHz sampling) and non-acoustic channels (120 kHz sampling) were sampled to a 12-bit resolution. A control PC equipped with an I/O card (AT-DIO32F from National Instruments) was used to monitor input data during recording on the DCRSi and analysis of replay data from the recorder.

### **7.4.3 Target control system**

Figure 7.4 shows the target deployment raft. The target was suspended by two steel rope strops, from a 2.75 m bar rigidly fixed to an independently floating vertical trussing section. This was connected to a stepper motor via a universal joint. The target raft was then attached to the tramlines as shown in Figure 7.2, allowing the whole construction to be moved relatively easily between them.

The length of the suspension cables was kept as short as possible to minimise skewing of the target relative to the stepper motor, whilst allowing the suspension bar to be outside the main beam of the transmit array. A counter-weight below the target was similarly placed outside the main beam to minimise unwanted reflections. Thin steel rope ( $>2$  mm) was used above and below the target, to minimise acoustic reflections from the suspension cables. These wires also provided a degree of mechanical de-coupling for the target from surface movement.

Insonification of the target was carried out both air-filled and water-filled. The total weight in air was 40.56 kg. With a total external volume of 0.05 m<sup>3</sup> the target experienced an up-thrust in salt water (density 1030 kgm<sup>-3</sup>) of the equivalent of 51.5 kg. A counter-weight of 10.94 kg was therefore required to make the target neutrally buoyant. No counter weight was used during the water filled case.

A target control system was developed and integrated into the main LU transmitter data-capture system on the FRS raft. Target aspect angles in the horizontal plane (azimuth) were varied using a computer-controlled stepper motor rotating through 360° to a 0.1° resolution. An end-stop sensor was included for target repositioning to a 0° position, which corresponded to approximately to the broadside aspect of the target. A full 360° rotation was possible in approximately 30 minutes.

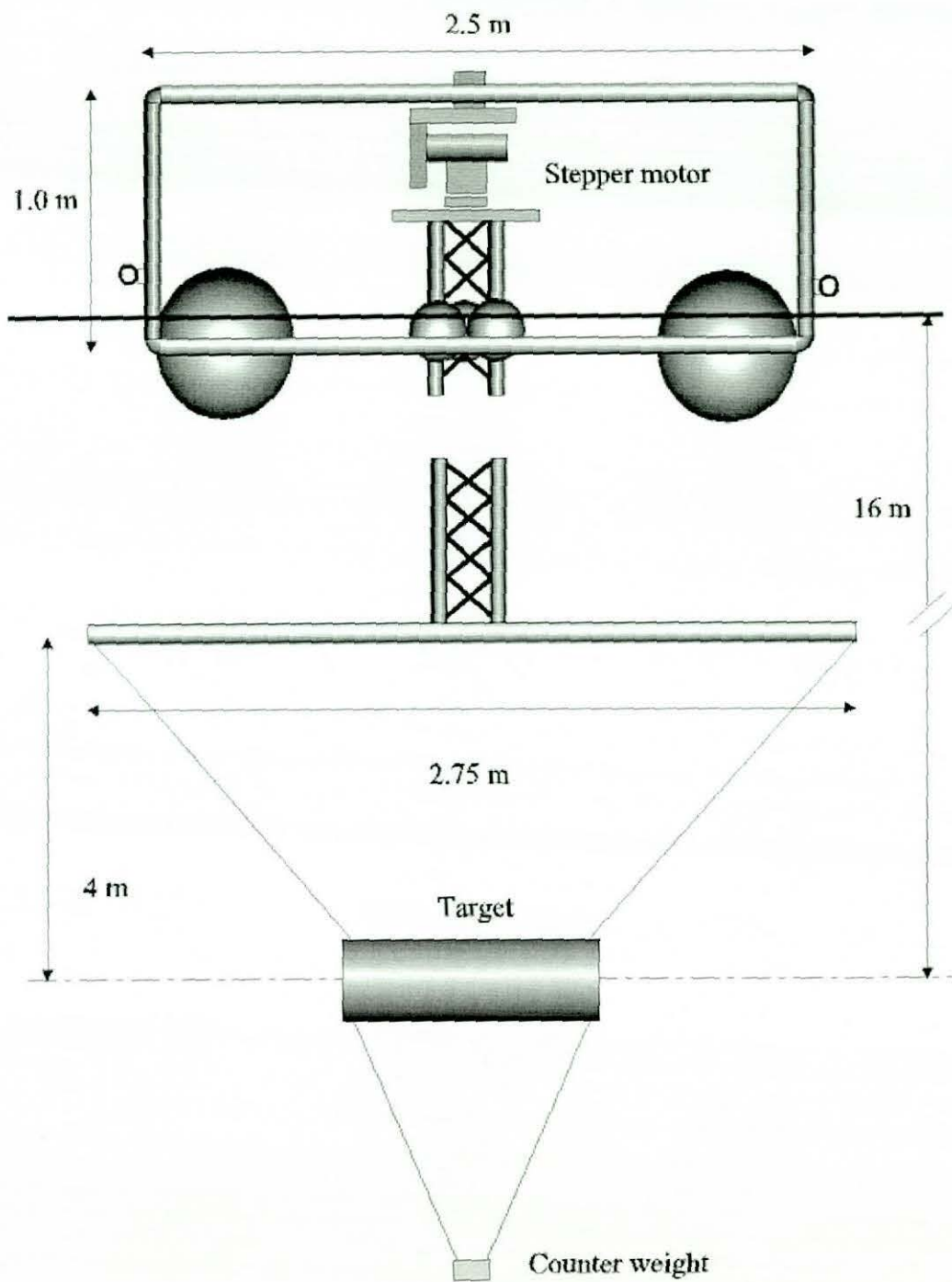


FIGURE 7.4 TARGET RAFT – FREE FIELD EXPERIMENT

#### 7.4.4 System integration

Figure 7.5 shows a system diagram for the complete transmitter – receiver system. All timing was synchronised using GPS a time code, which was recorded on a separate channel of the DCRSi recorder. Similarly, serial data from a Garmin x12 GPS system was read into the main transmitter system. Timing information from this was then used to update the system time used for logging purposes.

A separate computer was used to control the target position, allowing uniform movement of the target stepper motor. Control of the target motion from the sonar system computer would have resulted in interruptions in motion as other processes took place (loading of transmit signals, data capture etc.) Normal operation involved the uniform motion of the target through a range of angles with regular insonification of the target. The sonar computer would then request the current position of the target from the target control system. A 12-bit communication protocol, using the parallel ports on both machines, was developed to allow communication of the current target position to a sufficiently high resolution (i.e. 3600 levels equivalent to  $0.1^\circ$  resolution over  $360^\circ$ ). Additional parallel port bits on the target control computer were used to control the stepper motor and monitor the end stop sensor.

All transmission parameters, including target position, were logged locally on hard disk in the transmitter system. Data for each transmission was also sent to the receiver base, via a local area network set up across the FRS fibre-optic link. Transmit parameters were written to a mapped network hard drive, on the main control system. The hard drive was physically located in the parameter display computer in the TNO shore-base. Local software was then used to read the file and display transmission parameters, including target position, providing *real-time* updates of current transmission parameters.

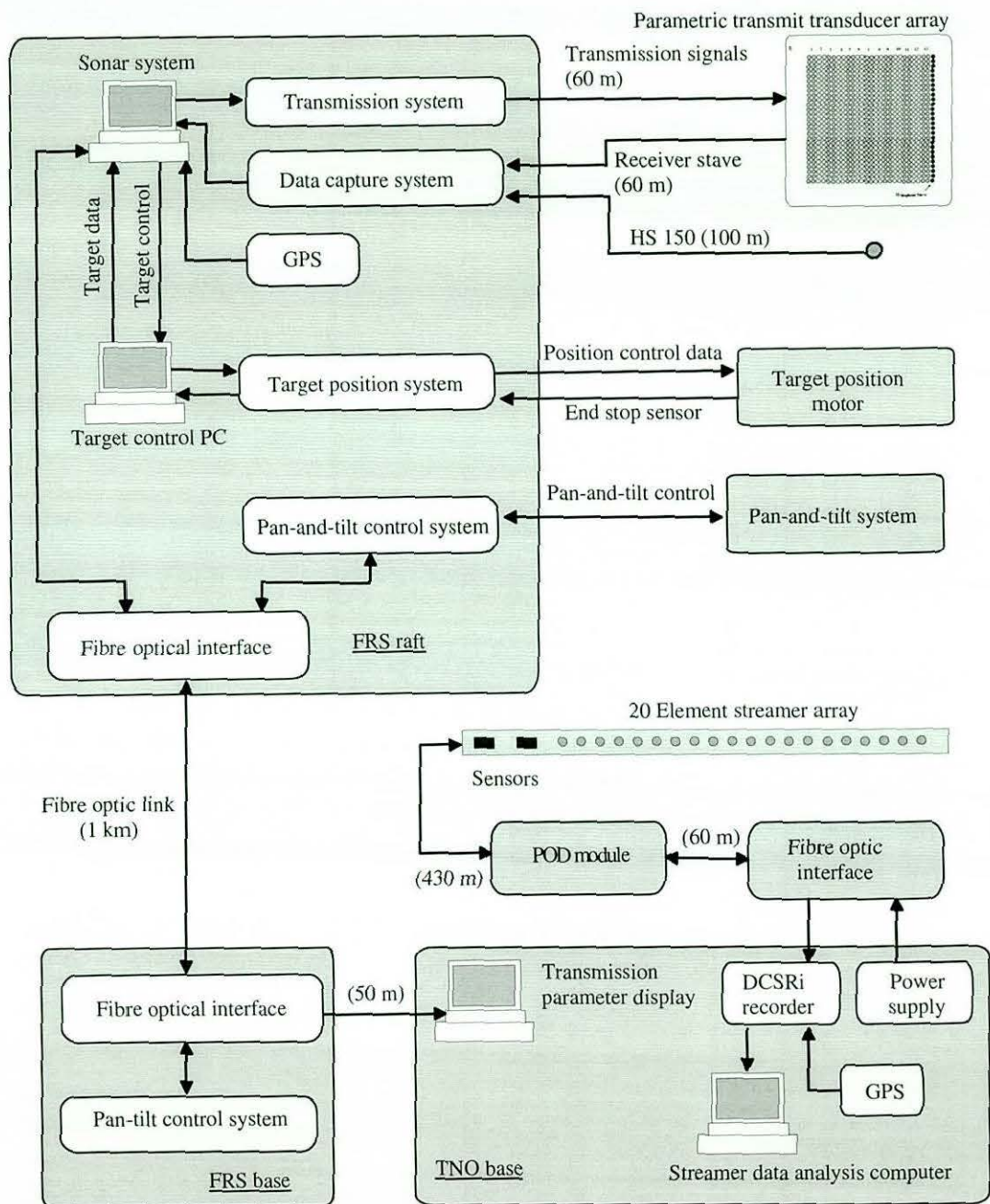


FIGURE 7.5 FREE FIELD EXPERIMENT SYSTEM DIAGRAM

## **7.5 Experimental procedure (free-field measurements)**

### **7.5.1 Equipment deployment / system testing**

The experimental deployment took place between the 2<sup>nd</sup> and the 5<sup>th</sup> of May 1997 at the Loch Duich site. The receiver cable was deployed first, taken from the beach to the FRS raft along the seabed. Care was taken with the receiver POD module due to the possibility of the electronics overheating. The module is usually cooled by towing it behind a ship, but use in a static situation above the water-line required additional cooling. This was done by construction of a small pool fed from a stream close to the FRS base. The tramlines and moorings were then put into place.

The target raft was constructed on the beach and floated out to the FRS raft. Once in place the air-filled target was deployed, at a depth of 16 m, and the target raft floated into position between the tramlines. Attachments were then made to the tramlines to secure the target relative to the main raft. The hydrophone receiver was floated out from the beach to the main raft and attached to the receiver cable before floating it into position between the tramlines. Initial deployment was with the array suspended vertically, with the centre of the acoustic aperture at 16 m depth. An additional single-element hydrophone was deployed between the target and receiver array. The transmitter array was finally deployed directly below the FRS raft on the pan-and-tilt system. Finally, the transmitter and receiver electronic systems were set up and tested on the FRS raft and the TNO shore base.

Initial system checks of the transmitter and receiver systems were then carried out. Various test signals was monitored on the TNO receiver array, transmitted from a 10 cm diameter ring transducer deployed close to the main raft. The transmit array system was then tested at low power and then at full power. All electronic logging and communication systems were also tested.

### 7.5.2 Target measurements

Initial acoustic testing was carried out with the target in a static position. Alignment tests were carried out using the single element hydrophone. The transmit array elevation and azimuth angles were adjusted for alignment, with the hydrophone placed close to the target. Several target rotations were carried out allowing the monitoring of transmitter-target alignment for both end-cap and broadside aspects.

Test sequences were then recorded using non-linear (NLA) CW signals in the range 2-10 kHz at 1 kHz steps, LFM chirp signals in the range 2-10 kHz and NLA Ricker <sup>[7.24]</sup> signals at 5, 7 and 10 kHz, for both the end-cap and broadside static positions. Direct and target echoes were monitored on the TNO streamer array and the single element hydrophone.

Target rotation tests were then carried out with the air-filled target rotating slowly through a range of angles in excess of  $220^\circ$ , including at least two broadside positions and one end-cap position. A single signal type was used for an entire rotational sequence. Continuous recordings were made from the streamer array on the DCRSi recorder. Sampled recordings were made using the LU data capture system with the single element hydrophone. Sequences were recorded using Ricker pulses, 2-10 kHz chirp signals and NLA CW at 10 kHz.

The target was then flooded with water and the static tests were repeated with a NLA Ricker signal, NLA CW signals at 1-10 kHz in 1 kHz steps and 2-10 kHz chirp signals for both end-cap ( $107.5^\circ$ ) and broadside ( $197.4^\circ$ ) positions. Finally, target rotation sequences were then carried out for Ricker signals and 2-10 kHz chirp signals.

### 7.5.3 Bottom scattering measurements

Bottom scattering measurements were carried out to provide some insight into problems that might be encountered in the second stage experiment, involving a



seabed-embedded object, scheduled for summer 1998. To achieve this, the streamer array was re-deployed horizontally at the same depth as the transmitter, as shown in Figure 7.6, with the centre of the acoustic aperture 55 m horizontally from the transmit transducer array. The transmit array was re-aligned at an oblique incident angle to allow interception of a bottom-scattered signals on the receiver array. Stainless steel wires were used to suspend the triangular section frame supporting the receiver array, which was held into place between the tramlines. The streamer array was then suspended 0.5 m below this using rubber strapping, shown in Figure 7.7, to a total depth of 16 m. The frame itself was a plastic coated lightweight steel construction. Signal types including a 5 kHz Ricker, 2-10 kHz chirp and 5 kHz CW signals were used. The final test involved the adjustment of the transmitter elevation angle to access different seabed incident angles centred around  $37^\circ$ . A  $10^\circ$  variation was the maximum achievable, whilst still obtaining good reception of the bottom-scattered signals by the receiver array.

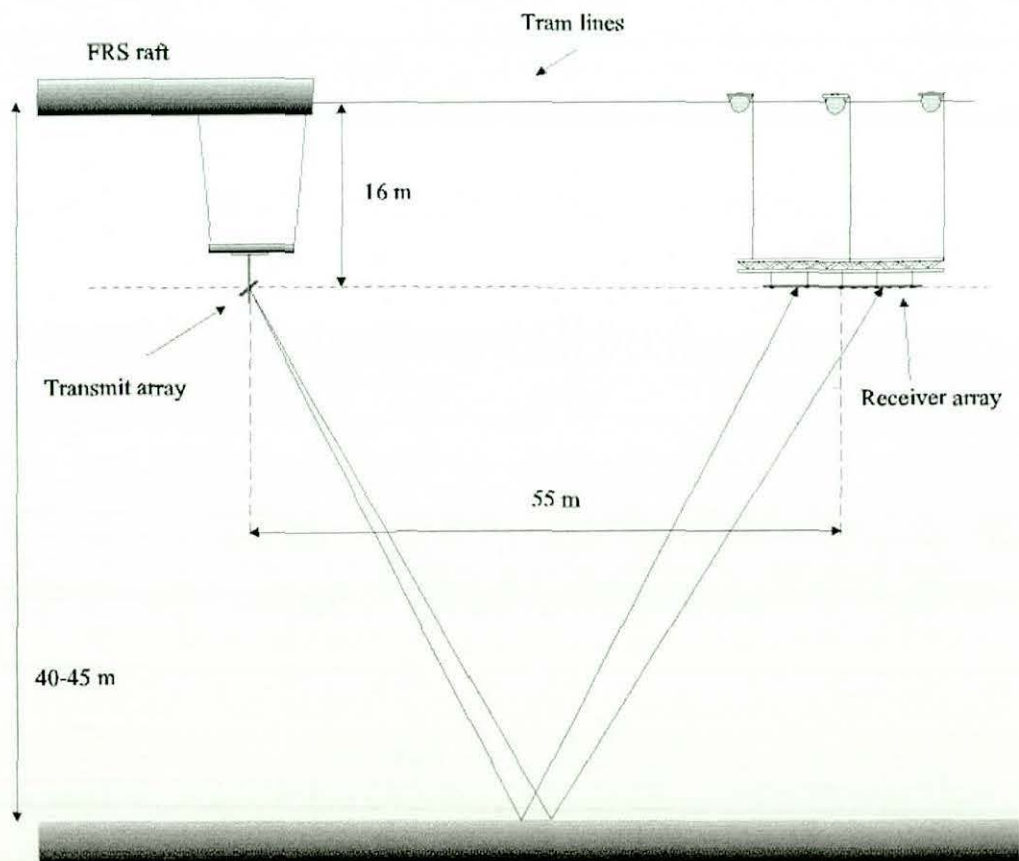


FIGURE 7.6 SIDE VIEW, EQUIPMENT DEPLOYMENT, BOTTOM-SCATTERING MEASUREMENT

Additional measurements, including CTD depth profile were carried out during the course of the trial, deployed from the FRS raft. Background noise measurements were also made on all recording systems. No acoustic data from the single hydrophone was available during the bottom scattering measurements.



FIGURE 7.7 STREAMER ARRAY, HORIZONTAL DEPLOYMENT FOR BOTTOM-SCATTERING MEASUREMENTS

## 7.6 Results (free-field measurements)

### 7.6.1 Introduction

The objective of the trial was the measurement of the free-field response of the target to various signal types and different aspect angles in the horizontal plane. Additional aims were the assessment of the performance of the various systems used in this trial and to be used in the succeeding (target embedded) trial.

On the whole these system operated well and a data set of reasonable quality was collected. Problems were, however, experienced with the hydrophone streamer array. Limited filtering on the hydrophone pre-amplifiers allowed the high

frequency primary component of the NLA signals to distort the desired lower frequency secondary signal. The time constant of the distortion was sufficiently long, such that a distortion caused by the direct signal was still present on the arrival of a target echo. Secondary frequency data could be obtainable by post-processing and removal of the distortion in the form of a large DC offset. Post-analysis of the data obtained led to a redesign of the hydrophone pre-amplifiers for the next trial.

Predictions of problems in geometric alignment due to environmental conditions, drifting of the floating platforms due to windage, changes in water depth and currents due to the tide, were overcome in the main by regular realignment. The tramlines for holding the floating platforms in relative positions and the target aspect angle control system seemed to perform well, showing good repeatability of target aspect angle and alignment with other systems.

Acoustic data from the single hydrophone recorded to a 100 kHz bandwidth was of a reasonable quality, showing both primary and secondary frequency components with a good signal-to-noise ratio, without distortion. Results presented in the following sections are derived from this data set.

### **7.6.2 Ricker signal analysis**

Short duration Ricker type pulses are used predominately in the development of techniques for detecting resonance in elastic walled targets. The Ricker signal provides a broadband impulsive signal of distinctive one and a half cycles, at the lower secondary frequencies, from a single higher frequency carrier. The pulse was generated from a single carrier (75 kHz) with a Gaussian-type envelope. This was achieved by applying a raised cosine function, equation (7.1), to define the envelope of the carrier signal. The pulse length is given as 1.5 times the time period of a single wavelength of the frequency at the centre of the desired frequency response.

$$f(t) = \frac{\left[ 1 - \cos\left(\frac{2\pi t}{T_{pl}}\right) \right]}{2} \quad (7.1)$$

where  $f(t)$  is a function of time ( $t$ ) and  $T_{pl}$  is the duration of the pulse. Figure 7.8 show the computed signal for Ricker pulse generation. In this case a 10 kHz carrier is used for ease of viewing. The amplitude of the pulse is then modulated by the function described in (7.1).

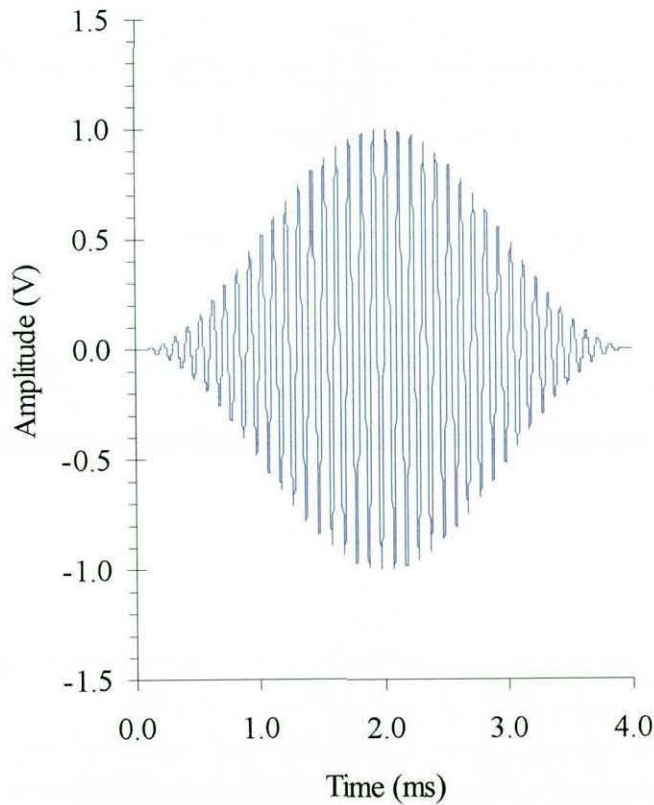


FIGURE 7.8 RICKER GENERATION SIGNAL, 10 kHz CARRIER, 4 ms PULSE LENGTH

The Ricker signal was considered useful in the free-field excitation of the elastic cylinder. This signal type was previously unused, so an initial assessment and calibration was made. Figure 7.9 shows the primary and secondary (low pass filtered) response for a 4, 7 and 10 kHz Ricker signals recorded in the water. Figure 7.9(a,c,e) show the broad band response (2-100 kHz bandwidth) of the direct signal, including the high frequency carrier used to generate the Ricker signal.

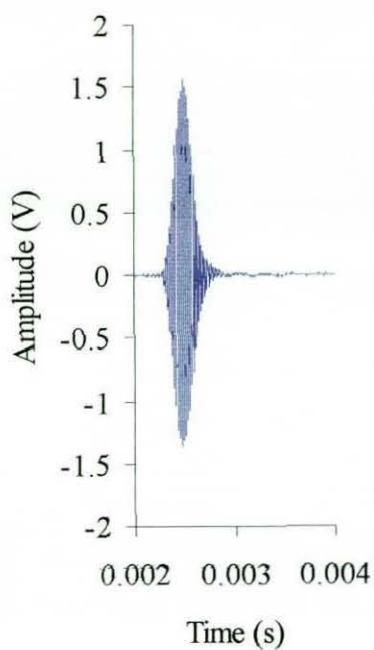


FIGURE 7.9(a) PRIMARY FREQUENCY SIGNAL, 4 kHz RICKER GENERATION

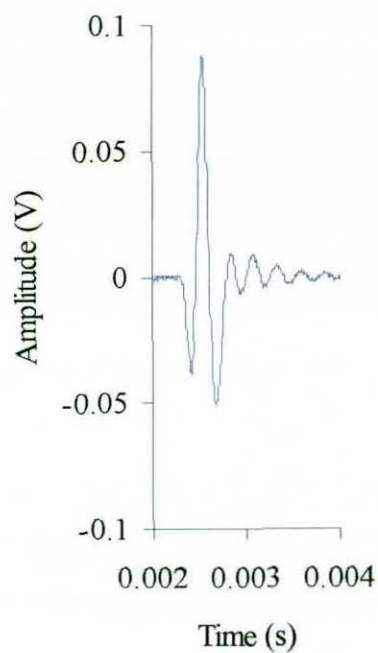


FIGURE 7.9(b) SECONDARY FREQUENCY SIGNAL, 4 kHz RICKER GENERATION

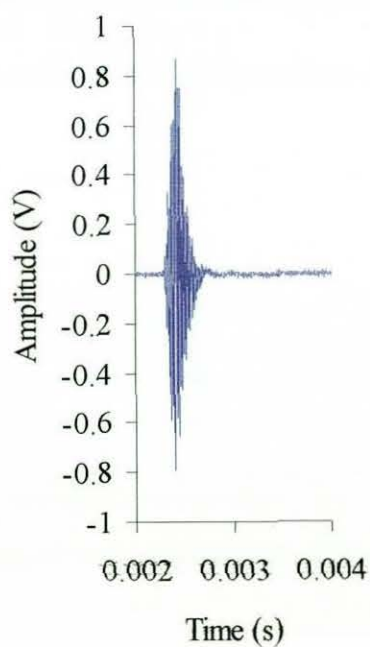


FIGURE 7.9(c) PRIMARY FREQUENCY SIGNAL, 7 kHz NLA RICKER GENERATION

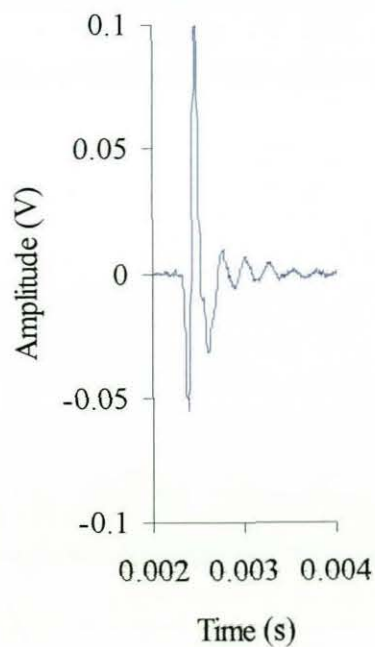


FIGURE 7.9(d) SECONDARY FREQUENCY SIGNAL, 7 kHz RICKER GENERATION

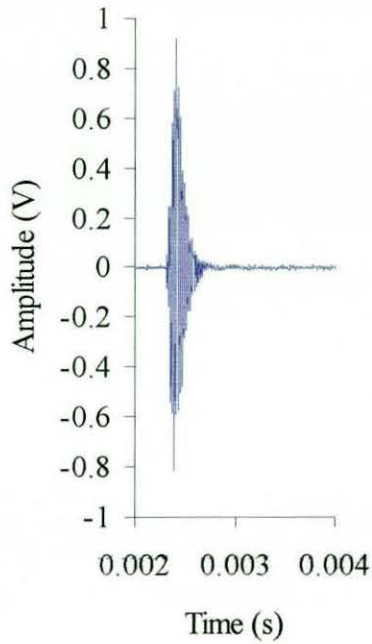


FIGURE 7.9(e) PRIMARY FREQUENCY SIGNAL, 10 kHz NLA RICKER GENERATION

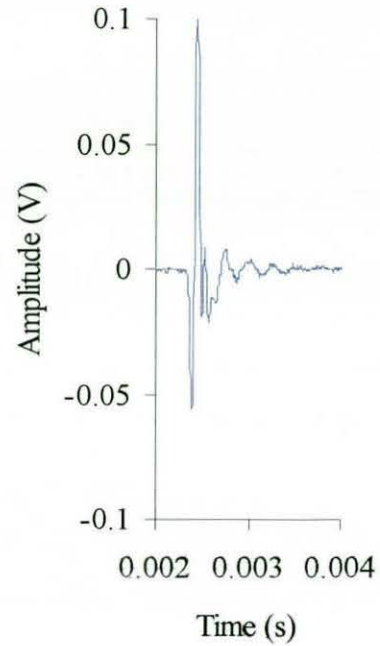


FIGURE 7.9(f) SECONDARY FREQUENCY SIGNAL, 10 kHz RICKER GENERATION

Figure 7.9(a) shows the transmitted signal for the Ricker frequency generation, centred on 4 kHz. The signal is generated using a 75 kHz carrier, with a raised cosine envelope and a pulse length of 375  $\mu$ s. The transmitted signal shows a degree of asymmetry in the envelope shape, particularly at the end of the pulse. An elongation of the signal was observed most likely due to the transducer array elements *ringing* down.

The filtered responses, in Figure 7.9(b), show a typical Ricker type response. A low frequency component can also be seen in the tail of the signal. The source of this energy is not fully understood but may be a mechanical characteristic of the transducer ringing down from its primary frequency excitation. Similar effects are seen in the filtered responses of the 7 and 10 kHz signals.

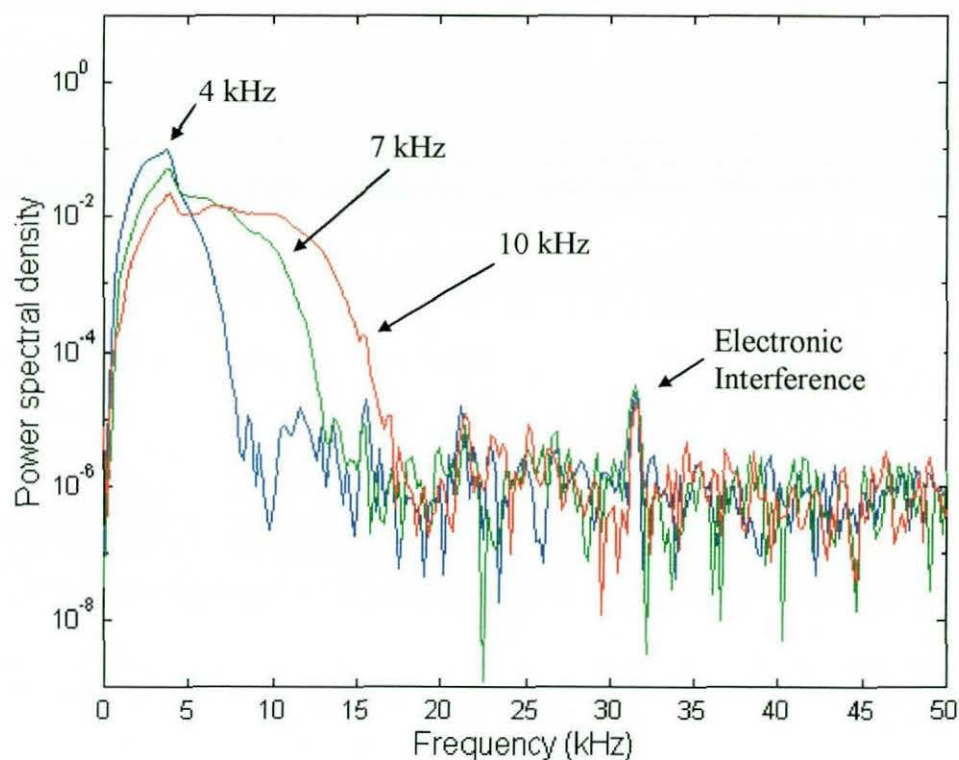


FIGURE 7.10 FFT ANALYSIS, SECONDARY FREQUENCY COMPONENT  
4, 7, 10 kHz RICKER SIGNALS

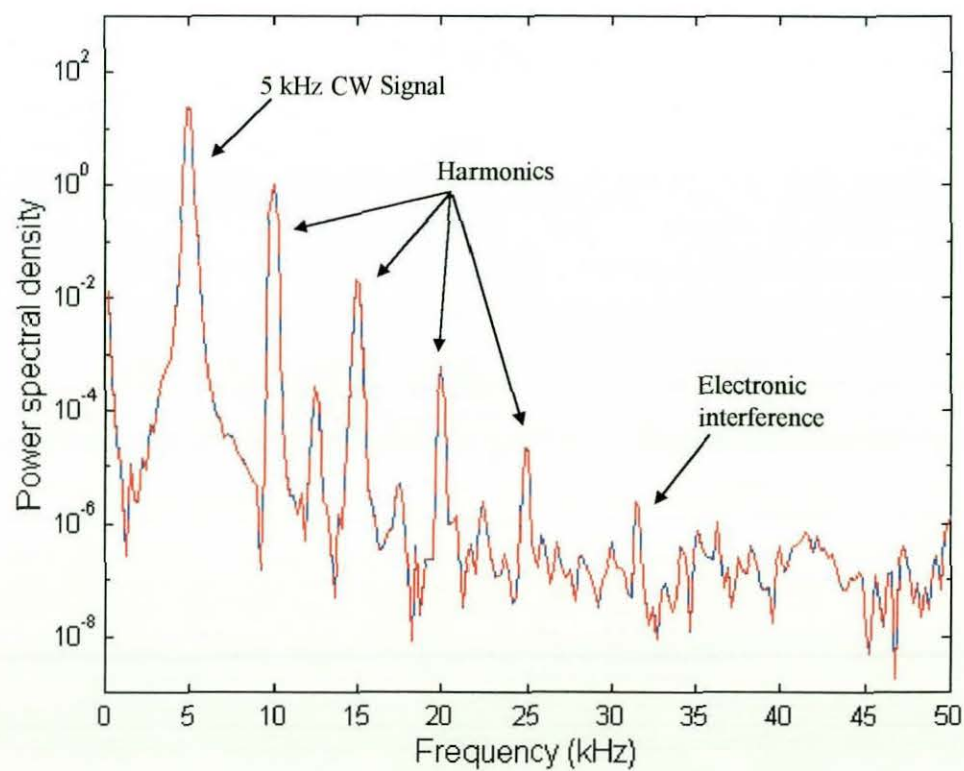


FIGURE 7.11 FFT ANALYSIS, 5 kHz CW NLA SIGNAL

A degree of distortion is also apparent in the second half of the signal at the higher frequencies. This effect was observed to worsen at higher carrier frequency source levels, similar to the effect observed when approaching saturation limits. The FFT analysis in Figure 7.10 shows the broadband response expected from the Ricker signal that is centred on the design frequency. Comparison can be made with the far narrower response observed with the FFT of a CW 5 kHz signal shown in Figure 7.11.

A considerable reduction in the peak signal level is also seen in the time domain with comparison with CW signal types. The shorter pulse lengths used in the Ricker generation signals do not fully allow the carrier frequency signal to reach its maximum signal level due to the transmit transducer *ringing* up. A longer pulse type has sufficient time for the transducer to fully respond before the end of the pulse is reached giving a higher primary frequency amplitude level.

Ricker source levels were calculated from the available data set. Peak signals were observed for 4, 7, and 10 kHz. Conventional source levels are estimated for CW signals using root mean square (rms) values. In the case of the Ricker signal this is misleading due to the Gaussian envelope extending theoretically from  $-\infty$  to  $+\infty$ . A *rule of thumb* valid for frequencies from 2-10 kHz was used, defining the mean level of the Ricker signal as the integral of the amplitude squared over a period  $\pm 0.25$  ms from the peak signal observed at time  $t_0$ , equation (7.2).

$$\text{Mean level} = \frac{1}{T_{pl}} \int_{t_0-0.25ms}^{t_0+0.25ms} V^2(t).dt \quad (7.2)$$

where V is the amplitude in volts. Table 7.1 shows the relative source levels for Ricker-type signals and equivalent frequency CW signals.



Frequency	Ricker source level	CW source level
4 kHz	176.4 dB re 1 $\mu$ Pa at 1m	189.8 dB re 1 $\mu$ Pa at 1m
7 kHz	176.6 dB re 1 $\mu$ Pa at 1m	194.9 dB re 1 $\mu$ Pa at 1m
10 kHz	174.4 dB re 1 $\mu$ Pa at 1m	196.3 dB re 1 $\mu$ Pa at 1m

TABLE 7.1 RICKER AND CW SIGNAL SOURCE LEVEL LU PARAMETRIC ARRAY

Unlike the CW estimates, a reduction in source level was observed at the higher frequencies, most likely due to the shorter pulse lengths required, in the 10 kHz case 150  $\mu$ s compared with a typical 4 ms long signal used when measuring a CW signal. The reduction in source level is, however, balanced against the broadband response, seen with the Ricker signal, in comparison with the sharper tonal response seen with a CW signal.

### 7.6.3 Free-field target echo analysis

Analysis of the single-element hydrophone data was carried out with the target in both an end-cap and the broadside position. The data set showed a reasonable signal-to-noise ratio, and lacked the distortion effects seen on the streamer array data. The hydrophone itself was, however, better suited to the higher primary frequencies, with a resonance in receiver sensitivity at around 80 kHz. Analysis of the lower frequency (1-20 kHz) characteristics of direct and target echoes was carried out in a limited number of cases, where data was available.

Figure 7.12 shows the direct and target echoes for a broadside position, water-filled target for a 4 kHz Ricker signal. Recordings were made broadband (1-100 kHz bandwidth). Surface and seabed multi-paths were observed at the hydrophone, approximately 5 ms and 13 ms after the direct signal respectively. The delay of 13 ms in the 1<sup>st</sup> seabed path corresponded to a water depth of 43 m. Measurement of the direct and first target echo times gave a horizontal range, from source to target of 66 m.

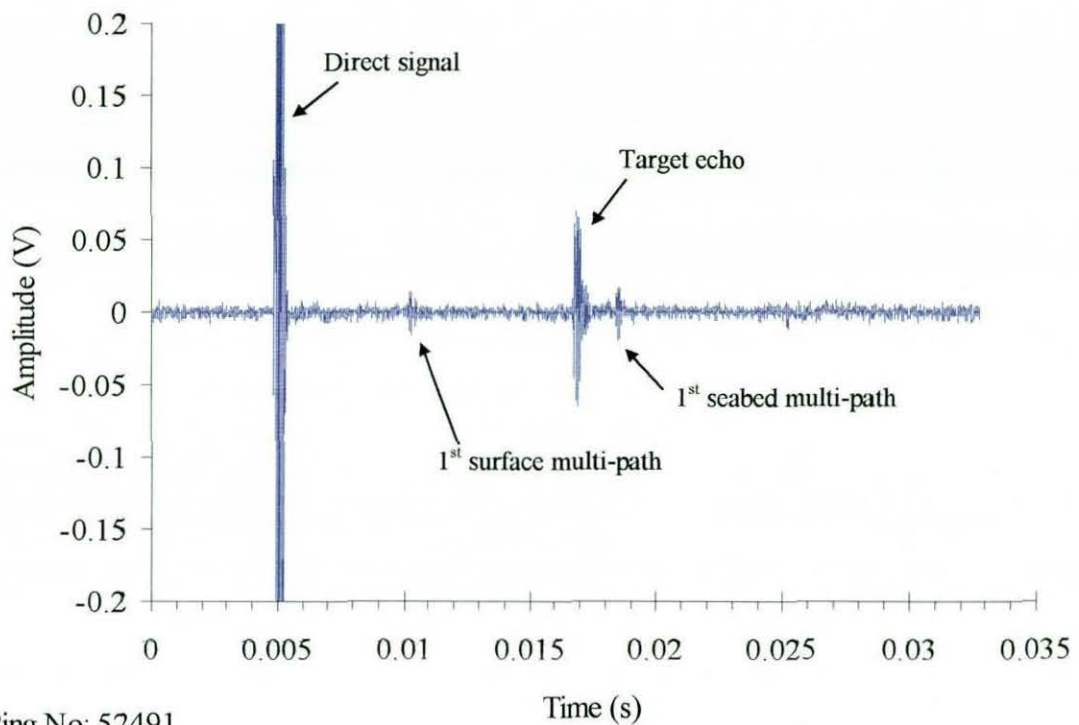


FIGURE 7.12 DIRECT AND TARGET ECHOES, WATER-FILLED TARGET, BROADSIDE POSITION

The active-sonar equation can be written in the form.

$$EL = SL - 2TL + TS \quad (7.3)$$

where EL is the echo level, SL is the source level, TL is the one-way transmission loss and TS is the target strength.

Figure 7.12 shows the vertical scale expanded to enhance the target echo but giving the direct signal the appearance of being clipped. Analysis of the raw data set shows no distortions, and direct comparison of the direct and target echoes is possible. Because both the direct and target echoes are available, target strength (TS) was estimated by comparison of the direct and target echo signal levels, with consideration of the additional transmission losses experienced by the target echo.

$$TS = RR + TL \quad (7.4)$$

where RR is defined as the received ratio between the direct and target echo signals, given by

$$RR = 10 \log_{10} \left( \frac{I_T}{I_D} \right) \quad (7.5)$$

where  $I_T$  and  $I_D$  are the direct and target scattered signal intensities received at the hydrophone. Figure 7.12 gives RR as the receiver ratio, for the direct and target echo signal levels, of -24.75 dB. Both direct and target echo signals are within the far-field of the parametric source. Transmission losses for the signal travelling from the hydrophone to the target are therefore taken as the difference in spherical spreading for two points in space, i.e.  $r_1$  is the source to hydrophone distance, and  $r_2$  is the source to target distance (see Figure 7.3). The hydrophone to target transmission loss  $TL_1$  is therefore given by;

$$TL_1 = 20 \log_{10}(r_2) - 20 \log_{10}(r_1) \quad (7.6)$$

With the target to source distance of 66 m and source to hydrophone distance of 11.2 m,  $TL_1$  is estimated as around 1.6 dB. The hydrophone itself is close to the Rayleigh distance from equation (3.6) at 75 kHz of 12.5 m. This is estimated as 1.17 m at 7 kHz. Due to the shape of the target the near-field / far-field distance estimate of the shorter dimension of the target in the broadside position (25 cm) gives a near-field of 3.125 m. It therefore seems likely that some degree of cylindrical spreading is possible on the target scattered signal. At the lower frequencies the hydrophone is in the far-field and spherical spreading is assumed in the calculation of transmission loss. Losses due to absorption were considered negligible at these frequencies and distances. At the higher frequencies the target to receiver transmission loss,  $TL_2$ , is assumed cylindrical, giving a  $TL_2$  loss of 10.5 dB. The total transmission loss  $TL = TL_1 + TL_2$  is around 12.1 dB. From equation (7.4), the 75 kHz broadside target strength is estimated as -12.6 dB. This can be compared with the target strength for a smooth convex surface of -23 dB given by expression (7.7).

$$TS = 10 \log \left( \frac{s}{16\pi} \right) \quad (7.7)$$

where  $s$  is the total insonified surface area and all dimensions are large compared to the wavelength  $\lambda$  [7.25].

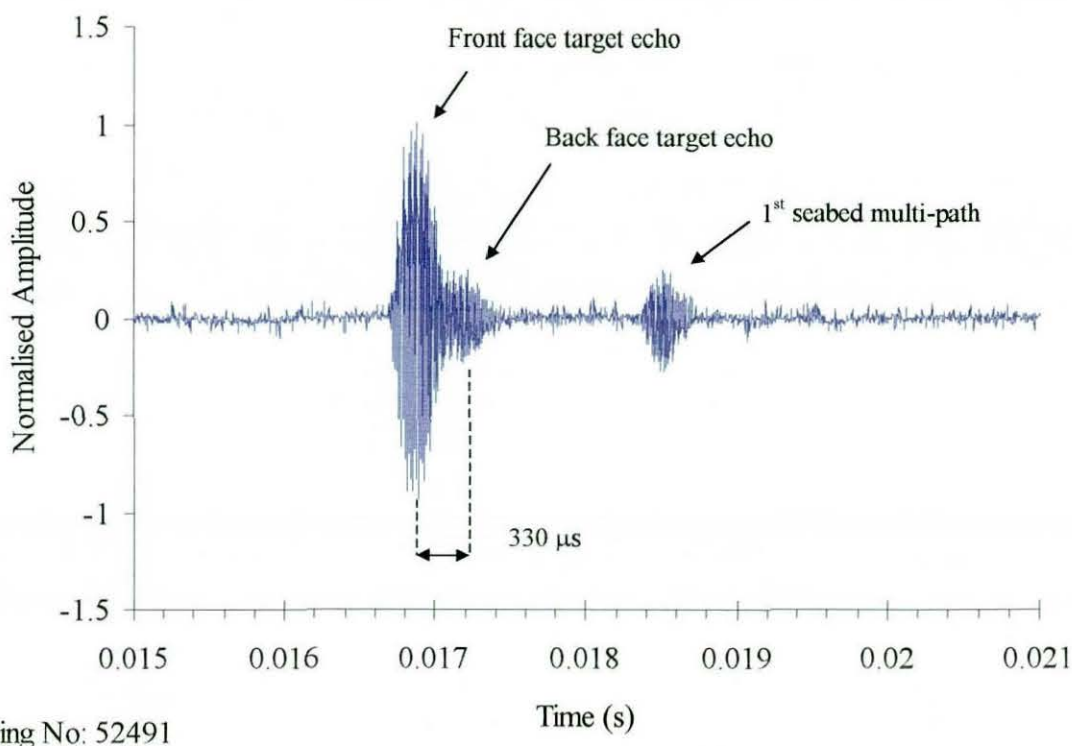


FIGURE 7.13 BROADSIDE POSITION, TARGET ECHO, WATER-FILLED CYLINDER

Closer analysis of the target echo at the higher frequencies shows an additional echo possibly from the back of the cylinder, Figure 7.13. The inter-pulse period of  $330 \mu\text{s}$  gave a one-way path propagation distance of 49.5 cm, corresponding closely to twice the cylinder diameter of 25 cm suggesting specular reflections from both the front and back face. Figure 7.14 shows the broadband frequency response of the 75 kHz carrier of the Ricker signals seen in Figure 7.13. The apparent pulse broadening of the target echo in comparison with the 1<sup>st</sup> seabed path is possibly due to the merging of the front and back face echoes.

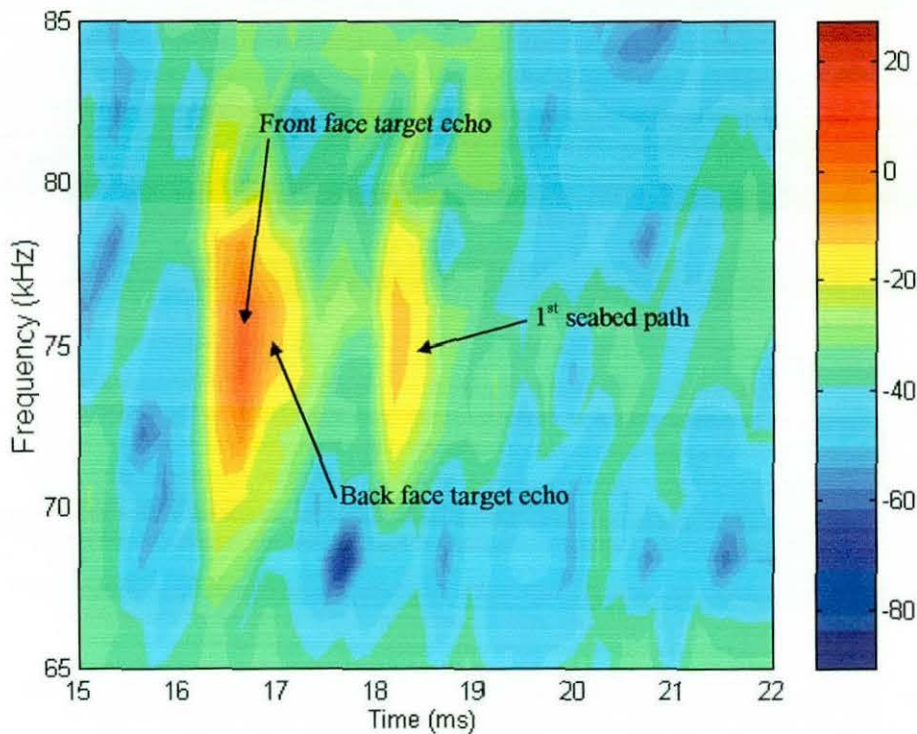


FIGURE 7.14 HIGH FREQUENCY RESPONSE, BROADSIDE TARGET ECHO, WATER-FILLED CYLINDER

Figure 7.15 shows the secondary frequency response in the target echo for a 7 kHz Ricker signal, with the target in the broadside position. Again the target echo position corresponds closely with that shown in Figure 7.13. Comparison can be made with the broadband 7 kHz Ricker spectrum shown in Figure 7.10. Most of the returned energy in the target echoes is below 6 kHz. The existence of low frequency resonance components, in addition to the specular returns seen from the target steel-water boundary faces, is therefore possible. Comparison of Figures 7.14 and 7.15 shows the peak of the lower frequency component lagging slightly in time behind the peak signal level, observed at the higher frequencies from the front face spectral return. The pulse lengthening seen at the lower frequencies also suggests that a significant amount of the returned low frequency energy may be due to the resonance effects of the elastic water filled-target.

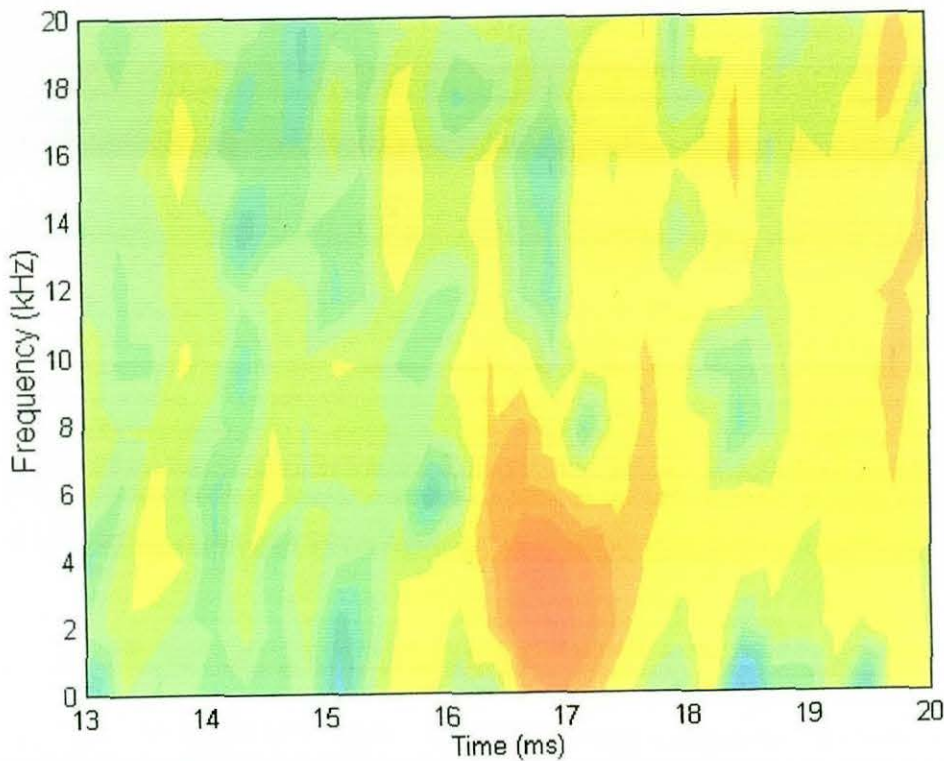


FIGURE 7.15 LOW FREQUENCY RESPONSE TARGET ECHO,  
BROADSIDE POSITION, 7 kHz RICKER SIGNAL.

Similarly Figures 7.16 – 7.17 show the high frequency end-cap response. In the end-cap position a number of additional target echoes are visible and those are early in Figure 7.17. Comparison with Figure 7.13 for the broadside position shows the main target echo,  $600 \mu\text{s}$  ahead of the equivalent signal from the broadside position. The change in the path delay of  $600 \mu\text{s}$  corresponds to a two-way path displacement of 45 cm. Due to the rotation of the target, by  $90^\circ$  about the cylinder's geometrical centre, the front face of a 1 m long target is approximately  $0.5 \text{ m} - \text{target radius } (0.125 \text{ m}) = 0.375 \text{ m}$  closer to the receiver, possibly accounting for the apparent variation in position. This expected target echo position, due to the cylinder rotation, is within 8 cm of the measured position.

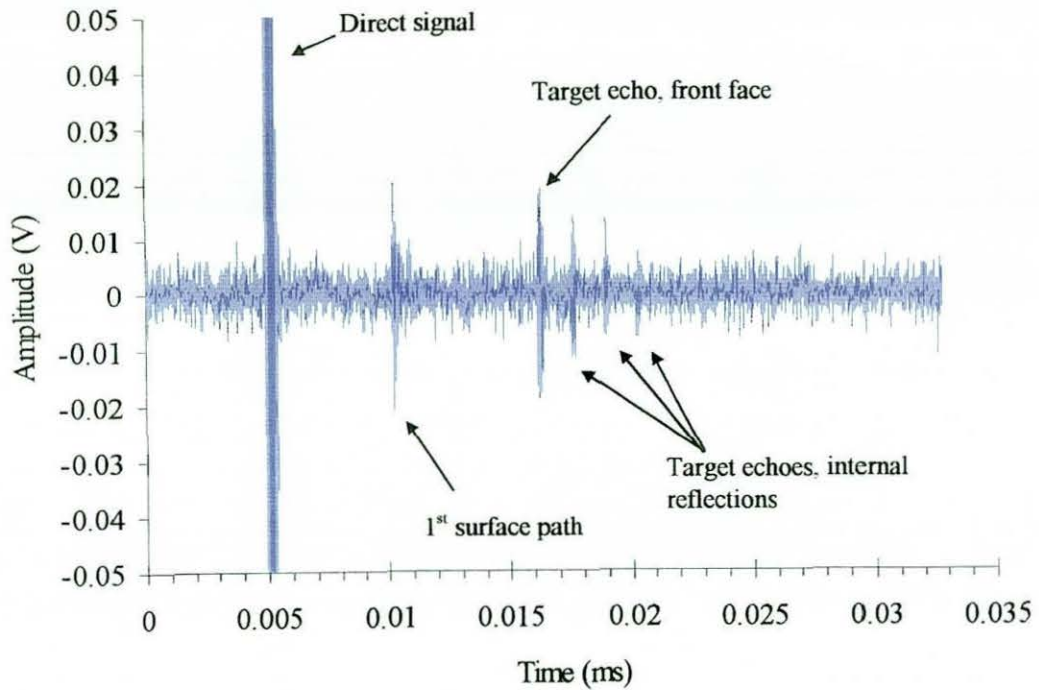
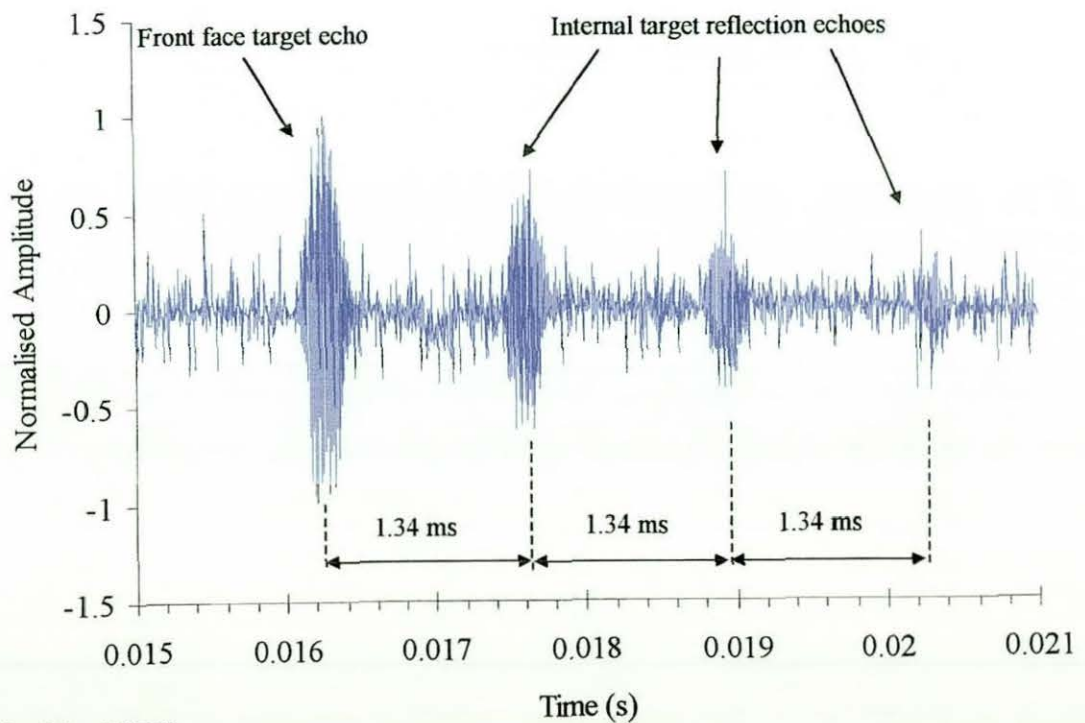


FIGURE 7.16 HIGH FREQUENCY DIRECT AND TARGET ECHO, WATER-FILLED TARGET, END-CAP POSITION



Ping No: 55782

FIGURE 7.17 END-CAP POSITION TARGET ECHOES FRONT AND BACK FACE

Figure 7.17 shows an expanded view of up to four internal reflected signals, at the carrier frequency (75 kHz). An inter echo-delay of 1.34 ms, corresponding to a 2.01 m propagation distance, equivalent to the 1 m separation of the two end-caps for a two-way path. Using a similar technique to that used in the broadside position, the end-cap target strength at 75 kHz was calculated as -13.32 dB. This is considerably lower than expected value compared with theoretical target strengths of +7.8 dB for a finite circular plate, given by equation (7.8), for normal incidence signal <sup>[7.25]</sup>.

$$TS = 10 \log_{10} \left( \frac{\pi a^2}{\lambda} \right)^2 \quad (7.8)$$

where  $a$  is the radius and  $\lambda$  the wavelength, here  $ka$  is larger than 1 and the range is greater than  $a^2/\lambda$ . The nearly 40 dB variation is probably due to the incident signal being away from the normal axis of the end-cap plate, illustrating the highly directional nature of the end-cap reflection.

The spectral response of the high frequency components from Figure 7.17 is shown in Figure 7.18. This shows the main reflection and the internally reflected signals centred around the 75 kHz carrier frequency.



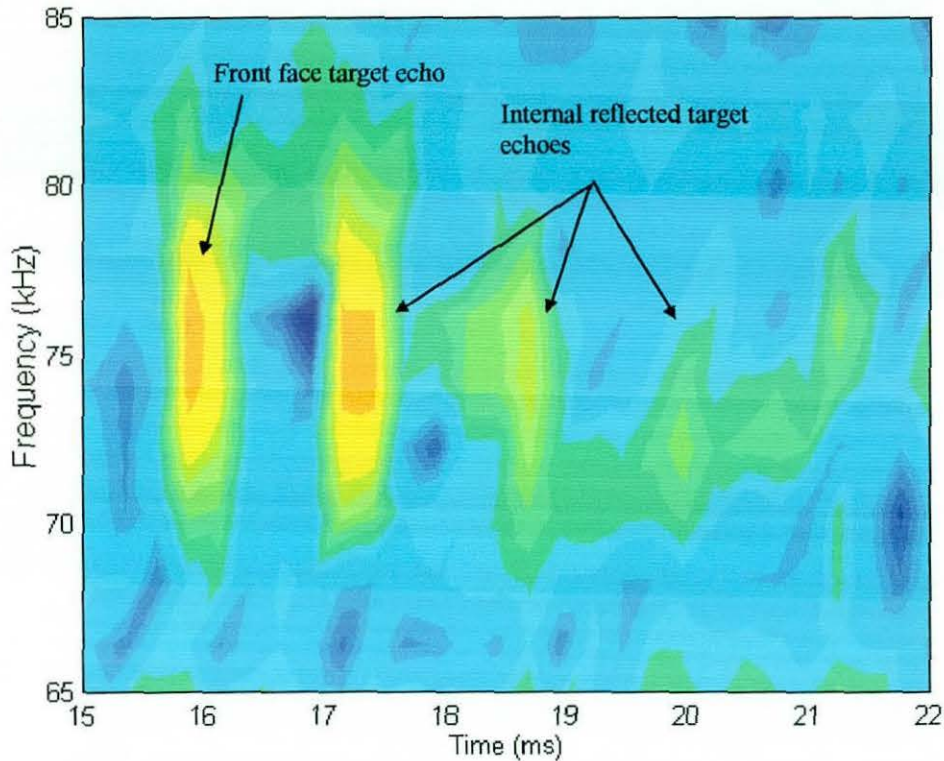


FIGURE 7.18 HIGH FREQUENCY RESPONSE, TARGET ECHOES, END-CAP POSITION, WATER-FILLED TARGET

Similar analysis of the filtered end-cap response for a 7 kHz Ricker signal is shown in Figure 7.19. In this case two strong target echoes are visible at the lower frequencies. The second echo again closely corresponds to an internal reflection from the inside of the back face in time. Spectral analysis of the target echoes, shown in Figure 7.20 display considerably wider energy distribution for the 7 kHz Ricker, in comparison with the broad-side position reflection, shown in Figure 7.15. The end-cap specular reflection shows characteristics much closer to the direct signal response seen in Figure 7.10, with energy distribution above 10 kHz.

Strong specular returns from the normal incidence end-caps provide the prominent energy distribution in the returned echoes. Although energy generated through possible resonance effects is evident, it is swamped by the specular returns. The peak energy signals are also shorter in time, matching the time-frequency distribution seen in the direct Ricker signal, in comparison with the pulse broadening effects seen in the broadside return.

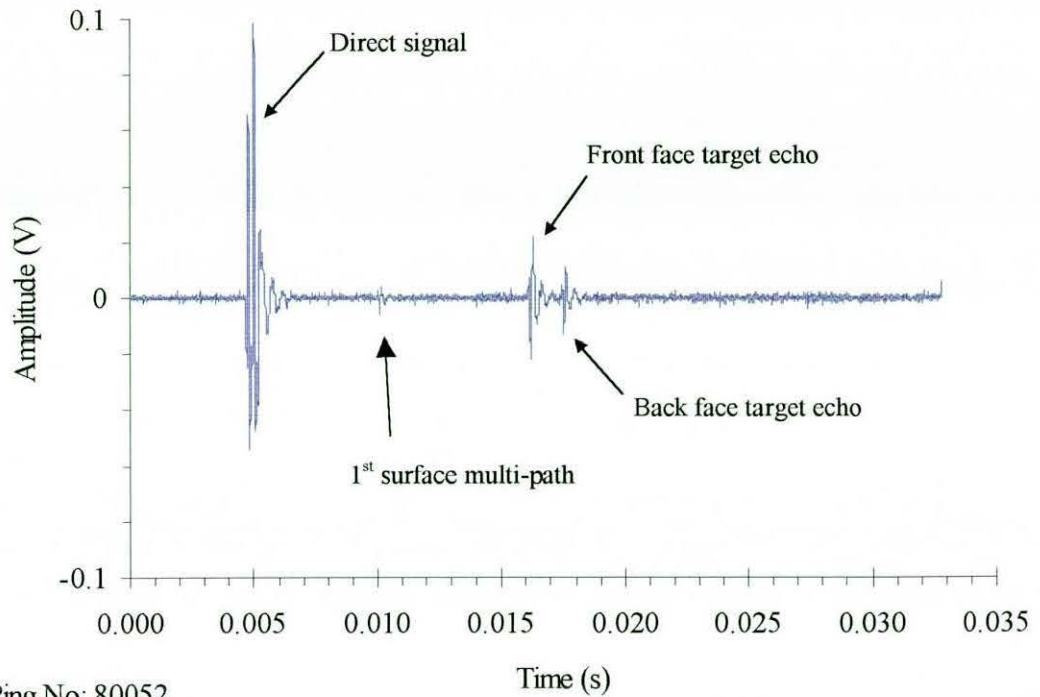


FIGURE 7.19 DIRECT AND TARGET ECHOES, END-CAP POSITION, LOW FREQUENCY RESPONSE, 7 kHz RICKER SIGNAL

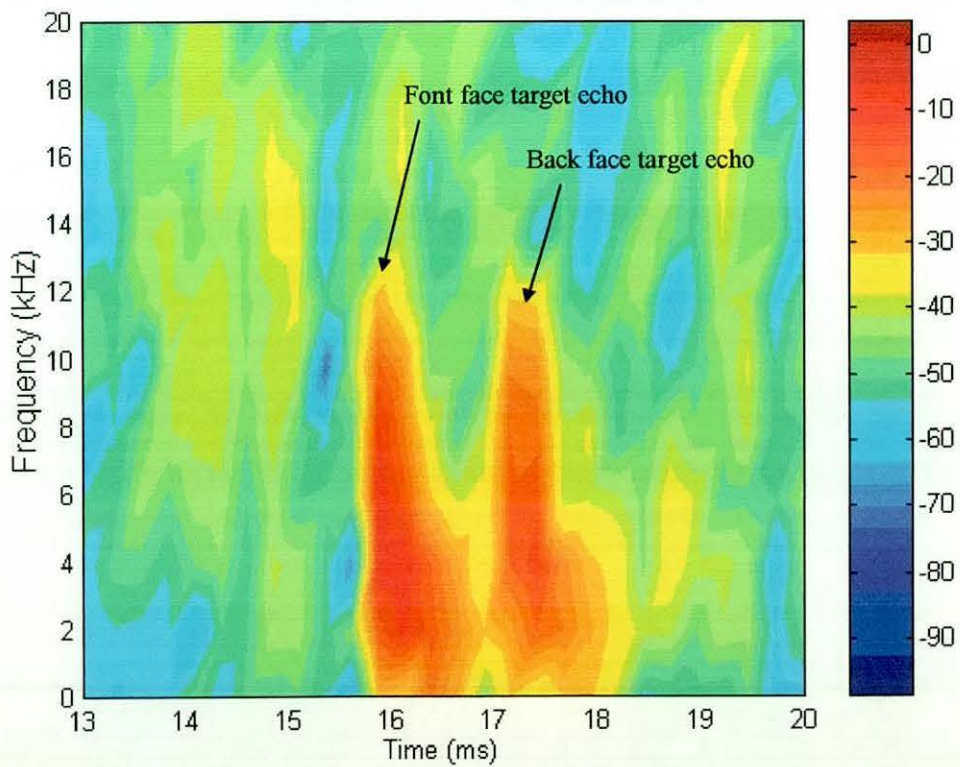


FIGURE 7.20 LOW FREQUENCY RESPONSE, END-CAP TARGET ECHOES, WATER-FILLED

Target strength estimations were possible from Figure 7.19, showing the low frequency response to a 7 kHz Ricker signal. At the lower frequencies the hydrophone placement is now within the far-field of the target, compared with the near-field placement seen at 75 kHz. From equation (7.6)  $TL_1$  is taken as 1.2 dB. Assuming cylindrical spreading as the hydrophone is in the far-field of the target gives a  $TL_2$  of 18.5 dB. Free-field target strengths of 7.46 and 1.85 dB for the front and back face echoes were calculated.

## 7.7 **Free-field measurement conclusions**

Although problems were experienced in the capture of good quality secondary frequency data, due to distortion effects in the streamer array, data from the single hydrophone provided several insights to the free-field scattering effects of the target under study. Target echoes, with good signal-to-noise ratios from water-steel boundaries were detected with the target in both an end-cap and broadside orientation. Evidence of multiple, internally reflected signals from boundaries allows classification of the target size in terms of length and diameter.

Spectral analysis of secondary frequency components of the return echoes revealed evidence of a possible low frequency resonance effect relating to the target geometry. The broadside position showed strong specular returns from the front and back face at the higher frequencies. In comparison, the low frequency component showed that the dominant echo energy distribution lagged in time and was more narrowly distributed in frequency compared with the equivalent high frequency return. Broadening of the pulse in time also suggested a larger portion of the returned energy was due to internal resonance effects. In the end-cap case, strong boundary reflection seemed to be dominant making the detection of the narrow-band resonance effects difficult.

The experimental set-up performed well. Expected difficulties in alignment due to surface movement and tidal changes were, in general, overcome and good repeatability was evident in the target aspect angle and the general geometry. Detection of changes in source-target ranges of around 0.5 m, due to the target

rotation from broadside to end-cap position, were also encouraging.

No data concerning the bottom scattering experiment is presented in this chapter, due to the problems with the streamer array. Target-free bottom scattering experiments were, however, repeated for various signal types during the embedded target measurements described in Chapter 8.

## REFERENCES: Chapter 7

---

- 7.1 Lim R., Lopes J.L. Hackman R.H. and Todoroff D.G.  
Scattering by objects buried in underwater sediments: Theory and Experiments  
*J.Acosutic.Soc.Am.*, Vol. 93, No. 4, pp. 1762-1783, 1993.
- 7.2 Guillermin R., Sessarego J.P. and Sageloli J.  
Characterization of buried objects in marine sediments  
*Proc. IEEE Oceans 98*, Vol. 1, pp. 18-21, 1998.
- 7.3 Gensane M., Fioravanti S., Granara M., Sabel J.C. Tesei A., Tran Van Nhieu M., Trucco. A. and Woodward.B  
Detection of Embedded Objects (DEO)  
*Third European Marine Science and Technology Conference*, Lisbon, 23-27 July 1998, pp. 1140-1153, 1998.
- 7.4 Fioravanti S., Maguer A., Lovik A. and Brussieux M.  
A parametric Synthetic Aperture Sonar  
*Proc. 3rd European Conference on Underwater Acoustics*, Heraklion Crete, Greece. 24-28th June 1996, vol. 2, pp. 1085-1096, 1996.
- 7.5 Maguer A., Fioravanti and Lovik A.  
Below critical angle detection of buried objects  
*Proc. IEEE Oceans '97*, pp. 512-517, 1997.
- 7.6 Tran Van Nhieu M., Gensane M., Tesei A. Fiovaranti S. and Maguer A.  
Scattering by a fluid-filled finite cylindrical shell: Comparison theory-experiments  
*Proc. 4th European Conference on Underwater Acoustics*, Rome, Italy, Vol. 2, pp. 819-824, 1998.
- 7.7 Sabel J.C. and Saanen A.M.G.H.  
Array focusing for buried object detection and identification.  
*Proc. 4th European Conference on Underwater Acoustics*, Rome, Italy, Vol. 1, pp. 401-406, 1998.
- 7.8 Cook J.C., Goodson A.D., Lepper P.A. and Woodward B.  
Measurement of acoustic scattering from a cylindrical shell using a parametric sonar  
*Proc. 4th European Conference on Underwater Acoustics*, Rome, Italy, Vol. 2, pp. 861-866, 1998.
- 7.9 Lecroq F., Tran Van Nhieu, M., Lematre M., Maze G. and Ripoche J.  
Acoustical scattering by a cylindrical shell terminated by flat plates.  
*Proc. 3rd European Conference on Underwater Acoustics*, Heraklion Crete, Greece. 24-28th June 1996, vol. 1, pp. 117-122, 1996.

- 
- 7.10 Gensane M.  
Applications of bottom backscattering theories to experiment.  
*Proc. IEEE Oceans'98*, 1998.
- 7.11 Granara M., Pescetto A., Repetto F., Tacconi G. and Trucco A.  
Statistical and neural techniques for buried object detection and classification  
*Proc. IEEE Oceans'98*, pp. 1269-1273, 1998.
- 7.12 Granara M., Pescetto A., Repetto F., Tacconi G. and Trucco A.  
Buried object detection and classification by means of a parametric sonar  
*Proc. 4th European Conference on Underwater Acoustics*, Rome, Italy, Vol. 1, pp. 57-61, 1998.
- 7.13 Numrick S.K., Dragonette L.R. and Flax L.  
Classification of submerged targets by acoustic means  
*Elastic wave scattering and propagation*, Edited by Varadan V.K. and Varadan V.V., Ann Arbor Science, pp. 149-174, 1982.
- 7.14 Zerr B., Tesei A., Maguer A., Fox W.L.J. and Fawcett J.A.  
Target classification methodology combining reconstruction from multiple aspects and resonance scattering analysis.  
*Proc. 4th European Conference on Underwater Acoustics*, Rome, Italy, Vol. 2, pp. 813-818, 1998.
- 7.15 Decuitot D., Lecroq F., Maze G. and Ripoche J.  
Acoustic scattering from cylindrical shell bounded by hemispherical endcaps. Resonance interpretation with surface waves propagating in cylindrical and spherical shells.  
*J.Acosutic.Soc.Am.*, Vol. 95, No. 5, pp. 2916-2923, 1993.
- 7.16 Faran J.J. Jr  
Sound scattering by solid cylinders and spheres  
*J.Acosutic.Soc.Am.*, Vol. 23, No. 4, pp. 405-418, 1951.
- 7.17 Dunsinger A.D.  
A study of acoustic echoes from solid cylindrical targets of square and circular section  
*J.Sound. Vib.*, Vol. 8, No. 2, pp. 229-239, 1968.
- 7.18 Barnard G.R. and Mckinney C.M.  
Scattering of acoustic energy by solid and air filled cylinders in water  
*J.Acosutic.Soc.Am.*, Vol. 33, No. 2, pp. 226-238, 1961.
- 7.19 Horton C.W. Sr. and Mechler M.V.  
Circumferential waves in thin-walled air-filled cylinder in a water medium.  
*J.Acosutic.Soc.Am.*, Vol. 51, No. 1(2), pp. 295-303, 1972.

- 
- 7.20 Morse S.F., Marston P.L. and Kaduchak G.  
High frequency backscattering enhancements by thick finite  
cylindrical shells in water at oblique incidence: Experiments,  
interpretation, and calculations  
*J.Acosutic.Soc.Am.*, Vol. 103, No. 2, pp. 785-894, 1988.
- 7.21 Tran Van Nhieu M.  
Scattering from a finite cylindrical shell  
*J.Acosutic.Soc.Am.*, Vol. 91, No. 2, pp. 670-679, 1992.
- 7.22 Tran Van Nhieu M. and Ywanne F.  
Sound scattering from slender bodies of arbitrary shape.  
*J.Acosutic.Soc.Am.*, Vol. 95, No. 4, pp. 1726-1733, 1994.
- 7.23 Tran Van Nhieu M.  
A slender-body approximation in scattering theory  
*J.Acosutic.Soc.Am.*, Vol. 85, No. 5, pp. 1834-1840, 1989.
- 7.24 Ricker N.  
The form and laws of propagation of seismic-wavelets  
*Geophysics*, Vol. 18, pp. 10-40, 1953.
- 7.25 Urick R.J.  
Principles of underwater sound, Second Edition  
*McGraw-Hill Book Company*, ISBN 0-07-066086-7, pp. 277, 1975.
- 7.26 Waite A.D.  
Sonar for practising engineers  
*Epic Printing Services*, Dorchester, ISBN 0 952033 1 3, pp. 87, 1988.

## CHAPTER EIGHT

# DETECTION OF EMBEDDED OBJECTS

### 8.1 Introduction

The second stage experiment took place between the 20<sup>th</sup> June and the 6<sup>th</sup> July 1998 at the Loch Duich site. As for the free-field experiment described earlier, the experiment was conducted as part of the European Commissions MAST III DEO project with collaboration between TNO-FEL of the Netherlands and the Underwater Acoustics Research Group Loughborough University

The purpose of the trial was to measure back-scattered signals from a seabed-embedded target, using a parametric sonar system at a range of target aspect angles. The initial aim was to measure the target echoes for a buried object, identical to that used in the previously described free-field measurements. The deployment of a buried object (0 - 1 m depth) was, however, consider impractical with water depths in the region of 40-45 m. Measurement were therefore made with a target proud of the seabed, allowing the target weight to self embed. Using the same steel target (1 m long and 0.25 m diameter), a typical burial depth of up to 50 % in soft sediment was possible, by simple placement on the seabed.

Measurements were made at a range of transmitter-target aspect angles and with a range of signal types. Only a water-filled target was considered, due to the difficulty of sinking an air-filled target. Recordings of target-scattered signals were made using a redesigned streamer array for low frequency secondary signals and single-element hydrophones for direct signal and target echoes.

### 8.2 Seabed topography survey

Due to the placement of the target on the seabed, improved knowledge of the topography of the seabed in the trial site was required. To overcome this, a pre-



trial survey was carried out in January 1998.

A small fish-finder echo sounder was deployed from a canoe. The canoe was then tracked from shore using two theodolites placed at fixed reference points, station P and Q. The relative theodolite angles, referenced to magnetic north, allowed triangulation of the boat position to the fixed reference points. This data was then collated with the echo sounder readings, allowing the building up of a three dimensional bottom topography model. Cross-referencing of positions was carried out using a GPS system. This was, however, limited in accuracy due to the high mountain coverage in the shore area.

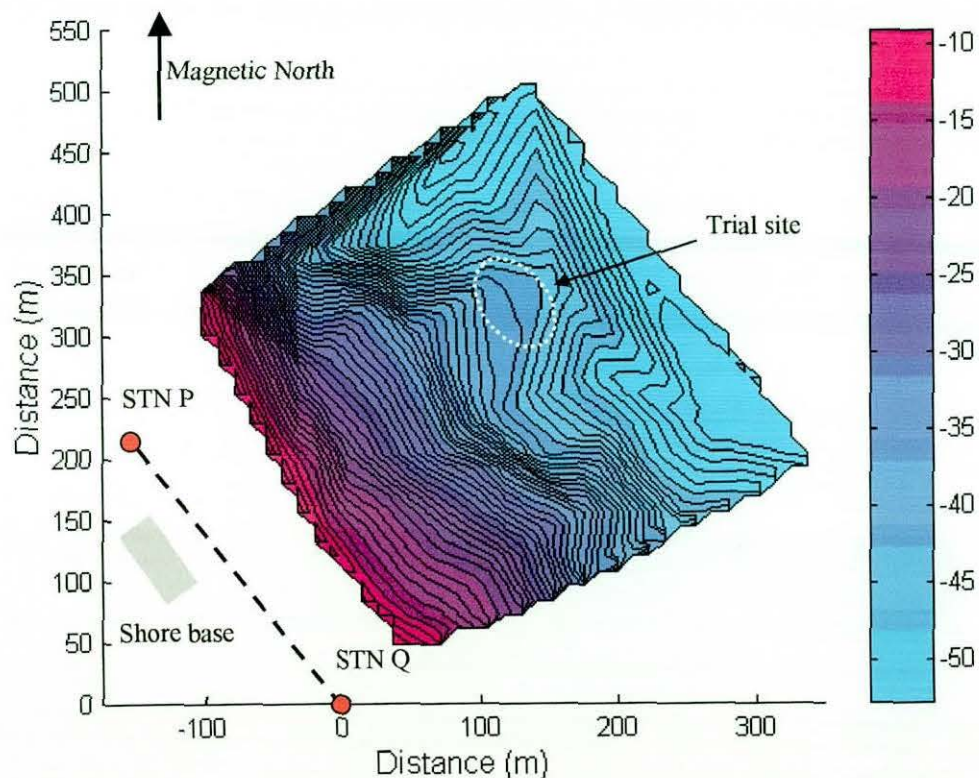


FIGURE 8.1 SEABED CONTOUR PLOT LOCH DUICH TRIAL SITE

Figure 8.1 shows a contour plot of the data obtained from the survey. The area indicated as trial site was eventually used in the second stage experiment. This site offered relative flatness of seabed and proximity to the shore base, critical because of equipment cable lengths. Stations P and Q were placed just above the high water line in front of the shore base, with station Q chosen arbitrarily as a zero

reference. All measurements were then defined from this point.

Figure 8.2 shows a three-dimensional representation of the seabed topography as viewed from the seaward side looking towards the shore. The small plateau eventually used, as the trial site is visible in the foreground. This provided an average water depth between 40-45 m and was relatively flat over the area of interest.

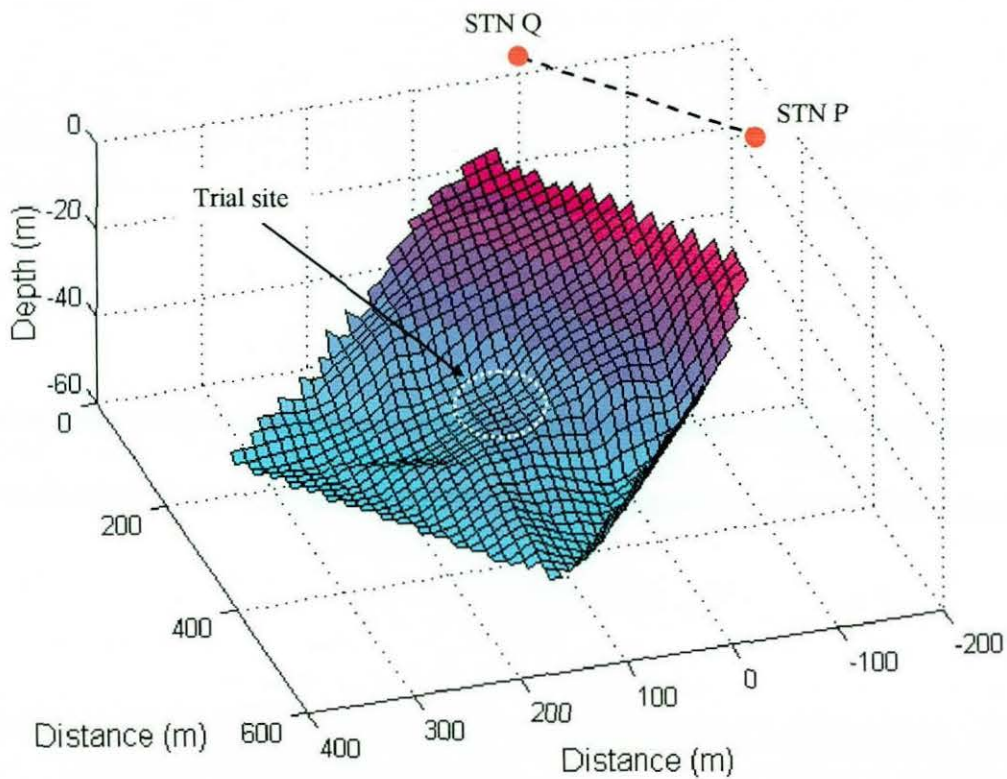


FIGURE 8.2 3D PLOT SEABED TOPOGRAPHY, LOCH DUICH TRIAL SITE

### 8.3 Equipment deployment

The trial site equipment, shown in Figure 7.2, was deployed in a similar fashion to that for the earlier free-field experiment. Knowledge of the seabed topography allowed placement of the target on the seabed close to the moored FRS raft. Tramlines were again used to position a target raft, for placement of the target and various hydrophones. Figures 8.3 and 8.4 show a top and side view of the equipment placement.

A redesigned streamer array was deployed from a separate set of tramlines set out perpendicular to the main FRS raft. This allowed placement of the receiver outside the main beam of the parametric source, hence minimising the chance of the distortion effects seen in the previous trial. The use of the tramlines allowed adjustment of the vertically deployed streamer's height and horizontal displacement sideways from the parametric source.

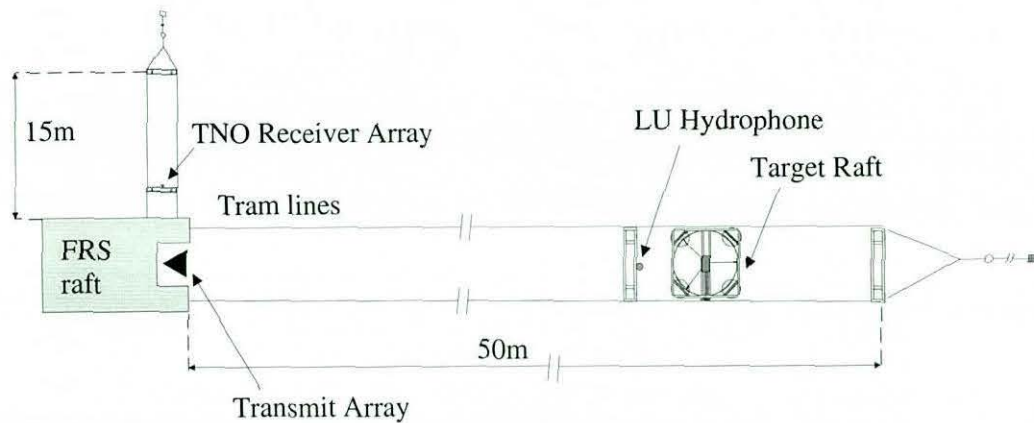


FIGURE 8.3 EQUIPMENT DEPLOYMENT TARGET EMBEDDED  
EXPERIMENT PLAN VIEW

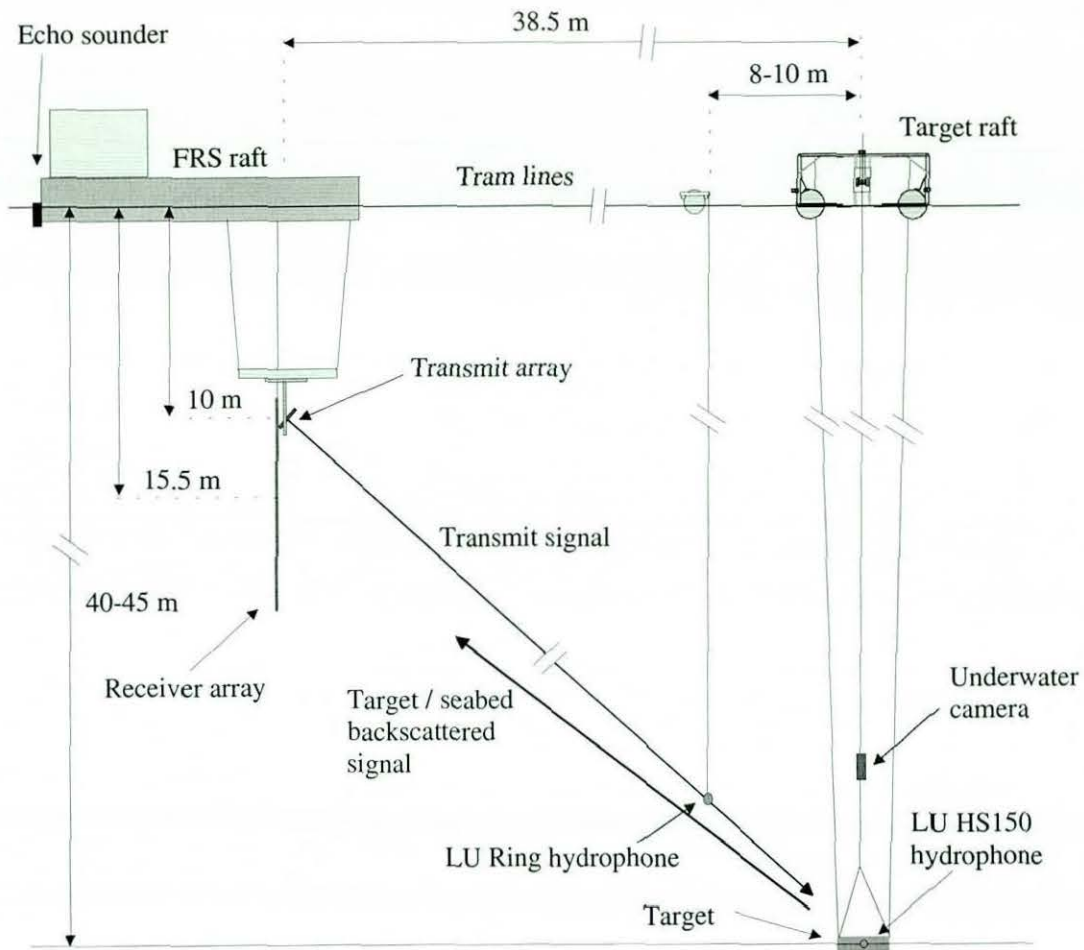


FIGURE 8.4 EQUIPMENT DEPLOYMENT, TARGET EMBEDDED EXPERIMENT, SIDE VIEW

The centre of the acoustic aperture of the receiver array was initially 15.5 m below the surface, with a 7.5 m horizontal displacement from the transmitter. Both the height of the source and receiver array was adjusted to provide different seabed incidence angles for a target in a fixed position.

Multiple target incident aspect angles were achieved, by raising and lowering the target on a three-wire suspension system deployed from the target raft. Different angles were achieved by adjustment of the three lifting points around the circumference of a 4 m diameter circle, shown in Figure 8.25. A special winching system was then used, to uniformly lower the three lifting wires, whilst maintaining the aspect angle of the target relative to the transmitter.

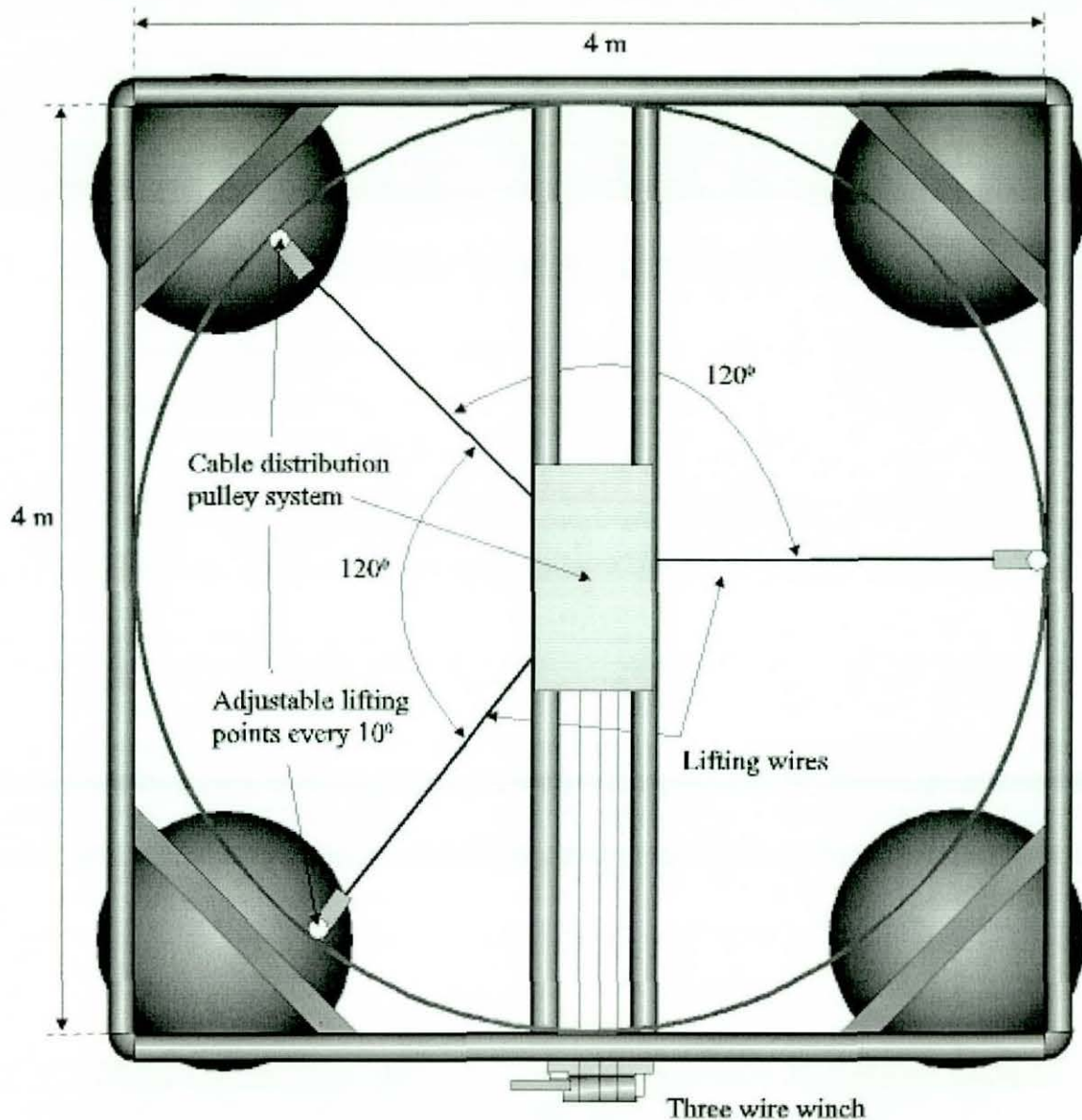


FIGURE 8.5 TARGET RAFT FOR ADJUSTMENT OF TARGET ASPECT ANGLE ON THE SEABED

The target was then lowered to the seabed, maintaining target-transmitter aspect angle. Once in place the wires were allowed to go slack, to avoid lifting due to tidal depth changes. A new aspect angle was achieved by adjustment of the lifting points, distributed around the 4 m ring every 10°, when the wires were slack. The target was then lifted clear of the seabed and allowed to settle in the new orientation before being lowered back on the seabed.

Two additional single-element hydrophones were used. A 10 cm ring hydrophone, from Sonar Products, was placed 8-10 m away from the target position, within the main signal beam. A smaller 12 mm ball hydrophone (HS150) was placed in the centre of the target. An underwater camera was deployed from the target raft to observe the aspect angle and degree of embedding.

## 8.4 Embedded target measurement equipment

### 8.4.1 Parametric source

The LU parametric source was again mounted on the FRS pan-and-tilt system, below the main FRS raft. Control of the transmission elevation angle was possible to  $\pm 20^\circ$  using the pan-and-tilt x-axis and azimuth control, by electronic steering of the beam by  $\pm 18^\circ$ . The array was initially deployed at 10 m below the surface, within the cavitation depth limit for high power operation. The array was mounted on an adjustable bracket, initially set for a seabed incident angle of around  $45^\circ$ , as shown in Figure 8.5. The array mounting can also be seen in Figure 3.3 in Chapter 3.

Once the target was in place, target alignment was carried out using the small 12 mm ball hydrophone placed in the centre of the target. Adjustment of the azimuth and elevation angles could then be made, by observation of the peak signal level on the hydrophone, monitored in real time at the FRS raft.

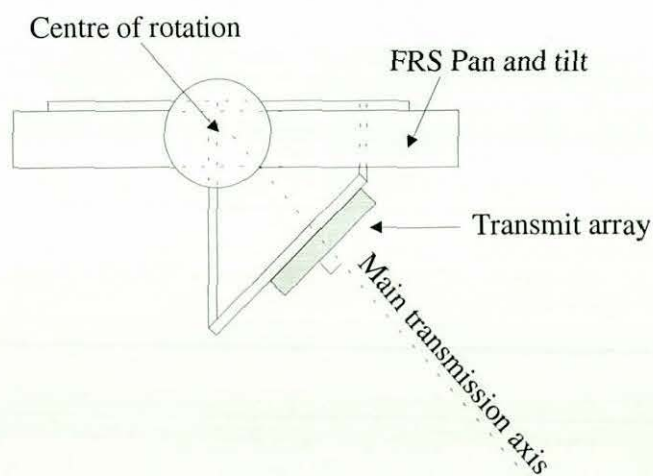


FIGURE 8.6 PARAMETRIC SOURCE  $45^\circ$  SEABED INCIDENT DEPLOYMENT

#### 8.4.2 Receiver systems (Embedded object)

A new streamer array was developed and operated by TNO-FEL, with improved anti-aliasing filtering and overload protection, to minimise the chance of distortion effects due to the primary frequency signal, as observed during the first trial. This array was reconfigured to use 20 AQ4 Benthos elements, spaced 25 cm apart. This gave an acoustic aperture of 4.75 m, approximately half the size of the previous array of 9.5 m. Hydrophones and redesigned pre-amplifiers were arranged symmetrically about the middle of a 15 m long oil-filled tube. The pre-amplifiers included a 5<sup>th</sup> order elliptical filter with a 15 kHz bandwidth. Gain was switchable, from 12 to 40 dB, with a -3 dB high pass set to 100 Hz. The AQ4 elements provided a receiver sensitivity of -161 dB re 1V/ $\mu$ Pa over the range of frequencies of interest (100 Hz – 15 kHz).

All data were fed ashore and recorded on a Sony SIR-1000 32-channel data recorder. Analogue data from the hydrophones were recorded on the first twenty channels, over a 48 kHz bandwidth. Additional non-acoustic data from the streamer heading and pitch-roll sensors were recorded on channels 21-25. Channel 26 was used to record a synchronisation trigger signal, supplied from the transmission system. The Sony recorder used a Sony SDX-T3C AIT (Advanced Intelligent Tape) tape with a 25 GB storage capacity. After recording a separate tape unit (Sony SDX-300C) it was used to read back the AIT tape. This device interfaced with a PC through a wide-SCSI interface. Using Sony's PCscan MK3, data would then be written to computer hard disk for further processing.

One of the additional hydrophones used was a 10 cm diameter ring transducer on a 100 metre cable, placed in the main beam 8-10 m from the target. The ring provided good low frequency receive sensitivity (1-15 kHz) with a peak of -181 dB re 1V/ $\mu$ Pa at 11 kHz. Both direct and target/seabed back-scattered signals were recorded and monitored in real-time using the LU data capture system incorporated into the transmission system. A 12 mm ball hydrophone was placed at the centre of the flooded target on the seabed. This hydrophone has a calibrated receiver sensitivity of -217 dB re 1V/ $\mu$ Pa, with a transducer size better suited to

the higher primary frequencies.

A ball hydrophone was also used primarily to align the transmit beam with the target, by adjustment of the transmit beam elevation and azimuth angles, whilst monitoring the high frequency signal component on the hydrophone. In addition, useful data was obtained concerning the high and low frequency reverberent effects, seen inside the target during insonification. Data from both hydrophones was recorded digitally to a 16-bit resolution, narrow-band (1-25 kHz) and broadband (1-100 kHz), using the LU data capture system sampled at 250 kHz.

As stated earlier, the TNO-FEL receiver array was initially deployed vertically with the centre of the acoustic aperture at 15.5 m. This depth was later adjusted with the source depth to achieve different seabed incident angles.

#### **8.4.3 System integration (Embedded object)**

The integration of the transmitter and receiver system operated by TNO-FEL and LU was essentially the same as for the previous year's experiment. Figure 8.7 shows a similar system diagram. Most transmitter systems were still operated from the FRS raft, with the hydrophone streamer and sensor data going ashore to the TNO-FEL base. The single-element hydrophones were monitored using a Tektronics 420 TDS digital oscilloscope and the LU data capture system, the latter providing real-time frequency and time domain analysis.



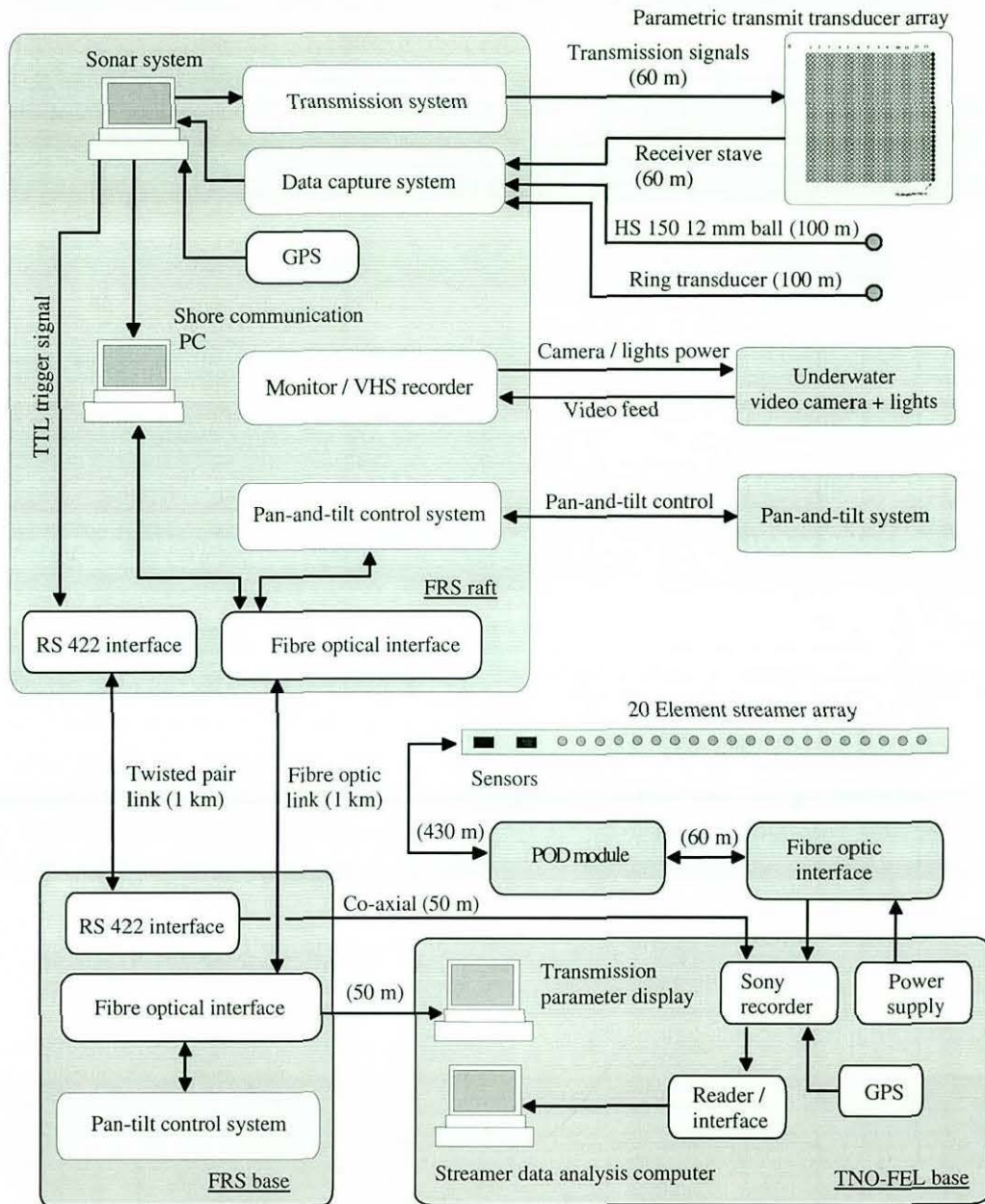


FIGURE 8.7 SYSTEM INTEGRATION DIAGRAM, TARGET-EMBEDDED EXPERIMENT

The target aspect angle control was no longer required but an underwater video camera was used from the target raft, looking down on the target placement on the seabed. Video images were monitored and recorded back on FRS raft.

Improved transmission-parameters to shore communications was achieved using Desklinc software. Using the 1 km fibre optic link, with the FRS shore base, a

local area network (LAN) was set up for shore-base and raft-based computers. With this, the remote operation of a raft-based PC was possible in the TNO base. Transmission parameters of the current ping were transferred from the main sonar control PC to the network PC, via a parallel port communications protocol. Data was then remotely viewed on a monitor PC at the TNO shore base via the 1 km fibre optic network.

In addition to the fibre optic link, a twisted-pair set in the same cable was used to send a trigger signal that was synchronous with the transmission time. RS-422 interfaces were used at either end. The signal was then fed from the FRS shore base to the TNO base, via a 50 m co-axial cable, where it was recorded on the Sony recorder, along with the hydrophone acoustic data. Both transmitter and receiver systems were synchronised, via the independent GPS timing system, used for all manual and automatic logging protocols. The trigger signal was a positive-going TTL level edge. At the shore end the signal was then attenuated to TTL levels, following the RS 422 interface stage.

## **8.5 Experimental procedure (target embedded measurements)**

### **8.5.1 Equipment deployment / system testing**

The initial deployment procedure was similar to that described in section 7.5.1. Additional systems, such as the underwater camera, were deployed and tested in parallel with the general system integration.

### **8.5.2 Target aspect angle measurement**

The flooded target was initially lowered to the seabed in a broadside position. The measurement of transmitter-target aspect angle, in the horizontal plane, was tried using two systems. Two acoustic pingers were placed at either end of the target separated by 1 m. They each transmitted a 4 ms long, 35 kHz CW signal, first one and then the other after a fixed delay. A third hydrophone ( $H_2$ ) a 25 mm ball HS70, was deployed from the main FRS raft, close to the transmit array, as shown in Figure 8.8. Figure 8.10 shows the target with the pinger transducers in place.

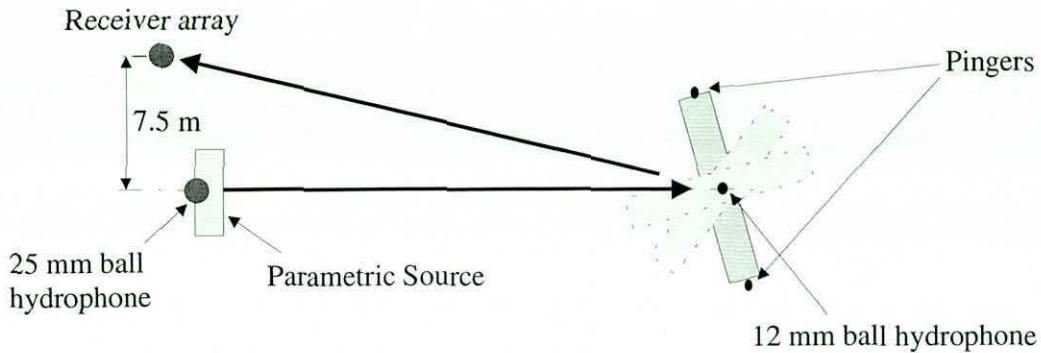


FIGURE 8.8 TARGET ASPECT ANGLE MEASUREMENT USING PINGER SYSTEM

The phase alignment of the two arriving signals could then be checked, with the fixed delay removed, giving an indication of any difference in the relative propagation distances of the two signals. A broadside position target should provide phase-aligned signals, once the known delay is removed. Any rotation of the target moved one pinger closer or further from the receiver, and vice versa for the other, hence altering the respective propagation distances and therefore the signal arrival times. The difference timing could then be translated into a rotation angle.

The time delay after removal of the fixed delay is given by

$$\Delta t = l_c \left[ \frac{2 \sin \theta}{l \cos \gamma} + \cos \theta \sin \gamma - \cos \theta \tan \gamma \right] \quad (8.1)$$

where  $\gamma = \tan^{-1} X$  and  $X = \frac{l_c \cos \theta}{l + l_c \cos \theta}$

$l$  is given by  $c \Delta t'$  where  $\Delta t'$  the time difference in signal arrival between hydrophone  $H_1$  and  $H_2$  as outlined in Figure (8.9) and  $c$  is the sound velocity in the water.

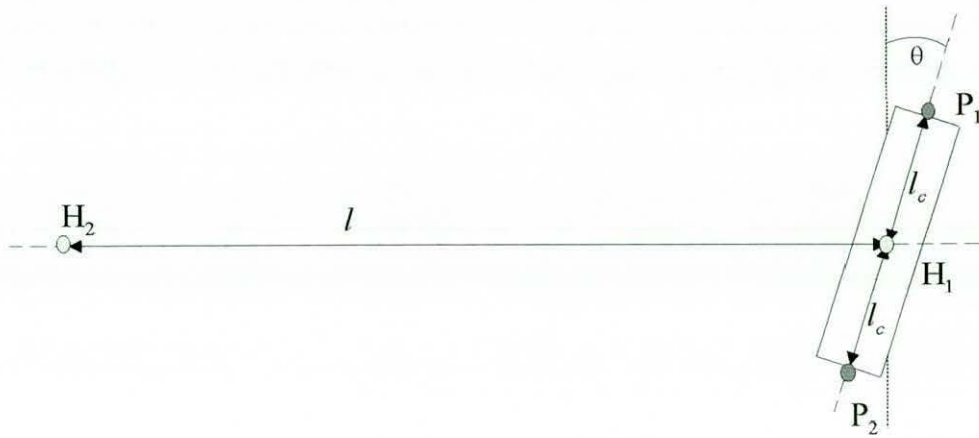


FIGURE 8.9 TARGET ORIENTATION USING ACOUSTIC PINGERS

Problems were, however, experienced with the system due to a strong local noise source at 32 kHz. Detection of the 35 kHz signal was therefore difficult in the continuous noise level. A 35 kHz carrier signal was originally chosen to be out of band for all other acoustic sources, i.e. at the parametric primary (65-85 kHz) and the secondary (1-13 kHz) frequencies. The noise source was believed to be equipment-based on the FRS raft and not seen in the laboratory tests of the system. The strong noise source evident in the acoustic spectrum shown in Figure 4.22 is believed to be from the same source.

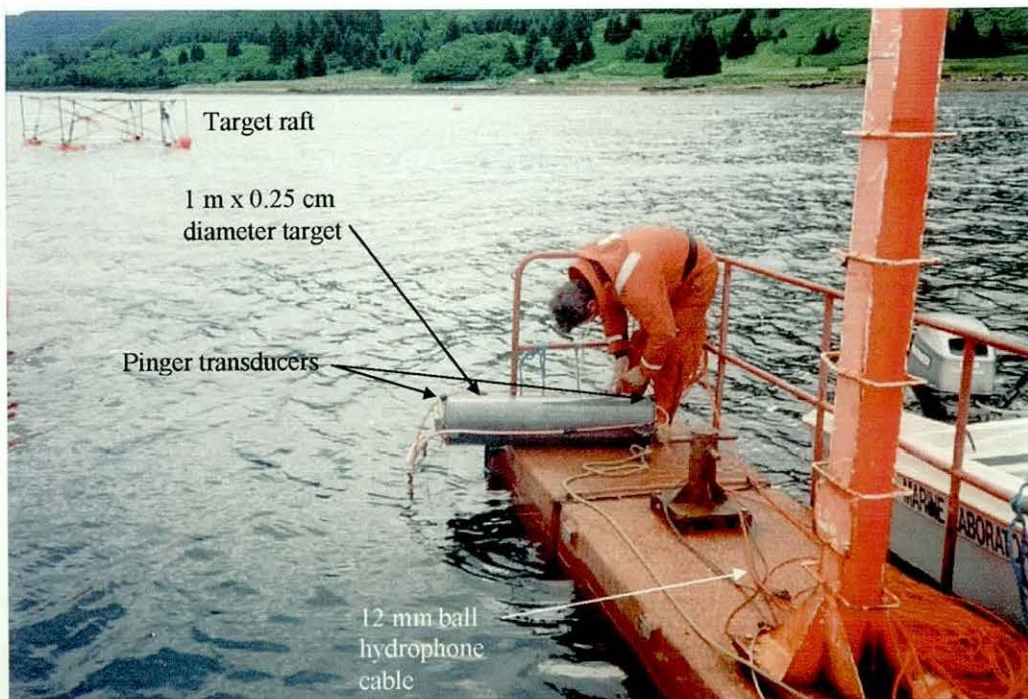


FIGURE 8.10 CYLINDRICAL TARGET SEABED EMBEDDED MEASUREMENTS

Because of the problems encountered with the pingers, the underwater camera was used to measure the target aspect angle. Once the target was positioned the camera and lights were lowered down one of the lifting wires, to guide the camera to the target. Figure 8.11 shows the highlighted target partially buried in the sediment. The slack lifting wires and the internal hydrophone cable are also visible. The quality of imaging varied, depending on the light level and the degree of suspended particles in the water, making it difficult to use the underwater lights. The degree of suspended matter depended on the weather conditions.

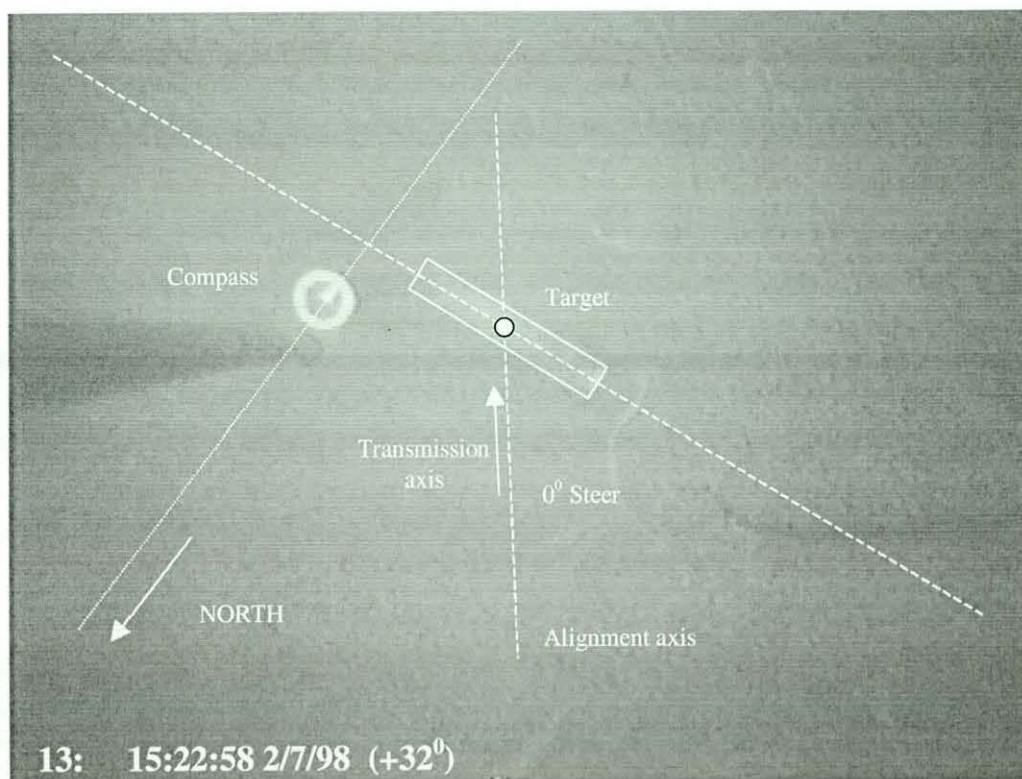


FIGURE 8.11 TARGET ASPECT ANGLE MEASURED RELATIVE TO MAGNETIC NORTH

To measure the target orientation an oil-filled compass was placed in the field of view of the camera. Post processing of images captured from the video allowed measurement of the horizontal aspect angle relative to magnetic North, as illustrated in Figure 8.11. Comparison with transmitter alignment relative to North, gave the transmitter-target orientation. Account was also taken of the steered angle used during the alignment stage.

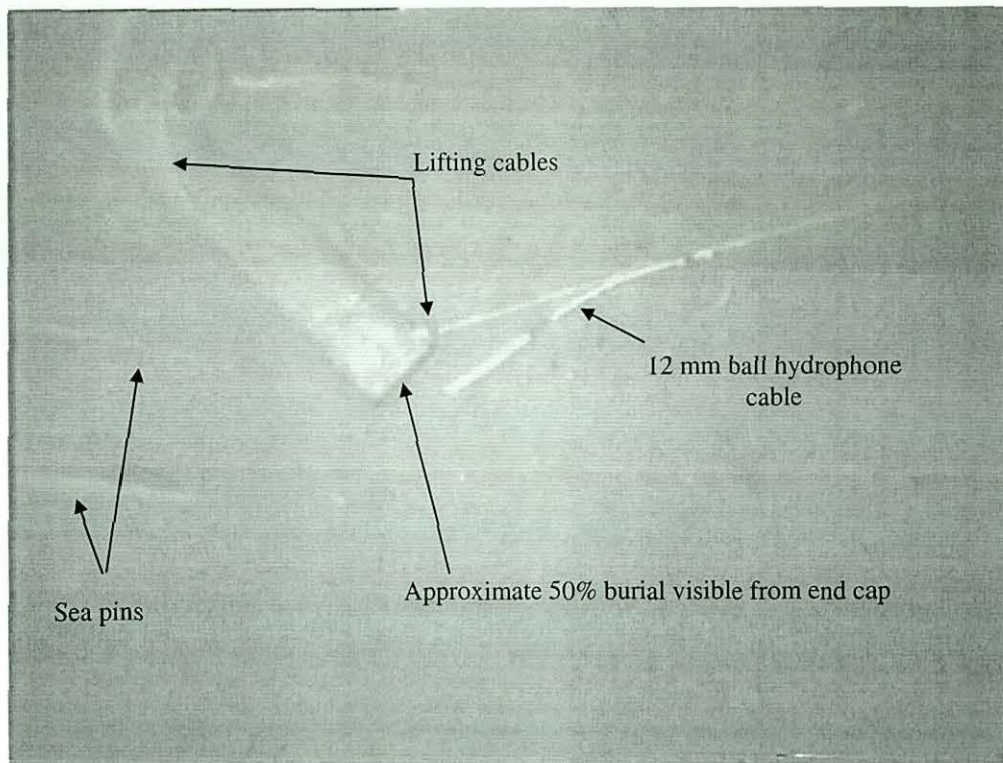


FIGURE 8.12 UNDERWATER CAMERA VIEW SEDIMENT EMBEDDED TARGET.

Figure 8.12 shows another underwater image where the degree of embodiment is visible. In this case the hydrophone entry point in the end-cap is buried in the sediment.

### 8.5.3 Acoustic measurements

Calibration tests of the TNO-FEL receiver array were conducted using a self-contained acoustic pinger, resonant at 10 kHz and with a source level of 130 dB re  $\mu\text{Pa}$  at 1 m. This was placed at various depths close to the vertically deployed streamer. Test sequences and levels were monitored ashore at the TNO base.

With the initial deployment of the parametric source at 10 m depth and at a horizontal range of 38.5 m, seabed grazing angles (source-target) of between  $37.9^\circ$  to  $42.3^\circ$  were achieved. The angular range was due to the variation in the water depth with tidal height. The target was then deployed at a range of aspect angles, in the horizontal plane between  $-43^\circ$  to  $+114^\circ$  where  $0^\circ$  is the broadside position and  $\pm 90^\circ$  is an end-cap position. Actual achieved target aspect angles were  $-43^\circ$ ,

$-42^\circ$ ,  $+33^\circ$ ,  $+43^\circ$ ,  $+51^\circ$ ,  $+77^\circ$ ,  $+96^\circ$ ,  $+114^\circ$ ,  $+83^\circ$ ,  $+26^\circ$ ,  $+32^\circ$  and  $-4^\circ$ . Due to difficulties in exact target placement the closest orientation to end-cap and broadside positions were  $+96^\circ$  and  $-4^\circ$  respectively.

Acoustic insonification on each target orientation was conducted using 4 ms CW signals, linear frequency modulated 'chirp' signals and shorter Ricker pulses, derived from the parametric source. These initially included CW signals at 5, 9 and 13 kHz; chirp signals over the range 2-10 kHz and 4-12 kHz; and Ricker signals centred on 4, 7 and 10 kHz. The chirp signals were replaced later by single octave chirp signals in the range 3-6 kHz and 6-12 kHz. Recordings of each signal type, for each target orientation, were made using the TNO streamer with a bandwidth of 1-15 kHz and the single-element hydrophones, both narrow-band (1-25 kHz) and broadband (1-100 kHz).

Target-free bottom-scattered measurements were then carried out, with the target raised 10 m clear of the seabed, for the same range of seabed grazing angles, for each signal type. The parametric source was then lowered from 10 to 15 m, altering the target grazing angle from the range  $37.9^\circ - 42.3^\circ$  to the range  $33.0^\circ - 37.9^\circ$ . A variation in seabed incident angle is seen due to the variation in water depth with the tide. Similarly the receiver array was also lowered, moving the acoustic centre from 15.5m to 30 m, adjusting the receiver bi-static back-scattered echo incidence angle, as measured from the horizontal, from the range  $32.5^\circ - 37.5^\circ$  to  $14.6^\circ - 21.2^\circ$  depending on the tidal height. Test sequences were recorded for the  $-4^\circ$  target orientation and the target-free measurement at this seabed incidence angle. The process was repeated with the centre of the receiver array at 10 m and 21 m. This deployment provided back-scattered echo incidence angles in the ranges  $37.9^\circ - 42.3^\circ$  and  $26.2^\circ - 31.9^\circ$  respectively.

#### **8.5.4 Additional measurements**

An additional, small echo sounder was deployed from the FRS raft to constantly monitor water depth variations due to tidal changes. CTD depth profiles were also measured from the FRS raft on a daily basis, providing more information about

the likely through-water propagation effects observed during the experiment. Pitch-roll sensors within the streamer gave information regarding the position stability of the streamer due to tidal currents.

Two sediment grabs were made, providing sediment samples to a depth of approximately 10-15 cm in the area of seabed directly below the main raft and the area used for the target. Later analysis and comparison with previously obtained data gave some indication of the seabed sediment in the area of interest.

## **8.6 Results (seabed embedded object measurements)**

### **8.6.1 Introduction**

In general, all systems functioned well. Back-scattered echoes from a seabed-embedded, water-filled target were measured over a range of target aspect and seabed grazing angles, for a range of CW, chirp and Ricker signal types. Data quality on all recording systems seemed of an acceptable standard.

Some problems were, however, experienced with the placement of the target at an exact aspect angle. The three-point suspension system was later altered to two points separated by  $180^\circ$  on the target raft frame. Due to this, some improvement in control of the angle was seen and angles within  $4\text{-}6^\circ$  of desired orientation, such as broadside and end-cap positions, were achieved. The use of the camera provided assessment of the target aspect angle and the degree of burial of the target in each orientation.

### **8.6.2 Acoustic data analysis**

As stated above, data from all recording systems was of a good quality, but only results from the single hydrophone elements will be presented here. Due to the positioning of the hydrophones, comparison of both direct and target-scattered signals can be made and is therefore preferred for this analysis of the data set available.



Figure 8.13 shows the wide-band recording for a 7 kHz Ricker generation signal, for both the direct signal and the target echoes, at both the primary and secondary frequencies. This spectrogram, was recorded from the ring hydrophone placed 13.3 m from the target in the beam of the incident signal. The target was at  $-4^\circ$  from the broadside position, water-filled, and approximately 50 % embedded. The time scale corresponding to the start of the data capture window and was selected to allow measurement of both the direct and seabed-scattered signals. The capture window was started 18 ms after the start of the transmission pulse. A corresponding source-target distance of 43.4 m was measured using the internal hydrophone. With a water depth of 43 m, a seabed-grazing angle of  $49.6^\circ$  was estimated.

Wide-band recordings were made with a 1-100 kHz bandwidth and a sample frequency of 250 kHz. Spectral analysis was carried out using a 128-point FFT with a 128-point sliding window. No compensation was made for the hydrophone response at the higher frequencies, but comparison of relative positions in time, of the high and low frequency components, was considered useful. Due to the reduced sensitivity of the hydrophone at 75 kHz, the high and low frequency components of the direct signal appear of similar amplitude. In reality the approximate 40 dB difference in signal level would tend to make the weaker, lower frequency components harder to distinguish in the display format shown in Figure 8.13.

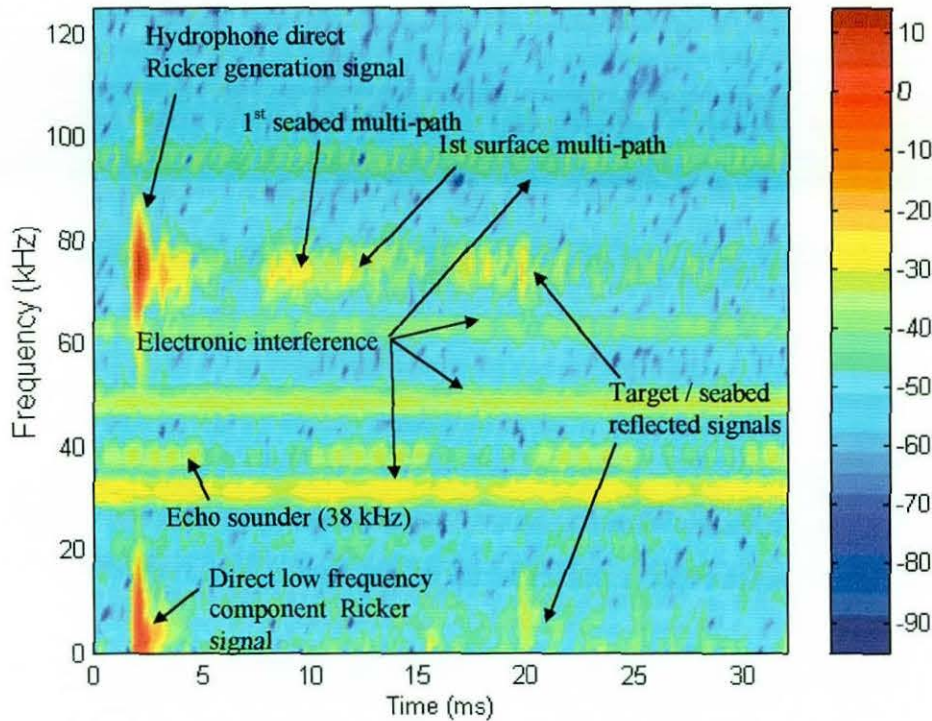


FIGURE 8.13 NEAR BROADSIDE TARGET, WATER-FILLED, WIDE BANDWIDTH RECORDING, 7 kHz RICKER AND RICKER GENERATION SIGNAL

Both the higher frequency component (centred on 75 kHz) and the lower frequency Ricker signals (centred about 7 kHz) are clearly visible for the direct signal. A strong echo is also visible in both frequency bands in the expected time position for the known target position. The higher frequency signal is however surrounded by additional echoes, making distinction of the target echo harder if the position was not known. The strong return at the expected target position was due to possible contributions from the target and from the sediment within the insonified area. Comparison with the lower frequency target / seabed echoes, shows a more distinct echo, suggesting that the majority of the back-scattered energy in this band is due to the presence of the target. The more cluttered higher frequency signals are due to a higher back-scattering strength often seen with higher frequencies [7.25]. The lower frequency component is more likely to penetrate the sediment and not provide significant back-scattered energy. The interaction with a sediment-embedded object of higher target strength, would in this case contribute to the majority of the back-scattered energy, assuming sufficient penetration and absorption of the incident signal by the sediment. This

could become particularly important in the case of sediment-buried objects.

Figure 8.13 also illustrates the directional properties of the secondary frequency signal from a parametric source, with little or no additional back-scattered signal, compared with the high frequency component. The additional back-scattered signal contributions at the higher frequencies, are due to the higher reflectivity of the signal and the energy available in the side-lobes of the signal. This is evident in the identification of the first seabed multi-path signal arriving at the ring transducer for this geometry. Little or no indication of this is seen at the lower frequency.

Figure 8.14 shows the narrow-band time domain response of the direct and target / seabed echoes for the broadside position target. The amplitude scale is again expanded to enhance the target echo relative to the direct signal, giving the appearance of being clipped. The hydrophone response at the lower frequencies is relatively flat over the frequencies of interest and no compensation for variations in hydrophone sensitivity with frequency was made in the analysis of narrow-band recordings.

An expanded view of the seabed / target echo is shown in Figure 8.15. The time delay of  $330 \mu\text{s}$ , between the positive-going peaks again closely matched the through water propagation distance of 49.5 cm. This is close to the two-way path across the diameter of the cylinder, suggesting specularly reflected, lower frequency energy from both the front and back face of the cylinder, whilst partially embedded in the broadside position. This can be compared with the free-field response at the higher frequencies, as seen Figure 7.13, showing evidence of both front and back face specular reflections.

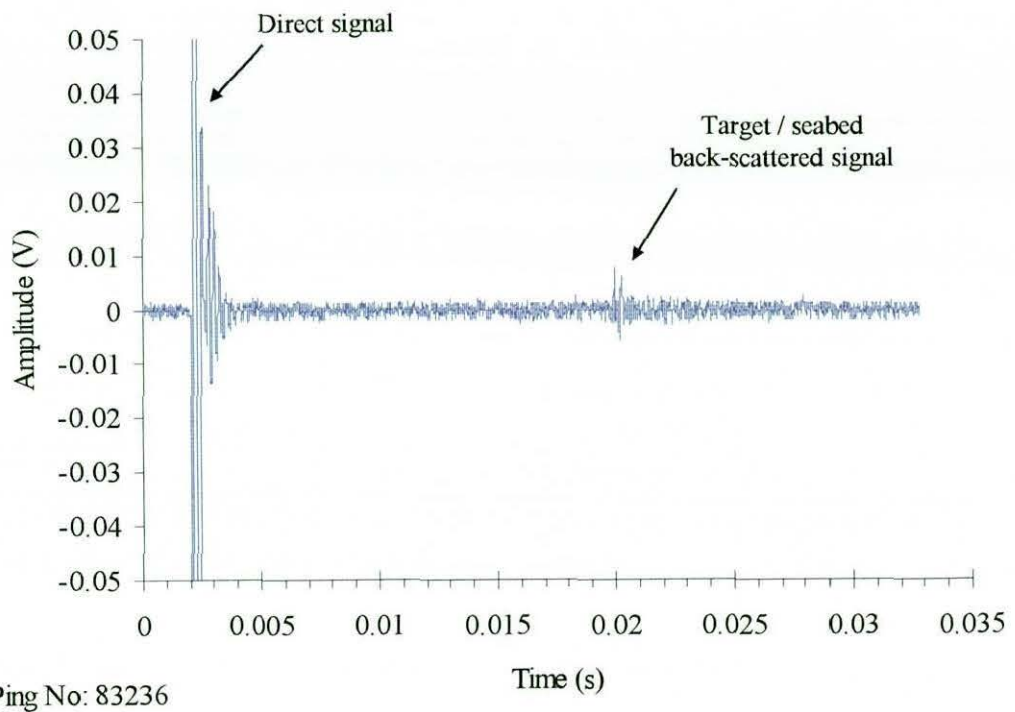


FIGURE 8.14 DIRECT AND SEABED / TARGET ECHO, BROADSIDE POSITION, SEDIMENT-EMBEDDED TARGET

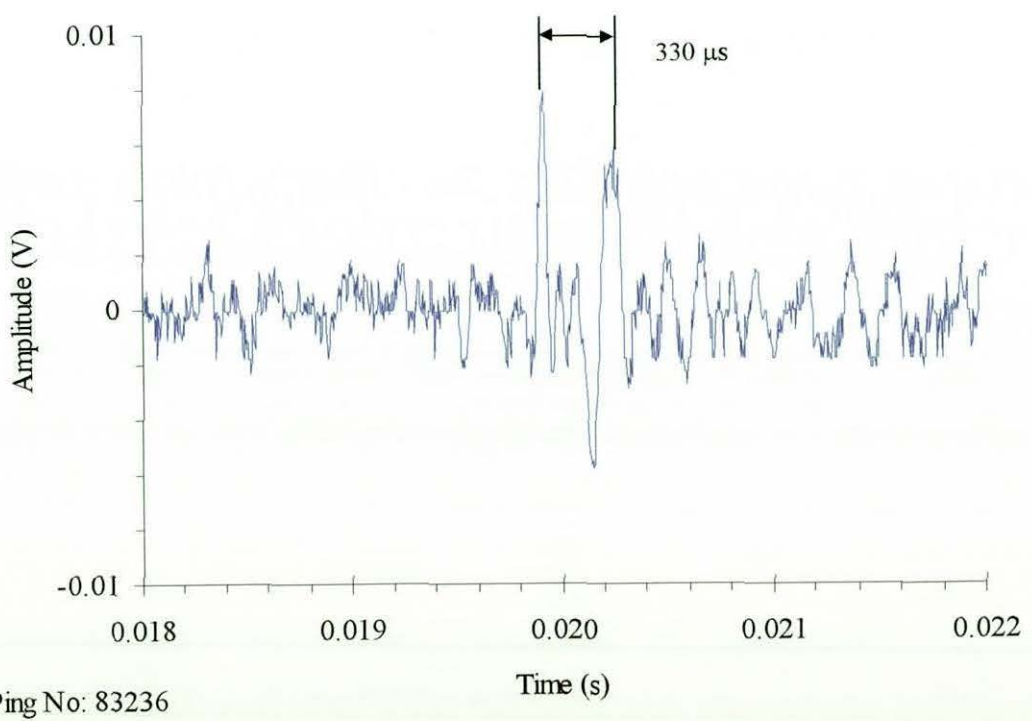


FIGURE 8.15 SEABED / TARGET ECHO, BROADSIDE POSITION, SEDIMENT-EMBEDDED TARGET, 7 kHz RICKER

The later part of the signal also shows a lower frequency component, seen to start as the negative-going part of the signal, slightly preceding the expected position of the back face specular reflection. This can be seen more clearly in Figures 8.16 and 8.17, showing the spectral analysis of the target echo signal observed at seabed grazing angles  $39.6^\circ$  and  $35^\circ$ .

Again, assuming spherical spreading losses for the propagation from the hydrophone to the target,  $TL_1 = 2.8$  dB. Similarly with the hydrophone is in the far-field of the target the returning transmission loss is estimated as 23.0 dB giving a target strength of  $-11.2$  dB.

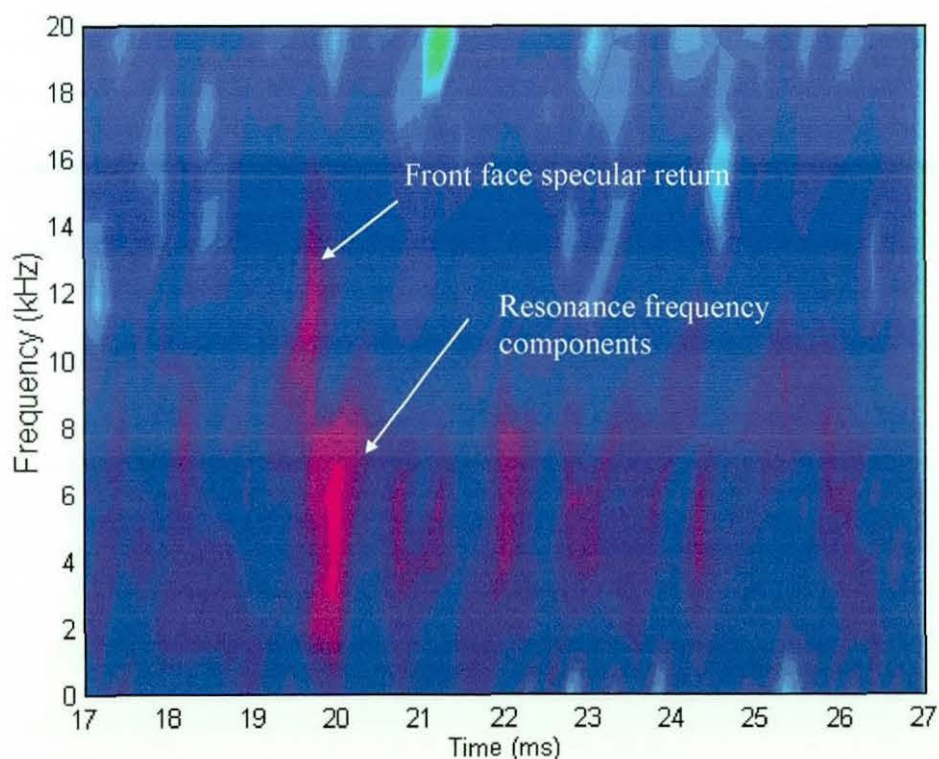


FIGURE 8.16 TARGET-ECHO, 7 kHz RICKER, WATER-FILLED TARGET, A  $-4^\circ$  ASPECT ANGLE, SEDIMENT-EMBEDDED, SEABED GRAZING INCIDENT ANGLE  $39.6^\circ$

Comparison was then made with a seabed-scattered signal, with the target removed at the same incident angle. Comparison of the direct signals still present in both recordings allowed the signals to be phase aligned. This allowed direct

comparison of the seabed echo with and without a target. Figure 8.16 shows the target echo contribution for the 7 kHz Ricker signal. This can be compared with Figure 7.15, the low frequency response of the target, in a similar orientation in the free-field. Both target echoes exhibit similar characteristics, with a leading edge broadband response between 6 and 14 kHz, most likely due to the front face specular return. The strongest return is seen in both cases between 3 and 6 kHz, slightly lagging the specular return, possibly corresponding to low frequency resonance effects characteristic of the target. In the embedded target case, this is of shorter duration, possibly due to the damping effects of the surrounding sediment.

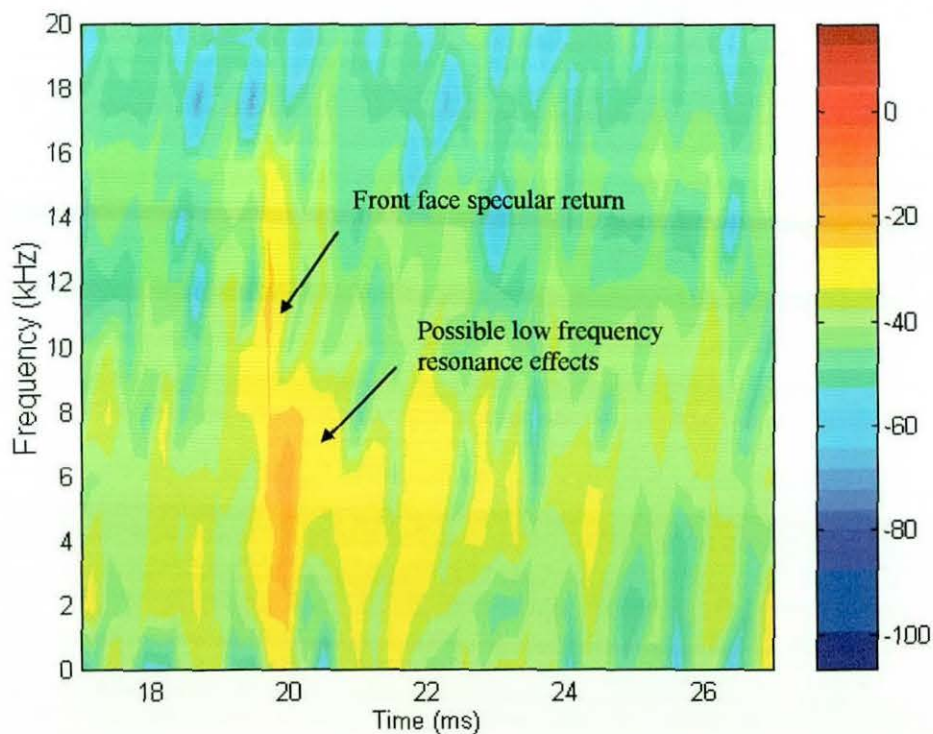


FIGURE 8.17 TARGET-ECHO, 7 kHz RICKER, WATER-FILLED TARGET, A  $-4^{\circ}$  ASPECT ANGLE, SEDIMENT-EMBEDDED, SEABED GRAZING INCIDENT ANGLE  $35^{\circ}$

A similar response, shown in Figure 8.17, shows the narrow-band (1-25 kHz) target echo signal, with the source lowered to 15 m below the surface, altering the seabed grazing angle from around  $39.6^{\circ}$  to  $35.0^{\circ}$  for the near broadside target position. The intensity colour scales were selected arbitrarily to provide the best contrast against the background for each echo. The target-free signals obtained at

both grazing angles showed little low frequency energy return from the expected area of seabed insonification. Comparison of the target *present* / *not present* cases suggests that most of the lower frequency energy components visible in Figures 8.16 and 8.17, are due to the presence of the target.

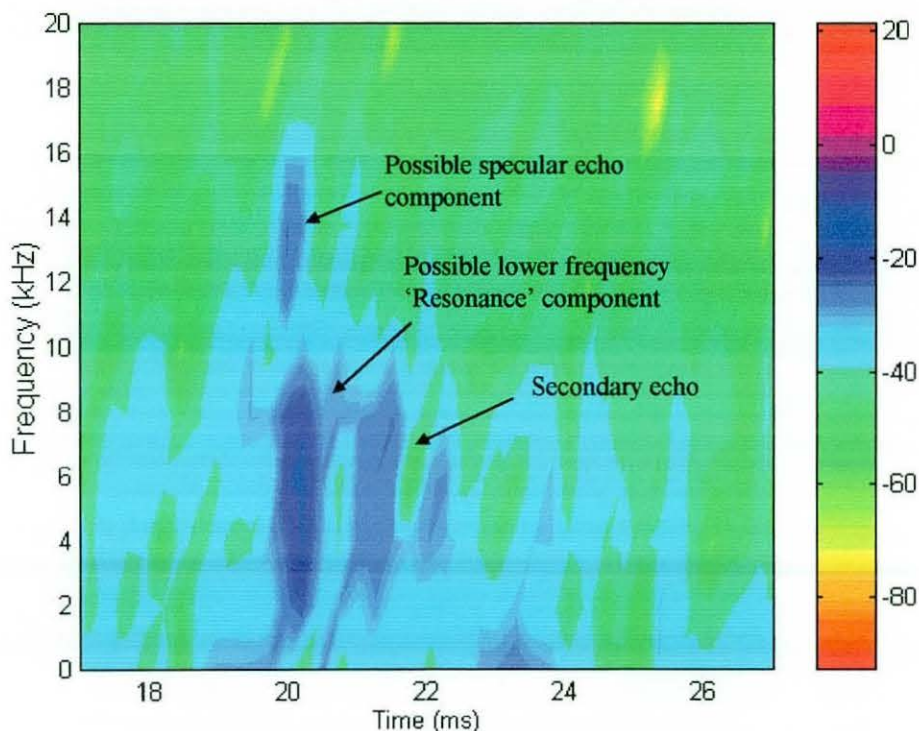


FIGURE 8.18 TARGET ECHO 7 kHz, WATER-FILLED TARGET, A +10° ASPECT ANGLE, SEDIMENT-EMBEDDED, SEABED GRAZING INCIDENT ANGLE 39.6°

Figure 8.18 shows the 7 kHz Ricker target response for a +10° aspect angle at a grazing angle of 39.6°. Some similarities in the echo structure from the near broadside position are evident. The specular echo from the front face is, however, less prominent, and the majority of the energy is returned in the range 2-8 kHz, corresponding to similar echo components seen in Figures 8.16 and 8.17. Again this component may be due to a combination of resonance effects similar to those seen earlier. A secondary echo, approximately 1.18 ms after the main resonance echo, is also evident. This echo was also observed in the near-broadside position but at a lower intensity relative to the main resonance and specular returns. The source of the secondary echo is not fully understood. Figure 8.19 shows the time

domain plot, for the above target echo.

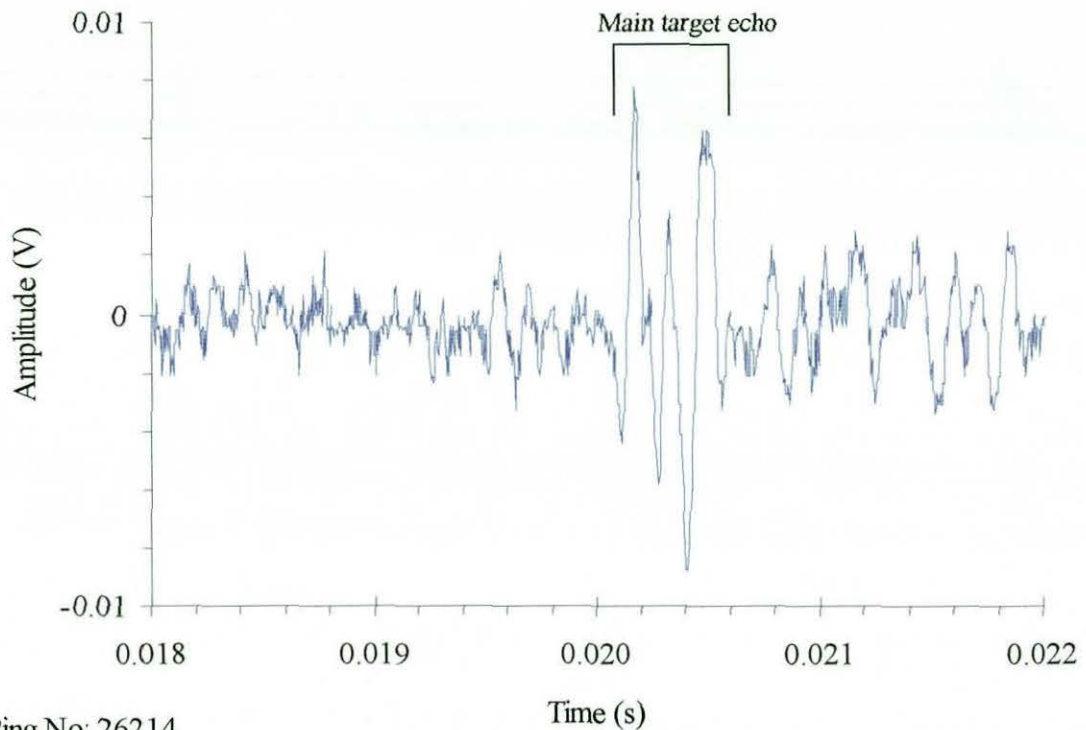
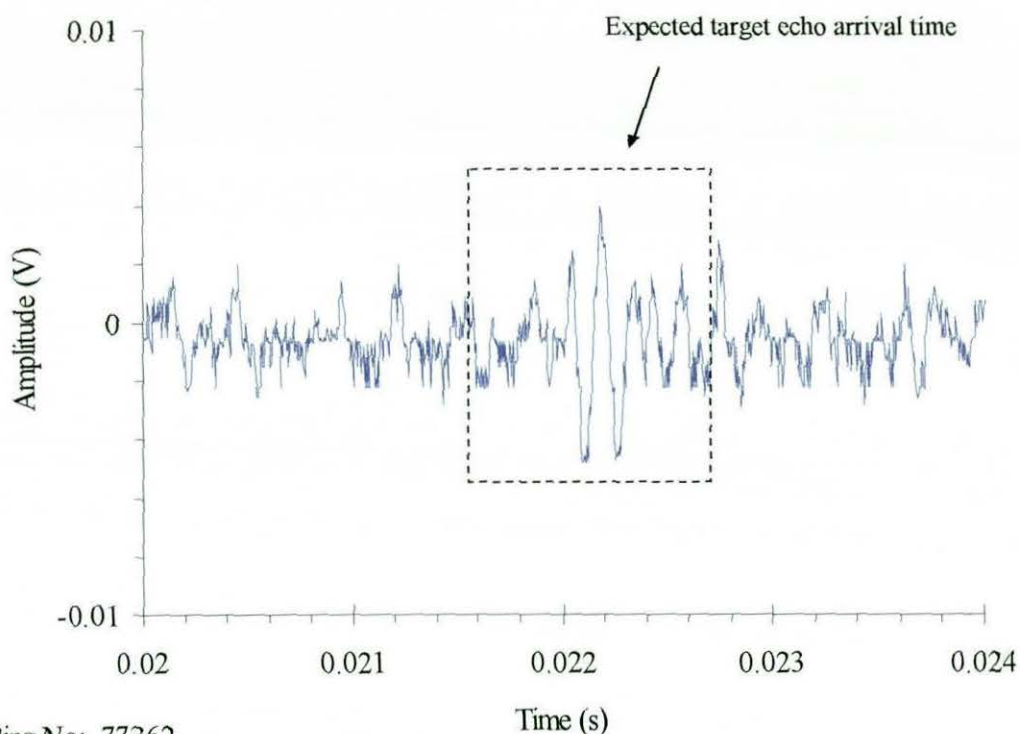


FIGURE 8.19 TARGET ECHO 7 kHz, WATER-FILLED TARGET, A  $+10^\circ$  ASPECT ANGLE, SEDIMENT EMBEDDED, SEABED GRAZING INCIDENT ANGLE  $39.6^\circ$

The echo structure is similar to that seen at near-broadside, with the separation of the two main positive-going peaks relating closely to the diameter of the cylinder. Comparison with Figure 8.15, shows the development of the signal between the two main peaks previously discussed. This internal echo structure was observed becoming more dominant compared to the specular return as the target aspect angle was increased. Figures 8.20 shows the time domain plot for a  $+26^\circ$  target position. The target echo still shows a reasonable signal-to-noise. The frequency distribution of the main echo is consistent with that observed previously but with little or no evidence of the target front and back face specular returns. Comparison of timings for the target internal hydrophone shows a 2-3 m displacement away from the source of the target from previous orientations. This was due to drifting of the target raft in varying current conditions during the target reorientation phase. A resulting, 2 ms shift in the target echo arrival time was therefore observed.





Ping No: 77362

FIGURE 8.20 TARGET ECHO 7 kHz, WATER-FILLED TARGET A  $+26^\circ$  ASPECT ANGLE, SEDIMENT EMBEDDED, SEABED GRAZING INCIDENT ANGLE  $39.6^\circ$

Both time and frequency domain analysis, of aspect angles greater than  $\pm 26^\circ$  showed a poor signal-to-noise ratio for returned signals, making identification of the target echo components difficult.

Analysis of the end-cap position signals also proved difficult. Comparison of target *present* / *not present* cases showed with no clear echo structure due to the presence of the target at the range of seabed angles measured.

The HS150 (12 mm ball hydrophone) deployed inside the target was primarily used for transmitter–target alignment and precise timing measurements. The recording of the signal on a parallel data channel, synchronous with the ring hydrophone recordings, allowed close estimation of hydrophone–target distances at the various aspect angles. Figure 8.21 shows the broad-band response for a 7 kHz Ricker generation signal on the internal hydrophone.

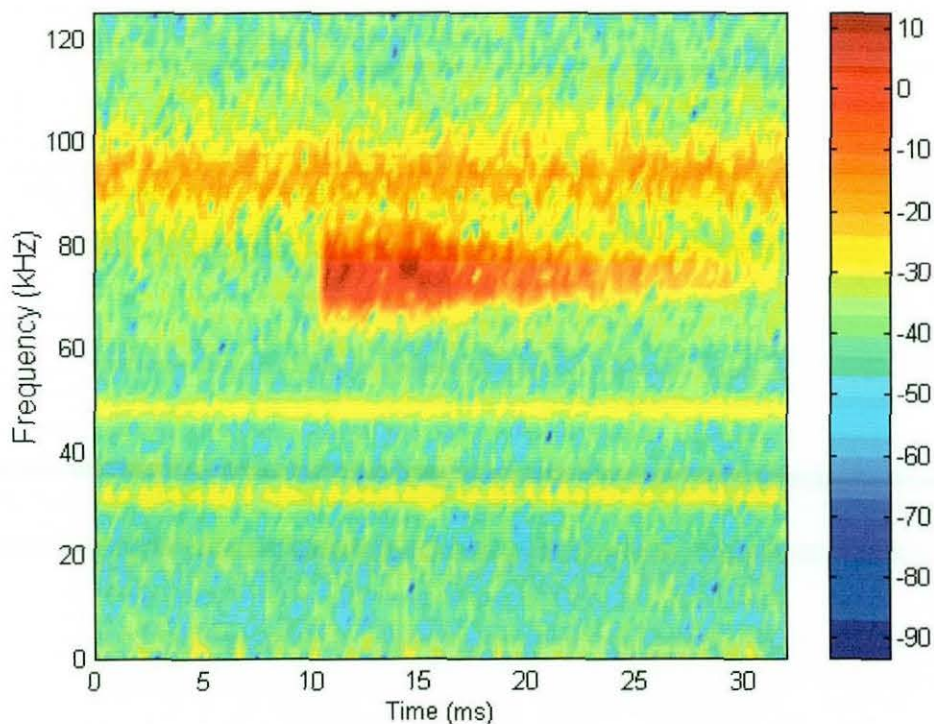


FIGURE 8.21 INTERNAL HYDROPHONE, 7 kHz RICKER GENERATION SIGNAL, TARGET NEAR BROADSIDE POSITION, WATER-FILLED.

Comparison with Figure 8.13, for the same transmission seen on the ring transducer, shows the main signal arrival, approximately equidistant in time between the direct and target echoes, observed on the ring. A slight disparity in timings will be due to the placement of the ball hydrophone, in the radial centre of the target, 12.5 cm from the outer surface, resulting in the specular reflections observed on the ring transducer.

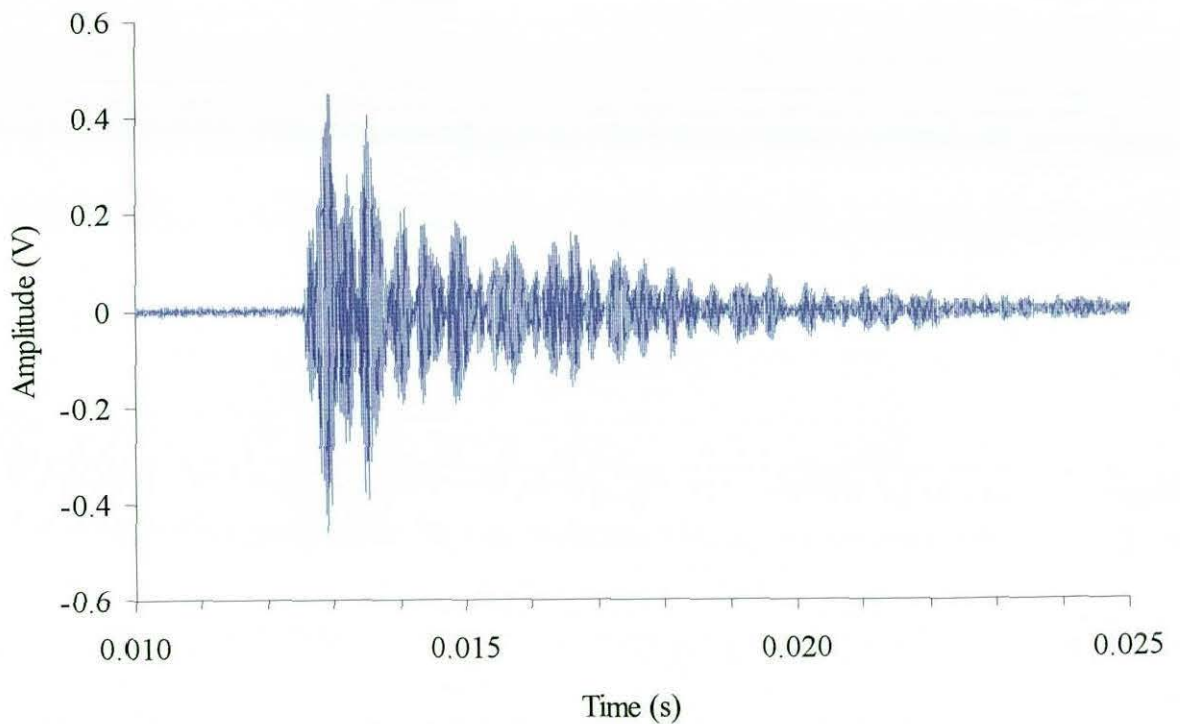


FIGURE 8.22 1-100 kHz BANDWIDTH INTERNAL HYDROPHONE, 7 kHz RICKER GENERATION SIGNAL, TARGET  $+26^\circ$  POSITION, WATER-FILLED.

Figure 8.22 shows the internal hydrophone time domain response for the  $+26^\circ$  target orientation. No direct predictions of the internal reflection characteristics of the target at the higher frequencies (75 kHz) have as yet been carried out. This Figure does, however, illustrate a development of multiple internal reflected signals inside the target. This can be compared with the direct signal pulse similar to that seen in Figure 7.9(c), of duration around 450  $\mu$ s. Primary frequency (75 kHz) energy was observed, shown in Figure 8.21, up to 20 ms (44 x the original pulse length) after the first arrival signal. Suggesting a complex interaction of the direct high frequency energy within the target and the surrounding seabed, resulting in multiple echo arrivals.

Spectral analysis of the narrow band response (1-25 kHz) for the same incident signal, shows a strong low frequency presence at the internal hydrophone,

confirming the penetration of low frequency components to the water-filled space inside the target, as shown in Figure 8.23.

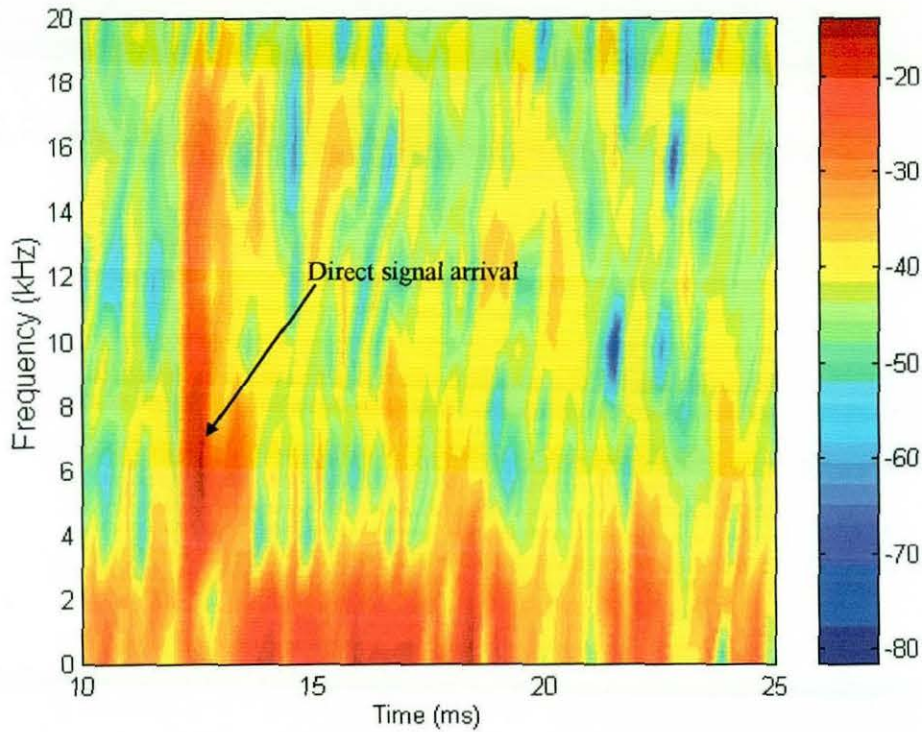


FIGURE 8.23 NARROW-BAND SIGNAL (1-25 kHz), INTERNAL HYDROPHONE, 7 kHz RICKER SIGNAL, TARGET +26° POSITION, WATER-FILLED.

Figure 8.23 shows a strong broad-band response, with the peak energy around 6-8 kHz, consistent with the 7 kHz Ricker signal used. This energy band is seen to decay within a few milli-seconds, with little or no energy in this band after this time.

### 8.6.3 Non-acoustic measurements

CTD profiles were carried out on a daily basis, using a Plessey Sound Velocity Sensor, Type M031 /SN 123 supplied by TNO-FEL. This allowed direct measurement of sound velocity and temperature with depth. Figure 8.24 shows a typical temperature versus depth profile, observed during the trial period. Temperature variations in the order of  $2^{\circ}\text{C}$  were observed over the 45 m water column. Comparison with previously obtained data showed little seasonal variation in the Loch.

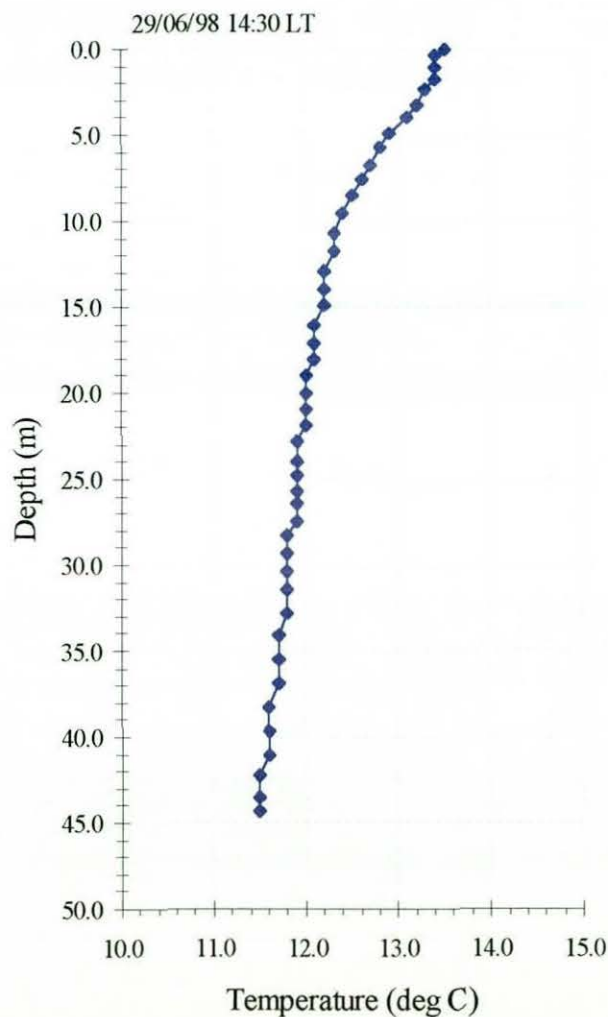


FIGURE 8.24 TEMPERATURE VERSUS DEPTH, LOCH DUICH 1998

Again a typical sound velocity–depth profile is shown in Figure 8.25. Sound velocity in the main water column showed little variation over the trial period,

with the average sound speed between  $1492 - 1493 \text{ ms}^{-1}$ . Variations in the top 2 m were however observed, due to fresh water run off from surrounding mountains during periods of heavy rain.

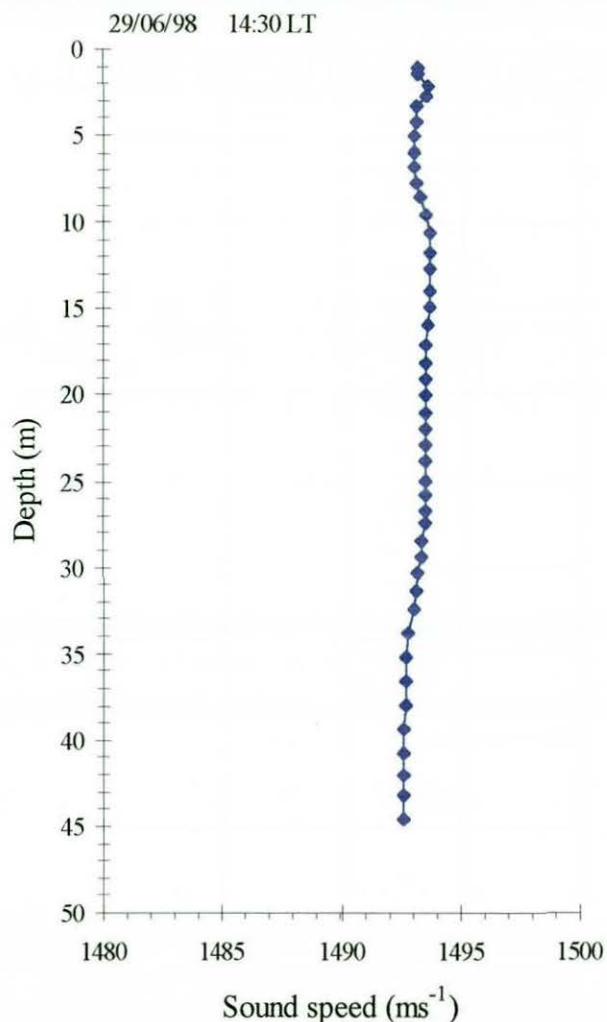


FIGURE 8.25 SOUND VELOCITY PROFILE

Two sediment samples were taken in the region of the seabed directly below the source and the target placement area. Samples taken were from the first 10-20 cm from the water sediment interface. These samples were frozen shortly after retrieval to maintain water content. Post analysis carried out by the School of Ocean Sciences, University of Wales, gave a compressional sound velocity at  $19.5^\circ \text{ C}$  and  $286 \text{ kHz}$  of  $1518 \pm 3.5 \text{ ms}^{-1}$ , and an attenuation coefficient of  $66 \pm 3 \text{ dBm}^{-1}$  or  $0.34 \text{ dB / wavelength}$  for the target seabed area. Some variation was seen in the sample taken directly below the source, with a higher attenuation and lower

velocity. It was not possible to take into account saturated gas content due to the hydrostatic pressure (40-45 m) experienced by the *in-situ* sediment and some variation between measured and *in-situ* characteristics seems likely.

Particle size and moisture content was measured for the same samples by the Environmental Chemistry Laboratories, Marine Laboratory, the Scottish Office. Both samples gave moisture contents between 60 % and 62 %.

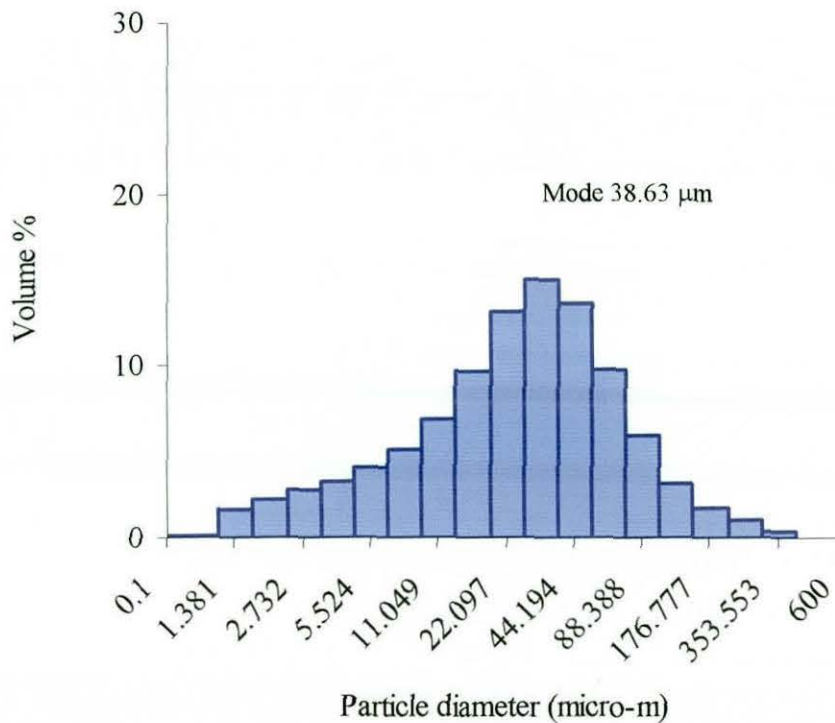


FIGURE 8.26 PARTICLE SIZE DISTRIBUTION OF SEDIMENT SAMPLE FROM LOCH DUICH 1998

Figure 8.26 shows the particle size distribution for the target area sample. This gave a mean particle diameter of 31.8  $\mu\text{m}$ , with 78 % of the particle volume having diameters below 63  $\mu\text{m}$ . The sample itself is described as poorly sorted coarse silt.

An additional study was carried out by the University of Wales on a 2 m long core, taken from Loch Duich in 1996. Measurements from the ends of the core were unfortunately not possible, due to the core drying out during storage. In the centre section sound velocity was found to vary from 1470 to 1490  $\text{ms}^{-1}$  at 21° C

for a 250 kHz signal, reasonably consistent with the sound velocity measured for the more recent samples. No evidence of sub-bottom layers was seen in any of the samples.

## 8.7 Conclusions

Both experiments provided reasonable data concerning the free-field and seabed embedded target responses of a 1 m long, 0.25 m diameter, thin-walled cylinder with flat end-caps. In the free-field case the target was insonified over a wide range of aspect angles with a range of signal types. Assessment of both target length and diameter was possible, with the target in end-cap and broadside positions respectively, from back and front face specular returns. Evidence of low frequency components, possibly due to target resonance effects, were also observed in the broadside position. Measurement of end-cap and broadside target strengths, also showed good correlation with theoretical figures.

In the second phase experiment a similar water-filled target was insonified, at a range of aspect angles to the source, whilst partially embedded (up to 50 %) in a soft sediment. Analysis of direct and target-scattered signals, showed the possibility of target detection for the seabed-proud target, at aspect angles up to 23° from the broadside position, for seabed grazing angles from 32° to 42°. Comparison of target *present / not-present* data also gave good evidence of the detection of target-generated, back-scattered components in the 1-20 kHz frequency region. Comparison with free-field data of similar signal type and orientation, showed a reasonable correlation in observed echo structure, including the identification of front face specular returns up to 10° from broadside and possible low frequency resonance components up to 23° from broadside. Analysis of seabed reverberation levels at the lower frequencies (1-20 kHz) showed little or no significant back-scattered energy from the target-free sediment, due to penetration and absorption of the signal. This was compared with the high reverb levels observed with the 75 kHz component, making target detection difficult.

The parametric source seems to be a viable option for the detection and possible



classification of seabed-embedded targets of this size. The low frequency, high directivity source showed considerable improvement in the ease of target detection over a higher frequency source. Some degree of target classification using relatively simple analysis techniques was possible through the measurement of front and back face specular returns, for a relatively narrow band of target aspect angles. The observation of low frequency resonance effects may also provide additional data, concerning target geometry and material over an aspect angle range of up to  $23^\circ$ .

## REAL-TIME CORRECTION OF TRANSMISSION PLATFORM INSTABILITIES USING A PARAMETRIC ARRAY

### 9.1 Introduction

The need for precise seabed incidence angles in a sub-bottom profiling system has led to the consideration of the various instabilities that can occur when using such a system at sea. The initial testing of the system from a ship took place in August 1994, in the Atlantic, as part of the REBECCA project and later as trials in the SIGMA project. In each case the oblique incidence transmissions were achieved by deploying the parametric array from a tow-fish. Forward-scattered signals from the bottom and sub-bottom layers were then collected using a streamer array towed behind the fish, as shown in Figure 9.1.

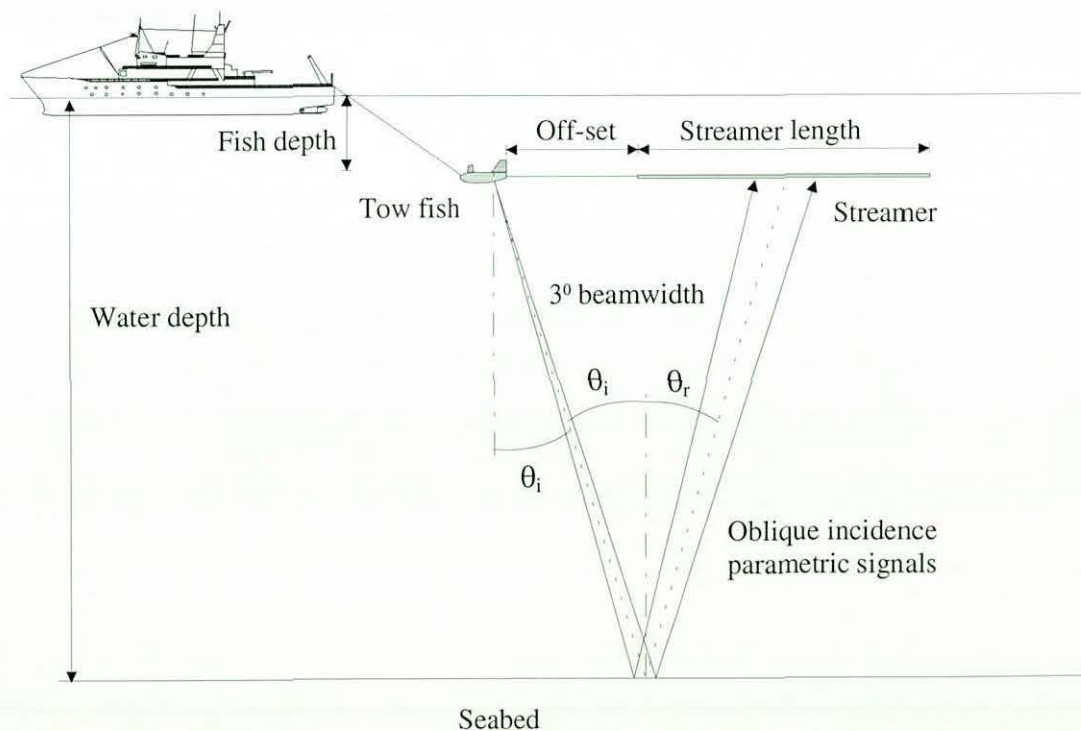


FIGURE 9.1 DEPLOYMENT OF THE NON-LINEAR ARRAY  
WHILST BEING TOWED.

The transducer array was deployed in a tow-fish, trailed behind the vessel at a depth between 10 and 20 m and at speeds of 2-3 knots. Instabilities in the motion of the tow-fish could lead to variations in the desired seabed incidence angle. Any error in this angle reduces the efficiency of the system and heightens the chance of misalignment between the reflected signals and the streamer used to monitor these signals. Similar variations in the seabed incidence angle are seen if there is any change in the slope of the seabed. Both of these effects were considered as potential sources of error in the transmitter-receiver alignment and therefore successful data capture. A successful stabilisation system would firstly have to predict possible errors (through knowledge of both the transducer array inclination and any seabed slope) and secondly, compensate for any errors in the transmitted signal. This, if achievable in real time, should lead to an overall improvement in the system efficiency and its usefulness whilst at sea.

This chapter sets out to discuss various methods of monitoring both the variations in transducer array orientation and the seabed slope, and then considers a number of techniques that would allow for the compensation of any errors encountered. The use of electronic beam steering to correct for alignment errors in at least one plane of movement is proposed. This is combined with real-time modelling of alignment errors, using a variety of sensor inputs.

## **9.2 Tow-fish and streamer deployment**

The positioning of the array within the tow-fish is shown in Figure 9.2. It was proposed that the transducer array be positioned so that the normal to the array face is at a fixed angle, measured to the vertical, in the fore-aft plane. Deployment angles of  $10^\circ$ ,  $15^\circ$  and  $20^\circ$  were possible within the tow-fish. Angles were selected depending on the geometry of the system components at the time, including fish-depth, water depth, streamer length, streamer offset, seabed slope, etc. The transducer array was arranged to allow electronic beam steering in the fore-aft plane. Assuming a steer capability of  $\pm 18^\circ$  (section 4.6), this would allow seabed incidence angles of between  $-8^\circ$  and  $38^\circ$ , utilising all three-deployment settings. This assumes that the seabed is perfectly flat and not sloping over the area of the

trial. The various seabed incidence angle ranges available for each deployment angle are shown in Table 9.1. Alteration of the proposed deployment angle  $\theta_0$  would require removal of the tow-fish from the water and mechanical changes made to the transducer array position within the tow-fish.

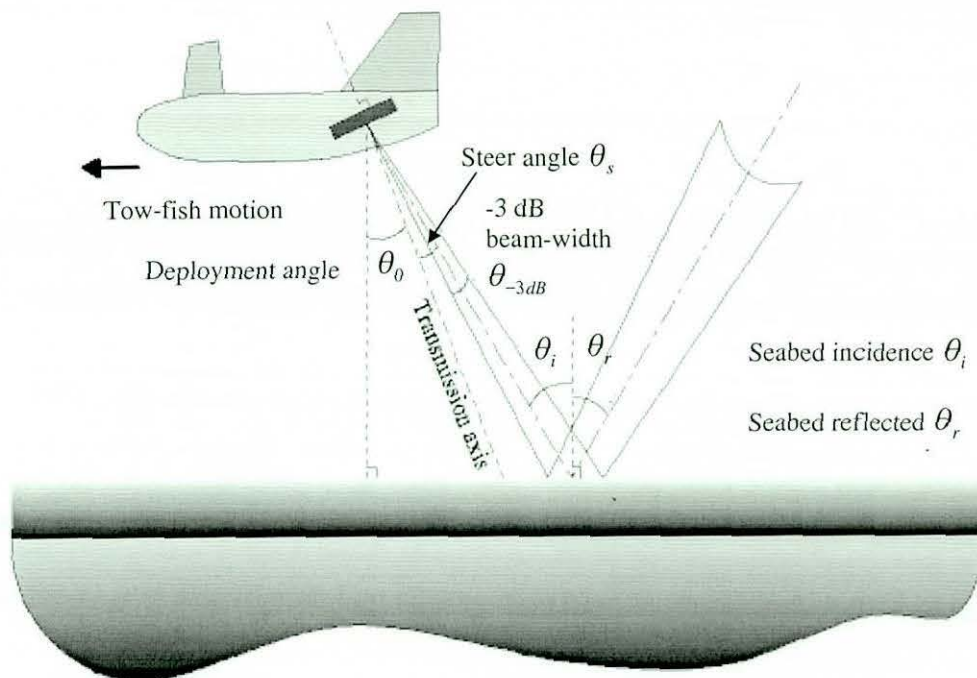


FIGURE 9.2 TRANSMISSION ANGLE ARRANGEMENT

Deployment angle	Minimum sea-bed incidence angle	Maximum sea-bed incidence angle
10°	-8°	28°
15°	-3°	33°
20°	2°	38°

TABLE 9.1 MAXIMUM AND MINIMUM SEA-BED INCIDENCE ANGLES FOR VARIOUS DEPLOYMENT ANGLES MEASURED IN THE FORE-AFT PLANE. (ANGLES IN THE AFT DIRECTION ARE TAKEN AS POSITIVE.)

### 9.3 Ship and tow-fish motion

Variations in the transducer array's orientation are usually due to normal ship motion. These variations are generally oscillatory in nature (with relatively regular cyclic periods). Matters are however further complicated by the deployment of the array from within a tow-fish, towed behind the vessel. Ship motion can be defined in terms of three rotational modes, around three mutually perpendicular axes and three transitional modes, along these axes, as shown in Figure 9.3. Movement in the (fore-aft) plane mentioned in section 9.2 may then be defined in terms of the rotational plane; pitch and the two transitional modes; surge and heave. Pitch is seen as a rotation about an axis shown perpendicular to the page in Figure 9.3. The surge axis is defined as running along the length of the ship. This is perpendicular to the sway axis across the ship. Both are defined as being mutually perpendicular to the heave axis, which is parallel with the vertical axis acting down through the ship. Movement of the tow-fish is defined using an identical reference system.

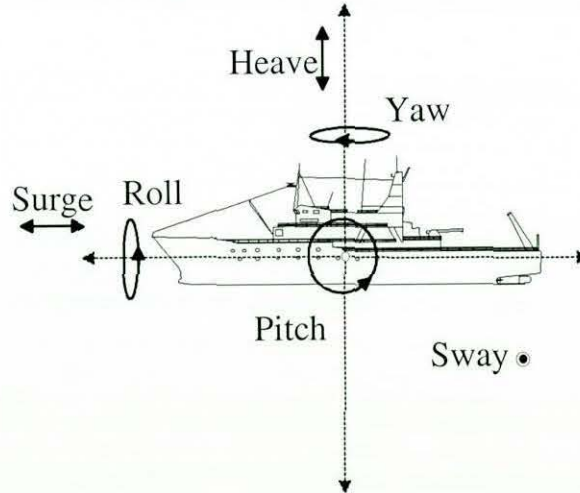


FIGURE 9.3 MOVEMENT IN ROTATIONAL AND TRANSITIONAL AXES DEFINING SHIP MOTION.

The ship itself, and therefore the tow-fish, is subject to a series of instabilities due to sea movement. Under consideration here are errors introduced due to the ship's pitch, roll, yaw, heave, surge and sway.

When the tow-fish is pulled behind the ship, as shown in Figure 9.4. it seems likely that the pitch, surge and heave components of the ship's movement result in a tugging of the towing cable along the line of the tow-fish's own forward motion. This movement is then translated into either pitch, surge or heave components of the tow-fish. The degree of movement in each of these is dependant on the tow-fish's own hydrodynamic properties. These can compensate for some of the translated movement but still leave some movement possible. Yaw, roll and sway movements in the ship are likely to introduce some sideways movement into the cable tugging action. The degree of effect this has on the tow-fish movement is again dependent on the tow-fish's dynamic properties.

Transitional movement in either the surge or heave axes of the tow-fish should not affect the seabed incidence angle. Movement in the heave axis would however change the area insonified on the seabed. This in turn could mean the loss of reflected signal at the streamer.

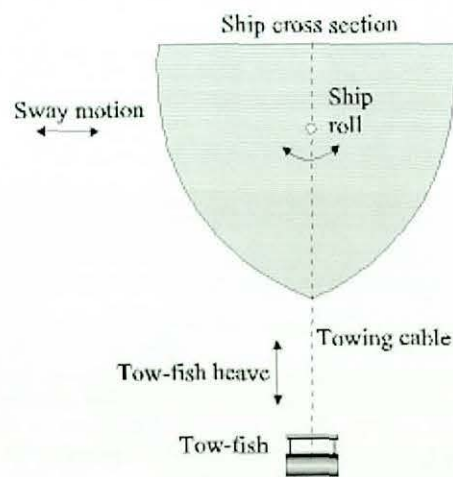


FIGURE 9.4 TRANSLATION OF SHIP MOVEMENT INTO VARIOUS MOVEMENT FUNCTIONS OF THE TOW-FISH.

Assuming 100 m water depth with the tow-fish at 10 m and a sea-bed incidence angle of  $20^\circ$  (measured from the centre of the beam), the centre of a reflected signal will reach the streamer (at the same depth) 65.6 m behind the tow-fish. A

downward displacement of 2 m in the tow-fish's heave axis, gives an equivalent reflected signal approximately 64 m behind the tow-fish. This gives a forward displacement of the reflected signal at the streamer of 1.6 m. Movement of this order was not felt significant for most practical deployments. A similar calculation was performed assuming a  $2^\circ$  shift in the tow-fish's pitch axis. This gives a seabed incidence  $\theta_i$  of  $22^\circ$ , the angular shift again translating to a displacement in the horizontal arrival point of the reflected signal. In this case the centre of the reflected signal is seen 72.7 m behind the tow-fish. This is a displacement of approximately 7 m. Angular variations of this order could potentially result in failure to capture any of the reflected signal, thus impairing the system's operation.

Movement in either the roll or yaw axes of the tow-fish results in a sideways and forward-backward displacement of the effective seabed sonar footprint (the area on the seabed insonified by the sonar). This gives a similar displacement in the area insonifying the hydrophone streamer. A  $3^\circ$  beam-width signal has a footprint width of around 10 m at the streamer (assuming the case as in the previous example). An angular movement in either the roll or yaw planes of the tow-fish of anything greater than  $\pm 1.5^\circ$  would result in the complete loss of the main reflected signal at the streamer.

Results obtained from pitch, roll and depth sensors in the tow fish are presented in section 6.2.4.1. These were recorded during the SIGMA trials and show both pitch and roll variations in sea-state 3 of  $\pm 5^\circ$  and  $\pm 2^\circ$  respectively and in sea-state 4-7 of  $\pm 6^\circ$  and  $\pm 3^\circ$ . In the case of the earlier REBECCA project, very little data was successfully obtained on the streamer due to pitch and roll variations of a similar order.

## **9.4 Dynamic stabilisation**

### **9.4.1 Introduction**

The problem of stabilisation is inherent in many sonar systems. Existing technology uses a number of methods including the use of stabilised platforms, electronic stabilisation and discontinuous transmissions. The use of phase-steering

techniques is also considered in this study, to allow for the correction of errors seen in the array's orientation.

- 1) Stabilised platforms have been widely used with sonar systems for a number of years. These usually incorporate a highly responsive platform, physically moved to compensate for any movement measured in the ship. This requires a high degree of mechanical precision and real-time processing but has been shown to provide a high degree of stability, in three rotational planes of movement. These systems do however require regular maintenance and are generally extremely costly.
- 2) An electronic stabilisation technique involves the collection of all available data, regardless of the instabilities experienced and then applies a degree of post correction to the collected data. The post-correction of all the collected data has been incorporated into a number of real-time systems, including use with sector-scanning sonars <sup>[9.1]</sup>.
- 3) Discontinuous transmission systems rely on the natural periodicity of ship motion. This disables the transmission of a signal until the transducer array is in alignment with the required target. This again requires knowledge of the degree of instability in the sonar system. The potential uses of such a system are discussed further in section 9.4.4.
- 4) Phase-steering techniques have also been considered as a possible method of angular compensation of the errors introduced due to ship/tow-fish motion. The introduction of phase differences in the various signals applied across the transducer array can be used to steer the beam away from the normal heading. This is a simplified case of the swept signals seen in section 4.6. A swept signal is generated through the application of a varying phase difference across the transducer array. If the phase difference is constant, a beam-pattern of constant heading is possible.



## **9.4.2 Error prediction**

### **9.4.2.1 Introduction**

It was hoped that, the tow-fish would be stable to within  $\pm 1.5^\circ$ , in the pitch and roll planes. A stabilisation system capable of correcting for any deviation in the tow-fish's orientation would however still be of some advantage. As demonstrated in section 9.3 movements in the surge and heave axes of the tow-fish are relatively insignificant, in terms of horizontal displacement of the reflected signal and receiver misalignment. Slight angular variations in either the pitch or roll axes are however considered of much greater consequence in terms of lost signal and loss of accuracy in the seabed incidence angle. Movement detection in either of these planes is therefore considered of primary importance when estimating potential errors in the seabed incidence angle. From the geometry shown in Figure 9.5, angular variations in pitch greater than  $\pm 3^\circ$  would result in the loss of data on the streamer. Correction of yaw, roll and sway based errors was also considered. Recent improvements in the tow-fish design show a marked improvement in fish roll stability. From Figure 6.6 and 6.7 roll errors of the order of  $\pm 3^\circ$  were observed but with the majority of signals the error was within  $\pm 1.5^\circ$ , allowing successful data capture.

Any real-time correction system will therefore have to predict likely errors due to the geometry and compensate before transmission. From Figure 9.1 some of the factors considered to allow variation in alignment included tow-fish pitch, roll, surge, heave, yaw, etc, tow-fish depth, water depth, streamer off-set, streamer depth and seabed slope.

### **9.4.2.2 Software models**

Software models were developed, allowing visualisation of the deployment geometries experienced during sea-trials. Incorporation of these models with real time sensors allowed real time prediction of alignment errors. Models developed during the ACUSTICA project included sub-bottom acoustic propagation paths for various propagation modes (compressional and shear), in at least one plane of

movement. These were initially developed to show alignment errors whilst post processing the data. Figure 9.5 shows a typical deployment configuration for the successful capture of forward-scattered data, from both the water-seabed interface and a 5 m thick sediment layer above an infinite substrate, obtained during the SIGMA trials. With a  $20^\circ$  deployment angle, a fixed  $-3.4^\circ$  steer angle is applied to allow collection of bottom and sub-bottom reflected data. The 12 m long streamer array is insonified by both the bottom (red) and sub-bottom (blue) reflected signals. Due to the difference in propagation paths, different times of arrival are seen at the streamer array. With knowledge of the sound velocity - depth profile, prediction of likely arrival times for various signals is possible, adding signal identification. Figure 9.5 shows the rear of the streamer array slightly higher in the water compared with the front. Post analysis of sensor data from the streamer showed this to be the case during the SIGMA trials. This was most likely due to drag experienced from a parachute on the rear of the streamer.

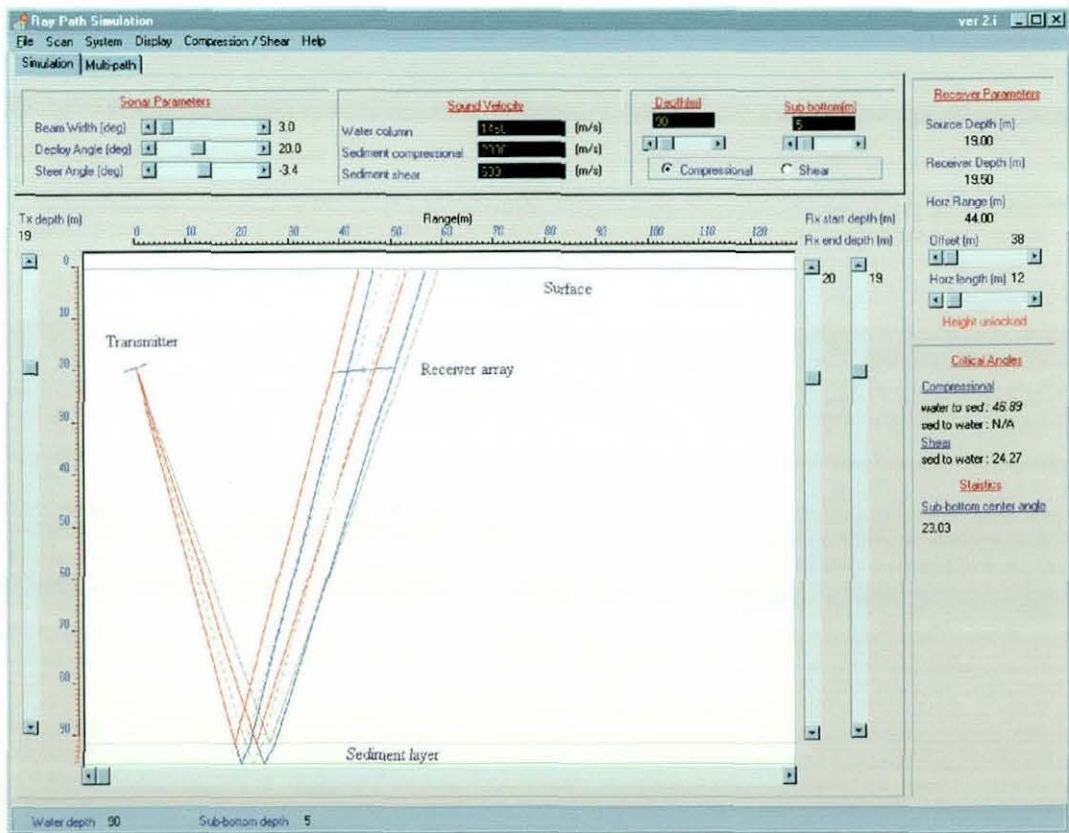


FIGURE 9.5 TRANSMITTER-RECEIVER ALIGNMENT FOR SUCCESSFUL DATA CAPTURE OF SEABED AND SUB-BOTTOM LAYER SCATTERED SIGNALS

To allow real-time prediction of geometry, an instrument pod was developed for the tow-fish, containing pitch-roll and depth sensors. Data was sent to the surface, via a serial link, to the main LU parametric sonar control computer. This data was combined with data from the ship's sensors, including speed over the ground and water depth (corrected for ship heave). This was again achieved using a serial data burst once a second. All acquisition was carried out in parallel with other processes, by using software 'threads'. This allowed other processes including transmission control and data capture to continue uninterrupted.

### 9.4.2.3 Assumptions

The models presented here make a number of basic assumptions regarding the complex nature of sound propagation, within the water column and sediment layers. The modelling of sound propagation within the water column has received considerable interest, due to the level of the development of numerous highly sophisticated modelling methodologies, for application to a variety of ocean environments <sup>[9.2]</sup>. This, combined with a large amount of research into sound propagation within marine sediments, has led to the ability to predict propagation paths to a high degree of accuracy. The use of simplified models for application to real-time systems is, however, felt to be valid with currently available technology. These models make a number of assumptions but error estimations are felt to be sufficiently low when applied to the specified geometries to allow predictions from them to be held as valid.

Numerous authors have studied the reflection and scattering effects of sound at both the surface and seabed. A perfectly smooth sea surface would form a near perfect reflector. More realistic situations, however, result in reflection losses around 3 dB, at frequencies of 25 – 30 kHz <sup>[9.3, 9.4]</sup>. The degree of scattering at the surface, in relation to reflection, can be described in terms of the *Rayleigh parameter*  $R = kH \sin \theta$  where  $k$  is the wave number ( $2\pi/\lambda$ ),  $H$  is the rms 'wave height' and  $\theta$  is the grazing angle <sup>[9.5]</sup>. For  $R \ll 1$ , the surface acts primarily as a reflector and for  $R \gg 1$ , it acts as a scatterer. The degree of coherent reflection of sound energy at identical reflection and incidence angles is therefore increased at

lower frequencies and smoother conditions. In the case of a 10 kHz signal and a 1 m wave height, both scattering and reflection take place. Sufficient acoustic radiation may however be reflected at a similar incident and reflected angle to allow detection of a 'reflected' signal.

Reflection, scattering and transmission losses must also be considered in the case of incident sound radiation arriving at the seabed. The predictions of reflection losses are however more complex due to a greater variety of seabed materials and multi-layering of the seabed itself. Additional reflected signals might be lost due to the acoustic radiation penetrating the sediment layer. This radiation may then be re-reflected back from a sub-bottom sediment layer. The study of sound propagation at and in the seabed has also received considerable attention, [9.6, 9.7, 9.8] illustrate some of early work on reverberation in the sea.

Refraction effects due to variations in sound velocity with depth may also cause bending of the propagation path seen by the acoustic signal. Variations in sound velocity with depth, which gives rise to curved paths, result in variations in the propagation times for signals travelling along different paths. The application of *Snell's law* when applied to sound propagation in water of varying sound velocities has become one of the most important features of ray path modelling [9.2].

Although the exact prediction of sound behaviour at the surface and the seabed is complex, the treatment of both as flat-planed reflectors was felt valid in the conditions considered. The relative time of arrival and direction, rather than amplitude, forms the basis of the ray path models used. Additional effects, such as phase shifting and frequency smearing (due to the frequency of surface wave movement [9.9]) were ignored in this application, as the resultant variations in signal at the ranges of interest (< 500 m) were not considered significant. Care also had to be taken to use relatively simple models, which allow software to run in real-time.

The inclusion of sound velocity-depth profiles in the models was also considered. These, when available, could allow prediction of the propagation path to a greater accuracy. However estimation of the variation in path seen in typical profiles for water depths in the range 50-100 m were considered negligible. Consideration of bottom and surface reflected signals, in this simplified way, is however felt valid for the precision needed for application to the models in hand <sup>[9,10]</sup>.

### 9.4.3 Error measurement

A wide range of commercial inclinometer devices has been available for many years. These are most commonly based on an accelerometer system, capable of measuring angular displacement in the device. Normal operation involves a 'suspension' device within the accelerometer housing that is free to move under the action of gravity. Angular displacement of the housing will cause a relative displacement in the suspension device and the housing. This displacement is detected electronically and converted to a current pulse. This is then used to return the suspension device to its original equilibrium position. The current required returning the system to equilibrium is proportional to the angular displacement of the housing. A single accelerometer is used to measure displacement in one angular plane. Several devices, contained in a single package, allow measurements on further axes.

The use of a Sensorex two-axis device was proposed for the August 1994 trial. These are capable of operating at several different angular ranges and are robustly packaged to allow installation within the tow-fish. The outputs are proportional to the sine of the angular displacement in either axis. Additional interfaces allow conversion of these signals to a PC compatible format, using a RS232 serial link. Over a  $0^\circ$  to  $20^\circ$  range, a resolution of  $0.001^\circ$  is expected but only  $0.01^\circ$  if the range is increased to  $20^\circ$  to  $70^\circ$ . These resolutions are still well within the required accuracy. The use of devices like those in the SENSOREX range should allow direct measurement of the array's orientation in real-time, in a PC-compatible format.

In the case of the REBECCA project pitch, roll and depth sensors were included in the tow-fish. They were primarily used to measure tow fish performance in various sea states. This data was also used in post analysis, to determine actual seabed incident angles. An additional pod, containing similar sensors, was developed during the SIGMA project to provide real time data to the transmission system for the purpose of dynamic stabilisation.

#### **9.4.4 Dynamic stabilisation using electronic beam steering**

##### **9.4.4.1 Methodology**

Section 4.6 discusses the practical demonstration of the phase steering capabilities of the present system, in the generation of a swept signal across the face of a hydrophone. The electronic steering of the parametric array in at least one plane was therefore considered for the real time correction of attitude errors. Figure 9.5 shows the use of a fixed steer angle to align with the receiver. Because the array is only steerable in one axis, it was deployed with the steered axis in the fore-aft plane. The prediction of likely errors due to tow-fish depth, pitch and water depth, phase steering is then used to realign the beam. Figure 9.6 shows a flow diagram of the stabilisation process.

On receipt of a trigger signal, geometric data was collected from the tow-fish instrument pod and from the ship's ODAS system. This was then applied to the propagation model, allowing prediction of alignment error angles ( $\theta_E$ ). Comparison of a 'desired' ( $\theta_D$ ) angle and the 'actual' ( $\theta_A$ ) angle then gave a 'correction' ( $\theta_C$ ) angle to realign. This angle is the required steering angle needed to align with the target, including the pre-programmed, fixed angle for alignment and any current variations in alignment geometry.

The re-programming of a new phase-scattered signal, incorporating the correction angles, was however not practicable in real-time. Developments in hardware have allowed near instantaneous access of up to 32 separate memory areas, within the transmitter's signal memory. This memory can then be pre-loaded with up to 32 signals. This allows instantaneous accesses to a number of pre-formed beam-

patterns under software control. The most appropriate signal is then selected and transmitted. In the case where correction is outside the capability of the steering, or due to errors such as roll and yaw, data is logged to allow easier extraction of good data in post analysis. In the case of the SIGMA trials, likely miss signals were transmitted anyway and noted in the automatic logs. The use of discontinuous transmission methodology is also considered further in section 9.4.4.

Eight pre-formed signals with a total phase steer capability of approximately  $\pm 18^\circ$  give an angular separation of  $4.5^\circ$  between beams. A minimum separation of  $3^\circ$  gives a total spread of  $\pm 12^\circ$ . With 32 pre-formed beams, the whole  $36^\circ$  sector is covered, with  $1.125^\circ$  beam separation. In practice, operation of the system whilst experiencing pitch greater than  $\pm 10^\circ$  is unlikely, due to the problems in deploying the equipment in high sea states. The correction of errors up to  $\pm 10^\circ$  is possible to within  $1.4^\circ$ , using eight pre-programmed signals, and  $0.35^\circ$  using thirty-two signals, for geometries similar to that seen in Figure 9.5. An angular range criterion must be formed, defining the angular separation of each signal, based on the optimal operational conditions and the anticipated effects of ship movement and changes in water depth. In both the above cases correction of the error in the fore-aft plane should lead to successful data acquisition.

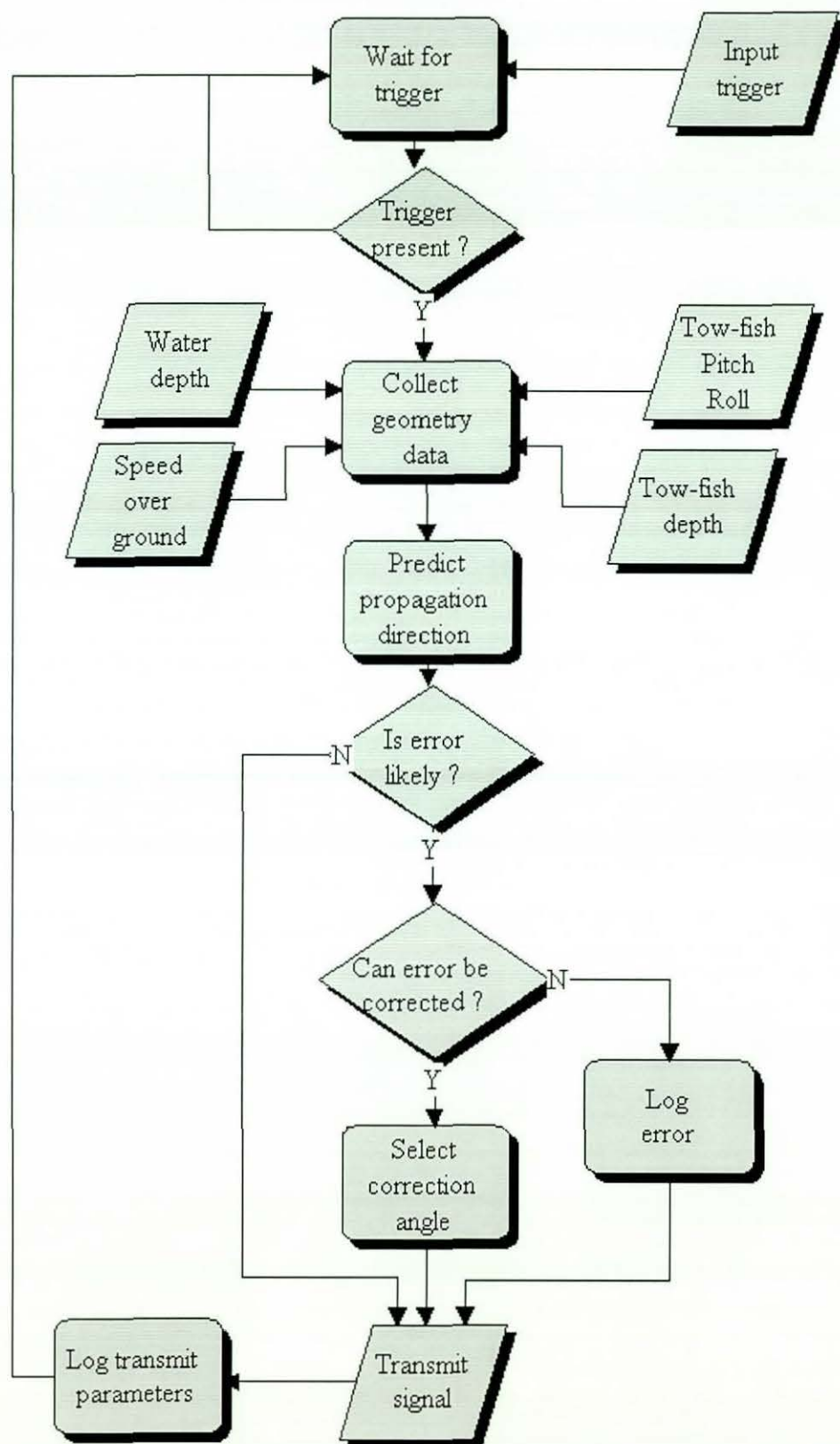


FIGURE 9.6 DYNAMIC STABILISATION FLOW CHART



#### 9.4.4.2 Results

Dynamic stabilisation using electronic beam steering was first tested during the second SIGMA trial. From the previous section, theoretical stabilisation to within  $0.35^\circ$  was possible for typical geometries. Due to the use of inverse procedures in the extraction of sediment geo-technical data, a large range of seabed incidence angles was required. With limited ship time this was achieved by introducing hysteresis into the stabilisation. The natural variation in pitch due to ship movement was used to allow the beam to move along the streamer array. The different seabed incident signals could then be monitored using different hydrophones without changing the streamer-tow-fish geometry. Limits were defined, to maintain the received signal within the streamer length. Figure 9.7 shows alignment error data for a series of transmissions. In this case an inter-beam angular spacing of  $4^\circ$  was allowed to cover the full length of the streamer array.

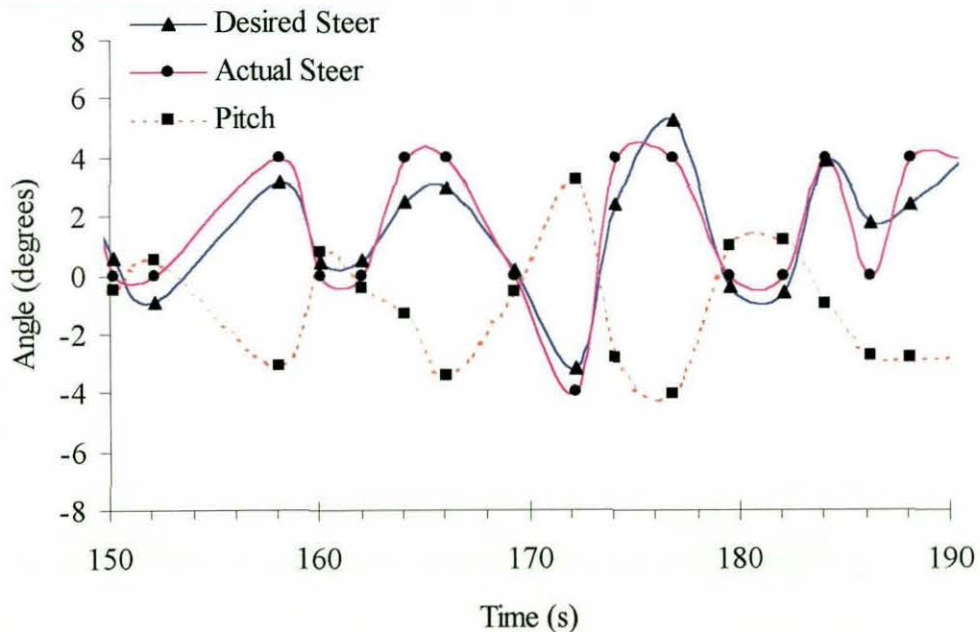


FIGURE 9.7 ALIGNMENT ANGLE VARIATION WITH TIME

Comparison of the desired and actual steer angles show a close correlation. The corrected signal angle closely follows the predicted required angle for successful data capture. The slight deviation is due to the deliberately introduced hysteresis in

the system. This can be seen more clearly in Figure 9.8, showing the error and compensated angles achieved using a  $4^\circ$  beam spread.

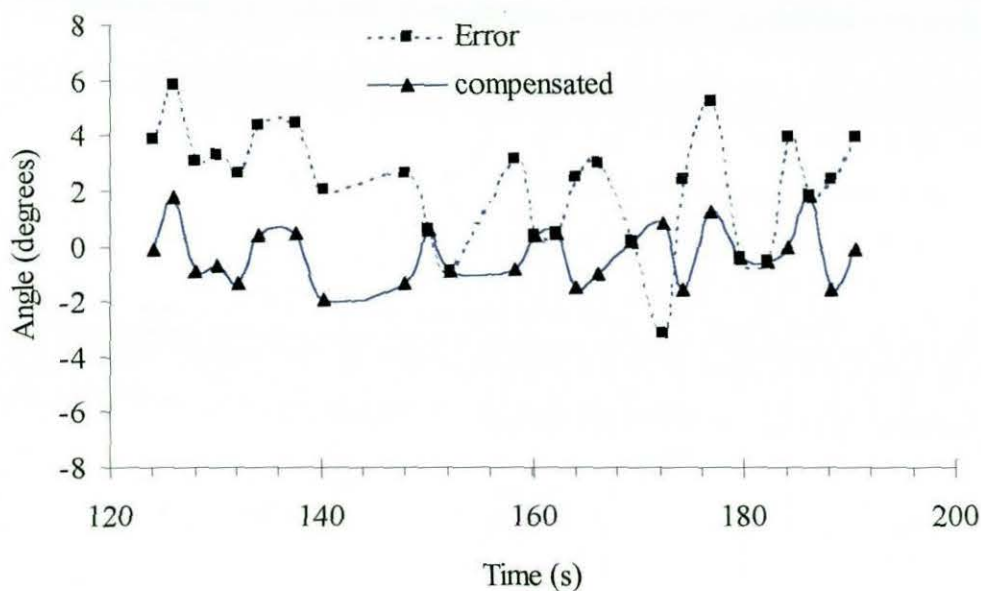


FIGURE 9.8 ERROR CORRECTION USING DYNAMIC STABILISATION

Variation in the compensated signal is never greater than  $2^\circ$ . This is due to the  $4^\circ$  beam separation selected in the pre-programmed signals. Beams at  $-12^\circ$ ,  $-8^\circ$ ,  $-4^\circ$ ,  $0^\circ$ ,  $4^\circ$ ,  $8^\circ$ ,  $12^\circ$ , etc. were computed; angles between  $2^\circ$  and  $-2^\circ$  would therefore use a  $0^\circ$  steer angle. Above  $2^\circ$ , a  $4^\circ$  steer is used and so on. Even with a deliberately coarse setting on the correction, data acquisition on the receiver array was achieved. Using all 32 beams over  $\pm 10^\circ$  sector would limit angular variation to within  $\pm 0.3125^\circ$ .

Figure 9.7 also show the variation of pitch in the tow-fish over the same time period. Angular variations in the range  $\pm 4^\circ$  were observed, in relatively good sea states, as with the examples above, and variations up to  $\pm 10^\circ$  were observed. It can also be seen in Figure 9.5 that the pitch error is in anti-phase with the desired steer angle, suggesting that a majority of the alignment errors are due to tow-pitch variations. This is consistent with the observation of tow-fish behaviour previously seen.

The seabed profiles, measured during the SIGMA trial, were generally flat with around a 5 m variation in depth over 1800 m horizontal plane. The system, however, easily compensated for variations in depth, from 90 to 50 m, maintaining bottom echo acquisition on the streamer.

Detailed analysis of target echo acquisition on the streamer is not possible at this time due to lack of dissemination of a full data set. Provisional analysis (Figure 6.14) shows good echo acquisition from the bottom and possibly sub-bottom layers, in a range of water depths, using dynamic stabilisation for a profile several km long. Acoustic bottom and sub-bottom data was acquired on 17 acoustic profile runs, over a five-day period, in a range of sea states provisional show good data acquisition.

#### **9.4.5 Discontinuous transmissions**

The present array configuration only allows phase steering in one plane of operation. This is in itself limited to a maximum steer range of  $\pm 18^\circ$ . If an error occurs either beyond this range of correction or along another axis (tow-fish roll, yaw) the majority of the signal may be lost. The establishment of a 'fire criterion' is proposed, limiting the transmission of non-linear signals to times when a useful signal is obtainable. In the case of roll errors movement of more than  $\pm 1.5^\circ$  will result in misalignment. The cyclic nature of the roll movement could however be used to transmit only when the array is pointing in the right direction. Figures 6.6, 6.7 show the roll-based errors for the tow-fish. These are generally in the range  $\pm 3^\circ$  to  $\pm 4^\circ$ , with a majority of the errors within  $\pm 1.5^\circ$ , which still allows good data acquisition.

### **9.5 Sea-bed inclination**

#### **9.5.1 Seabed profile using back-scatter**

The measurement of the seabed inclination is of primary interest in the establishment of an overall stabilised system. In the earlier trials, sites were

selected partially due to their 'flatness'. The use of back-scattered data was therefore considered as a tool for assessment of the seabed profile. In the case of a parametric array, the use high frequency seabed back-scattered components usually considered a bi-product of the non-linear generation was considered.

Test signals transmitted at the seabed may provide sufficient information on reflection to allow some determination of the seabed inclination. Several signals at various angles were considered, including a seabed incidence angle of  $0^\circ$  (depth sounding) and the use of two (or more) test signals transmitted at different angles.

### **9.5.2 Seabed slope through depth sounding**

One possible method for determining the seabed inclination is the use of the transducer array as an echo sounder. This would require the transmission of signals to a point on the seabed directly below the tow-fish. For this knowledge of the array's orientation relative to the vertical plane is required. A signal is then fired directly downwards, giving a depth sounding directly below the transducer. Two modes of operation are shown in Figure 9.9. The array is used parametrically at oblique angles; beam steering is then used to align the beam vertically. The high frequency, back-scattered signal from the seabed is then monitored on the receiver stave of the transducer.

The distance  $z$  is determined using the time taken  $t$  (s) for the first bottom echo from the test signal to return to the array. The transmission angle  $\theta_t$  relative to vertical is also known. The horizontal displacement  $d$  (m) of the two echoes on the sea-bed is then measured using the expression  $d = z \cdot \tan(\theta_t)$ . Regular depth soundings can produce an interpolated bottom profile. If the ship is travelling at a constant velocity  $v$  (m/s) the area directly below the tow-fish is insonified by the non-linear signal after time  $t = d/v$ .

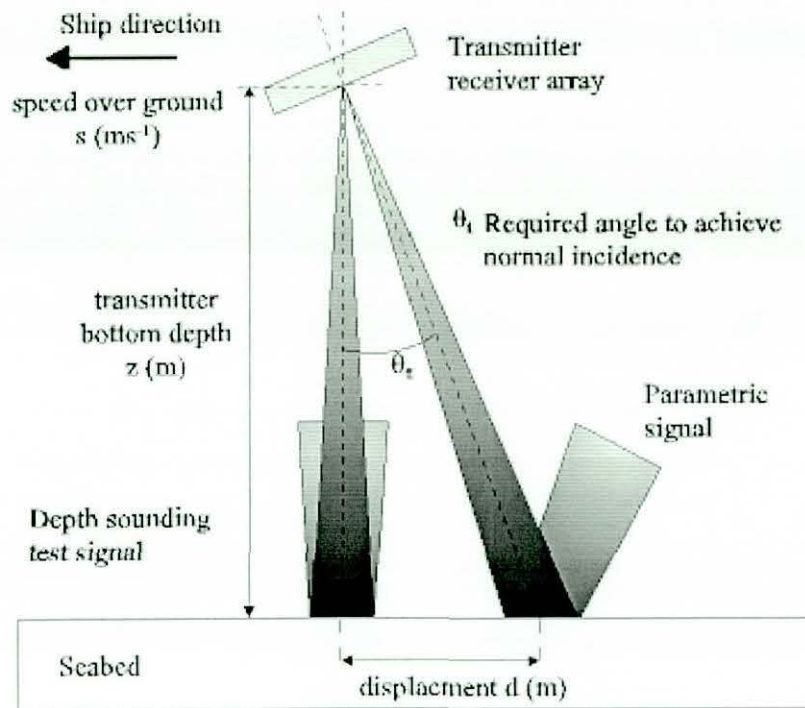


FIGURE 9.9 ECHO SOUNDING TO DETERMINE BOTTOM PROFILE

Each depth sounding can be treated mathematically, forming an interpolation of the seabed profile relative to vertical. Having determined the seabed profile, suitable angular adjustments to the transmitted signal can be made. As the depth-sounding echo is of normal incidence, even with variations in bottom angle, the shortest path signal should yield the depth profile. This has the advantage of a much higher echo source level than the method outlined in previously.

The resolution is dependent on the regularity of the depth soundings and the ship velocity. A ship speed of 2 knots corresponds approximately to a 1 m/s displacement along the seabed. Soundings every second would have around a 1m resolution. The use of a phase-steered signal to achieve the angular switching of the signals is thus appropriate. This is possible at deployment angles of 10° and 15° from the vertical inside the tow-fish but out of range at 20° due to the  $\pm 18^\circ$  steer limitation of the transducer array.

In the SIGMA trials the ship's own echo sounder was used. This data was then read directly into the propagation model software. Figure 9.10 shows a typical

profile. Less than a 5 m variation is seen in 1800 m horizontal displacement, corresponding to a seabed slope of less than  $0.2^\circ$ . The large variations seen at 395 s, 1050 s and 1450 s are due to errors in acquisition of data from the ship's echo sounder; these variations are ignored.

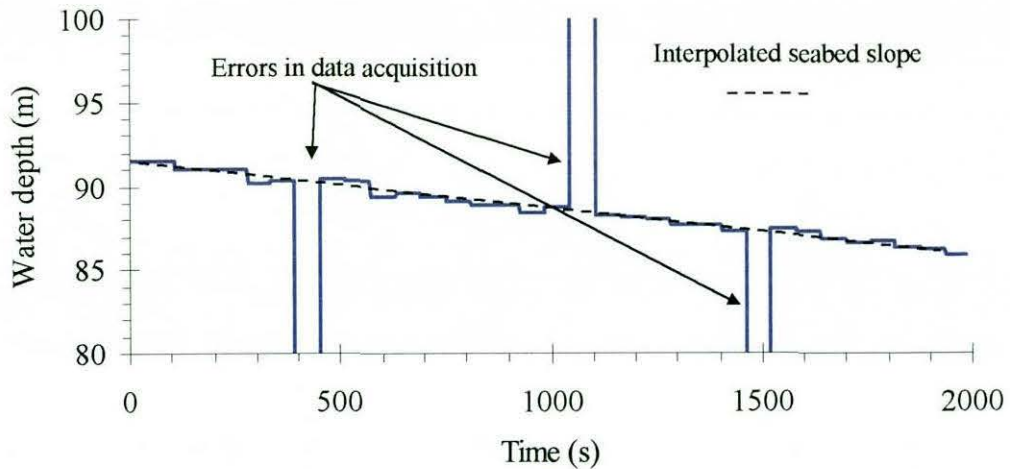


FIGURE 9.10 TIME DEPTH PROFILE GIVING SEABED SLOPE

## 9.6 Conclusions

Due to the difficulty of data collection from an oblique incidence bottom bounce sonar system whilst at sea, dynamic stabilisation of the transmit array was considered. The visualisation of specific geometries and transmitter-receiver alignment was carried out using simplified ray path models. Software and hardware was developed to allow the real-time modelling and visualisation of specified geometries. These were then developed to allow the real-time prediction of alignment errors, allowing correction in at least one plane using dynamic beam steering of the parametric array source. A number of pre-programmed signals on different angles were loaded into memory. On prediction of an alignment error the selected beam was adjusted to achieve the best possible transmission angle, compensating for transmission platform pitch and heave errors and variations in water depth in real time.

The system was tested over a five-day period from the Belgian research vessel, *Belgica*, off the French coast, in a range of water depths and sea states. Initial data analysis shows good acquisition of bottom and possible sub-bottom reflected non-linearly generated acoustic signals. Comparison with earlier trials without dynamic stabilisation shows a considerable improvement in signal acquisition and could prove essential in the development of a practical system for use at sea.

The development of a new transmit array was considered to allow steering in two axes. With access to each element of the array, beam steering could be achieved in two mutually perpendicular directions. This, combined with developments in the propagation path modelling, would allow for the correction of the errors introduced in the transmission platform in pitch, heave, roll, sway and yaw planes of movement in real-time.

## REFERENCES: Chapter 9

---

- 9.1 Carey-Smith C.  
The practical implementation of electronic stabilisation for sector scanning sonar displays  
*IEEE J.Oceanic Engineering*, Vol. 18, pp. 123-129, 1993.
- 9.2 Etter P.C.  
Underwater Acoustic Modelling (Principles, techniques and applications)  
Elsevier Applied Science, ISBN : 1-85166-528-5, 1991.
- 9.3 Urick R.J. and Saxton H.L.  
Surface reflection of short supersonic pulses in the oceans  
*J.Acoust.Soc.Am*, Vol. 19, No. 8, 1947.
- 9.4 Libermann L. N.  
Reflection of undersea sound from the sea surface  
*J.Acoust.Soc.Am*, Vol. 20, pp. 498, 1947.
- 9.5 Urick R.J.  
Principles of underwater sound  
*McGraw and Hill Book company*, 2<sup>nd</sup> edition, ISBN 0-07-066086-7, 1975.
- 9.6 Cron B.F. and Schumacher W.R.  
Theoretical and experimental study of underwater sound reverberation  
*J.Acoust.Soc.Am*, Vol. 33, No. 7, pp. 881-888, 1961.
- 9.7 Mackenzie K.V.  
Reflection of sound from a coastal bottom  
*J.Acoust.Soc.Am*, Vol. 32, No. 3, pp. 351-355, 1960.
- 9.8 Eyring C.F., Christensen R.J. and Raitt.  
Reverberation in the sea,  
*J.Acoust.Soc.Am*, Vol. 20, No. 4, pp. 462-475, 1948.
- 9.9 Roderick W.I. and Cron B.F.  
Frequency spectra for forward scattered sound from the ocean surface,  
*J.Acoust.Soc.Am*, Vol. 48, pp. 759, 1970.
- 9.10 Lepper P.A., Kaschner K., Connelly A.D. and Goodson A.D.  
Development of a simplified ray path model for estimating the range and depth of vocalising marine mammals.  
*Proc. Institute of Acoustics, Underwater Bio-sonar and Bioacoustic Symposium*, Loughborough University (UK), 1997.



## CHAPTER TEN

# CONCLUSIONS

### 10.1 System operation

The initial deployment of the 75 kHz non-linear sonar system at the Loch Duich trial site was considered satisfactory. The primary function of these early trials was to determine the system's operational characteristics. In general the system parameters were close to predicted theoretical levels. A maximum primary source level of around 245 dB re 1 $\mu$ Pa at 1m was obtained at the resonance frequency of 75 kHz and the transducer array bandwidth was found to be around 6 kHz. The array itself was shown to be power limited by saturation effects within the near-field of the primary frequencies.

The generation of difference frequency non-linear signals was proven and the source levels measured for frequencies in the range 1-13 kHz. Secondary source levels of around 195 dB re 1 $\mu$ Pa at 1m were observed for frequencies above 7 kHz with a maximum of around 196 re 1 $\mu$ Pa at 1m. This level was seen to drop to 178 dB re 1 $\mu$ Pa at 1m for non-linear generation at 1 kHz. At frequencies above 7 kHz the effect of decreasing the step-down-ratio to increase the parametric gain was balanced by the loss of primary frequency source level due to the transducer bandwidth limitations. This was seen as a reduction in the achievable source levels at both primary and secondary frequencies. These source levels were, however, sufficiently high to allow detection of both the direct and the reflected non-linear signals.

Both primary and secondary frequency beam-patterns were measured. The primary beam-pattern shows a number of side-lobes and a half-power beam-width of around 2.5° in both axis of the transducer array. Measurements of the secondary beam-patterns gave beam-widths of from 2.5° to 6° for frequencies between 11 and 3 kHz respectively. These secondary beam-patterns showed greatly reduced

side-lobe radiation compared with the primary patterns. Beam steering over a  $\pm 18^\circ$  sector was demonstrated with both primary and secondary frequency signals, although some loss of source level was seen as the steer angle approached the outer limits of the steer sector. Within-pulse sector scanning was also demonstrated at both primary and secondary frequencies.

## **10.2 Use of a parametric array for sediment classification.**

Open-sea trials conducted during the REBECCA and SIGMA projects saw the development of a system to enhance sub-seabed sediment classification techniques using acoustics. Two parametric sources were deployed from a tow-fish behind a surface vessel in water depths ranging from 40-90 m. The seabed was insonified using vertical (40 kHz) and oblique incident non-linear arrays (75 kHz). Back-scattered and forward-scattered oblique incident data was then collected using a hydrophone and a streamer receiver array respectively.

Initial results showed that the concept of collection of oblique incident data using this deployment was feasible but problematic. Transmitter-receiver alignment was particularly hard to achieve, and therefore good data collection, consistent with a highly directivity source ( $\sim 3^\circ$  beam-width) due to variations in water depth and transmission platform motion. The use of dynamic beam steering of the parametric array was therefore considered to achieve real-time correction of alignment errors in at least one plane of motion. The development of ray path models for the through-water and sediment propagation of acoustic signals combined with real time sensor data (tow-fish pitch, roll, depth and water depth) allowed the prediction of likely alignment errors. This was then used to realign the transmitter array using beam-steering in real-time. Results from trials held off the French coast in 1999 showed a considerable improvement in the data collection capability of the system using real-time stabilisation. These trials also provided evidence of bottom and sub-bottom-scattered signals using an oblique incident parametric source.

Work was also conducted to develop of a new parametric system for the Indian Institute of Technology. A 16 x 2 element 40 kHz primary array was designed and tested. The development of compact power amplifiers and a new PC based signal synthesis system was carried out. An open-water trial for testing the system was carried out on Lake Edukki, Kerala State in Southern India. The operation of the system was considered satisfactory and evidence of secondary frequency generation at a range of frequencies was observed at relatively short ranges in fresh water. Source levels and beam-patterns at both primary and secondary frequencies showed reasonable approximation with expected theoretical values.

### **10.3 Detection of embedded objects**

Two sea-trials were conducted to investigate the use of a parametric sonar for detection and classification of sediment buried objects. These took place on the Loch Duich trial site. The first involved the free-field measurement of a thin-walled cylindrical target, both air-filled and water-filled, at a range of aspect angles. Data collection was made at both the primary and secondary frequencies for direct and target echoes at target aspect angles from over a 270° sector including broadside and end-cap positions. In the case of a water-filled target evidence of internally reflected signals was observed at the end-cap and broadside positions. This data allowed some assessment of the cylinder geometry in terms of length and diameter.

The second phase measurements were conducted using an identical target, water filled only. This was placed on the seabed and allowed to partially embed (up to approximately 50%). The target was then insonified at a range of aspect angles and seabed incident angles. Measurements were again made in both frequency ranges of both the direct and target-scattered signals.

Analysis of direct and back-scattered data showed good evidence of the internal penetration of low frequency signals into a target placed at the water-sediment boundary. Evidence of the detection possibility of the target at secondary frequencies was also seen at angles around the broadside position due to the

presence of the target. Study of back-scattered target echo structures revealed front face specular returns in the broadside position and some evidence of low frequency resonance effects occurring. These signal components were observed up to  $\pm 20^\circ$  from the broadside position, and may yet provide a valuable detection classification mechanism. Little or no detection capabilities were observed from the target end-cap position whilst partially embedded. Additional data from inside the target showed a complex internal reflection structure for incident acoustic signals.

#### **10.4 Summary**

An understanding of the principles behind non-linear acoustics is well established, with the development of a substantial body of work both theoretical and experimental over the last forty years. More recent years have seen the practical implementation of non-linear sonar systems for a variety of applications. The work outlined in this thesis summarises the development of a new parametric sonar system and its application to a variety of *real* tasks. The work carried out has involved the development of both a hardware and a software system for practical implementation. Experimental work and subsequent data analysis has been conducted at all stages of the development allowing the establishment of a practical acoustic tool. The current system is felt to be well optimised for the compromised parameters of size, frequency, directivity and achievable power levels, combined with dynamic beam-steering and the development of real-time stabilisation techniques, making it a viable option for a variety of applications

#### **10.5 Future work**

The development of the current dynamic stabilisation system used with the transducer array is limited to the correction of errors in just one plane. The development of a two-dimensional steerable array has been proposed. This would allow steering in two mutually perpendicular axes. Correction for a much wider range of movement would then be possible. Advances in compact power supplies

and multi-channel signal synthesis now make this a viable option for two-dimensional steering in real time.

Software models are also currently limited to a single plane of motion, due to the limits in the steering of the array. This could be extended to the additional correction plane available with two-dimensional steering. These models were deliberately kept simple to allow computation in real-time. They could be further extended to include variable sound velocity-depth profiles and a variety of sub-seabed sediment structures. These software tools have already proven valuable not only in terms of the stabilisation systems but in the visualisation of geometries at the planning and post analysis stages of a variety of experiments. Optimised programming and increased processing power may also make the real-time estimation of echo levels at a range of frequencies viable. The development of more sophisticated and hopefully more accurate three-dimensional models for visualisation of the acoustic propagation in the water and sediment layers is seen as a way forward for better understanding of the use of acoustics in these environments.

Also under consideration is the use of the high frequency component of the non-linear signal for assessment of seabed topography. A better understanding of the seabed slope, roughness, etc. can only help in the understanding of the environment under analysis and improve the chances of good data collection. Work already conducted (but not presented here) has shown that the back-scattered primary frequency signals could provide valuable information about seabed slope. It is foreseen that this information could be obtained without interruption of the normal operation of the parametric array and could then be incorporated into the visualisation models for the non-linear components, again enhancing the systems performance.

Provisional analysis of target echo data carried out as part of the DEO project has suggested the possibility of embedded object detection using a parametric array. Relatively simple analysis gave some insight to the complex echo structure associated with the insonification of a buried target. Application of more

sophisticated signal processing techniques, already in existence and the development of new optimised systems should further enhance the understanding of the acoustic wave interaction with a variety of target types. The use of more advanced signal processing and improved receiver technology would allow considerable improvements in target echo acquisition and therefore detection. Similarly the use of improved characterisation methods in terms of the target acoustic 'signature', measured in the free-field could then be used to perform target detection and classification. These optimised methodologies could then be applied to a real-time system allowing the development of a practical sonar system for detection and characterisation of buried objects.

The on-going development of optimised inversion techniques for the extraction of bottom sediment geo-physical properties from acoustic echoes with improved data collection capabilities should lead to development of a practical remote sensing, sediment classification system. Comparison of both tank and real acoustic data can be used to validate inversion algorithms. This combined with 'ground truthing' with real sediments would then hopefully lead to a better understanding of the relationship between geo-physical sediment properties and acoustic wave propagation and therefore enhance the development of a practical sediment classification tool.

## AUTHORS PUBLICATIONS

- 1 Cook J. C., Goodson A. D., Lepper P. A. and Woodward B.  
The design and evaluation of a phase steered parametric sonar system intended for sediment characterisation.  
*Journal of the Society for Underwater Technology*, Vol. 22, No 2, Winter 1996-1997, pp. 43-54; ISSN 0141 0814, 1997.
- 2 Lepper P. A., Kaschner K., Connelly P. R. and Goodson A. D. Development of a simplified ray path model for estimating the range and depth of vocalising marine mammals;  
*Institute of Acoustics, Underwater Bio-Sonar and Bioacoustics*, 19(9), December 1997, pp. 227-234; ISSN: 309 8117, 1997.
- 3 Kaschner, Goodson A D, Connelly P R and Lepper P A  
Species characteristics features in communication signals of cetaceans: Source level estimates for some free ranging North Atlantic odontocetes;  
*Institute of Acoustics, Underwater Bio-Sonar and Bioacoustics*, 19(9), December 1997, pp. 217-226; ISSN: 309 8117, 1997.
- 4 Woodward B., Goodson A. D., Cook J. C. and Lepper P. A.  
Sea bed characteristics using non-linear acoustics;  
*Proc. 2<sup>nd</sup> European Conference on Underwater Acoustics, Copenhagen, Denmark, 4-8 July 1994*, Edited by Bjorno L, Elsevier Science Publishers BV, ISBN 92-826-8000-2, ISSN 1018-5593, pp. 875-880, 1994.
- 5 Woodward B., Cook J. C., Goodson A. D. and Lepper P.  
A phase steered parametric array for sub-bottom profiling;  
*Proceedings of the 6<sup>th</sup> International Conference on Electronic Engineering in Oceanography, Cambridge, UK, 19-21 July 1994*, IEE Conference Publication No 394, pp. 77-82, 1994.
- 6 Mayo R. H., Klinowska M., Goodson A. D., Sturtivant C. R. and Lepper P. A. Surfacing behaviour of the Harbour Porpoise (*Phocoena phocoena*); Document reference: IWC/SC/47/SM34, *International whaling Commission Scientific Committee*, Dublin, pp. 16, 1995.
- 7 Coggrave C. R., Goodson A. D., Lepper P. A. and Woodward B.  
An experimental technique for tracking dolphins in the vicinity of a trawl net;  
*Proceedings Acoustics Society India Silver Jubilee National Symposium on Acoustics(NSA-95), 21-23 December 1995, New Delhi, India*; in *journal of the Acoustical Society of India*, Vol. XXIII, No 4, pp. 194-198, 1995.
- 8 Lepper P. A. and Woodward B.  
Technique for achieving dynamic stabilisation of a sonar array platform;  
*Proceedings Acoustics Society India Silver Jubilee National Symposium on Acoustics(NSA-95), 21-23 December 1995, New Delhi, India*; in *journal of the Acoustical Society of India*, Vol. XXIII, No 4, pp. 181-186, 1995.

- 9 Goodson A. D. and Lepper P. A.  
A simple hydrophone monitor for cetacean acoustics;  
*9<sup>th</sup> Annual Conference of the European Cetacean Society*, Lugano, Switzerland, in *European Research on Cetaceans – 9*, Edited by Evans P G H and Nice H, pp. 46-49, 1995.
- 10 Mayo R. H., Goodson A. D., Klinowska M., Sturtivant C. R. and Lepper P. A.  
The use of a drilling rig in tracking the Harbour Porpoise (*Phocoena phocoena*); *9<sup>th</sup> Annual Conference of the European Cetacean Society*, Lugano, Switzerland, in *European Research on Cetaceans – 9*, Edited by Evans P G H and Nice H, pp. 92-95, 1995.
- 11 Mayo R. H., Goodson A. D., Klinowska M., Sturtivant C. R. and Lepper P. A.  
Tracking cetaceans by sonar click detection;  
*9<sup>th</sup> Annual Conference of the European Cetacean Society*, Lugano, Switzerland, in *European Research on Cetaceans – 9*, Edited by Evans P G H and Nice H, 1995.
- 12 Connelly P., Woodward B. Goodson A. D., Lepper P. A. and Newborough D.  
Remote sensing methods for cetacean interactions with pelagic trawl fishing gear;  
*11<sup>th</sup> Annual Conference of the European Cetacean Society*, Stralsund, Germany, in *European Research on Cetaceans – 11*, Edited by Evans P, Parson E and Clark S, published: Kiel University, pp. 23-25, 1997.
- 13 Kaschner K., Lepper P. A. and Goodson A. D.  
Analysis of Cetacean sounds obtained from a hydrophone attached to a pelagic trawl;  
*11<sup>th</sup> Annual Conference of the European Cetacean Society*, Stralsund, Germany, in *European Research on Cetaceans – 11*, Edited by Evans P, Parson E and Clark S, published: Kiel University, pp. 26-29, 1997.
- 14 Connelly P. R., Goodson A. D., Kaschner K., Lepper P. A., Sturtivant C. R. and Woodward B.  
Acoustic techniques to study cetacean behaviour around pelagic trawls;  
*ICES Annual Science Conference 1997*, October 1997, 85<sup>th</sup> Statutory Meeting, Baltimore, USA, pp 137, 1997.
- 15 Goodson A. D., Simmonds E. J., Curtis T., Lepper P. A. and Armstrong E.  
Implementing a wide band constant beam-width constant source level: A variable aperture approach;  
*Abstracts of the ICES International Symposium on Fisheries and Plankton Acoustics*, 12-16 June 1995, Aberdeen, Scotland, pp. 12, 1995.
- 16 Cook J. C., Goodson A. D., Lepper P. A. and Woodward B.  
The Loughborough University parametric sonar system;  
*Proceedings of the 1<sup>st</sup> European Workshop on Parametric Arrays*, April 1995, C.P.E Lyon, Lyon, France, pp. 35-38, 1995.



- 17 Woodward B. and Lepper P. A.  
Real time dynamic beam steering with a parametric array;  
*Proceedings of the 1<sup>st</sup> European Workshop on Parametric Arrays*, April 1995, C.P.E Lyon, Lyon, France, pp. 39-42, 1995.
- 18 Woodward B., Cook J. C., Goodson A. D. and Lepper P. A.  
The REBECCA project: Acoustical remote sensing with a parametric sonar;  
*Proceedings of the 2<sup>nd</sup> MAST Days and EUROMAR Market*, 7-10 November 1995, Sorrento, Italy, 1995.
- 19 Goodson A. D., Connelly P. R. and Lepper P. A.  
Aversive sounds and the Harbour Porpoise (*Phocoena phocoena*);  
International BioAcoustics Council XV IBAC, October 1996, University of Pavia, Pavia, Italy, pp. 15, 1996.
- 20 Goodson A. D., Amundin M., Mayo R. H., Newborough D., Lepper P. A., Lockyer C., Larsen F. and Blomquist C.  
Aversive sounds and sound pressure levels for the Harbour Porpoise (*Phocoena phocoena*): An initial field study;  
*Annual Science Conference of the International Council for Exploration of the Sea*, Baltimore, USA, pp. 5, 1997.
- 21 Amundin M., Blomquist C., Larsen F., Lepper P. A., Lockyer C., Goodson A. D., Mayo R. H. and Newborough D.  
The initial reaction of two wild Harbour Porpoises to a wide-band acoustic gill-net deterrent;  
*Abstract of the 25<sup>th</sup> International Symposium of the European Association for Aquatic Mammals*, Duisburg, Germany, pp. 1, 1997.
- 22 Mayo R. H., Amundin M., Goodson A. D., Lockyer C., Lepper P. A., Newborough D., Larsen F. and Blomquist C.  
Observing surfacing behaviour of wild harbour porpoises;  
*11<sup>th</sup> Annual Conference of the European Cetacean Society, Stralsund, Germany, in European Research on Cetaceans – II*, Edited by Evans P, Parson E and Clark S, published: Kiel University , pp. 4, 1997 .
- 23 Kaschner K., Goodson A. D., Connelly P. R. and Lepper P. A.  
Estimating source levels for communication signals from some North Atlantic odontocete species in open water;  
*Abstracts from the World Marine Mammal Science Conference*, 1 (1), January 1998, pp. 70, 1998.
- 24 Woodward B., Lepper P. A., Vyas A. L., Balaji-Raj V. S., Taroudakis M. I. and Papadakis P. J.  
Acoustic Characterisation of Undersea Sediments To Initiate Commercial Applications (*ACUSTICA*);  
*Proceedings of the 4<sup>th</sup> European Conference on Underwater Acoustics*, 21-25 September 1998, Rome, Italy, 1998.

- 25 Cook J. C., Goodson A. D., Lepper P. A. and Woodward B.  
Measurement of acoustic scattering by a cylindrical shell using a parametric sonar;  
*Proceedings of the 4<sup>th</sup> European Conference on Underwater Acoustics*, 21-25 September 1998, Rome, Italy, 1998.
- 26 Lepper P. A. and Woodward B.  
Signal processing considerations for the detection and characterisation of objects on the seabed;  
*Proceedings of the Institute of Acoustics Conference on Sonar Signal Processing*, 21-23 December 1998, Weymouth, UK, 1998.

